Rochester Institute of Technology
RIT Digital Institutional Repository

Theses

8-30-2013

Comprehensive Mapping and Benchmarking of Esaki Diode Performance

David John Pawlik

Follow this and additional works at: https://repository.rit.edu/theses

Part of the Electronic Devices and Semiconductor Manufacturing Commons, and the Other Electrical and Computer Engineering Commons

Recommended Citation
Pawlik, David John, "Comprehensive Mapping and Benchmarking of Esaki Diode Performance" (2013). Thesis. Rochester Institute of Technology. Accessed from

This Dissertation is brought to you for free and open access by the RIT Libraries. For more information, please contact repository@rit.edu.

R·I·T

Comprehensive Mapping and Benchmarking of Esaki Diode Performance

by

David John Pawlik

A dissertation submitted in partial fulfillment of the requirements
for the degree of Doctorate of Philosophy in Microsystems Engineering

Microsystems Engineering Program
Kate Gleason College of Engineering

Rochester Institute of Technology
Rochester, New York
August 30, 2013

Comprehensive Mapping and Benchmarking of Esaki Diode Performance
by
David Pawlik

Committee Approval:

We, the undersigned committee members, certify that we have advised and/or supervised the candidate on the work described in this dissertation. We further certify that we have reviewed the dissertation manuscript and approve it in partial fulfillment of the requirements of the degree of Doctor of Philosophy in Microsystems Engineering.

____

Prof. Sean L. Rommel Date
Associate Professor, Electrical and Microelectronic Engineering Department

____

Prof. Santosh K. Kurinec Date
Professor, Electrical and Microelectronic Engineering Department

____

Prof. Seth Hubbard Date
Associate Professor, Physics Department

____

Prof. Suman Datta Date
Professor, Electrical Engineering Department

____

Prof. Andreas Savakis Date
Professor, Computer Engineering Department

Certified by:

____

Prof. Bruce Smith Date
Director, Microsystems Engineering Program

____

Prof. Harvey Palmer Date
Dean, Kate Gleason College of Engineering

ABSTRACT

Kate Gleason College of Engineering
Rochester Institute of Technology

Degree: Doctor of Philosophy **Program**: Microsystems Engineering

Authors Name: David John Pawlik

Advisors Name: Prof. Sean L. Rommel

Dissertation Title: Comprehensive Mapping and Benchmarking of Esaki Diode Performance

The tunneling-FET (TFET) has been identified as a prospective MOSFET replacement technology with the potential to extend geometric and electrostatic scaling of digital integrated circuits. However, experimental demonstrations of the TFET have yet to reliably achieve drive currents necessary to power large scale integrated circuits. Consequentially, much effort has gone into optimizing the band-to-band tunneling (BTBT) efficiency of the TFET. In this work, the Esaki tunnel diode (ETD) is used as a short loop element to map and optimize BTBT performance for a large design space. The experimental results and tools developed for this work may be used to (1) map additional and more complicated ETD structures, (2) guide development of improved TFET structures and BTBT devices, (3) design ETDs targeted BTBT characteristics, and (4) calibrate BTBT models. The first objective was to verify the quality of monolithically integrated III-V based ETDs on Si substrates (the industry standard). Five separate GaAs/InGaAs ETDs were fabricated on GaAs-virtual substrates via aspect ratio trapping, along with two companion ETDs grown on Si and GaAs bulk substrates. The quality of the virtual substrates and BTBT were verified with (i) very large peak-valley current ratios (up to 56), (ii) temperature measurements, and (iii) deep sub-micron scaling. The second objective mapped the BTBT characteristics of the $In_{1-x}Ga_xAs$ ternary system by (1) standardizing the ETD structure, (2) limiting experimental work to unstrained (i) GaAs, (ii) $In_{0.53}Ga_{0.47}As$, and (iii) InAs homojunctions, and (3) systematically varying doping concentrations. Characteristic BTBT trendlines were determined for each material system, ranging from ultra-low to ultra-high peak current densities (J_P) of 11 μA/cm^2 to 975 kA/cm^2 for GaAs and $In_{0.53}Ga_{0.47}As$, respectively. Furthermore, the BTBT mapping results establishes that BTBT current densities can only be improved by ~2-3 times the current record, by increasing doping concentration and In content up to ~75%. The E. O. Kane BTBT model has been shown to accurately predict the tunneling characteristics for the entire design space. Furthermore, it was used to help guide the development of a new universal BTBT model, which is a closed form exponential using 2 fitting parameters, material constants, and doping concentrations. With it, J_P can quickly be predicted over the entire design space of this work.

ACKNOWLEDGMENTS

It was my parents (John and Diane) who, through their nurturing and encouragement, set me on the path towards becoming an intellectual in the areas of math, science, and engineering. They never needed to push me in any direction. However they were, and are, great at showing me the various avenues of approach and helping me peer down the way to judge the best course of action. I am forever grateful to them for being superb parents. I never doubted being able to complete this dream, just like I know they will always be there for me (in one way or another). Their work ethic and strength of character continually inspires me to improve my own character. I also want to thank my brother, Michael, who has always had my back. His support and encouragement has always been there, sometimes behind the scenes, even when I didn't realize I needed it. Recently he has shown me, by example, what it takes to be a strong and effective family member.

Prof. Rommel is personally responsible for retaining me at RIT for many years past my undergraduate days, and I have loved all of it. As an intern in his research group I fell in love with the topic area, and gained a great relationship with my advisor and mentor. I cannot imagine having completed this work with anyone else. I know that we will continue our friendship into the future, and look forward to many more discussions regarding research, lab work, fellow researchers, and of course pop culture science fiction.

I would like to thank Prof. Lynn Fuller for stimulating my initial interest and pursuit in this highly technical and diverse profession. All of my professors, especially committee members, have added invaluable knowledge and skills to my repertoire over the years. It is in large part due to their passion for this profession that I am expertly prepared and enthusiastically ready to actively contribute to the next generation of micro/nano electronic technologies. Additionally, I may pursue a professorship in order to help share my own passion and knowledge to future generations.

It would not have been possible to complete any of the experimental results in this work without the uncounted hours of help from the Semiconductor & Microsystems Fabrication Laboratory (SMFL) staff. Specifically I would like to thank Richard Battaglia, Thomas Grimsley, John Nash, David Yackoff, Scott Blondell, Prof. Karl Hirschman, Sean O'Brien, and Bruce Tolleson. They have always generously donated their time, knowledge, and expertise. This work would have been relegated to the realms of theory if it were not for them and the fabrication facility at RIT.

Finally, my sanity throughout any year ebbed and flowed with my friends and family. I apologize to Paul Thomas, for spending so much time cursing out my computer while in the office or explaining how I "hate" X, Y, and Z. But you will never know how much that helped. Furthermore, game nights with Paul and Athena, Andy, and Marybeth were/are always welcome. Finally, beating up my body while mountain biking (thanks Athena) always seems to heal my mental state. And that is largely due to riding with Paul, Athena, Josh, Ben, Shone, Marybeth, John, Ryan, Scott, Katie, Carrie, Chelse, and everyone else I've met on the trails. Though we are separated by 1 small continent… let's peddle!

TABLE OF CONTENTS

List of Tables viii

List of Figures ix

List of Abbreviations xvi

List of Variable xviii

1. Introduction and Motivation 1

    1.1. Introduction 1

    1.2. Importance of Subthreshold Slope 2

    1.3. Subthreshold Limit of MOSFETs 5

    1.4. Objective, Implementation, and Application of Work 7

2. Theory of Quantum Tunneling Devices 12

    2.1. Esaki Tunnel Diodes 12

    2.2. Analytical Band-to-Band Tunneling Models 14

    2.3. Tunneling FET 17

    2.4. TFET Subthreshold Slope 18

3. Tunnel Diode Modeling 25

    3.1. General Discussion on BTBT Models 27

    3.2. Kane Model: Assumptions, Approximations, and Form 30

        3.2.1. Kane Model Equation 31

        3.2.2. Common BTBT Probability Error 34

        3.2.3. Overlap Integral 36

            3.2.3.1. Detailed Behavior of Overlap Integral 38

    3.3. Fermi Energy Calculations 45

    3.4. Relative Effective Mass Parameters 48

3.5. Kane Model Program ... 49

3.5.1. KMP Flow & Operation ... 52

3.6. Conclusion ... 55

4. Ge and III-V Tunnel Diodes on Si ... 60

4.1. Ge/III-V on Si Integration Methods ... 61

4.1.1. Relaxed, Compositionally Graded Buffers ... 63

4.1.2. Substrate Transfer Process ... 64

4.1.3. Aspect Ratio Trapping Hetero-Integration ... 65

4.2. Materials Analysis of Ge on Si ART ... 67

4.3. Ge on Si Tunnel Junction ... 68

4.3.1. Ge ETD Results and Conclusions ... 70

4.4. GaAs on Si Tunnel Junctions ... 72

4.4.1. Basic Fabrication Process ... 78

4.4.2. DC Electrical Results ... 79

4.4.3. Temperature Analysis ... 86

4.4.4. Deeply Scaled Tunnel Junctions ... 92

4.5. Conclusions ... 96

5. $In_{0.53}Ga_{0.47}As$ Esaki Tunnel Diodes ... 103

5.1. Ultra High Current Density $In_{0.53}Ga_{0.47}As$ Esaki Diodes ... 105

5.1.1. Electrical Characterization of High Current Density $In_{0.53}Ga_{0.47}As$ ETDs ... 110

5.1.2. Modeling InGaAs-1 and InGaAs-2 ... 116

5.1.3. Benchmarking $In_{0.53}Ga_{0.47}As$ ETDs ... 122

5.2. Low Current Density $In_{0.53}Ga_{0.47}As$ ETD ... 123

5.2.1. Electrical Results for InGaAs-3 ... 124

5.2.2. Investigating the Low J_P of InGaAs-3 ... 126

5.2.3. Simulation Results for InGaAs-3 ... 128

5.3. Medium Current Density $In_{0.53}Ga_{0.47}As$ ETDs ... 129
5.3.1. Results for Medium Current Density ETDs ... 131
5.4. Conclusions ... 133
6. GaAs and InAs Esaki Tunnel Diodes ... 138
6.1. GaAs Esaki Diodes ... 139
6.1.1. Results for GaAs ETDs ... 141
6.2. InAs Esaki Diodes ... 144
6.2.1. InAs ETD Electrical Results ... 147
6.2.2. NDR from Metal on P^+ InAs Contacts ... 150
6.3. Conclusions ... 153
7. Universal BTBT Model ... 157
7.1. Final Mapping of $In_{1-x}Ga_xAs$ BTBT Characteristics ... 157
7.2. Universal BTBT Model ... 160
7.2.1. Model Limitations ... 165
8. Conclusions ... 166
8.1. Beyond Unstrained Homojunction Esaki Diodes ... 166
8.2. Enhancements to the Kane Model Program ... 169
8.3. Summation of Work Completed ... 171
8.3.1. Developed Tools and Procedures ... 172
8.3.2. Experimental Results ... 174
Appendix A. Kane Model Program ... 177
Appendix B. ImageJ Area Analysis Macro ... 196
Appendix C. Fabrication & Processing Traveler ... 200
Appendix D. Peak Including Valley Extraction Tool ... 204

LIST OF TABLES

1.1 "Constant field scaling" (CFS) and "general field scaling" (GFS) schemes 2

2.1 Experimental Reports of TFETs... 23

3.1 Doping parameters, Fermi energies, and calculated D values used for detailed analysis if (i) cone, (ii) mesa, and (iii) complex mesa shapes using fictitious mater parameters 44

3.2 Material parameters stored in the Excel file used by KMP 51

4.1 Doping concentrations as measured by SIMS. Middle columns are maximum absolute values measured adjacent to the tunnel junction. Right hand columns are the maximum compensated values; |C-Si|. 76

4.2 TD1, TD2, TD3, and TD4 parameters as well as the highest reported PVCR TDs fabricated on Si, GaAs, and InP substrates.. 86

5.1 Constants for calculating bandgap narrowing (BNG). 116

5.2 Modeling results for InGaAs-1 and InGaAs-2. The Kane model is not setup to include an *i*-layer (d), and therefore all J-V results assume d is 0 nm............................. 117

6.1 Modeling results for all three GaAs ETDs. As expected, w_d, tunnel barrier width, $E_{F,p}$, E_V, and J_P proportionately increase with each other. $E_{F,p}$ for GaAs-1 is greater than E_V, and therefore lies within the bandgap.. 141

6.2 Modeling results for all three InAs ETDs. As expected, w_d and tunnel barrier width decrease as doping, $E_{F,n}$, and J_P increase. Interestingly, V_P and "*n*" significantly increases, even though $E_{F,p}$ remains constant 148

8.1 Breakdown of the different ETD structures fabricated and characterized for this work.. 170

LIST OF FIGURES

1.1 Generic I_{DS}-V_{GS} characteristics for an (a) ideal switch, (b) quadratic MOSFET model, and (c) actual subthreshold characteristics. 3

1.2 Generic I_{DS}-V_{GS} characteristics showing the V_{DD} scaling for a (i) Si channel MOSFET with low I_{Off}, (ii), Si channel MOSFET with large I_{Off}, (iii) high mobility III-V channel MOSFET, and (iv) TFET. 4

1.3 The conduction band portion of the source, body, drain (left to right) regions of a MOSFET; including electron carrier concentration. 5

1.4 The conduction band portion of the source, body, drain (left to right) regions of a MOSFET with engineered electron distribution. 7

2.1 ETD device structure. 12

2.2 (a) I-V characteristic, and schematic band diagram for (b) reverse bias, (c) equilibrium, (d) peak tunneling current, (e) minimum direct tunneling current, and (f) diffusion current for a generic ETD 13

2.3 J_P versus PVCR for key ETD structures of various material systems. InP substrate refers to lattice matched InGaAs ETD 14

2.4 Simplified band diagram used for Kane's BTBT model [2]. 15

2.5 TFET Device structure 16

2.6 Band diagrams showing the operation of the TFET: (a) at equilibrium, (b) with an applied V_{DS}, and (c) V_g turned on 19

2.7 Calculated SS limits of TFETs 22

3.1 Left (a), Generic E-*k* diagram indicating direct bandgap (Γ-valley), indirect bandgaps (L- and X-valleys), and light-, heavy, and split-off holes (adopted from [13]). Right (b), generic E-*k* diagram showing parabolic tunneling path through imaginary *k*-space that carriers travel when through the forbidden bandgap (adopted from [1]) 30

3.2 Sketch of ETD band diagram with simplified, triangular depletion region. This is the idealized shape of the bands used in the Kane model 32

3.3 Left (a), plot of Term 1 on the left axis and T_{Kane} on the right axis. Right (b), Term 1 and T_{Kane} multiplied together as well as the sign of D to account for the direction of current flow 33

3.4 Overlap integral for three different situations; (i) cone, (ii) simple mesa, and (iii) complex mesa shapes. The dash-dot-dot lines are idealized D characteristics................. 38

3.5 Graphical representation of overlap integral calculations for $N_D = N_A$ ($E_{F,n} = E_{F,p}$) for V_A of (a) -0.25 V, (b) 0.1 V, (c) 0.457 V, and (d) 0.8 V. (e-h) Respective band diagram sketches for each biasing conditions shown to the right 40

3.6 Graphical representation of overlap integral calculations for $N_D > N_A$ ($E_{F,n} > E_{F,p}$) for V_A of (a) -0.25 V, (b) 0.1 V, (c) 0.457 V, and (d) 0.8 V. (e-h) Respective band diagram sketches for each biasing conditions shown to the right 41

3.7 Graphical representation of overlap integral calculations for $N_D >> N_A$ ($E_{F,n} >> E_{F,p}$) for V_A of (a) -0.25 V, (b) 0.1 V, (c) 0.457 V, and (d) 0.8 V. (e-h) Respective band diagram sketches for each biasing conditions shown to the right 42

3.8 Plot of y vs. x used to determine E_F from a given doping density and DOS. The solid line is from numerical evaluation of the carrier-energy distribution function. Dashed lines are approximations of non-degeneracy (right) and super-degeneracy (left).. 47

3.9 GUI interface (a) for the Kane Model program. The drop-down box (b) can be used to select from a multitude of material systems.. 50

3.10 Flow diagram for operation of KMP... 52

3.11 Plotting functionality for J-V analysis... 53

3.12 Left (a), fully calculated BTBT J-V characteristics calculated using with KMP. Material and doping parameters are the same as those used for the detailed discussion on "*D*" (section 3.2.3.1). Right (b), characteristic trendlines for the same fictitious material system. The doping sweep analysis was performed for J_P and V_A = -0.5 V.. 56

3.13 Calculated band diagrams for the (i) cone, (ii) mesa, and (iii) complex mesa examples used in Section 3.2.3.1.. 57

4.1 Left (a), schematic diagram of graded buffer layers. Solid line shows a threading dislocation moving through the layers without generating new dislocations and terminating below the virtual-Ge substrate. Right (b) is a TEM of a $Si_{1-x}Ge_x$ graded buffer with defect free GaAs-on-Ge-virtual substrate integrated on a Si substrate (adopted from [36]) 63

4.2 SmartCut[tm] substrate transfer Process flow, adopted from [38]. Shows the (a) initial epitaxial layer start on temporary substrate, (b) H^+ implant, (c) wafer bonding, (d) layer exfoliation, and (e) surface preparation.. 65

4.3 (A) Schematic diagram of threading dislocations being trapped inside an ART trench (adopted from [43]). (b) TEM of overgrown Ge epitaxial growth inside a wide ART trench. White lines are thin layers of SiGe, showing the dynamics of growth inside and over the oxide barriers (adopted from[44]).. 66

4.4 TEM cross-section of coalesced Ge integrated on a Si substrate using ART. The majority of TDD resulting from the 4% lattice mismatch between Ge and Si is trapped by the oxide sidewalls within the trenches. A few extra dislocations are created around the coalescence planes 67

4.5 Defect density of virtual Ge substrate integrated on Si via ART. In general, (a) as the aspect ratio (height by width) of the oxide trenches increases TDD decreases. Additionally, (b) increasing the trench pitch (spacing) also decreases TDD. Optimal measured results reduced TDD from ~1.25×10^9 /cm^3 for a blanket film, down to ~1.25×10^6 /cm^3. 69

4.6 Schematic cross-section of the Ge alloy junction TD 70

4.7 I-V characteristics of Ge on Si ETDs for four separate anneal temperatures........ 71

4.8 TEM cross-sections of (a) entire GaAs TD on Ge ART layers and (b) a close-up of the TD junction itself. The bulk of the TDD is trapped within the ART structure, though a few defects remain present within the coalesced Ge. Visually, the Ge/GaAs interface traps more of the defects, providing a high quality GaAs virtual substrate. The high resolution micrograph shows a well defined junction with regular crystalline structure 72

4.9 Schematic diagrams of GaAs/InGaAs TDs. All four structures have the same nominal doping concentrations and film thicknesses. Each structure systematically varies material composition; (a) TD1 is a replica of Richard, *et al.* [13], (b) TD2 is a replica of TD1 but with 20% In mole fraction, (c) TD3 contains 10% In on both sides of the junction, (d) TD4 employs a graded heterojunction from 0% to 10% In, and (e) TD5 is a replica of TD1 with a nominally intrinsic GaAs layer inserted between the n- and p-type layers 73

4.10 Band diagram of TD3 calculated via OMEN, provided in collaboration with M. Luisier and G. Klimeck from Purdue University. The $In_{0.1}Ga_{0.9}As$ layer is assumed to be biaxially strained........ 73

4.11 SIMS analysis of C (p-type), Si (n-type) concentrations, and In/As normalized count. Includes results for (a) TD1, (b) TD2 and TD2-GaAs, and (c) TD3 and TD3-GaAs. Finally, (d) is included for direct comparison of In layer location........ 75

4.12 Schematic diagrams showing the basic TD process flow; (a) lift-off resist profile past develop, (b) metal deposition, (c) post metal lift-off, and (d) mesa isolation etch 78

4.13 High angle SEM image of GaAs TD on ART substrate. The large undercut (~2 µm on a side) clearly visible is due to the aggressive mesa isolation etch 79

4.14 Typical I-V characteristic of three TD1 samples with (i) no anneal (PVCR of 4), (ii) 425^0C anneal (PVCR of 24), and (iii) 480^0C anneal (PVCR of 18)........ 80

4.15 Typical I-V characteristic of ~30 µm radii devices for (a) TD1, TD5, TD1-Si, TD5-Si, and (b) TD2, TD3, TD2-GaAs, TD3-GaAs. Devices grown on virtual ART substrates exhibit much greater PVCR and Current, indicating high quality material quality........ 81

4.16 Benchmarking of J_P vs. reduced doping (N*) for TD1, TD2, TD3, TD2-GaAs, and TD3-GaAs. Measured data is plotted against unstrained InGaAs homojunction trendlines, calculated using Kane's [61] (discussed in the previous chapter, and shown to be accurate in the following chapter). Measured J_P is up to 100x predicted magnitude, with a much steeper trendline 83

4.17 High angle (82^0) SEM image of mesa isolation etched TD3. As highlighted by the wet chemical etch, the surface is marked by many large defects (there may be smaller ones not visible here). These defects would tend to degrade device performance 84

4.18 (a) I-V characteristics with the best PVCR's measured for TD1, TD2, TD3, and TD4. (b) Benchmarking of TD1, TD2, TD3, and TD4 against key TDs in literature [5-18]. TD3 has the 3rd largest PVCR over all and the largest of all GaAs TD or TD on a Si substrate 85

4.19 Measured I-V characteristics of TD3 at (a) low temperatures (77 K to 325 K) and (b) high temperatures (312 K to 480 K). Contrary to the model prediction, J_P decreased with temperature. However, J_V increased and J_{Zener} remained fairly constant 87

4.20 (a) J_P, J_V, and PVCR versus $1/kT$ Most of the variation occurs at high temperatures with J_V. The other 3 graphs are normalized (b) J_P, (c) J_V, and (d) PVCR versus temperature for direct comparison with Si TD 88

4.21 Left (a) is measured current density versus temperature for various voltages. On the right (b) is extracted ideality factors and x-intercepts versus temperature 90

4.22 The top picture of the Leo EVO 50 sample SEM and NPGS PC used for this work. On the bottom are measured feature size versus exposure dose for (a) low beam currents (~400 pA) and (b) large beam currents (~1.75 nA) 91

4.23 Schematic diagram (top) and high angle SEM images (bottom) of the sub-micron fabrication process after (a) mesa isolation, (b) BCB planarization and etchback, and (c) metal 2 deposition and liftoff 93

4.24 Measured I-V characteristics of TD1 scaled to deep submicron dimensions. I_P ranges 8 orders of magnitude, indicating a large range in device dimensions 94

4.25 Measured (a) I_P and (b) PVCR versus mask defined area for deep sub-micron scaled TD1 junctions. Due to noise in the actual junction areas, the maximum, average, minimum, and standard deviation of each size is shown 95

5.1 Schematic diagrams of (a) basic p-*i*-n TD, (b) InGaAs-1, and (c) InGaAs-2. InGaAs-1 & -2 have same basic structure (p-i-n). To avoid growth defects for InGaAs-1 the maximum doping levels were kept within 10 nm of the junction. On InGaAs-2, a sacrificial InP capping layer protects the anode surface, and additional InP layers in the cathode act as etch stops 105

5.2 (a) Maximum doping concentrations and profile slopes acquired from (b) SIMS measurements of InGaAs-1 and InGaAs-2 107

5.3 SEM images of ETD after mesa isolation from a (a) top-down, (b) vertical cross-section, and (c) horizontal cross-section view points. Undercut values measured from bottom of contact metal to edge of mesa, 60 nm below contact metal (location of the metallurgical junction 108

5.4 Metal contact (a) major diameters, (b) minor diameters, and (c) areas across InGaAs-1 for 400 nm radii patterns. Major and Minor axis used a surface fit. Area surface was calculated from the surface fits 109

5.5 Measured I-V characteristics for (a) InGaAs-1 and (b) InGaAs-2 over a wide range of sizes. Each curve is labeled with its average estimated radius 111

5.6 SEM images of Au probe pad blow out due to localized heating This does not kill the device, but causes problems with measurements (noise and opens) 112

5.7 Variation of V_P versus I_P. Slope of the line fit provides average R_{Series}. Y-intercept is the average minimum measureable V_P, which is usually the intrinsic V_P. 113

5.8 Scaling properties of PVCR for (a) InGaAs-1 and (b) InGaAs-2. The solid lines indicate smoothed averages of the dataset. The maximum PVCR improved a small amount as the junctions were scaled 114

5.9 On the left is the (a) scaling properties of I_P for InGaAs-1 and InGaAs-2. On the right are the J_P histograms for both ETDs. The Gaussian fits were used to calculate the average J_P and standard deviation (table inset) 115

5.10 Calculated band diagrams assuming 2-band approximation, abrupt junctions, and full depletion approximation. Top row are at equilibrium for (a) InGaAs-1 and (b) InGaAs-2. The 3 nm *i*-layer has a minimal effect on the tunnel barrier. The Bottom row is biased at the calculated VP for (a) InGaAs-1 and (b). V_P is largely dependent on $E_{F,p}$. 118

5.11 Calculated BTBT J-V characteristics vs. measured for (left) InGaAs-1 and (right) InGaAs-2. Top row (a, d) are 2-band, middle row (b, e) are 4-band, and the bottom row (c & f) are the 4-bands & BGN results. The 2-band model gave the best pre-J_P current densities. Whereas, the 4-band & BGN model gave the best post-J_P results 120

5.12 Contrasting InGaAs-1 and InGaAs-2 with previous results and other ETDs from literature by compare J_P versus (a) PVCR [4-18] and (b) reduced average doping (N^*) [18-23]. Solid and Dashed lines are Kane model predictions using 2-bands, 4-bands, and 4-Bands/BGN. 121

5.13 Left, (a) Schematic diagram of InGaAs-3 with original target doping concentrations. Right, (b) vertically and horizontally oriented TLM results for Mo contacts on n-type $In_{0.53}Ga_{0.47}As$ 124

5.14 Left, (a) I-V characteristics for InGaAs-3. NDR in reverse bias is from the device used as a virtual short to ground. Right, (b) J_P histogram with Gaussian fit. J_P is much smaller than predicted 125

5.15 Left, (a) $In_{0.53}Ga_{0.47}As$ trendline including predicted placement of InGaAs-3 (measured J_P of 14 A/cm^2). Right, (b) isometric reduced doping curve for an N^* = 4.2x10^{18}/cm^3. Labeled points assume (i) N_A is off target, (ii) N_A=N_D, or (iii) N_D is off target ... 126

5.16 Left, (a) SIMS results for InGaAs-3. Be concentration if much smaller than targeted. Right, (b) calculated band diagram biased at V_P using 2-bands and 4-bands E_F model ... 127

5.17 Calculated J-V characteristics using (a) 2-bands and (b) 4-bands. For improved accuracy post valley, J_{Excess} was added via an exponential line fit. Additionally, a 96.2 Ω R_{Series} was added to improve the fit at high current magnitudes ... 128

5.18 Schematic diagram of medium current density $In_{0.53}Ga_{0.47}As$ ETD with (b) coping concentrations, measured J_P, and PVCR for InGaAs-4, InGaAs-5, and InGaAs-6 ... 129

5.19 (a) Typical J-V characteristics for InGaAs-4, InGaAs-5, and InGaAs-6. Solid lines are calculated using the basic 2-bands model, cut-off at the measured V_P. A ~6 μΩ-cm^2 R_{Series} was added to the model. (b) Characteristic trendline for $In_{0.53}Ga_{0.47}As$, covering 5 orders of magnitude, including the 3 additional data points added ... 130

5.20 Calculated band diagrams for (a) InGaAs-4, (b) InGaAs-5, and (c) InGaAs-6. The bands were calculated with a 0 nm *i*-layer and an applied bias of V_P as predicted by the Kane model. For easy reference, the quasi-Fermi levels were extended into the bandgap. Bottom right, (d) the depletion and tunnel barrier widths are listed ... 132

6.1 Left, (a) Schematic diagram of GaAs ETD structures. Right, (b) table of target doping concentrations, as well as measured J_P and PVCR for GaAs-1, GaAs-2, and GaAs-3 ... 139

6.2 Left, (a) typical J-V characteristics (symbols), modeling results (solid line), and "D" (dashed line; right y-axis) for GaAs-1, GaAs-2, and GaAs-3. Right, (b) GaAs trendling (solid line) including data points from literature (circles) and this work (stars) [18-27]. $In_{0.53}Ga_{047}As$ ETD trendline included as reference ... 140

6.3 Calculated band diagrams at a bias of V_P for (a) GaAs-1, (b) GaAs-2, and (c) GaAs-3. Only 2-bands $E_{F,n}$ (Γ-valley) calculations were available. Quasi Fermi energies were extended into the bandgap for easy reference. Shaded region is the *i*-layer ... 142

6.4 Left, (a) Schematic diagram of InAs ETD structures. Right, (b) table of target doping concentrations, as well as measured J_P and PVCR for InAs-1, InAs-2, and InAs-3 ... 143

6.5 SIMS results of the doping calibration growth for the InAs ETDs. Three Si steps and one Be mesa indicate the doping concentrations for all three InAs ETDs ... 144

6.6 I-V characteristics for (a) InAs-1, (b) InAs-2, and (c) InAs-3. InAs-1 shows clear NDR and I_P scaling with area. InAs-2 shows strong kinks, indicating the location an magnitude of the pure BTBT J_P. InAs-3 mostly looks ohmic ... 145

6.7 Left, (a) measured I_P versus junction area. Slope of line fit indicates J_P. Right, (b) histogram of J_P, with Gaussian fit indicating average J_P of 2.3 kA/cm^2. 146

6.8 Left, (a) measured J-V characteristics (symbols) as well as modeled characteristics (solid line) and "*D*" (dashed line). Right, (b) characteristic trendlines for GaAs, $In_{0.53}As_{0.47}As$, and InAs [18-27]. The InAs trendline, calculated from the Kane model, is greater than the previous trendlines 147

6.9 Calculated band structure for (a) InAs-1, (b) InAs-2, and (c) InAs-3. $E_{F,n}$ was calculated using only the Γ-valley 149

6.10 Proposed band diagrams of the metal-InAs interface at (a) equilibrium and (b) with an applied bias. Between the metal and InAs is an ultra thin insolative layer providing an additional tunnel barrier, and Fermi level pinning at the interface 151

6.11 Measured I-V characteristics displaying NDR in reverse bias due to the (a) Mo and (b) Al metal contacts to p^{++} InAs 152

7.1 Left (a), standard J_P versus doping for GaAs, $In_{0.53}Ga_{0.47}As$, and InAs ETDs. Vertical cutlines indicate N^* values used for (b) the plot on the right, which shows the relationship between J_P and E_G for various doping conditions. Solid lines are calculation results from the KMP… 158

7.2 Universal model transformation applied to the (a) Kane model ($N_A = N_D$), as well as, (b) experimental results from this work. The dashed line in (b) is the exponential fit from (a). Most deviations in the experimental data are a result of $N_A \neq N_D$ 161

7.3 Left (a), characteristic trendlines for (i) GaAs, (ii) $In_{0.53}Ga_{0.47}As$, (iii) GaSb, (iv) InAs, (v) InSb calculated by Kane (solid) and UBM (data points). The solid points use the base-line UBM, where the open points use correction factors. Right (b), UBM trendline (solid) marked with the predicted maximum J_P. 164

8.1 Left (a), Si/SiGe resonant interband ETD band diagram illustrating (adopted from [3]) δ-doping and Type II band alignment. Right (b), GaAs/InGaAs heterojunction ETDs. The measured J_P for each structures far exceeds the 10% (TD1, TD3, and TD3-GaAs) and 20% (TD2 and TD2-GaAs) $In_xGa_{1-x}As$ characteristic trendlines 167

8.2 Band diagrams showing the improved tunneling tunneling barrier widths for a (a) type II staggered gap and (b) type III broken gap heterojunction ETDs (adopted from [8]) 169

A.1 Main window for PIVET 177

A.2 Secondary window plotting J-V results 192

D.1 Main window for PIVET 204

D.2 Window for manually picking peak and valley locations (algorithm David-2) 213

LIST OF ABBREVIATIONS

AFM	Atomic Force Microscopy
ART	Aspect Ratio Trapping
BCB	Bis-benzocyclobutene
BGN	Band Gap nNarrowing
BTBT	Band-to-Band Tunneling
CFS/GFS	Constant/Generalized Field Scaling
CMOS	Complementary Metal Oxide Semiconductor
CMP	Chemical Mechanical Planarization
CNT	Carbon Nano-Tube
CVD	Chemical Vapor Deposition
MOCVD	Metal-Organic CVD
RPCVD	Reduced Pressure CVD
UHVCVD	Ultra High Vacuum CVD
DC	Direct Current
DOS	Density of States
E-Beam	Electron Beam
EDX	Energy Dispersive X-ray
ETD	Esaki Tunnel Diode
FET	Field Effect Transistor
MOSFET	Metal Oxide Semiconductor FET
TFET	Tunneling FET
GUI	Graphical User Interface
IC	Integrated Circuit

ILD	Inter-Layer Dielectric
ITRS	International Technology Roadmap for Semiconductors
KMP	Kane Model Program
MBE	Molecular Beam Epitaxy
MOMBE	Metal-Organic MBE
NDR	Negative Differential Resistance
NPGS	Nano-Pattern Generation System
PC	Personal Computer
PIVET	Peak Including Valley Extraction Tool
PR	Photoresist
PVCR	Peak to Valley Current Ratio
RTA	Rapid Thermal Anneal
RTP	Rapid Thermal Processor
SEM	Scanning Electron Microscope
SIMS	Secondary Ion Mass Spectroscopy
SOG	Spin-on-Glass
SOI	Silicon-on-Insulator
SS	Sub-threshold Slope
TCAD	Technology Computer-Aided Design
TDD	Threading Dislocation Density
TEM	Transmission Electron Microscope
TLM	Transfer Length Modulation
UBM	Universal BTBT Model
WKB	Wentzel-Kramers-Brillouin approximation
XRD	X-Ray Diffraction

LIST OF SYMBOLS

Symbol	Description
I_P/I_V	Peak/Valley Current
J_P/J_V	Peak/Valley Current Density
e^-, h^+	electrons, holes
n, p	Electron/Hole carrier concentration
N_A, N_D, N^*	Acceptor & Donor concentrations, reduced average doping concentration
q	Magnitude of the charge on an electron
$\hbar$	Reduced Plank's constant
kT	Thermal energy (Boltzmann's constant & temperature)
ε_s, ε_r	Dielectric constant, Relative dielectric constant
E_G	Bandgap
m^*	Effective mass
m_r, $m_{r,n}$, $m_{r,p}$, $m_{r,BTBT}$	Relative effective mass, electrons, holes, average for BTBT
$m_{r,light}$, $m_{r,heavy}$	Relative effective mass for light and heavy holes
E_F, $E_{F,n}$, $E_{F,p}$	Fermi energy, n-side of junction, p-side of junction
$\Delta E_{F,n}$, $\Delta E_{F,p}$	$E_{F,n} - E_{C,n}$ and $E_{V,p} - E_{F,p}$
E_C, $E_{C,n}$, $E_{C,p}$	Conduction band, n-side of junction, p-side of junction
E_V, $E_{V,n}$, $E_{V,p}$	Valence band, n-side of junction, p-side of junction
N_C, N_V	Density of states (DOS) constants for the conduction & valence band
g_C, g_V	DOS energy distributions for conduction & valence bands
$f(E)$, $f_n(E)$, $f_p(E)$	Fermi-Dirac distribution, n-side, p-side
w_d, w_n, w_p	Depletion width, n-side, p-side
ξ	Electric field
V_{bi}	Built-in voltage

V_A	Applied bias
V_P, V_V	Peak, valley voltage
D, $D'(E)$	Overlap integral, integrand of D (differential with respect to energy)
T_{Kane}, T_{WKB}	BTBT probability from E. O. Kane [], using WKB approximation []

CHAPTER 1

Introduction and Motivation

1.1. Introduction

The success of the microelectronics industry is the result of continued MOSFET scaling to progressively smaller dimensions. Consequently, the number of transistors and functions per unit area has doubled approximately every two years, in accordance with Moore's Law [1-4]. Additionally, with proper scaling (Table 1.1), the transistors can operate at faster switching speeds [2-5]. The final results are computer chips with greater processing power with a cheaper price per function.

In 1974, Dennard, *et al.*, developed "constant field scaling" (CFS) wherein dimensions, voltages, and dopings are methodically reduced at the same rate (Table 1.1: CFS column) [5]. However, limitations in the scalability of subthreshold slopes (SS) for MOSFETs necessitated a "generalized field scaling" (GFS) method, wherein voltages are decreased at a slower rate than the physical dimensions [6]. In this fashion, circuit density and speed may be increased at the same rate as the CFS scheme. **The tradeoff is an increased power density**. Even with new channel materials, voltages can be scaled only so much before I_{On}/I_{Off}, I_{Leak}, and power densities rise to unacceptable levels. Therefore, a new type of switch will be needed for continued scaling.

> *"Eventually, toward the end of the Roadmap or beyond, scaling of MOSFETs is likely to become ineffective and/or very costly, and advanced non-CMOS solutions will need to be implemented to continue to improve performance, power, density, etc. …"*

"… Alternate channel materials and/or devices such as tunnel field-effect transistor can provide some relief in this area by potentially allowing more aggressive V_{dd} scaling or/and steeper subthreshold slope."

The 2009 International Technology for Semiconductors (ITRS) [7] clearly identifies the tunneling-FET (TFET) as a replacement technology with the potential to alleviate some of the scaling challenges that that look to be insurmountable in the future. TFETs have the potential to exceed the limited SS scalability of MOSFETs [8-20].

1.2. Importance of Subthreshold Slope

Ideally, the drain current (I_D) versus gate voltage (V_G) characteristics for a switch would be a perfect square function as shown in Fig. 1.1a. Specifically, I_D would be 0 A for all V_G less than the threshold voltage (V_t). For V_G greater than or equal to V_t, I_D instantaneously jumps to a target on current (I_{on}). Assuming V_t can be scaled, the minimum operating bias (V_{DD}) would approach 0 V as $V_t \rightarrow$ 0 V.

Table 1.1: "Constant field scaling" (CFS) and "general field scaling" (GFS) schemes

Parameter	Scaling Factors	
	CFS	GFS
Physical Dimensions L, W, T_{OX}, wire pitch	$1/\lambda$	$1/\lambda$
Voltage	$1/\lambda$	$1/\alpha$
Body Doping	λ	λ^2/α
Circuit Density	$1/\lambda^2$	$1/\lambda^2$
Electric Fields	1	λ/α
Current Density	1	λ^2/α^2
Current	$1/\lambda$	λ/α^2
Power/Energy per circuit	$1/\lambda^2$	λ/α^3
Power Density	**1**	λ^3/α
Capacitence per circuit	$1/\lambda$	$1/\lambda$
Circuit speed	λ	λ (goal)

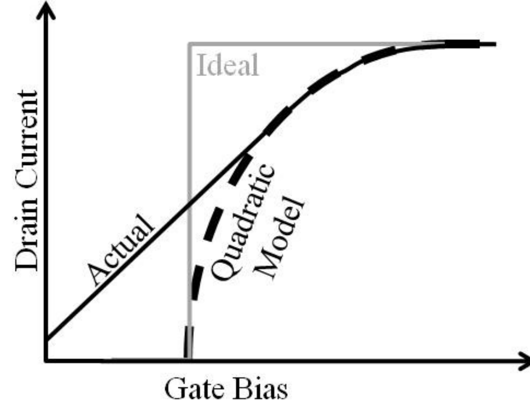

Fig. 1.1: Generic I_{DS}-V_{GS} characteristics for an (a) ideal switch, (b) quadratic MOSFET model, and (c) actual subthreshold characteristics.

However, the standard switches in modern digital integrated circuits (ICs) use MOSFETs. The basic quadratic MOSFET model, (1.1) and (1.2), describes half of an ideal switch seen in Fig. 1.1**Error! Reference source not found.**b. Specifically, there is no current flow (I_D = 0V) when V_G is less than or equal to V_t. Once V_G is greater than V_t, the transistor will suddenly turn on, providing a non-zero I_D. However, I_D does not immediately increase to I_{ON}. Instead, it increases at the rate of $(V_G\text{-}V_t)^2$, as seen in (1.2), which makes the reasonable assumption that the channel is fully saturated. To achieve I_{ON}, V_G must increase to V_t plus an additional amount "ΔV_G". Therefore, the minimum V_{DD} is ΔV_G, assuming that V_t can be engineered down to 0 V.

$$I_{DS} = \mu C_{Ox} \frac{W}{L} \left[\left(V_{GS} - V_t\right) V_{DS} - \frac{V_{DS}^2}{2} \right], \; V_{DS} < V_{GS} - V_t \tag{1.1}$$

$$I_{DS} = \mu C_{Ox} \frac{W}{L} \frac{\left(V_{GS} - V_t\right)^2}{2}, \; V_{DS} > V_{GS} - V_t \tag{1.2}$$

As one may expect, the quadratic model is incomplete and does not accurately capture the MOSFETs subthreshold characteristics. In reality, there is a non-zero leakage current (I_{Off}) at V_G of 0 V, which increases exponentially in the subthreshold region, Fig. 1.1c. The SS is proportional to the inverse exponential slope, quantitatively describing how fast a MOSFET turns on. For a given SS there is a minimum threshold voltage, $V_{t,min}$, for which I_{Off} and I_{On} remain at

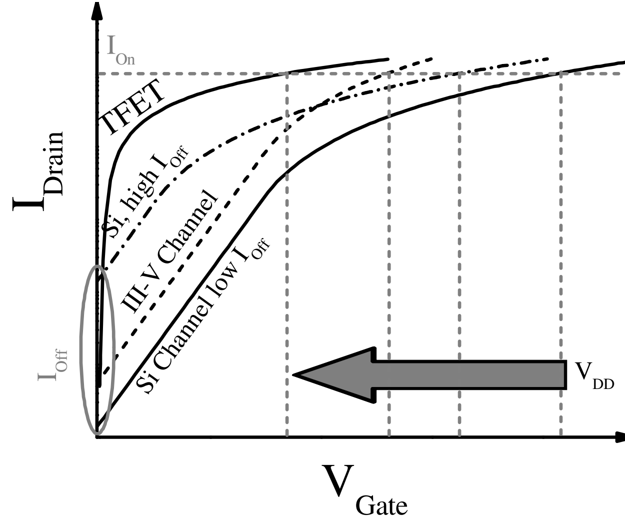

Fig. 1.2: Generic I_{DS}-V_{GS} characteristics showing the V_{DD} scaling for a (i) Si channel MOSFET with low I_{Off}, (ii), Si channel MOSFET with large I_{Off}, (iii) high mobility III-V channel MOSFET, and (iv) TFET.

their target values. In order for $V_{t,min}$ to decrease while keeping I_{Off} and I_{On} constant, the SS would have to decrease (an increased slope). Therefore, the minimum V_{DD} is roughly equal to $V_{t,min}$ + ΔV_G.

The main challenge regarding the scaling of MOSFET electrostatics pertains to a fundamental limitation in the scalability of SS; regardless of material type or device structure [11]. This situation is depicted in Fig. 1.2. For instance, assume that the "Si channel device with low I_{Off}" is the current technology generation to be scaled. If the device is scaled without any dramatic changes ("Si, high I_{Off}"), V_{DD} can be reduced a significant amount. However, a large sacrifice is made by drastically increasing I_{Off}. Eventually, the I_{ON}/I_{Off} ratio would become too small, killing noise margins.

Replacing channel materials to a semiconductor with higher mobility and smaller effective mass can be a great help. As seen in Fig. 1.2, the "III-V channel device" has the same SS. However, all else being equal, the higher mobility and smaller effective mass results in a higher current density. As a result, there is a substantial reduction in V_{DD} with a minimal increase in I_{Off}, compared to the original Si device. In other words, by using various methods and materials to increase carrier mobilities, V_{DD} can still be aggressively scaled with only a small

reduction in I_{ON}/I_{Off} ratios. This can only be maintained as long as methods to increasing carrier mobilities are feasible.

Recall that the 2009 ITRS [7] states that methods to maintain the scalability of MOSFETs are "likely to become ineffective and/or very costly". To overcome this issue, it is desirable to have a switch with an SS below the MOSFET limit such as the TFET [8-20]. As seen in Fig. 1.2, such a switch could enable continued scaling of power supplies and maintain the desired I_{ON}/I_{Off} targets.

1.3. Subthreshold Limit of MOSFETs

As a direct consequence of Fermi-Dirac statistics, MOSFETs have a minimum SS of 60 mV/dec. The origins of this limit are easily understood as the result of carrier diffusion over the source/body barrier formed by the forbidden bandgap. Fig. 1.3 shows the conduction band (E_C) of an *n*-channel MOSFET biased in the sub-V_t regime. Those carriers with energy greater than E_C in the body region ($E_C(B)$) will diffuse across the junction, creating a sub-threshold current.

As a direct result of Fermi-Dirac statistic, the distribution of carriers above E_C quickly becomes a decaying exponential of the form $A \times \exp[-qV/kT]$; where "qV" is any energy a few kT above E_C and E_f. Recall that current is proportional to the number of carriers taking part in the

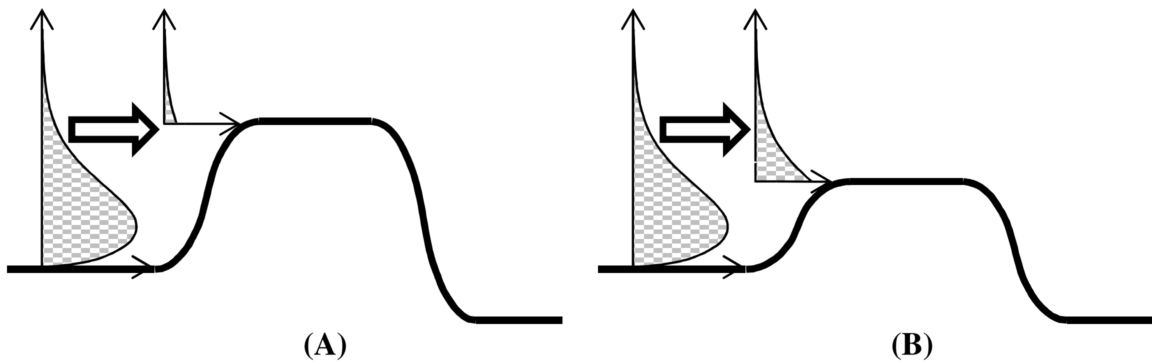

Fig. 1.3: The conduction band portion of the source, body, drain (left to right) regions of a MOSFET; including electron carrier concentration.

conduction. Therefore, I_D in the sub-threshold regime is,

$$I_{DS} = \int_{V_{bi} - V_G/n}^{\infty} A \exp\left[-\frac{q}{kT}V\right] dV \tag{1.3}$$

Where A is a constant, k is Boltzmann's constant, T is the temperature, and "n" is a measure of how effectively the gate can modulate the barrier ($E_C(B)$). The built in potential, V_{bi}, is equal to the barrier height when V_G = 0 V. Performing the integration, and grouping all constants into I_0, the subthreshold current clearly becomes an exponential controlled by V_G.

$$I_{DS} = I_0 \exp\left[\frac{q}{nkT}V_G\right]; \quad V_G < V_T \tag{1.4}$$

The leakage current, I_0, is dependent on material properties, device design, and V_{DS}. From (1.4), the SS of a MOSFET can be calculated as,

$$SS = \frac{dV_G}{d\log\left(I_{DS}\right)} = n\frac{kT}{q}\ln\left(10\right) \tag{1.5}$$

Under optimal conditions the gate has perfect control of $E_C(B)$. Therefore the minimum value for "n" is one, resulting in a minimum SS of 60mV/dec at room temperature (300 K). From this analysis it can be seen that the SS limit cannot be overcome for MOSFET structures, regardless of the device structure or materials used.

The above conclusion is true unless one of the assumptions used for this derivation is violated. For all typical MOSFET structures this would be very difficult to do. It has recently been proposed that the application of magnetic materials to the gate oxide would result in an effective negative dielectric constant. The gate would then modulate $E_C(B)$ faster than V_G is changed, effectively reducing "n" below one and proportionately reducing the minimum achievable SS. This method has only recently been researched, and much work has yet to be done before it can be determined if it is a practical method to reduce SS.

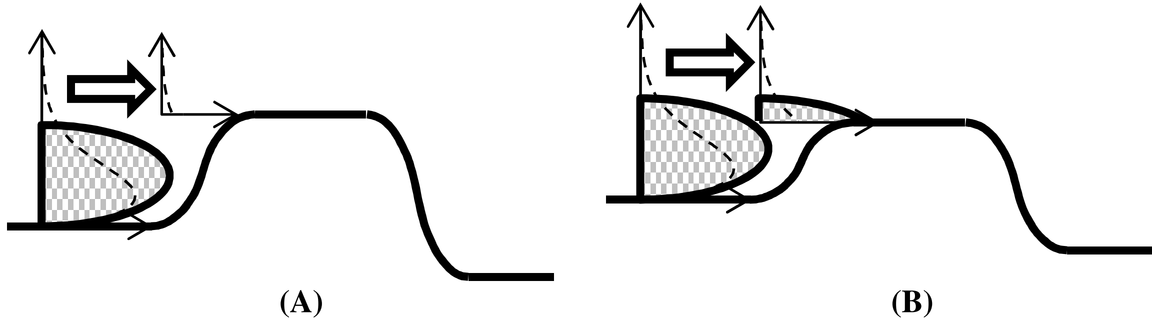

Fig. 1.4: The conduction band portion of the source, body, drain (left to right) regions of a MOSFET with engineered electron distribution.

Another potential way of reducing SS in a MOSFET is by engineering the carrier distribution to decay at a rate faster than the standard Fermi-Dirac statistics dictate (Fig. 1.4). Most semiconductors cannot deviate from that exponential rate because their density of states (DOS) predictably increase as you move away from the band edge and Fermi-Dirac statistics are fundamental physics. However, using a material who's DOS decreases after a few KT above E_C would result in a carrier distribution that falls off at a rate faster than q/kT, thereby reducing SS. Regardless, finding a suitable material or way to provide the necessary changes in dielectric constant or carrier distribution is beyond the scope of this proposal.

1.4. Objective, Implementation, and Application of Work

The over-all objectives of this work are geared towards improving the potential for integrating BTBT devices in commercial production settings. Towards this end, there are two main thrusts. The first is an investigation into the integration of III-V based ETDs onto Si substrates, which will likely remain the industry standard. Afterwards, BTBT characteristics will be systematically characterized and mapped over a large design space. This will provide an experimental baseline for future BTBT device development and advancement.

Si will remain a popular substrate of choice for production fabrication for a variety of reasons. Si is mechanically strong, with a long established history of use in industry. Furthermore, it is a commonly available element which can be purified and shaped into the

necessary the desired forms at low cost. However, the material properties of III-V semiconductors can provide superior device characteristics needed for continued scaling of CMOS. Unfortunately, III-V semiconductors are much more expensive and relatively weak or brittle, thereby limiting substrates to smaller dimensions (usually less than four inch diameters). Therefore, much effort has gone into integrating III-V virtual-substrates onto bulk Si wafers in order to obtain the benefits of both systems and minimize the drawbacks.

It is important to understand that none of the hetero-integration methods are perfect, and the density and electrical effects of the threading dislocations must be characterized. Typically these defects negatively impact carrier lifetimes, and provide deep level traps within the forbidden bandgap. This will typically increase leakage currents and decrease desirable current control. In an ETD, J_V will be increased and the PVCR will decrease. ETD structures designed to exhibit large PVCR will be more sensitive to these defects, making them a prime candidate for determining the electrical quality of virtual substrates. Specifically, this work will utilize a relatively new hetero-integration method known as aspect ratio trapping (ART) to generate GE and GaAs virtual-substrates on Si. Primarily, a series of high PVCR GaAs/InGaAs ETDs will be fabricated and tested, along with companion samples grown directly on Si and GaAs bulk substrates. Comparing the results of these structures will verify the quality of the virtual substrates. Additionally, low and high temperature measurements of the ETDs be used to gain addition insight into the quality of the semiconductor.

After verifying that high quality ETDs and virtual substrates can be integrated on Si, work will proceed with the second thrust. Even though there is a long history of literature reports on ETDs, most papers present fairly novel structure designs which cannot easily be compared with each other. Furthermore, the lack of calibrated BTBT models for a large design space makes it difficult, at best, to quantitatively predict BTBT behavior. This has been a large difficulty concerning the development of TFETs, which generally have suffered from limited on-state currents. Even though the gate stack is one dimension of the problem, BTBT efficiency from the

source to body region play a very large role for maximizing I_{on}. This work is geared towards determining a systematic way of engineering the source/body junction in order to optimize BTBT efficiency for maximum I_{on}. Additionaly, without mapped BTBT behavior or adequate models, the main guide to targeting desired BTBT characteristics is past experience. In other words, it is difficult to design and ETD structure that meets desired specification, unless a previously fabricated structure already meets those criteria.

In this work, methods will be developed that will enable the efficient mapping of BTBT characteristics over a large design space. Experimental results from this mapping technique will provide the basis for (i) BTBT model calibration, (ii) determination of BTBT limitations, (iii) paths towards improved BTBT characteristics, and (iv) BTBT trendlines for quantitative relationship between ETD structure and BTBT characteristics. Furthermore, with a large database of self-consistent structure designs, a universal (or series of semi-universal) BTBT model may be developed. Such a model would add concrete relationships between material parameters and BTBT current density.

A basic ETD structure template will be developed for the mapping effort. To help eliminate and simplify the variables, the ETDs with be designed with unstrained, direct bandgap semiconductors with well known material parameters. Furthermore, layer thicknesses will be standardized and SIMS analysis used to determine final doping concentrations. Three material systems from the $In_{1-x}Ga_xAs$ ternary system will be chosen; (i) GaAs, (ii) $In_{0.53}Ga_{0.47}As$, and (iii) InAs. The N_A and N_D doping concentrations will be systematically varied, generating characteristic trendline for each material system. Interpolation can be used for In mole fractions between the chosen materials. The final results will be a mapping of the BTBT characteristics for the entire $In_{1-x}Ga_xAs$ ternary system. Completion of this objective requires the development of (i) a modular fabrication process, (ii) formalized electrical testing procedure, and (iii) universal analysis and organization methods. Once proven, the tools developed for this mapping scheme can be applied to additional material systems, included complicated heterjunctions which do not

conform to the structure template used here. In other words, the developed tools and methods are just as useful as the results reported on in Chapters 4, 5, and 6.

Finally, the modeling effort in this work will be limited to a single physics based, analytical model. It is preferable to have a model which most clearly displays the relationship between material parameters, ETD operation, and BTBT current density. The model is to be calibrated to the mapped ETD design space, and compared with the experimental J-V measurements. One of the results will be the ability to predict BTBT characteristics for basic ETD structures, given a material system and the doping concentrations or J_P. Secondly, the model will be used as the basis for the development of a universal BTBT model or trend. Ideally, the model would accurately predict J_P for a wide range of material parameters and doping concentrations.

The methods, modeling, and experimental results provided in this work will be the basis for further BTBT development and model calibration. Device engineers can utilize the experimental results and characteristic trendlines to target desired BTBT current densities. The experimental results can be used to calibrate TCAD models over a large design space, enabling accurate modeling of complicated BTBT structures, beyond basic ETDs. Additionally, the mapping effort will provide clear direction on improving BTBT characteristics. Furthermore, the methods developed here will enable the consistent and efficient characterization of innumerable material systems.

References for Chapter 1

[1] G. E. Moore, "Cramming More Components Onto Integrated Circuits (Reprinted from Electronics, pg 114-117, April 19, 1965)," *Proc. IEEE,* vol. 86, pp. 82-85, Jan 1998.

[2] D. L. Critchlow, "MOSFET Scaling - The Driver of VLSI Technology," *Proc. IEEE,* vol. 87, pp. 659-667, Apr 1999.

[3] S. E. Thompson, R. S. Chau, T. Ghani, K. Mistry, S. Tyagi, and M. T. Bohr, "In Search of "Forever," Continued Transistor Scaling One New Material at a Time," *IEEE Trans. Semicond. Manuf.,* vol. 18, pp. 26-36, Feb 2005.

[4] W. Haensch, E. J. Nowak, R. H. Dennard, P. M. Solomon, A. Bryant, O. H. Dokumaci, *et al.*, "Silicon CMOS Devices Beyond Scaling," *IBM J. of Res. and Develop.,* vol. 50, pp. 339-361, 2006.

[5] R. H. Dennard, Gaenssle.Fh, H. N. Yu, V. L. Rideout, E. Bassous, and A. R. Leblanc, "Design of Ion-Implanted MOSFETs With Very Small Physical Dimensions," *IEEE J. Solid-State Circuits,* vol. 9, pp. 256-268, 1974.

[6] G. Baccarani, M. R. Wordeman, and R. H. Dennard, "Generalized Scaling Theory and its Application to a 1/4; Micrometer MOSFET Design," *IEEE Trans. Electron Devices,* vol. 31, pp. 452-462, 1984.

[7] (2009). *Process Integration, Devices, and Structures*.

[8] S. O. Koswatta, S. J. Koester, and W. Haensch, "On the Possibility of Obtaining MOSFET-Like Performance and Sub-60-mV/dec Swing in 1-D Broken-Gap Tunnel Transistors," *IEEE Trans. Electron Devices,* vol. 57, pp. 3222-3230.

[9] P. F. Wang, K. Hilsenbeck, T. Nirschl, M. Oswald, C. Stepper, M. Weis, *et al.*, "Complementary Tunneling Transistor for Low Power Application," *Solid-State Electron.,* vol. 48, pp. 2281-2286, 2004.

[10] T. Nirschl, P. F. Wang, C. Weber, J. Sedlmeir, R. Heinrich, R. Kakoschke, *et al.*, "The Tunneling Field Effect Transistor (TFET) as an Add-On for Ultra-Low-Voltage Analog and Digital Processes," in *in IEDM Tech. Dig.*, 2004, pp. 195-198.

[11] K. K. Bhuwalka, J. Schulze, and I. Eisele, "Scaling the Vertical Tunnel FET With Tunnel Bandgap Modulation and Gate Workfunction Engineering," *IEEE Trans. Electron Devices,* vol. 52, pp. 909-917, May 2005.

[12] W. Y. Choi, B. G. Park, J. D. Lee, and T. J. K. Liu, "Tunneling Field-Effect Transistors (TFETs) With Subthreshold Swing (SS) Less than 60 mV/dec," *IEEE Electron Device Lett.,* vol. 28, pp. 743-745, Aug 2007.

[13] Z. Qin and A. Seabaugh, "Can the Interband Tunnel FET Outperform Si CMOS?," 2008, pp. 73-74.

[14] A. C. Seabaugh and Z. Qin, "Low-Voltage Tunnel Transistors for Beyond CMOS Logic," *Proc. IEEE,* vol. 98, pp. 2095-2110, 2010.

[15] A. Seabaugh, "Tunnel Field-Effect Transistors - Status and Prospects," in *IEEE Dev. Res. Conf.*, 2010, pp. 11-14.

[16] J. Appenzeller, Y. M. Lin, J. Knoch, and P. Avouris, "Band-to-Band Tunneling in Carbon Nanotube Field-Effect Transistors," *Phys. Rev. Lett.,* vol. 93, pp. 196805-1-196805-4, 2004.

[17] T. Krishnamohan, D. Kim, S. Raghunathan, K. Saraswat, and Ieee, "Double-Gate Strained-Ge Heterostructure Tunneling FET (TFET) With Record High Drive Currents and < 60mV/dec Subthreshold Slope," in *IEEE IEDM Tech. Dig.*, ed, 2008, pp. 947-949.

[18] K. Jeon, W.-Y. Loh, P. Patel, C. Y. Kang, J. Oh, A. Bowonder, *et al.*, "Si Tunnel Transistors With a Novel Silicided Source and 46mV/dec Swing," in *Symp. VLSI Technol.*, 2010, pp. 121-122.

[19] R. Gandhi, Z. Chen, N. Singh, K. Banerjee, and S. Lee, "Vertical Si-Nanowire *n*-Type Tunneling FETs With Low Subthreshold Swing (< 50 mV/decade) at Room Temperature," *IEEE Electron Device Lett.,* vol. 32, pp. 437-439, 2011.

[20] W.-Y. Loh, K. Jeon, C. Y. Kang, J. Oh, P. Patel, C. Smith, *et al.*, "Sub-60nm Si Tunnel Field Effect Transistors With Ion 100 mA/um," in *Proc. European Solid State Dev. Res. Conf.*, 2010, pp. 162-165.

CHAPTER 2

Theory of Quantum Tunneling Devices

2.1. Esaki Tunnel Diodes

In the 1950's, intensive investigation into the internal field emission of p-n junctions in the semiconductor materials was being performed. Of great interest was the relationship between the I-V characteristics and doping concentration of p-n junctions. Chynoweth, and other research groups, systematically increased the doping concentration in p-n junctions, looking at breakdown voltages. With large enough concentrations, the breakdown was shifted to below one volt. These diodes would start to conduct a greater current density in reverse bias than in forward bias, earning them the name of *Backward Diodes*. Once the doping levels became highly degenerate for both terminals, Esaki [1] began to notice a breakdown of zero volts in reverse bias. The forward bias characteristic would initially rise to a peak current (I_P), then exhibit NDR and fall to a valley current (I_V), and then rise again in the traditional thermal current. This typical "N" shape characteristic was the first direct observation of quantum mechanical tunneling, earning Esaki the Nobel prize in Physics in 1973. The device structure of an Esaki tunnel diode (ETD) is a degenerately doped p-n junction, sometimes with the inclusion of a thin (< 10 nm) *i*-layer in the middle, as shown in Fig. 2.1.

Without any applied bias, Fig. 2.2c, E_f is flat and above E_C on the n-type side ($E_C(n)$), and below E_V on the p-type side ($E_v(p)$). Qualitative carrier density versus energy curves are provided for electrons and holes. In reverse bias, Fig. 2.2b, Zener tunneling occurs immediately, allowing

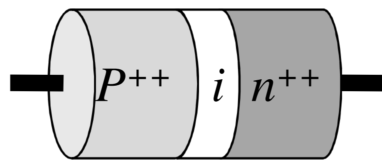

Fig. 2.1: ETD device structure.

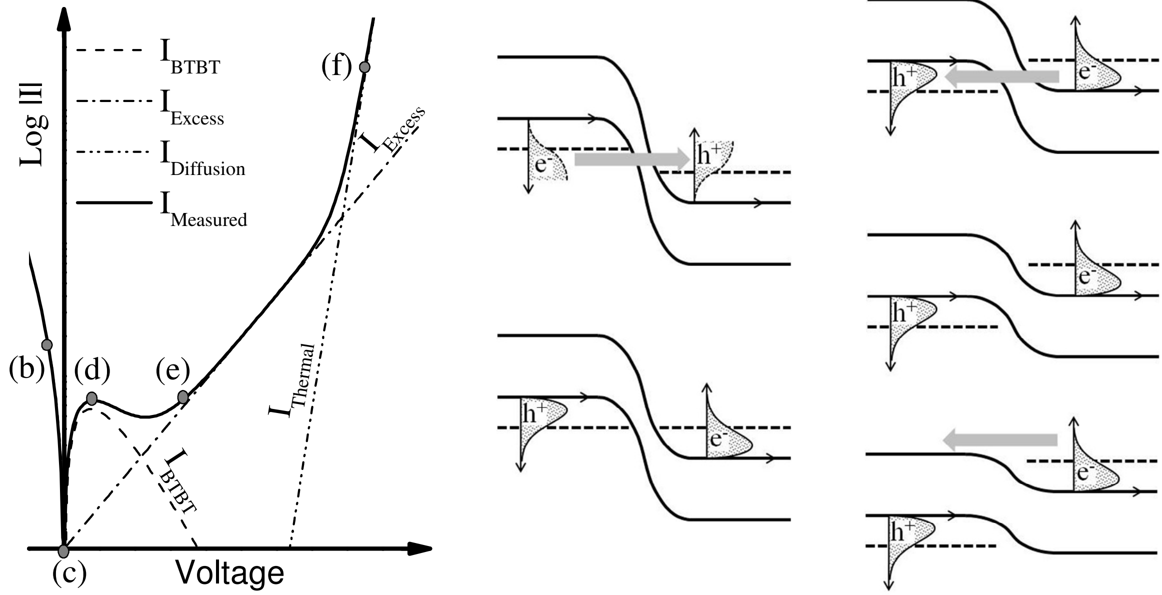

Fig. 2.2: (a) I-V characteristic, and schematic band diagram for (b) reverse bias, (c) equilibrium, (d) peak tunneling current, (e) minimum direct tunneling current, and (f) diffusion current for a generic ETD.

for large amounts of current to flow. With a small amount of forward bias, electrons occupying states below E_f in the n-side can begin tunneling to unoccupied states (holes) above E_f on the p-side, Fig. 2.2d. Eventually, E_C on the n-side is shifted above E_V on the p-side, which stops direct tunneling, Fig. 2.2e. However, the current does not drop down to 0 A; instead, carriers tunnel via indirect paths resulting in an excess current. Finally, after a large enough bias is applied, the p-n junction starts to behave like a standard diode, and a diffusion current begins to flow, Fig. 2.2f.

There have been many experimental reports of ETDs of various material systems, structures, current densities, and peak-to-valley current ratios (PVCR) over the last five decades. Depending on the application, the PVCR may be more important (Ex. Tunneling SRAM) or the current density (Ex. TFET). It is therefore useful to plot J_P vs. PVCR, Fig. 2.3. It quickly becomes evident that to achieve greater J_P, a trade-off in PVCR is made. Direct bandgap materials typically have been used to improve PVCR with respect to Si ETDs. However, very high current densities have been achieved for Si, InGaAs, staggered gap, and broken gap material systems. These structures are also prime candidates for the fabrication of TFETs with large I_{On}.

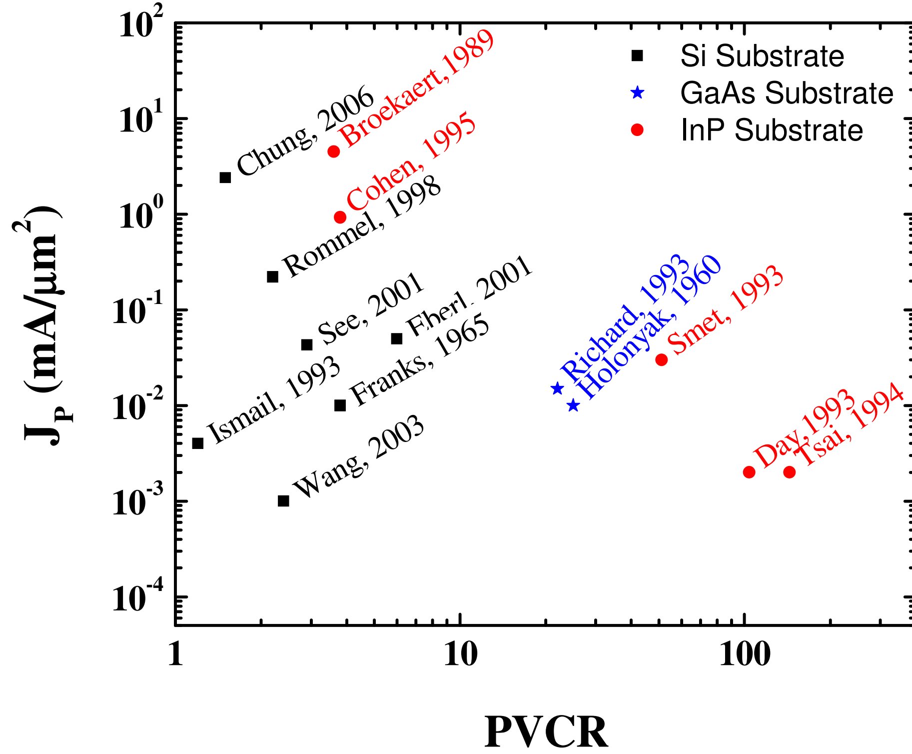

Fig. 2.3: J_P versus PVCR for key ETD structures of various material systems. InP substrate refers to lattice matched InGaAs ETD.

However, there is currently no way to predict the maximum I_{ON} or minimum subthreshold slopes (SS) that area achievable.

2.2. Analytical Band-to-Band Tunneling Models

Numerically based TCAD tools, such as Synopsys™ Sentaurus or Silvaco's Atlas, have the potential for accurate simulation of simple and complex BTBT structures. However, such methods lack the insight that analytical models quickly and easily provide; For instance, constant field scaling is easily understandable in conjunction with the MOSFET quadratic model. Therefore, this research will concentrate on physics based analytical models. The first such model to be fully derived and published was by E. O. Kane in 1961 [2]. Afterwards, many of the new BTBT models, such as Hurkx [3] and Milovanovic [4], have been derived from Kane's original model. Even though the new models are simplified, they typically only satisfy a subset of BTBT which does not include high current density ETDs and BTBT in forward bias. Other

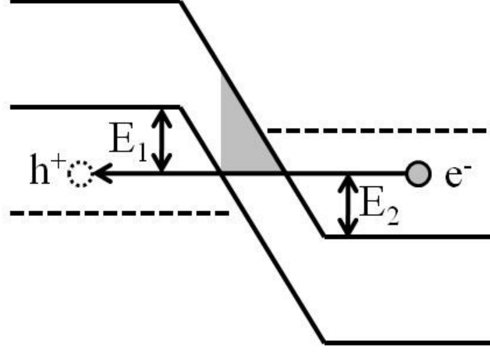

Fig. 2.4: Simplified band diagram used for Kane's BTBT model [2].

models from Schenk [5] and Solomon [6] are much more complex, and are not easily applicable fabricated structures.

The primary focus of this proposal will begin with the Kane model [2], which is described below. In the area of the tunnel junction, the electric field (ξ) is assumed to be constant, resulting in a triangular tunneling barrier as denoted by the shaded region in Fig. 2.4. Kane's original BTBT model for Esaki diodes is shown in (2.1). Where "*D*", (2.2), is referred to as the "overlap integral". This factor looks at the probability of an e^- occupying an energy state above $E_C(n)$ minus the probability of occupancy below $E_V(P)$. The factor E_S is defined as the smaller value of $E_V(p)$ - $E_{particle}$ or $E_{particle} - E_C(n)$. Notice that the overlap integral cannot be explicitly solved without any approximations.

$$J_{BTBT} = \frac{q^2 \xi}{36\pi\hbar^2}\sqrt{\frac{2m^*}{E_g}} \cdot D \cdot \exp\left(-\frac{\pi\sqrt{m^*}E_g^{3/2}}{2\sqrt{2}\hbar\xi}\right) \tag{2.1}$$

$$D \equiv \int_{E_C(n)}^{E_V(p)} \left[F_C(E) - F_V(E)\right]\left[1 - \exp\left(-\frac{2E_S}{\overline{E}}\right)\right] dE \tag{2.2}$$

$$\overline{E} = \xi\sqrt{\frac{2\hbar^2}{\pi^2 m^* E_g}} \tag{2.3}$$

The constant electric field, (2.4), is calculated from the built in voltage (ψ_{bi}) minus applied bias (V_{app}) divided by the entire depletion width (w_d) as calculated from the full depletion

approximation typically used for p-n junctions. The term N^* is a form of reduced averaged doping on the p- and n-side of the junction calculated from (2.5). Given the exponential relationship between BTBT probability and tunnel barrier width, $N*$ will be used as the control variable for constructing characteristic J_P trendlines.

$$\xi = \frac{(\psi_{bi} - V)}{\omega_d} = \sqrt{\frac{q(\psi_{bi} - V)}{2\varepsilon_S} N*} \tag{2.4}$$

$$N* = \frac{N_A N_D}{N_A + N_D} \tag{2.5}$$

Also, the effective mass (m^*) is an average of the conductivity effective masses for holes and electrons. Typically, (2.6) is used to calculate this average.

$$m* = \left[\frac{1}{m_h} + \frac{1}{m_e} \right]^{-1} \tag{2.6}$$

Recall that momentum must be conserved, even for BTBT. As formulated above, the Kane model assumes that the momentum associated with the electron wave vector does not change during BTBT. Therefore, (2.1) is only valid for direct bandgap. Additionally, only two bands are treated in this model. The model will begin to breakdown if multiple valence and conduction bands are populated as a result of material and doping conditions.

In literature, the Kane model has been applied to Ge ETDs [7-10] with good agreement. Since both Si and Ge are indirect bandgap materials, phonon interactions were included in order to provide the momentum shift necessary for BTBT. This was accomplished by changing E_g to

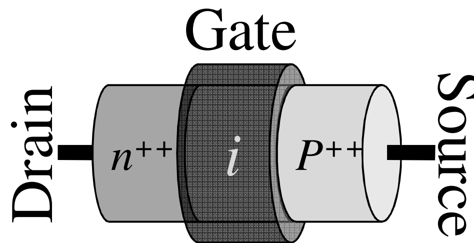

Fig. 2.5: TFET Device structure.

(E_g + E_P) in the argument of the exponential. For this work phonon interactions are not included and all BTBT transitions are assumed to be direct (no momentum shifts needed). This is an appropriate approximation for all of the ETDs modeled in this work, whose primary bandgaps are located in the Γ-valley.

2.3. Tunneling FET

In a TFET, the primary current mechanism is BTBT, which does not suffer from the same SS limitations as MOSFETs [9, 11-21]. The typical structure of a TFET takes the form of a gated p^{++}-*i*-n^{++} diode, as shown in Fig. 2.5. The Source and Drain wells are degenerately doped, with sharp profiles near the gated body region, which is intrinsic or moderately doped (*i*-layer). For the best gate control and SS, a wrap around or multi-gate structure is often assumed. Currently the best doping profiles, and tunnel junctions, are grown epitaxialy. Therefore, TFETs are often represented as vertical structures.

Fig. 2.6a shows the equilibrium band structure for the TFET. As drawn in the figure, to the left is the Source, in the middle is the body region, and the drain is at the end. The electron ("e^-") distribution below the valence band (E_V) and hole ("h^+") distribution in the conduction band are shown for the source and body region, respectively. These are the primary carriers contributing to current conduction in the TFET. Notice that the shape of the distribution of the electrons largely follows Fermi-Dirac statistics, which is scaled by the DOS. Conversely, due to the low E_f in the body region the distribution of holes are directly limited by the DOS in the conduction band.

The application of the positive drain bias ($V_{DS} > 0$) shifts the drain and body region down, as shown in Fig. 2.6b. For this discussion it is assumed that nearly all of the electric fields are confined to the p-*i* and *i*-n junctions. Without an applied V_G, the full thickness of the *i*-layer prevents BTBT from occurring, thereby reducing I_{DS} to a leakage current similar to a standard p-*i*-n diode.

A positive bias to the gate will lower the body region ($E_C(B)$ and $E_V(B)$), shown in Fig. 2.6c. With a large enough bias, $E_C(B)$ will be shifted below the E_V in the source region ($E_V(S)$), thus reducing the tunneling barrier thickness from the entire body region to less than the depletion width. Electrons in the source region are then free to tunnel through the barrier formed by the forbidden bandgap and into a vacant state in the conduction band of the body. The *i*-n junction will then sweep the carriers into the drain, forming a gate controlled BTBT current (I_{BTBT}). Further increases in V_G will increase the number of electrons available for tunneling and slightly reduce the tunneling barrier thickness. Recall that tunneling probabilities are exponentially dependent upon the barrier thickness. Therefore, the modulations in the barrier thickness caused by V_G will result in significant tunneling probably increases.

2.4. TFET Subthreshold Slope

Presented here are two ways to show that sub-60 mV/dec SS are achievable with TFETs. The first method presented looks at the electron distributions ($n(E)$) and assumes that tunneling probabilities (T) are approximately constant for all energies between $E_V(S)$ and $E_C(B)$. For the quantitative analysis we will also assume that there is always a hole ($h(E)$) or vacancy for electrons to tunnel into. In other words, it is assumed that $h_B(E) >> n_S(E)$ for energies bounded by $E_V(S)$ and $E_C(B)$. Therefore, the number of carriers taking part in I_{BTBT} can be written as,

$$I_{BTBT} \propto n_{BTBT} = \mathrm{T} \cdot \int_{E_C(B)}^{E_V(S)} n(E)\, dE \tag{2.7}$$

Where $n(E)$, given by (2.8), is the distribution of electrons below $E_V(S)$, and $n_C(E)$ is calculated as the density of states ($g_V(E)$) times the Fermi-Dirac statistics for electrons ($F_e(E)$). Note that $F_e(E)$ can be approximated as an exponential as long as the energy (E) is greater than a few kT above E_f in the source region, similar to the approximation used for the MOSFET.

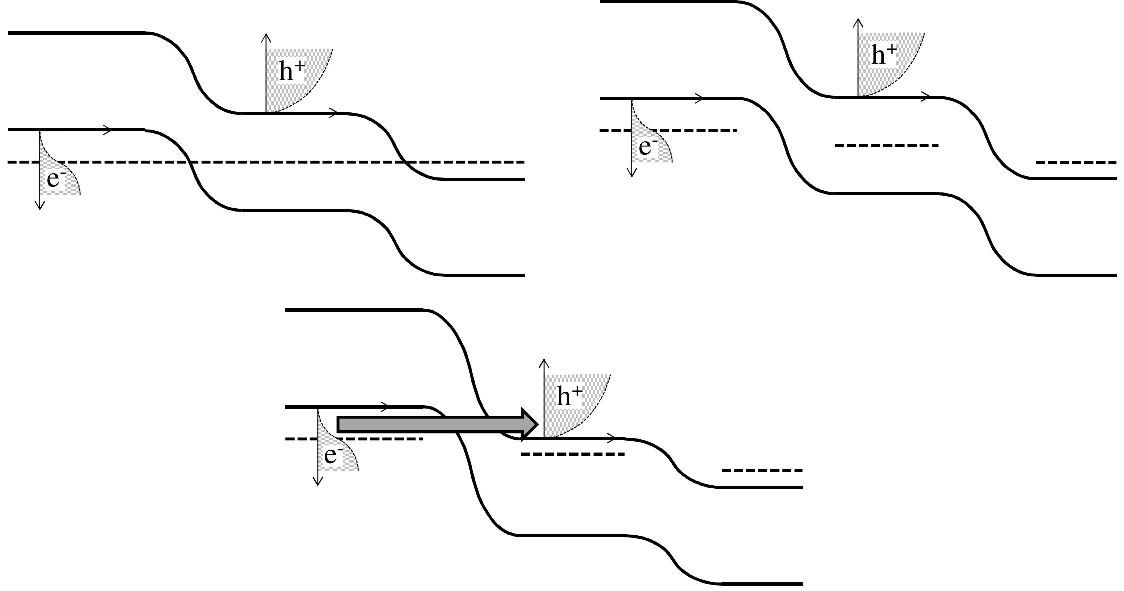

Fig. 2.6: Band diagrams showing the operation of the TFET: (a) at equilibrium, (b) with an applied V_{DS}, and (c) V_g turned on.

$$n(E) = g_V(E) \times F_e(E) = A\sqrt{E_V - E}\exp\left(\frac{E_f - E}{kT}\right) \tag{2.8}$$

Where "*A*" is the collection of material constants normally associated with DOS calculations. For this calculation the constant "*A*" does not affect the final result. The integral used to calculate n_{BTBT} results in an imaginary error function ("erfi"). It will is assumed that $E_V(B)$ drops below $E_C(S)$ as soon as V_G is increased above 0 V. Ideally, V_G will have perfect control over $E_C(B)$ as well. The final integration will look as follows, where B is a collection of constants.

$$n_{BTBT} = B\left[-\frac{1}{4}\sqrt{\pi(kT)^3}\, erfi\left(\sqrt{\frac{V_G}{kT}}\right) + \frac{kT}{2}\sqrt{V_G}\exp\left(\frac{V_G}{kT}\right)\right]$$
(2.9)[1]

At small V_G, the first term will reduce the rate at which n_{BTBT} increases, thereby reducing SS. However, the erfi function increases in magnitude at a slower rate than the exponential term.

---

[1] $erfi(x) = -i \times erf(ix) = -i\frac{2}{\sqrt{\pi}}\int_0^{ix}\exp(-t^2)dt = \frac{2}{\sqrt{\pi}}\int_0^{x}\exp(k^2)dk$

Therefore, for larger applied biases, the first term becomes negligible. As a result, the erfi function may be ignored as a first order approximation. The natural log of I_{BTBT} then becomes,

$$\ln(I_{BTBT}) \approx \ln\left(\frac{kT}{2}\right) + \frac{1}{2}\ln(V_G) + \left(\frac{V_G}{kT}\right) \tag{2.10}$$

The SS is then calculated as;

$$SS \approx \left[\frac{1}{2V_G} + \frac{1}{kT}\right]^{-1} \ln(10) \tag{2.11}$$

From (2.11), the gate will have direct control of the SS for small V_G. Once "2V_G" becomes ~1/10 of kT, the gate will no longer directly control the SS. This is advantageous since the SS will approach ln(10)/kT, which is the classical MOSFET limit as shown in (1.5). This means that the average achievable SS is less than 60 mV/dec at room temperature.

The above analysis is only valid when $E_C(B)$ remains a couple kT above $E_f(S)$. For greater accuracy the full Fermi-Dirac statistics is needed, which makes closed form approximations difficult. Numerical solutions are easily achieved. In Fig. 2.7 (dotted line), an example calculation is given where $E_f(S)$ of 0.3 eV is assumed. The SS approaches 60 mV/dec. up to a V_G of ~250 mV, at which point $E_C(B)$ is no more than a few kT above $E_f(S)$ and (2.11) breaks down. At greater V_G the SS rapidly increases, which does not matter as long as the power supplies are scaled small enough.

Another approach to calculating achievable SS is through the use of a BTBT Zener current model [4, 9, 16, 17, 22], approximated from the following version of the E.O. Kane Esaki diode model [2, 23], which will be discussed in greater detail later.

$$I_{BTBT} = aV_{eff}\xi \exp\left(-\frac{b}{\xi}\right)$$
$$a = \frac{q^3\sqrt{2m^*/E_g}}{4\pi^2\hbar^2}$$
$$b = \frac{4\sqrt{m^*}E_g^{3/2}}{3q\hbar} \qquad (2.12)$$

Where ξ is the electric field at the tunnel junction, m^* is the averaged effect mass of electrons and holes, and V_{eff} is the tunnel junction bias. Taking the derivative of (2.12), the SS can be calculated as,

$$SS = \left[\frac{1}{V_{eff}}\frac{dV_{eff}}{dV_G} + \left(\frac{\xi + b}{\xi^2}\right)\frac{d\xi}{dV_G}\right]^{-1}\ln(10) \qquad (2.13)$$

As usual, it is assumed that the gate would have perfect control of $E_C(B)$, therefore dV_{eff}/dV_G equals one. The second term is more complicated, but can be simplified by assuming that the junction width, w_d, does not change much with respect to V_G or V_{DS}. Assuming that the tunnel junction is roughly triangular; $\xi = (V_G + V_{bi})/w_d$, therefore $d\xi/dV_G = 1/w_d$. The above SS equation can then be rewritten as,

$$SS \approx \left[1/V_G + (\xi + b)/(w_d\xi^2)\right]^{-1}\ln(10) \qquad (2.14)$$

As can be seen, there are two terms similar to (2.11). The first term can be seen as extrinsic, since it is only affected by the external application of V_G. The second term involves intrinsic characteristics such as material parameters and device structure/design as well as V_G. Looking at just the extrinsic portion, we can gain a "worst case" scenario where SS = $V_G \times \ln(10)$, shown in Fig. 2.7 (dash dot dot). The SS starts at 0 mV/dec, and rises linearly with a slope of ln(10). At V_G of 26.06 mV the SS becomes 60 mV/dec; the MOSFET limit. However, when the second term is included in the calculation, (2.14), the SS rises slower and significantly increases

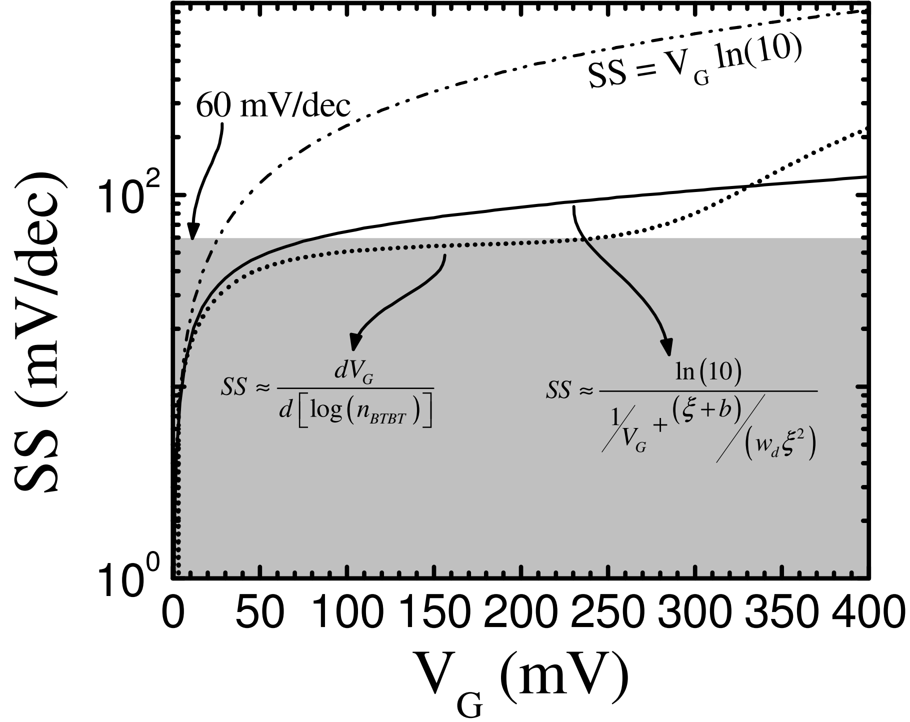

Fig. 2.7: Calculated SS limits of TFETs.

the range of sub-60 mV/dec SS operation, Fig. 2.7 (solid line). The exact change depends on material parameters and device structure (such as doping).

The two different methods presented here are to show that TFETs can achieve SS smaller than MOSFETs. In fact, to achieve sub-60 mV/dec SS, V_G should be minimized for TFETs. Since the goal is to reduce supply voltages, this makes TFETs look very promising for continued scaling. Additionally, it should be noted that the SS calculated here are instantaneous numbers. Meaning, they are valid only at one specific V_G. Of greater importance is the average SS = (V_{on} - V_{off})/log(I_{on}/I_{Off}), which will extend the usable V_G for a TFET even further.

There have been many reports of carious TFET structures. Typically, experimental reports of TFETs have had poor SS, I_{ON}, I_{Off}, and/or I_{ON}/I_{Off} ratios. Table 2.1 lists a handful of experimental TFET results, which have been fabricated in CNT [19], Ge [14], Si [11, 12, 24], and InGaAs [25, 26] materials. However, they all have had small I_{ON}. Some structures have been able to dramatically improve drive currents by increasing V_{DD} above one volt, which is much

Table 2.1: Experimental Reports of TFETs

Study	Year	Material	Best SS V_{DS} (V)	Best SS SS (mV/dec)	Best SS I_{on} (μA/μm)	Best I_{ON} V_{DD} (V)	Best I_{ON} SS (mV/dec)	Best I_{ON} I_{on} (μA/μm)	Lg (nm)	Dielec./thickness
Appenzeller	2004	CNT	<0.5	40	0.1				200	Al_2O_3/4 nm
Krishnamohan	2008	Ge	0.5	50	~1	3	~250	300	1,000	SiO_2/NA nm
Gandhi	2011	Si	0.1	30	<0.01	1.2	50	~0.1	170	SiO_2/4.5 nm
Jeon	2010	Si	-1	46	2.5	-1.5		4.2	20,000	HfO_2/0.9 nm
Loh	2010	Si		80		-1	~200	109	56	"highK"/1.1 nm
Mookerjea	2009	InGaAs	0.05	200	0.5	0.75	~300	20	100	Al_2O_3/10 nm
Zhoa	2010	InGaAs	0.05	86	2	1.05	93	50	100	HfO_2/1.2 nm
Mohata	2011	Hetero*				0.75	~750	190	150	Al_2O_3/HfO_2 1/3.5
Dewey	2010	InGaAs	0.05	<60	4.7				150	$TaSiO_x$/4 nm

greater then target supply voltages (< 0.5 V) for deeply scaled devices. There has not been a reported TFET with a high I_{ON}, low I_{Off}, and sub-60 mV/dec. SS.

Recall that TFETs can achieve low SS because I_D is dominated by BTBT as the Source/Body junction. The band diagram for that junction (See Fig. 2.6) is similar to that of an ETD (discussed below, Fig. 2.3). With some amount of V_{DD}, an increase in V_G corresponds to a reverse biased ETD with greater n-type doping. Therefore, ETDs are simple structures that can be used to investigate BTBT, calibrate models, and predict TFET characteristics.

References for Chapter 2

[1] L. Esaki, "New Phenomenon in Narrow Germanium p-n Junctions," *Physical Rev.,* vol. 109, p. 603, 1958.

[2] E. O. Kane, "Theory of Tunneling," *J. Appl. Phys.,* vol. 32, p. 83, 1961.

[3] G. A. M. Hurkx, "On The Modeling of Tunneling Currents in Reverse-Biased P-N-Junctions," *Solid-State Electron.,* vol. 32, pp. 665-668, Aug 1989.

[4] V. Milovanovic and R. van der Toorn, "A Novel Physics-Based Compact Model of Band-to-Band Tunneling Current in p-n Junctions," *IEEE Trans. Elect. Dev.,* vol. 57, pp. 1583-1589, Jul 2010.

[5] A. Schenk, "Rigorous Theory and Simplified Model of the Band-to-Band Tunneling in Silicon," *Solid-State Electron.,* vol. 36, pp. 19-34, 1993.

[6] P. M. Solomon, J. Jopling, D. J. Frank, C. D'Emic, O. Dokumaci, P. Ronsheim*, et al.*, "Universal Tunneling Behavior in Technologically Relevant P/N Junction Diodes," *J. Appl. Phys.,* vol. 95, pp. 5800-5812, May 2004.

[7] D. Meyerhofer, G. A. Brown, and H. S. Sommers, "Degenerate Germanium. I. Tunnel, Excess, and Thermal Current in Tunnel Diodes," *Physical Rev.,* vol. 126, p. 1329, 1962.

[8] R. M. Minton and R. Glicksman, "Theoretical and Experimental Analysis of Germanium Tunnel Diode Characteristics," *Solid-State Electron.,* vol. 7, pp. 491-500, 1964.

[9] A. C. Seabaugh and Z. Qin, "Low-Voltage Tunnel Transistors for Beyond CMOS Logic," *Proc. IEEE,* vol. 98, pp. 2095-2110, 2010.

[10] R. A. Logan and A. G. Chynoweth, "Effect of Degenerate Semiconductor Band Structure on Current-Voltage Characteristics of Silicon Tunnel Diodes," *Physical Review,* vol. 131, p. 89, 1963.

[11] R. Gandhi, Z. Chen, N. Singh, K. Banerjee, and S. Lee, "Vertical Si-Nanowire *n*-Type Tunneling FETs With Low Subthreshold Swing (< 50 mV/decade) at Room Temperature," *IEEE Electron Device Lett.,* vol. 32, pp. 437-439, 2011.

[12] K. Jeon, W.-Y. Loh, P. Patel, C. Y. Kang, J. Oh, A. Bowonder*, et al.*, "Si Tunnel Transistors With a Novel Silicided Source and 46mV/dec Swing," in *Symp. VLSI Technol.*, 2010, pp. 121-122.

[13] S. O. Koswatta, S. J. Koester, and W. Haensch, "On the Possibility of Obtaining MOSFET-Like Performance and Sub-60-mV/dec Swing in 1-D Broken-Gap Tunnel Transistors," *IEEE Trans. Electron Devices,* vol. 57, pp. 3222-3230.

[14] T. Krishnamohan, D. Kim, S. Raghunathan, K. Saraswat, and Ieee, "Double-Gate Strained-Ge Heterostructure Tunneling FET (TFET) With Record High Drive Currents and < 60mV/dec Subthreshold Slope," in *IEEE IEDM Tech. Dig.*, ed, 2008, pp. 947-949.

[15] T. Nirschl, P. F. Wang, C. Weber, J. Sedlmeir, R. Heinrich, R. Kakoschke*, et al.*, "The Tunneling Field Effect Transistor (TFET) as an Add-On for Ultra-Low-Voltage Analog and Digital Processes," in *in IEDM Tech. Dig.*, 2004, pp. 195-198.

[16] Z. Qin and A. Seabaugh, "Can the Interband Tunnel FET Outperform Si CMOS?," 2008, pp. 73-74.

[17] A. Seabaugh, "Tunnel Field-Effect Transistors - Status and Prospects," in *IEEE Dev. Res. Conf.*, 2010, pp. 11-14.

[18] P. F. Wang, K. Hilsenbeck, T. Nirschl, M. Oswald, C. Stepper, M. Weis*, et al.*, "Complementary Tunneling Transistor for Low Power Application," *Solid-State Electron.,* vol. 48, pp. 2281-2286, 2004.

[19] J. Appenzeller, Y. M. Lin, J. Knoch, and P. Avouris, "Band-to-Band Tunneling in Carbon Nanotube Field-Effect Transistors," *Phys. Rev. Lett.,* vol. 93, pp. 196805-1-196805-4, 2004.

[20] K. K. Bhuwalka, J. Schulze, and I. Eisele, "Scaling the Vertical Tunnel FET With Tunnel Bandgap Modulation and Gate Workfunction Engineering," *IEEE Trans. Electron Devices,* vol. 52, pp. 909-917, May 2005.

[21] W. Y. Choi, B. G. Park, J. D. Lee, and T. J. K. Liu, "Tunneling Field-Effect Transistors (TFETs) With Subthreshold Swing (SS) Less than 60 mV/dec," *IEEE Electron Device Lett.,* vol. 28, pp. 743-745, Aug 2007.

[22] Z. Qin, Z. Wei, and A. Seabaugh, "Low-Subthreshold-Swing Tunnel Transistors," *IEEE Electron Device Lett.,* vol. 27, pp. 297-300, 2006.

[23] E. O. Kane, "Zener Tunneling in Semiconductors," *J. Phys. Chem. of Solids,* vol. 12, pp. 181-188, 1960.

[24] W.-Y. Loh, K. Jeon, C. Y. Kang, J. Oh, P. Patel, C. Smith*, et al.*, "Sub-60nm Si Tunnel Field Effect Transistors With Ion 100 mA/um," in *Proc. European Solid State Dev. Res. Conf.*, 2010, pp. 162-165.

[25] S. Mookerjea, D. Mohata, R. Krishnan, J. Singh, A. Vallett, A. Ali*, et al.*, "Experimental Demonstration of 100nm Channel Length In0.53Ga0.47As-Based Vertical Inter-band Tunnel Field Effect Transistors (TFETs) for Ultra Low-Power Logic and SRAM Applications," in *IEDM Tech. Dig.*, 2009, pp. 949-951.

[26] Z. Han, Y. Chen, Y. Wang, F. Zhou, F. Xue, and J. Lee, "In0.7Ga0.3As Tunneling Field-Effect Transistors With an I on of 50 uA/um and a Subthreshold Swing of 86 mV/dec Using HfO2 Gate Oxide," *IEEE Electron Device Lett.,* vol. 31, pp. 1392-1394, 2010.

CHAPTER 3

Tunnel Diode Modeling

This chapter discusses the modeling of BTBT characteristics for ETD structures. First, an appropriate BTBT model is chosen after a brief discussion on the merits of several prominent models are examined. As the criteria for selection, the chosen model should be (i) a simplified analytical expression with the (ii) fewest fitting parameters, (iii) forward and reverse bias modeling capabilities, and (iv) applicable to multiple material systems (primarily direct bandgap systems). The chosen model will then be calibrated to experimental results (Chapters 4, 5, and 6), and used for gaining a greater understanding of ETDs. Specifically, identifying quantifiable relationships between J_{BTBT} and material/structural device parameters and determining optimal device structures.

The Kane model [1] will be chosen as the best option, since it most closely satisfies the previously stated criteria. Regardless, the Kane model is still sufficiently rigorous for calculating full BTBT characteristics, and therefore has only been compared to Ge and Si ETD experimental results in a few studies. First, the assumptions, approximations, and general form of the Kane model will be discussed. This is then followed by detailed qualitative and quantitative analysis of each component. Of particular interest is a comparison between the original BTBT probability by Kane and the more common WKB approximation, detailed by Sze, *et al.* [2]. This section concludes with an extensive discussion detailing the calculation and behavior of the overlap integral.

Following the discussions specific to the Kane model, the equations and methods used to accurately calculate degenerate Fermi energies (E_F) is detailed. Accurate E_F values are calculated using a numerical integration technique specifically developed for this work. Results are compared with non-degenerate and super-degenerate approximations, which are used as initial

guesses when determining E_F. Following this discussion, the type of effective mass, and formulas used to average various effective masses together is discussed.

Finally, the chapter discusses the Kane Model Program (KMP) developed for this work. First, the operation and organization of the graphical user interface (GUI) of the program is discussed. Then, the different types of analysis types available are explained, as well as the operation flow that the program uses to perform the calculations.

List of Variables:

e^-, h^+	electrons, holes
q	Magnitude of the charge on an electron
$\hbar$	Reduced Plank's constant
kT	Thermal energy (Boltzmann's constant & temperature)
ε_s, ε_r	Dielectric constant, Relative dielectric constant
E_G	Bandgap
m^*	Effective mass
m_r, $m_{r,n}$, $m_{r,p}$, $m_{r,BTBT}$	Relative effective mass, electrons, holes, average for BTBT
$m_{r,light}$, $m_{r,heavy}$	Relative effective mass for light and heavy holes
E_F, $E_{F,n}$, $E_{F,p}$	Fermi energy, n-side of junction, p-side of junction
$\Delta E_{F,n}$, $\Delta E_{F,p}$	$E_{F,n} - E_{C,n}$ and $E_{V,p} - E_{F,p}$
E_C, $E_{C,n}$, $E_{C,p}$	Conduction band, n-side of junction, p-side of junction
E_V, $E_{V,n}$, $E_{V,p}$	Valence band, n-side of junction, p-side of junction
N_A, N_D, N^*	Acceptor & Donor concentrations, reduced average doping concentration
N_C, N_V	Density of states (DOS) constants for the conduction & valence band
g_C, g_V	DOS energy distributions for conduction & valence bands
$f(E)$, $f_n(E)$, $f_p(E)$	Fermi-Dirac distribution, n-side, p-side

w_d, w_n, w_p	Depletion width, n-side, p-side
ξ	Electric field
V_{bi}	Built-in voltage
V_A	Applied bias
D, $D'(E)$	Overlap integral, integrand of D (differential with respect to energy)
T_{Kane}, T_{WKB}	BTBT probability from E. O. Kane [1], using WKB approximation [2]

3.1. General Discussion on BTBT Models

For the theoretical analysis in this work, an analytical, physics based, expression is desired. It is recognized that TCAD simulations using finite element numerical methods have the potential of providing far more accurate predictions for a much larger range of device structures. However, such models require much greater effort to calibrate with experimental results. On the other hand, closed form analytical expressions are great for (i) quick calculations, (ii) revealing underlying physics and relationships, and (iii) indentifying paths to optimizing and scaling device structure. *Additionally, it is desirable for the model to work with multiple material systems without altering generic fitting parameters, as that mitigates the previous two benefits.* Therefore, models that are relatively complex, or material specific such as those developed for Si and Si/SiGe interband tunnel diodes [3], will not be chosen for this work.

The E. O. Kane model [1], was developed to be a physics based analytical expression for the BTBT behavior of ETDs. It is appropriate for both the forward and reverse bias BTBT characteristics. As with any analytical model, there are a number of reasonable approximations and simplifications made (see Section 3.2). There exists one term, named the overlap integral, which has no closed form solution. However, a detailed qualitative and quantitative analysis simplifies its behavior into three generic forms. With this model, only basic physical and material constants, as well as doping concentrations, are needed to obtain a full direct BTBT J-V

characteristic. Even though it is one of the earliest BTBT models developed, it is the most appropriate for this work for it best fits the previously mentioned criteria.

Another original model was developed by Bergner and Kircher [4]. The author's in [4] were able to achieve excellent agreement between their model and experimental results for low and high electric fields. However, the model is built primarily for determining gate induced BTBT and is comprised of a double integral. Furthermore, within the paper a series of fitted parameters and parabolic fit to the tight binding calculation of the complex band structure for Si were key to the models accuracy. Once again, this model is not appropriate for this work due to the large use of various fitted parameters, which likely change with material systems.

Hurkx, *et al.* [5] and Milovanović, *et al.* [6] based their models directly off of Kane's [1]. In Hurkx, some of the constants (numeric, physical, and material) were combined into generalized constants which need to be determine for each material. Of greater importance is the simplification of the complex overlap integral, described in Section 3.2.3, as V_A. This is a limited approximation, and is not valid beyond very small forward V_A, and sometimes not even for small reverse V_A. As a result, the model will not capture the forward bias characteristics, including J_P and NDR. Milovanović improves the overlap integral approximation to work up to $V_A = 0$ V in most cases. However, the model was not designed, and therefore will not capture J_P and NDR.

Schenk, *et al.* [7] developed a rigorous model primarily for comparing direct BTBT, indirect phonon assisted BTBT, and trap assisted tunneling in Si. The final model form is reported as a tunnel rate function, which is presented as more appropriate for device simulation purposes, and was simplified specifically implementing the complex band structure of Si. Therefore, the J_{BTBT} function presented is still fairly generalized, with over a dozen terms, directional effective masses, wave vector functions, and multidimensional summations. However, the final complex J_{BTBT} formulation was developed out of a direct (zero-phonon) BTBT formulas which the authors admit as agreeing with a form of Kane's model [1]. Given that the

final model is specifically for Si, and the intermediate model is similar to Kane, Schenk's model is inappropriate for the goal's of this work.

In 2004, Solomon, *et al.* [8] reported on a method for determining universal tunneling behavior. The work was specifically geared towards, and analyzed experimental data from Si based structures. However, the method presented could easily be adopted for additional material systems. Each material system would exhibit is own "universal" tunneling behavior. The model simply relates $J_{BTBT}(V_A)$ to the tunnel barrier width for that V_A. For large doping concentrations and/or fields, an exponential relationship was observed. The additional of a band curvature correction factor improved the exponential relationship over eight orders of magnitude in J_{BTBT}. The model is quite reasonable, and was even used to extract an effective tunnel mass. However, in its present form the model would not capture J_P or NDR, thereby predicting J_{Zener}, and potentially $J_{Forward}$ for very small VA depending on the device structure and doping concentrations. Therefore, Solomon's model will not be used for calculating BTBT characteristics. It may become useful for developing a more generalized method of extracting material parameters, or even the development of a true universal BTBT model.

An interesting model by Jandiery, *et al.* [9] was developed to look at the ability of controlled mid-bandgap states enhancing the BTBT current density of an ETD. This may be a useful way to improve TFET drive currents, similar to intermediate band [10] and Quantum dot [11, 12] solar cells. However, it may also turn out that a TFET implementing midgap states would have unmanageable I_{Off}. In this work, ideally the tunnel junctions are formed with high quality epitaxy, with a negligible density of midgap states. Therefore, the model will not be pursued in this work.

3.2. Kane Model: Assumptions, Approximations, and Form

The E. O. Kane model, as described in [1], is the main physics based method for predicting the BTBT current densities of ETDs in this work. The model was developed shortly after the initial discovery of the ETD by Esaki in 1957 [14]. However, over the years the model has rarely been matched with experimental data, and typically only J_P. Furthermore, application of the model has been obscured by gross approximation of one of the major terms in the model [5, 6, 15] and inaccurate reproduction of the BTBT probability term [2, 15], both of which are discussed in sections 3.2.3 and 3.2.2, respectively.

As with any analytical model, several assumptions and approximations were made in its development. There have been many attempts to generalize the model [5-7, 16], potentially increasing its accuracy over a larger design space. This work concentrates on the most basic form, discussed in Section 3.2.1 (Eq. (3.1)). In this version, the E-k band valleys and maximums are assumed to be perfectly parabolic resulting in a constant m_r DOS.

The 2nd order derivative, and therefore m_r, does change as one moves away from the band

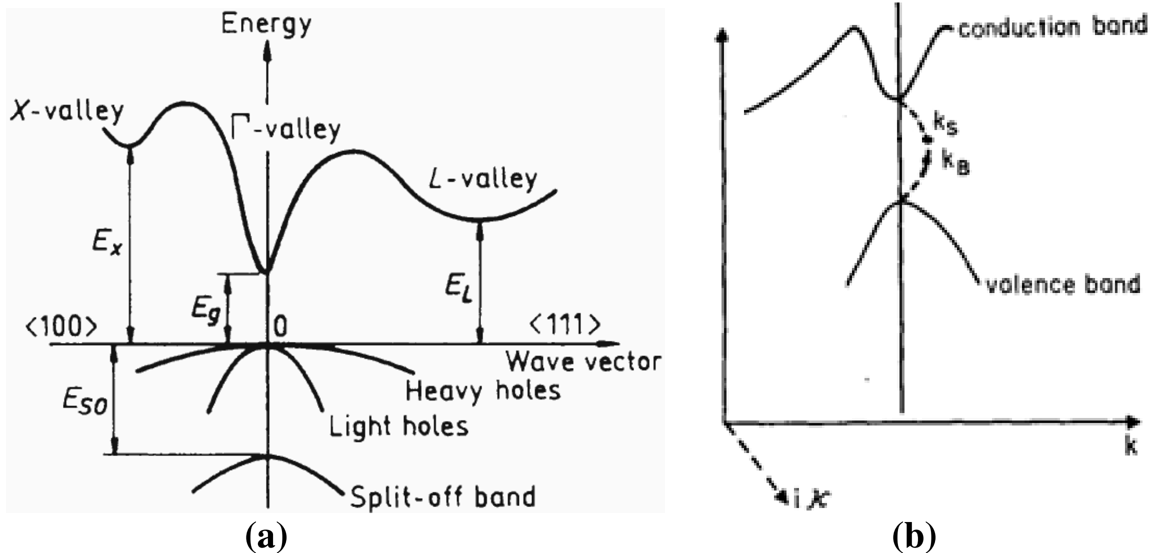

Fig. 3.1: Left (a), Generic E-k diagram indicating direct bandgap (Γ-valley), indirect bandgaps (L- and X-valleys), and light-, heavy, and split-off holes (adopted from [13]). Right (b), generic E-k diagram showing parabolic tunneling path through imaginary k-space that carriers travel when through the forbidden bandgap (adopted from [1]).

minimums and maximums. However, generally the changes are fairly minor until one moves far from these points. Additionally, with very large doping the L- and X-valleys (shown in Fig. 3.1a) begin filling with e^-, limiting further increases $E_{F,n}$.

As indicated above, the material systems used are assumed to have a direct bandgap (Γ-valley), similar to Fig. 3.1a. Additionally, the vast majority of BTBT current is generated at the direct bandgap. Specifically, BTBT occurs between the Γ-valley and maximum in the conduction and valence bands of the n- and p-sides of the p-n junction, respectively. This is known as the "2-bands" approximation. Furthermore, the tunneling path through the forbidden bandgap is approximated as parabolic in shape, along the imaginary k-space as shown in Fig. 3.1b.

If additionally band are occupied (L- and X-valleys), typically their m_r and E_G are much larger than the direct gap. Combined with the need for a momentum shift in k-space, usually through phonon or photon interactions, the BTBT probabilities between these extra bands are generally negligible. Therefore, the $m_{r,BTBT}$ is an average of the conductivity $m_{r,e}$ and $m_{r,h}$ along $k(\Gamma)$.

The doping profiles are assumed to be perfectly square, fully activated, adjacent to each other, and fully-depleted. However, as a simplification of the BTBT probability, the tunnel barrier formed by the forbidden bandgap (Fig. 3.2) is assumed to be triangular as determined with a height of E_G and slope of ξ. Where ξ (average electric field) is the built in bias scaled by the applied bias, linearly dropped over the entire depletion width. In other words, it is the average electric field over the entire depletion width of the p-n junction.

3.2.1. Kane Model Equation

The Kane model, (3.1), can be separated into three terms. The pre-factor (first term) is a function of physical and material constants as well as ξ in (3.2), whose magnitude changes with

V_A and the reduced average doping (N^*) as defined by (3.4). As previously mentioned, ξ is approximated as a constant and defined by the magnitude of $(V_{bi}-V_A)/w_d$, which is represented in the band diagram in Fig. 3.2. Equation (3.3) is the depletion width calculated using the full depletion approximation of two square doping profiles with no *i*-layer in the middle of the p-n junction. This term is always positive, but it does attenuate the BTBT current density in forward bias and enhances it in reverse bias (Fig. 3.3a left y-axis).

$$J_{BTBT} = \frac{q\xi}{36\pi\hbar^2}\sqrt{\frac{2m^*}{E_G}} \times D \times \exp\left(-\frac{\pi\sqrt{m^*}E_G^{3/2}}{2\sqrt{2}\hbar\xi}\right) \tag{3.1}$$

$$\xi = \frac{V_{bi}-V_A}{w_d} = \sqrt{\frac{q\left(V_{bi}-V_A\right)}{2\varepsilon_s}N^*} \tag{3.2}$$

$$w_d = \sqrt{\frac{2\varepsilon_s\left(V_{bi}-V_A\right)}{qN^*}} \tag{3.3}$$

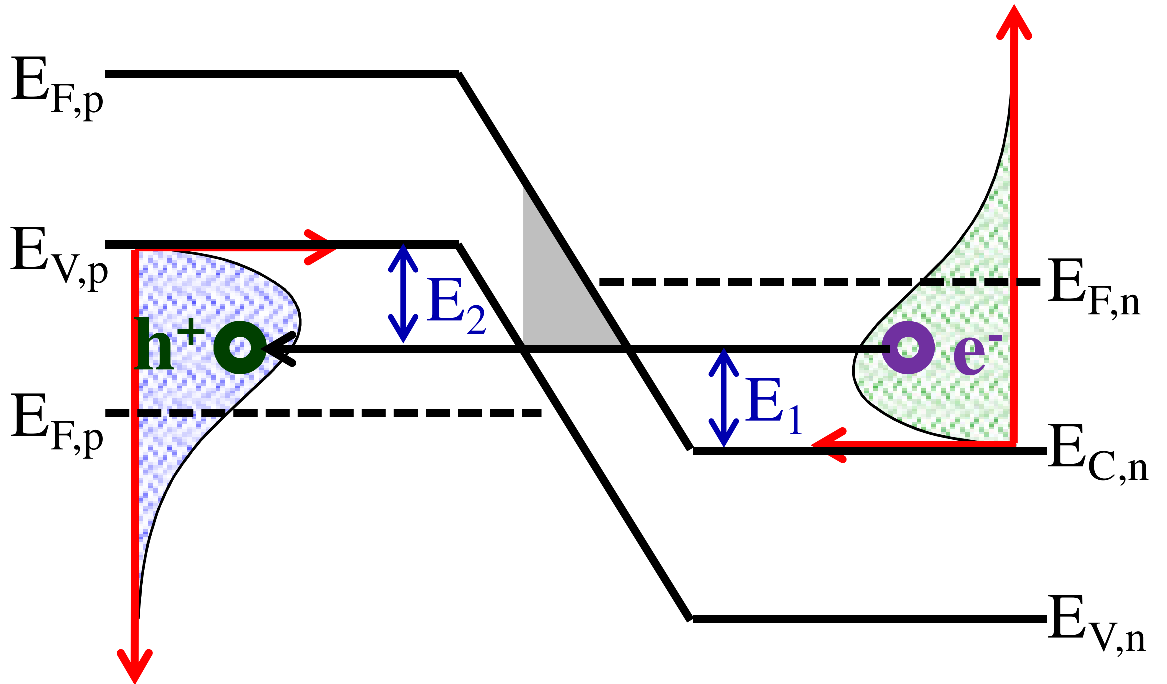

Fig. 3.2: Sketch of ETD band diagram with simplified, triangular depletion region. This is the idealized shape of the bands used in the Kane model.

$$N^* = \frac{N_A N_D}{N_A + N_D} \quad (3.4)$$

The second term is the overlap integral (D) and accounts for the degree of overlapping carrier distributions, which provides the actual current flow. Fig. 3.2 shows the generic band diagram of an ETD biased just prior to V_P. Due to the forward bias, there are a large number of electrons in the conduction band (right hand side) whose energy aligns with a similarly large quantity of holes (empty states) in the valence band (left hand side). This overlap of carrier distributions has provided an imbalance of electrons, which are free to tunnel through the bandgap (approximated as triangular) and into an empty states (holes) on the other side of the junction. As such, a BTBT current is generated. For the situation shown in Fig. 3.2, the current flows from right to left. However, in the Zener direction electrons in the valence band on the p-side will tunnel into hole states in the conduction band of the n-side, this reversing the current flow. Therefore, D handles the availability of carriers (electrons and holes) for BTBT and

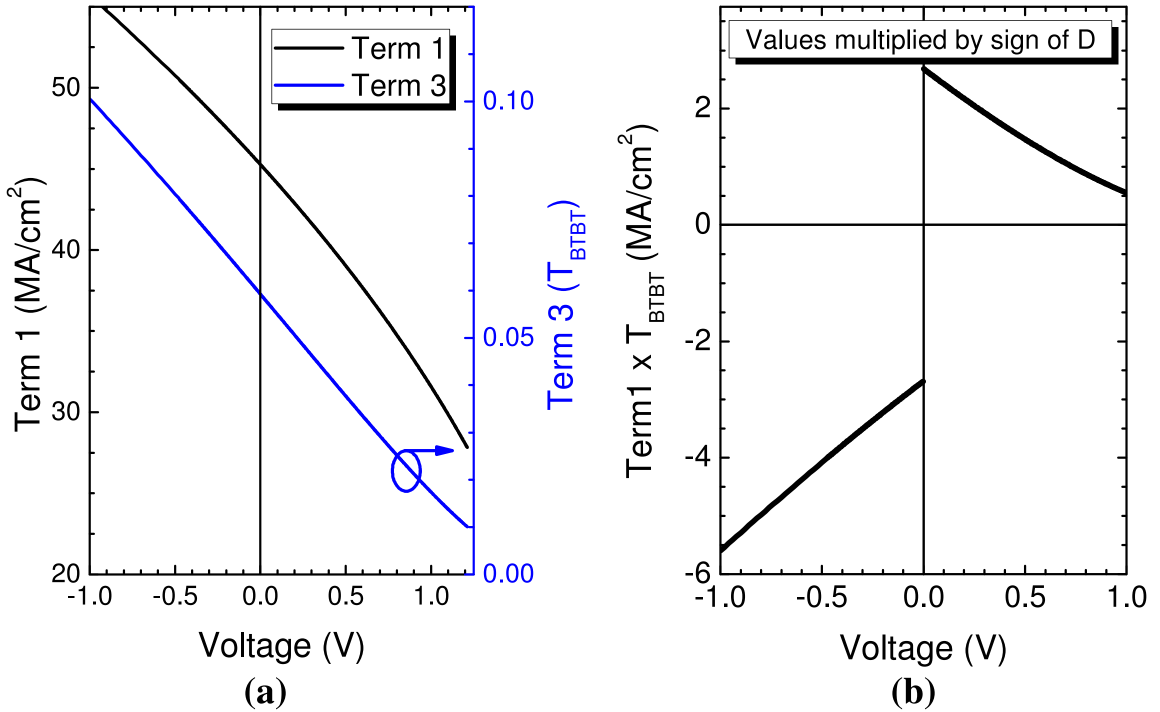

Fig. 3.3: Left (a), plot of the pre-factor on the left axis and T_{Kane} on the right axis. Right (b), pre-factor and T_{Kane} multiplied together as well as the sign of D to account for the direction of current flow.

dictates the direction of current flow. The complexity of D is symbolically and quantitatively discussed in sections 3.2.3 and 3.2.3.1.

The final term (the exponential) represents the BTBT probability associated with carriers tunneling through the forbidden bandgap. Similar to the pre-factor, the exponential is a function of physical and material constants, as well as ξ. As before, decreasing N^* or increasing V_A decreases BTBT current density (Fig. 3.3a right y-axis). However, J_{Kane} is naturally more strongly related with the exponential (BTBT probability), and therefore will tend to change exponentially with N^* and N_A. Furthermore, the pre-factor and exponential continually decreases with $\sqrt{V_{bi} - V_A}$ which, by themselves, would turn the entire forward J-V characteristics into NDR (Fig. 3.3b). Therefore, it is the behavior of D that causes J_{Kane} to initial increase, form a peak, and then decreasing (NDR) as V_A in forward bias. In other words, it is the overlap of carrier distributions on either side of the tunnel junction that is primarily responsible for the ETDs unique "N" shape characteristic in forward bias. The other terms are shaped by material parameters and biasing conditions, which primarily manipulate the magnitude of the various regions of the ETD J-V characteristic.

3.2.2. Common BTBT Probability Error

It has become common to calculate T_{BTBT} directly from the WKB approximation [1, 15] as in (3.5). Just like Kane's original formulation, the ξ is assumed to be constant and triangular over the full depletion width. As per WKB, the absolute value of the wave vector (k(x)) is integrated over the classical turning points x = 0 to E_G/ξ (the tunnel barrier width). The tunnel barrier potential is the shaded triangular region in Fig. 3.2, with a slope of ξ, and y-intercept of E_{e-} (same as the tunnel electron). Therefore, the waver vector for the electron is (3.6). Performing the integral provides (3.7), which is similar the exponential term in (3.1).

$$T_{WKB} \approx \exp\left(-2 \int_0^{E_G/\xi} |k(x)| dx \right) \tag{3.5}$$

$$k(x) = i\sqrt{\frac{2m^*}{\hbar^2}\left[U(x) - E_{e^-}\right]};\ U(x) = \xi x + E_{e^-} \tag{3.6}$$

$$T_{WKB} \approx \exp\left(-\frac{4\sqrt{2m^*}E_G^{3/2}}{3\hbar\xi} \right) \tag{3.7}$$

The only differences between Kane's model and the WKB approximation end up in T_{WKB} and T_{Kane}, as shown in (3.8). Specifically, the numerical constants in T_{WKB} turn out to be ~70% larger than T_{Kane}, (3.9). Since this difference resides within an exponentially, there can be very large discrepancies between the two models. For instance T_{Kane}/T_{WKB} for GaAs with an E_G on 1.42 eV, m_r of 0.54, and an ξ as low as 1.13×10^8 V/m ($N^*=1\times10^{19}$ /cm^{-3}) would be ~18,000x. As the Current density increases, by increasing N^* to 2.5×10^{19} /cm^{-3}, the ratio decreases to ~250x. Moving towards a material system (InSb) with a smaller bandgap (0.18 eV) and m_r (0.019) reduces the ratio to 1.4x and 1.2x for the same doping concentrations. *In other words, the WKB approximation version of the model can substantially underestimate J_{BTBT} with respect to the original Kane model.* If one version of the model is more accurate than the other, it will become very apparent at low BTBT current densities, even if they both match well for very large current densities.

$$T_{Kane} = \exp\left(-\frac{\pi\sqrt{m^*}E_g^{3/2}}{2\sqrt{2}\hbar\xi} \right) \neq \exp\left(-\frac{4\sqrt{2m^*}E_g^{3/2}}{3\hbar\xi} \right) = T_{WKB} \tag{3.8}$$

$$\frac{\pi}{2\sqrt{2}} \approx 1.1107 \neq 1.8856 \approx \frac{4\sqrt{2}}{3} \tag{3.9}$$

3.2.3. Overlap Integral

The overlap integral, D in (3.10), accounts for the degree of overlapping carriers which provides the actual current flow. This takes place in the energy space above $E_{C,n}$ and below $E_{V,p}$, primarily between $E_{F,n}$ and $E_{F,p}$, which is depicted in Fig. 3.2. As dictated by Fermi-Dirac statistics, within this region most of the conduction band states are filled with electrons, which are free to tunnel through the bandgap into the largely empty states on of the p-side of the junction. Above $E_{F,n}$ and $E_{F,p}$, the majority of states are empty (filled with holes) on both sides of the junction and therefore there are few electrons available for tunneling. Conversely, below $E_{F,n}$ and $E_{F,p}$ there are very few states for readily available electrons to tunnel into.

$$D = \int_{E_{C,n}}^{E_{V,p}} \left[f_n(E) - f_p(E) \right] \left[1 - \exp\left(-\frac{2E_S}{\overline{E}} \right) \right] dE \tag{3.10}$$

The overlap integral,(3.10), is the product of two separate terms. The first term is the difference between the Fermi-Dirac distributions, as defined in (3.11), on the n- and p-sides of the junction. This is the term that specifically accounts for the distribution of electrons and holes (empty states). The greatest imbalance between $f_n(E)$ and $f_p(E)$ occurs between $E_{F,n}$ and $E_{F,p}$, with a maximum value of one reached within a few kT of $E_{F,n/p}$. Outside of this region, the first term reduces to ~0 after a few kT. After a small reverse bias, the integral of the first term will increase at the same rate as V_A. In forward bias there will be an initial rise in D, until $E_{C,n}$ is less than $E_{F,p}$ when $\Delta E_{F,p} >> \Delta E_{F,n}$, or $E_{V,p}$ is greater than $E_{F,n}$ when $\Delta E_{F,n} >> \Delta E_{F,p}$. When one of the previous conditions are met, the integral of $f_n(E) - f_p(E)$ becomes pegged at a constant value by the smaller of $\Delta E_{F,p}$ or $\Delta E_{F,n}$, causing D to flatten out into a mesa type shape (discussed in 3.2.3.1, Fig. 3.4). When a very large V_A is applied, eventually $E_{F,n}$ will begin to drop below $E_{V,n}$ and $E_{F,n}$ will starts to rise above $E_{C,n}$. In this regime, the bounds of the integral directly impact the sum of $f_n(E) - f_p(E)$ between $E_{C,n}$ and $E_{V,p}$, thereby decreasing the output of D to 0 eV when $E_{C,n}$ equals $E_{V,p}$. In forward bias, $E_{F,n}$ is greater than $E_{F,p}$, allowing for electrons to tunnel from right to left and

providing positive current flow. In reverse bias, $E_{F,p}$ is greater than $E_{F,n}$, causing electrons to tunnel for left to right and providing a negative current flow.

$$f_{n/p}(E) = \frac{1}{1+\exp\left(\frac{E-E_{f,n/p}}{kT}\right)} \tag{3.11}$$

$$\overline{E} = \frac{\sqrt{2}\hbar\xi}{\pi\sqrt{m^{*}E_G}} \tag{3.12}$$

The second term is an attenuation factor, where E_S is the smaller of E_1 and E_2 and always positive, as defined in Fig. 3.2. Additionally, $\bar{E}$ is always positive and decreases as V_A increases due to its relation with ξ as shown in (3.12). Consequentially, the second term ranges between zero and one (unitless), depending on material parameters and biasing condition. The maximum value of E_S increases with doping and is linearly related to $-V_A$, whereas $\bar{E}$ is related to $(V_{bi} - V_A)^{1/2}$. Therefore, E_S has a faster effect on the second term. Since E_S has a larger influence than $\bar{E}$, the second term will quickly approach a value of one in reverse bias. Consequentially, for large reverse bias and sometimes for small forward/reverse biases, both terms approach unity at energies between $E_{F,n}$ and $E_{F,p}$. Therefore, D increases at the same rate as the first term, which will increase the same as V_A ($D \approx V_A$). At forward V_A, E_S does not increase as large or fast with respect to $\bar{E}$, thereby attenuating the first term.

$$D(V_A) \approx \Delta E \sum_{n=0}^{N} \left[f_n(E_n) - f_p(E_n) \right] \left[1 - \exp\left(-\frac{2E_S(E_n)}{\overline{E}(E_n)} \right) \right] \tag{3.13}$$

$$E_n = n \times \Delta E = n \times \frac{V_{bi} - V_A - E_G}{N} \tag{3.14}$$

As previously mentioned, the overlap integral does not have a closed form solution. Therefore, D is calculated using rectangular numerical integration as defined in (3.13). The energy range of interest ($E_{C,n} \rightarrow E_{V,p}$) is divided into 500 ($N$) equal step sizes ($\Delta E$) as defined in (3.14). Furthermore, D must be calculated for all V_A of interest.

3.2.3.1. Detailed Behavior of Overlap Integral

There are three basic shapes that D may exhibit, shown in Fig. 3.4; (i) simple cone, (ii) Simple mesa or trapezoidal, and (iii) complex mesa. The final shape obtained depends on the ratio of $E_{F,n}$:$E_{F,p}$. To simplify the analysis, the examples in this section assume $m_{r,e} = m_{r,p} = 0.1$, with a tunneling m_r of 0.065. Consequentially, the electron and hole DOS are the same at 7.94×10^{17} /cm^{-3}. Therefore, with this fictitious material system, changes in N_A and N_D affect $E_{F,p}$ and $E_{F,n}$ to the same degree. E_G and ε_r were taken as the average of several common III-V compound semiconductors; (i) 0.67 eV and (ii) 15.14, respectively.

The simplest shape is cone-like, which occurs when $E_{F,n} \approx E_{F,p}$ ($N_D = N_A$ in Fig. 3.4). The dashed line is the ideal shape of D when the 2nd term in (3.10) is approximated as one. For V_A less then the peak value ($\sim V_{bi} - E_G$), D is approximately equal to V_A for both cases. As expected, the ideal case (dashed line) peaks at $(V_{bi} - E_G)/2$, then drops off to zero at $(V_{bi} - V_A)$ with a slope of -1. The rounded top is purely due to thermal spread in the Fermi-Dirac statistics. For the real

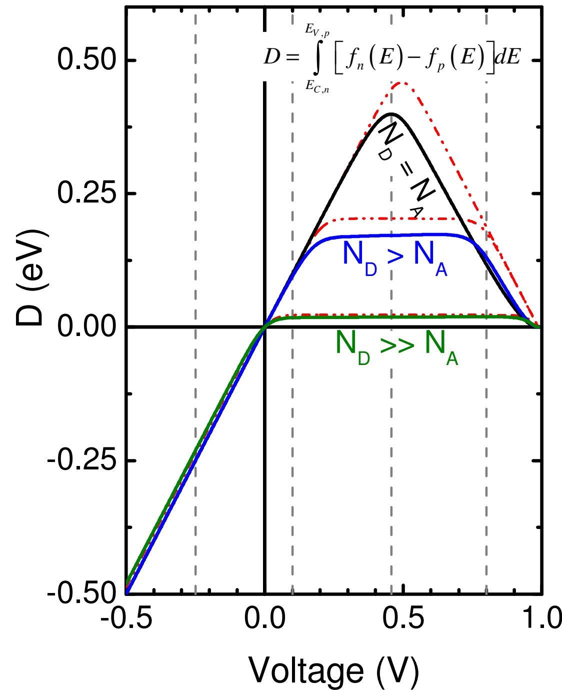

Fig. 3.4: Overlap integral for three different situations; (i) cone, (ii) simple mesa, and (iii) complex mesa shapes. The dash-dot-dot lines are idealized D characteristics.

D (solid line) characteristic, the 2nd term begins to significantly dampen the final values shortly before the peak. This has the effect of reducing the maximum peak, and shifting it slightly to the left. The post peak slope is still -1 until shortly before D reaches zero.

In Fig. 3.5, the 1st and 2nd terms comprising D are plotted for V_A of (a, e) -0.25 V, (b, f) 0.1 V, (c, g) 0.457 V, and (d, h) 0.8 V. The left hand portion of each plot constructs the 1st term involving $f_{n/p}$. The right hand portion plots the 1st and 2nd terms (solid lines) as well is the combined value ($D'(E)$) which is designed by the "*" symbols. *The area of the shaded region, bounded by $D'(E)$, is the final value of D for the given V_A.* To the right of each plot are representative band diagram sketches with appropriately scaled carrier distributions.

For V_A of -0. 25 V (Fig. 3.5a, e), the BTBT current is generated symmetrically between $E_{V,p}$ and $E_{C,n}$. The first term reaches its maximum (~1) exactly in the middle of the bands, which corresponds to an equal match in e^- and h^+ concentrations. The entire 1st term fits within the region of the 2nd term that is ~1, and therefore does not play a significant role in D. Consequentially, the actual D value is equivalent to the ideal case. Additionally, it is the e^- distribution in the p-side and the h^+ distribution in the n-side that provide the BTBT currents. This is opposite to the standard orientation expected in forward bias.

At a small forward bias of 0.1 V (Fig. 3.5b, f) there is only a small region of energies that provide BTBT. Additionally, within energy range the currier distributions do not reach full occupancy of available states due to $f_{n/p}$. However, the 1st term still fully resides within the 2nd term, and therefore D continues to increase with V_A. This trend continues until near the peak (Fig. 3.5c, g), at which time the 2nd term begins to restrict $D'(E)$, and attenuate the final value. As $E_{F,n/p}$ approach the bandgap edges (according to kT and $f_{n/p}$), the 2nd to begins to "cut-off" the Fermi distribution tails. Notice that the maximum carrier distributions are not fully aligned. After $E_{F,n/p}$ are a few kT beyond the bandgap edges the carriers will fully occupied the available states, 1st will equal one, and $D'(E)$ will become fully defined by the 2nd term, as shown in Fig. 3.5d, h.

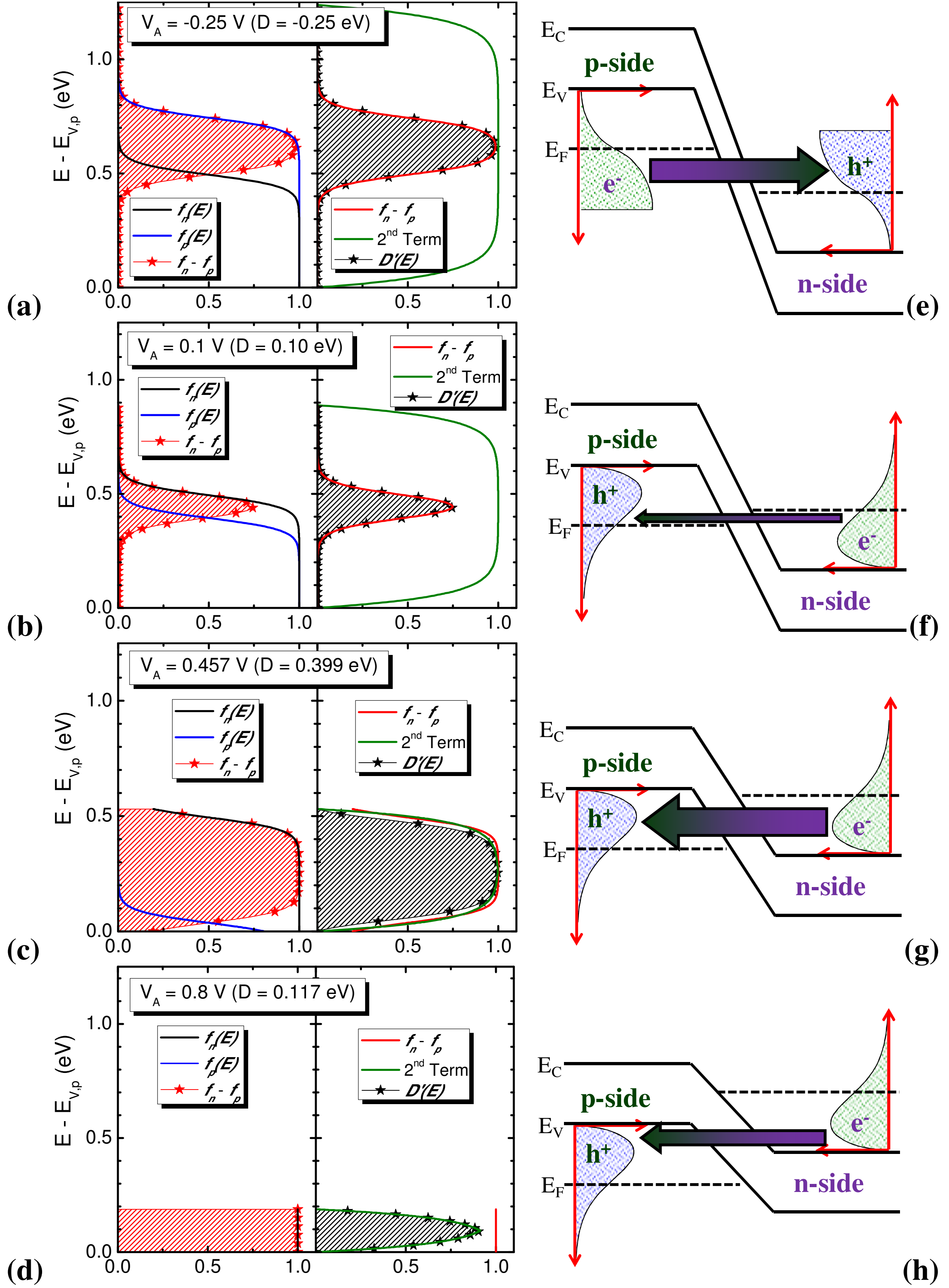

Fig. 3.5: Graphical representation of overlap integral calculations for $N_D = N_A$ ($E_{F,n} = E_{F,p}$) for V_A of (a) -0.25 V, (b) 0.1 V, (c) 0.457 V, and (d) 0.8 V. (e-h) Respective band diagram sketches for each biasing conditions shown to the right.

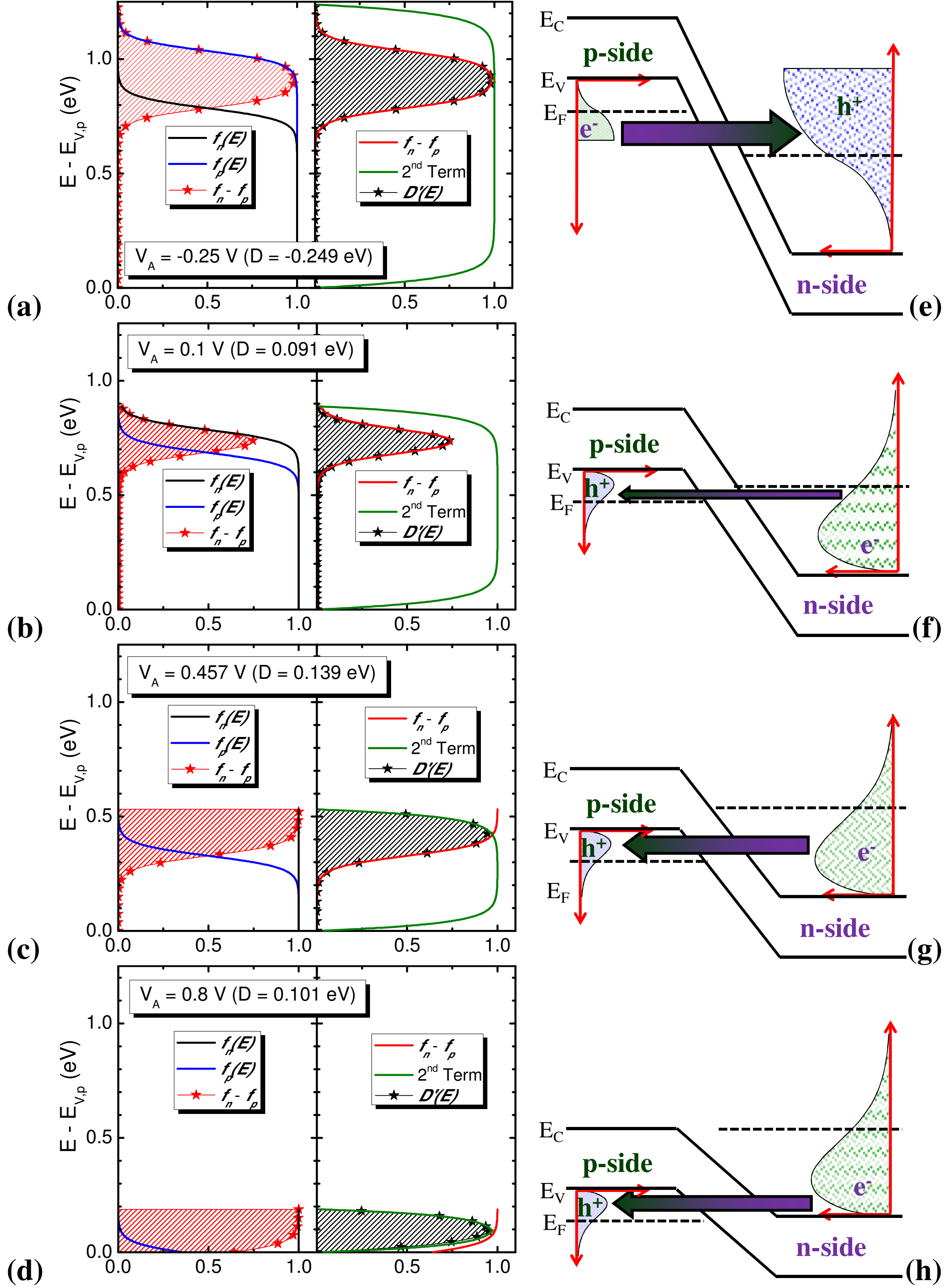

Fig. 3.6: Graphical representation of overlap integral calculations for $N_D > N_A$ ($E_{F,n} > E_{F,p}$) for V_A of (a) -0.25 V, (b) 0.1 V, (c) 0.457 V, and (d) 0.8 V. (e-h) Respective band diagram sketches for each biasing conditions shown to the right.

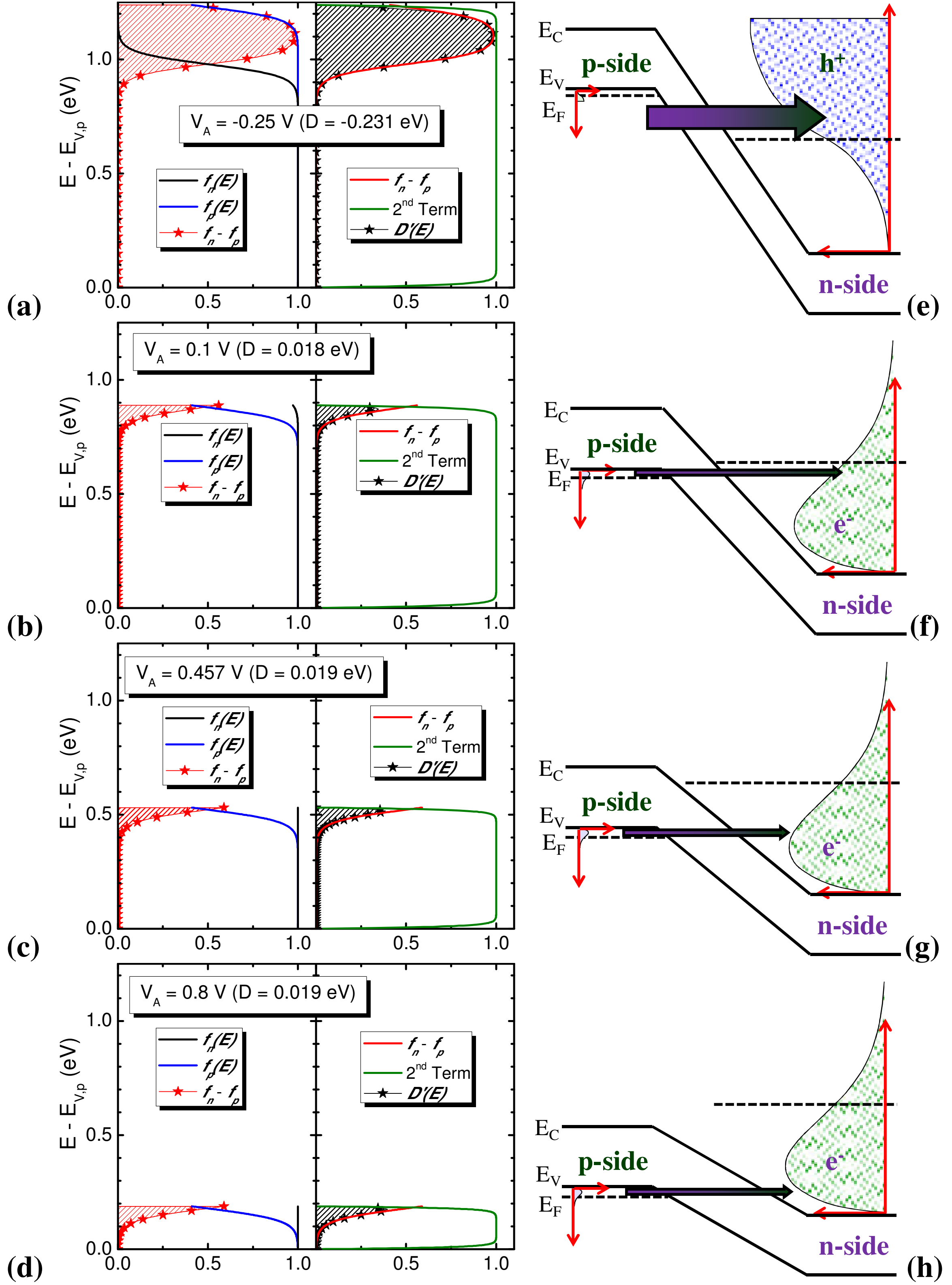

Fig. 3.7: Graphical representation of overlap integral calculations for $N_D >> N_A$ ($E_{F,n} >> E_{F,p}$) for V_A of (a) -0.25 V, (b) 0.1 V, (c) 0.457 V, and (d) 0.8 V. (e-h) Respective band diagram sketches for each biasing conditions shown to the right.

The second basic shape in Fig. 3.4, a simple mesa or trapezoidal, occurs when $E_{F,p}$ is significantly smaller then $E_{F,n}$ ($N_D > N_A$). Note, that this behavior is fully reversible between the $E_{F,n}$ and $E_{F,p}$. Before D flattens out, it is approximately equal to V_A, similar to the previous case studied. Shortly before V_A reaches the value of $E_{F,p}$, D begins to deviate from the previous trend. After a little further, the ideal D (dashed line) reaches its maximum value a flat mesa). As with the previous case, introducing the 2nd term attenuates that maximum value. Additionally, the mesa has a slight, positive slope. Eventually D begins to decrease with a slope of -1, and is approximately the same value and shape as the previous case. Notice the mesa portion of D is roughly symmetrical around the peak biasing condition of the cone shape.

As with the cone shape, Fig. 3.6 shows plots detailing the structure of $D'(E)$, along with their respective band diagram sketches for the same biasing conditions as before. In the band diagrams, notice that the shift in $E_{F,p}$ towards $E_{V,p}$ moves the 1st term closer to the band edge. For the first biasing condition in Fig. 3.6a, e, the 1st term is far enough away from the band edge such that the 2nd term does not affect it. As a result, the reverse bias characteristic looks the same the previous case.

For small forward bias (Fig. 3.6b, f), the 1st term is still confined within the 2nd. However, once $E_{F,n}$ is close to $E_{V,p}$, the 2nd term will begin to "clip" the 1st term's composite Fermi distribution, limiting further increases in D. This is evident in Fig. 3.6c, g. Looking at the band diagram, one can clearly identify that the BTBT current is limited by the region between $E_{V,p}$ and $E_{F,p}$. Further increases in V_A shift the p-side down, but do not increase the region of BTBT. However, this BTBT region becomes align with larger e^- concentrations, providing a small boost in D. Eventually V_A is large enough that $E_{F,p}$ shifts below $E_{C,n}$, and the BTBT region is once again bounded by both band edges (Fig. 3.6d, h). Quickly, $D'(E)$ is dominated by the 2nd term, and behaves similarly to the previous case.

The final shape is being called a complex mesa. In this case, $E_{F,p}$ is much smaller than $E_{F,n}$ ($N_D >> N_A$), shown in Fig. 3.4. At first glance, it looks the same as the simple mesa shape,

Table 3.1: Doping parameters, Fermi energies, and calculated D values used for detailed analysis considering (i) cone, (ii) mesa, and (iii) complex mesa shapes using fictitious mater parameters.

	Constant V_{bi} for all conditions (1.66 V)								
	N_D ($\times 10^{19}$ cm^{-3})	N_A ($\times 10^{19}$ cm^{-3})	$\Delta E_{F,n}$ (eV)	$\Delta E_{F,p}$ (eV)	$D(V_P)$ (eV)	D(-0.25 V) (eV)	D(0.1 V) (eV)	D(0.46 V) (eV)	D(0.8 V) (eV)
Cone	5	5	1.16	0.494	0.373	-0.250	0.100	0.399	0.117
Mesa	10	1.34	1.45	0.203	0.158	-0.249	0.0957	0.172	0.130
Complex Mesa	13.91	0.08	1.650	0.0093	0.0157	-0.231	0.0178	0.0188	0.0194

only with a smaller maximum value due to its smaller N_A ($E_{V,p} - E_{F,p}$). However, after a small amount of reverse bias, D becomes equal to V_A - ΔeV (~0.02 eV for this example). The cause of this deviation from the previous cases is visible in Fig. 3.7. $E_{F,p}$ is close enough to its own band edge ($E_{V,p}$), such that f_p is permanently clipped by the band edge. Therefore, no matter how large the reverse bias gets (Fig. 3.7a, e), D will always be missing that portion of the 1st term. As a result, D will increase with a slope of ~1, but will be shift by an amount roughly equal to that portion of the 1st term clipped by $E_{V,p}$. The forward bias characteristics behave similarly to the basic mesa condition. The mesa width is still roughly centered around the cone peak, and is much wider and smaller in height due to the large disparity between $\Delta E_{F,p}$ and $\Delta E_{F,n}$.

The doping concentrations used, Fermi energies, and calculated D values for the previous examples are summarized in Table 3.1. For the complex cone, the ΔeV shift in the reverse bias D characteristics is simply calculated as $V_A - D(V_A)$. Doping concentrations were varied such that V_{bi} and $\Delta E_{F,n} + \Delta E_{F,p}$ remained constant to help elucidate the previously discussed properties. Given that the negative slope of the exponential and its 1st coefficient in the Kane model (3.1) (Fig. 3.3b) is fairly shallow, V_P is close to the V_A at which D has mostly leveled off. For the cone shape, this occurs just before the peak. For both mesa shapes, this typically occurs within a few kT of the smaller of $\Delta E_{F,p}$ and $\Delta E_{F,n}$.

3.3. Fermi Energy Calculations

Since ETDs require degenerate levels of doping E_F must be calculated in a rigorous manner for accurate results. Traditionally, the total carrier concentration (3.15) is calculated from the integration of $g_C(E)$, (3.16), and $f(E)$, (3.17), product. The dimensions of the ETDs considered in this work will not quantum mechanically confine the transport carriers. Therefore, it is appropriate to use the 3D density of states distribution function shown in (3.16). The following discussion is specifically written for electrons (n). However, the equations can be made equally valid for holes by substituting (i) m_e with m_h, (ii) E with $-E$, (iii) E_C with $-E_V$, (iv) E_F with $-E_F$, and (v) integrate from $-\infty$ to E_V.

$$n = \int_{E_C}^{\infty} g_C(E) \times f(E) dE \tag{3.15}$$

$$g_C(E) = \frac{8\pi\sqrt{2} m_e^{3/2}}{h^3} \sqrt{E - E_C} \tag{3.16}$$

$$f(E) = \frac{1}{1 + \exp\left[\frac{E - E_F}{kT}\right]} \tag{3.17}$$

By introducing three substitutions, (3.15) can be generalized over all material systems and temperatures; where (i) x is defined by (3.18), (ii) β is defined by (3.19), and (iii) y is defined by (3.20). Wherein N_C is the standard DOS, defined in (3.21).

$$x = \frac{E_C - E_F}{kT} \tag{3.18}$$

$$\beta^2 = \frac{E - E_C}{kT} \tag{3.19}$$

$$y = \frac{\sqrt{\pi} n}{4 N_C} \tag{3.20}$$

$$N_C = 2\left(\frac{2\pi \times kT \times m_e^*}{h^2}\right)^{3/2} \tag{3.21}$$

In the new form, (3.22), relates the material parameters (y) to the integral of a new function (F) with parameters x and β. As before, this new form still has no closed form solution. Therefore, it can only be solved numerically for with limited approximations. However, a table of numerical solutions can be generated without knowledge of material parameters or temperature. This is accomplished by assuming a value for x and then numerically integrating $F(x,\beta)$ to determine the corresponding value for y. Afterwards, with a given material system and doping concentration, y is easily computed then looked up in the pre-generated table for the corresponding x value. Finally, using the desired temperature and (3.18), E_F is easily calculated. For improved accuracy, linear interpolation was used in the table lookup process.

$$y = \int_0^\infty F\left(x,\beta\right) d\beta = \int_0^\infty \frac{\beta^2}{1+\exp\left[x+\beta^2\right]} d\beta \tag{3.22}$$

Simpsons rule was used to numerically integrate $F(x, \beta)$, as shown in (3.23). Where N is the total number of discrete integration steps, and $\Delta\beta$ is the step size as defined by (3.24). β_{Max} is the maximum value of β needed to accurately capture the entire integral. Above β_{Max}, the contribution of $F(x, \beta)$ is assumed to be negligible. For this work, β_{Max} was set to 10 and 500 steps were used. In other words, E-E_C up to 100 eV was calculated at 2 meV steps. For rare occurrences when x is less than -90, β_{Max} was doubled to 20. These parameters yield reliable and accurate results.

$$y \approx \frac{\Delta\beta}{6} \sum_{n=1}^{N} F\left[x, 2\left(n-1\right)\Delta\beta\right] + 4F\left[x, \left(2n-1\right)\Delta\beta\right] + F\left[x, \left(2n\right)\Delta\beta\right] \tag{3.23}$$

$$\Delta\beta = \frac{\beta_{Max}}{N} \tag{3.24}$$

When there is non-degenerate levels of doping, $(E_C$-$E_F)/kT$ is less than three, $f(E)$ can be approximated as a simple exponential. Consequently, y can be approximated as (3.25), which has a familiar closed form solution. A value for x, and therefore E_F, can be directly computed from

(3.26). For E_C - E_F = $3kT$ (x = 3), the approximated E_F is 0.58% less than the actual value. For added accuracy this work uses the approximation at E_C - E_F = $6kT$ (x = 6), which has an error of less than 0.015%.

$$y \approx \int_0^\infty \beta^2 \exp\left(-x-\beta^2\right) d\beta \tag{3.25}$$

$$x = -\ln\left[\left(\frac{4}{\sqrt{\pi}}\right) y\right] \tag{3.26}$$

A separate approximation can be made with extremely large levels of doping, which will be designated as super-degenerate. In this situation, the rate in change of $g_C(E)$ near E_F is very slow (almost flat). Consequentially, the number of electrons above E_F is approximately equal to

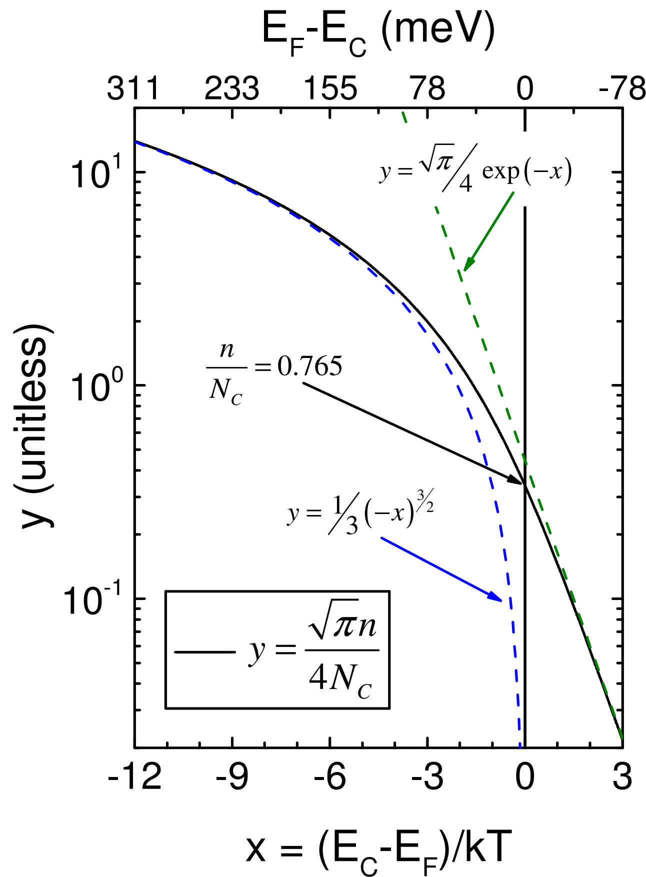

Fig. 3.8: Plot of y vs. x used to determine E_F from a given doping density and DOS. The solid line is from numerical evaluation of the carrier-energy distribution function. Dashed lines are approximations of non-degeneracy (right) and super-degeneracy (left).

the number of empty states below E_F (i.e. not filled due to Fermi-Dirac statistics). Another way to look at it is, the range needed for *f(E)* to transition from ~1 to ~0 is negligible. Therefore, only $g_C(E)$ needs to be integrated from E_C to E_F, similar to the case at absolute zero (T = 0 K). The integral becomes(3.27), with closed form solution of (3.28). Super-degeneracy occurs at E_C - E_F ≈ -12kT (x = -12), with a 0.57% over-estimate of E_F. For this work, super-degeneracy was only used as an initial guess when looking up values in the pre-generated table.

$$y \approx \int_0^{\sqrt{-x}} \beta^2 d\beta \tag{3.27}$$

$$y = \left(\frac{1}{3}\right)(-x)^{3/2} \tag{3.28}$$

The solid line in Fig. 3.8 is a plot of y versus x as calculated numerically using (3.23), for the region of low to medium degeneracy. Also shown are the super degeneracy (dashed line on the left) and non-degeneracy (dashed line on the right) approximations. As can be seen, the solid line approaches the approximations for both the left and right hand extremes. The greatest error occurs for x between negative six and one, which covers a large range of doping conditions for ETDs. Additionally, E_F will equal E_C when N_D equals 76.5% of N_C, or approximately 3/4. With the methods and equations described above, accurate degenerate E_F values can be calculated, which is necessary for the Kane model and accurate band diagram calculations.

3.4. Relative Effective Mass Parameters

It is important that appropriate effective mass values are used when calculating the various parameters needed for the Kane model. For all E_F calculations, the DOS m^* is used. Typically these values are taken from measured values in literature [13]. Since there are generally two (light and heavy holes) valance band maximums centered at 0 eV in the Γ direction, they are typically averaged together using (3.29). Given the type of average used, the DOS for h^+ will be dominated by $m_{r,heavy}$, as one would expect. The split-off valence maximum is

ignored in this work. However, the split-off band may significantly impact $E_{F,p}$ with large enough N_A, but tunneling to that band will be negligible due to the large tunnel barrier height experienced by the carriers.

$$m_{r,h} = \left(m_{r,light}^{3/2} + m_{r,heavy}^{3/2}\right)^{2/3} \tag{3.29}$$

Given the presence of the electric field, conductivity effective masses are used in the Kane model itself. For direct bandgap semiconductors, the $m_{r,e}$ is taken to be the same as the DOS m_r. Equation (3.30) is used to average the light and heavy $m_{r,h}$ values. This average accounts for the larger number of heavy holes present, but the higher mobility and tunneling probability of the light holes. Finally, the model equation uses an average $m_{r,BTBT}$ as defined in (3.31), which follows the same form as resistors in parallel. That is because the Kane model presumes that e^- and h^+ tunnel into the bandgap in imaginary k-space, where they meet and recombine. Lighter carriers tunnel more easily through the bandgap/barrier, and therefore travel further than their heavier counter parts.

$$m_{r,h} = \frac{\left(m_{r,light}^{3/2} + m_{r,heavy}^{3/2}\right)}{\left(m_{r,light}^{1/2} + m_{r,heavy}^{1/2}\right)} \tag{3.30}$$

$$m_{r,BTBT} = \left(m_{r,e}^{-1} + m_{r,h}^{-1}\right)^{-1} \tag{3.31}$$

3.5. Kane Model Program

The Kane Model Program (KMP) was developed using VB.net to efficiently and accurately compute ETD characteristics for a wide variety of material systems and parameters. The graphical user interface (GUI), shown in Fig. 3.9a, is easy to operate and quickly generates desired information. The "Run" button initializes computation for desired analysis type. "E_F Only" will calculate $E_{F,n/p}$ and the DOS for e^-/h^+ (N_C/N_V), then display the results in the top right table. "N* Sweep" generates a standard list of N_A and N_D concentrations for a doping sweep

analysis. The "Ef2" checkbox includes L- and X-valleys for added $E_{F,n}$ accuracy, but is only valid for $In_{0.53}Ga_{0.47}As$ material system. The "BNG" checkbox adds bandgap narrowing effects for the $In_{0.53}Ga_{0.47}As$ material system. The top right text box is used to notify the user of simulation progress.

The drop-down box is used to select the desired material system from a pre-defined list (Fig. 3.9b), which may be easily amended by the user. The known material systems are stored in "ETD_Calculations.xlsx", which is created during initial installation of KMP. The room temperature values for the pre-loaded group-4, and binary III-V material systems are listed in Table 3.2. The Ternary systems use linear interpolation to estimate most material parameters. Within the data file, there are six spreadsheets used for (i) listing available material systems, (ii) storing/calculating effective masses, (iii) relative dielectric constants, and (iv) bandgaps. In each of those sheets the first column contains the name of the material system. The second column contains the value for the parameter of interest to be used. The third column designates the composition of a generic ternary system ($In_{1-x}Ga_xAs$). The rest of the worksheet may be used for

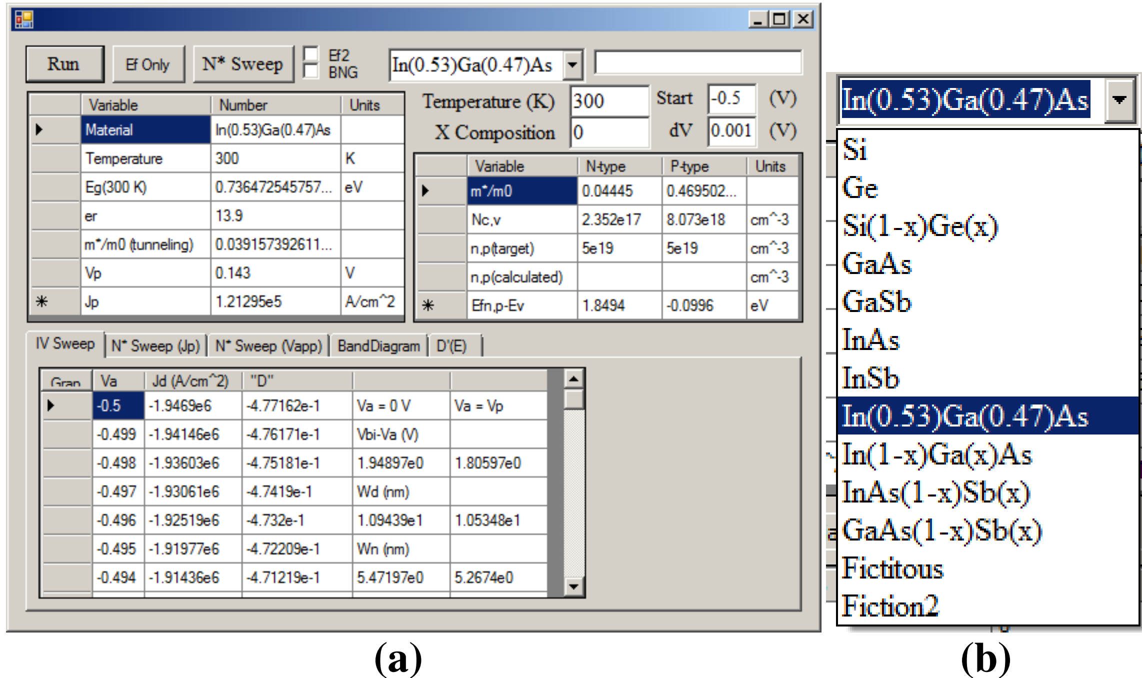

Fig. 3.9: GUI interface (a) for the Kane Model program. The drop-down box (b) can be used to select from a multitude of material systems.

Table 3.2: Material parameters stored in the Excel file used by KMP.

	E_G (eV)	ε_r	$m_{r,e}$ DOS	$m_{r,e}$ Cond.	$m_{r,h}$ DOS	$m_{r,h}$ Cond.	$m_{r,h}$ light	$m_{r,h}$ heavy	$m_{r,BTBT}$	N_C (10^{18} cm^{-3})	N_V (10^{18} cm^{-3})
Si	1.12	11.68	1.08	0.26	0.81	0.39	0.16	0.49	0.16	28.2	18.3
Ge	0.66	16	0.56	0.12	0.29	0.21	0.044	0.28	0.076	10.5	3.92
GaAs	1.42	12.91	0.063	0.063	0.53	0.39	0.082	0.51	0.054	0.397	9.73
GaSb	0.73	15.7	0.041	0.041	0.41	0.31	0.050	0.40	0.036	0.208	6.63
InAs	0.35	15.15	0.028	0.028	0.41	0.33	0.026	0.41	0.026	0.118	6.69
InSb	0.18	16.8	0.02	0.02	0.43	0.36	0.015	0.43	0.019	0.0710	7.12

basic formulas and references used to calculate the final desired values. At startup, KMP reads the list of material systems and makes them available I the drop-down box. In this fashion, a user can easily add and edit material systems without modification to the program code.

When calculating Fermi energies, the same Excel workbook is used. The Fermi_Integral worksheet contains the lookup table of "x" (Column one) and "y" (column two) values used in (3.22). If "y" exceeds the pre-calculated values, the program will automatically increment "x", and numerical calculate the corresponding "y" value using (3.23), until and appropriate value is achieve. For improved accuracy, the final "x" value used is linearly interpolated from the two nearest points listed in the table.

In the top left table the current material system and temperature are selected. When a new material system is selected, E_G, ε_r, $m_{r,tunnel}$ are updated from the Excel file. The user may modify these parameters in the table without affecting the stored values. This way, the user can easily investigate the effects of a single parameter on the output without changing any of the other values. Finally, when a J-V calculation is performed, J_P and V_P are reported at the bottom of this table.

The four text boxes directly above the right hand table may be modified by the user to designate a new (i) temperature, (ii) material composition, (iii) starting V_A, and (iv) voltage step (dV). The program will automatically update all dependent parameters when any of the previously mentioned values are changed. The table directly below is updated with the $m_{r,e/h}$ for

the desired material system. As before, the user may change the value within the table instead of modifying the Excel workbook. The user must enter n- and p-type doping concentrations before any analysis can be performed, except for the N^* sweeps. $N_{C/V}$ are calculated at the start of every analysis, then reported here. The calculated $\Delta E_{F,np}$ are reported at the bottom. The calculated n/p concentrations, 4th row, is no longer used.

The Tabs at the bottom of the window are used to select the desired analysis. Each tab is a separate analysis type, and may require additional input parameters. When the "Run" button is executed, the analysis for the selected tab will run.

3.5.1. KMP Flow & Operation

The flow diagram determining the operation of KMP is straight forward (Fig. 3.10). The user must first input some general parameters used by all analysis types. This includes the material system, composition, temperature, starting V_A, and voltage steps (dV). This is also the

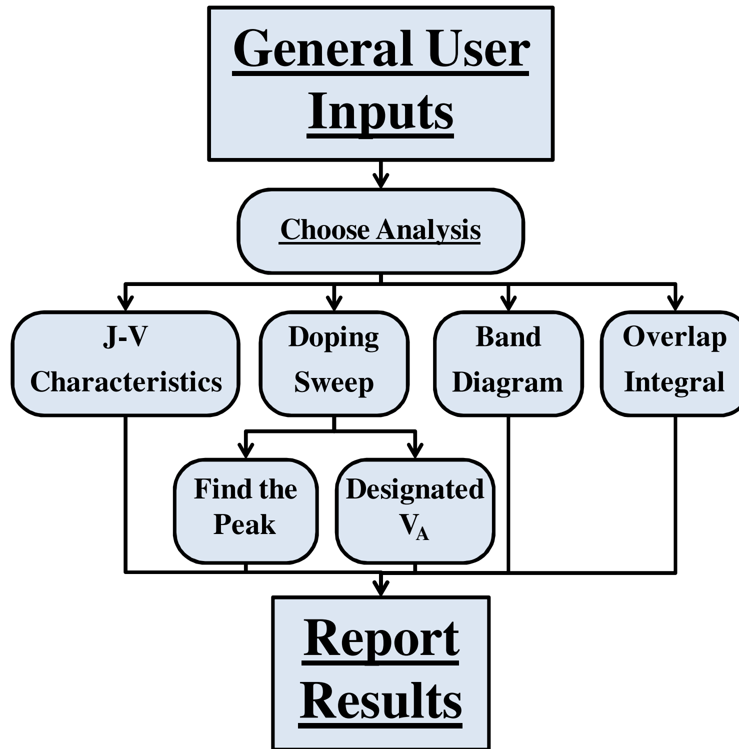

Fig. 3.10: Flow diagram for operation of KMP.

optimal point to alter any material parameters that the user wishes. Then the analysis type is chosen. The first choice is to calculate the full J-V characteristics, which require the additional input of N_A and N_D in the top right table. After "Run" is selected, N_C, N_V, $E_{F,n}$ and $E_{F,p}$ are immediately calculated. Then, for each biasing condition (i) the average ξ, (ii) D, and (iii) Kane model is calculated.

In the table for the selected tab at the bottom of the GUI, the calculated J_{BTBT} and D values are recorded for each V_A. Also in the same table the following parameters are recorded which may be used to reproduce any part, or the whole of the Kane model; (i) V_{bi}, (ii) w_d, (iii) $w_{n/p}$, (iv) average ξ, (v) exponent pre-factor, (vi) argument inside the exponential, (vii) $E_{F,n/p}$, (viii) $N_{D,A}$, (ix) V_P, (x) J_p, and (xi) $D(V_P)$. Many of the parameters are reported at V_A of 0 V and V_P.

After the J-V results are reported, there is the additional option of generating plots of the various parameters involved (Fig. 3.11). The y1-axis (left) and y2-axis (right) can be linear or logarithmic using the check boxes on the side. The axis ranges can be adjusted using the top

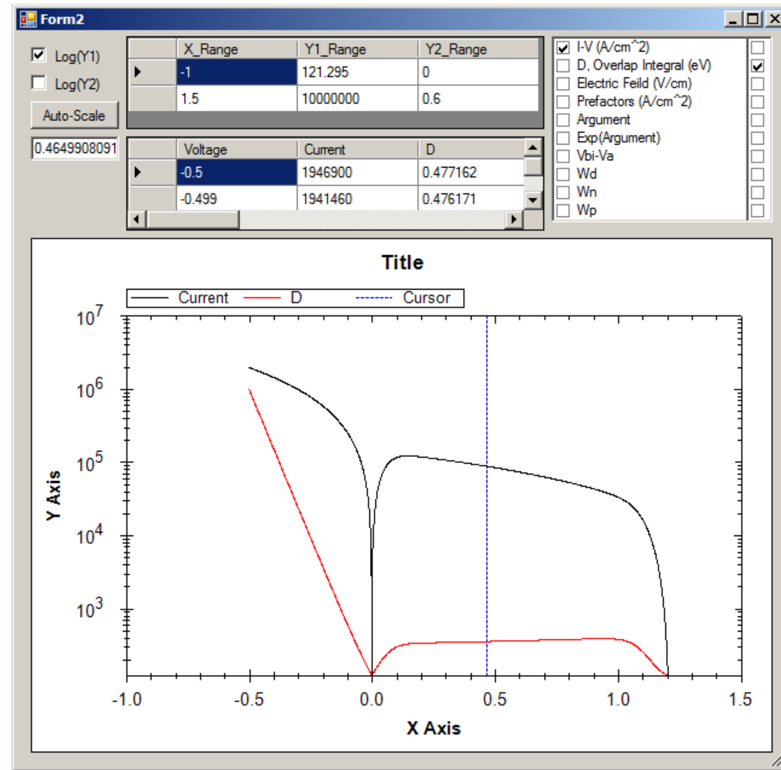

Fig. 3.11: Plotting functionality for J-V analysis.

table, or by clicking the “Auto Scale” button. The bottom table lists all values that change with V_A for the entire sweep range. The text box to the left displays the position of the vertical blue line, which moves with the cursor. The parameters shown in the plot are determined by the chock box lists on the right. Checking to the left of the parameter plots it on the y1 axis. The left hand side is for the y2 axis. This function is for quick reference only.

One of the large portions of the experimental work to be discussed in this work is mapping the behavior of ETD characteristics over a large design. The most common and appropriate approach to this will be looking at J_{BTBT}, usually J_P, versus $N^{*-1/2}$ in order to generate trendlines for each material system. To facilitate modeling these trendlines, there are two separate N^* sweep options. For both methods, a list of N_A and N_D are supplied to the table within the appropriate tabs in the main GUI. There is the option of finding the values of interest at the peak, or a specified V_A.

When calculating band diagrams, an optional intrinsic layer may be inserted between the p- and n- sides. The layers are assumed to be perfectly abrupt, with full dopant activation. Full depletion approximation is used to not only calculate the depletion widths in (3.32) and (3.33), but also the curvature of the band bending near the p-i-n junction (3.34). In the following equations, the x-axis is centered in the middle of the *i*-layer. E_V is simply calculated as $E_C - E_G$. Additionally, the results use $E_{F,n}$ is used as the reference energy. Finally, $D'(E)$ and its individual elements are calculated in the final tab/analysis option. Only the material system, doping concentrations, and V_A need to be supplied.

$$w_d = \sqrt{i^2 + \frac{2\varepsilon_s \times (V_{bi} - V_A)}{qN^*}} - i \qquad (3.32)$$

$$w_n = w_d \left(\frac{N_A}{N_A + N_D} \right); \;\; w_d = w_n + w_p \qquad (3.33)$$

$$E_C(x) = \begin{cases} \frac{qN_D}{2\varepsilon_s}\left(x + w_p + i/2\right)^2 - E_{F,n}; & -w_n - \frac{i}{2} \le x \le -\frac{i}{2} \\ \frac{qN_D}{2\varepsilon_s} w_n \left(2x + w_n + i/2\right) - E_{F,n}; & -\frac{i}{2} \le x \le \frac{i}{2} \\ \left(V_{bi} - V_A\right) - \frac{qNA}{2\varepsilon_s}\left(x - w_p - i/2\right)^2 - E_{F,n}; & \frac{i}{2} \le x \le w_p + \frac{i}{2} \end{cases} \tag{3.34}$$

3.6. Conclusions

The Kane model for predicting ETD characteristics has been discussed, beginning with the assumptions and approximations in the model. In particular, only direct bandgap BTBT (Γ-direction) is considered. Many material systems have a direct bandgaps that is much smaller than the L- and X-valleys, resulting in a much larger BTBT probability for the Γ-valley. The assuming a constant average ξ and m^* significantly simplify the calculations, without adding large error to the calculations.

The Kane model itself was broken up into three parts; (i) a pre-factor/coefficient, the (ii) overlap integral (*D*), and (iii) BTBT probability exponential. The BTBT probability (exponential term) has often been calculated using the WKB approximation, which can underestimate what the original model predicts by ~20% to ~18,000x depending on material parameters and doping concentrations. This work proceeds with the original formulation []. Qualitative analysis of the pre-factor and exponential terms indicates that they are always positive, with a fairly shallow, negative logarithmic slope.

The overlap integral is solely responsible for indicating the direction of BTBT current flow, and providing positive differential resistance for V_A less than V_P. This is reasonable, given that *D* accounts for the overlap of e^- and h^+ distributions available for BTBT. Detailed analysis of "*D*", which needs to be calculated numerically, shows that there are three basic shapes that it may take which depend on the ratio of $E_{F,n}$ to $E_{F,p}$; (i) simple cone, (ii) simple mesa, and (iii) complex mesa. For the 1st two shapes, *D* is equivalent to V_A in reverse bias, which is a common

approximation. However, for the complex mesa the approximation must be modified by a constant (*ΔeV*), and is generally invalid for small V_A.

The degenerate levels of doping concentrations needed for ETD structures requires full Fermi-Dirac statistics when determining E_F. As with *D*, there is no closed form solution to the Fermi-Direc/DOS integral, and must be solved numerically. Additionally, the dependent variable (E_F) is within the integral and the output is the known, independent variable (doping concentration). A simple variable substitution removed all material parameters from the integral, enabling the generation of a lookup table of values which is generic to all material systems and conditions. This greatly enhances the speed and accuracy of determining E_F.

Finally, the structure and operation of a GUI based program, KMP, was discussed in

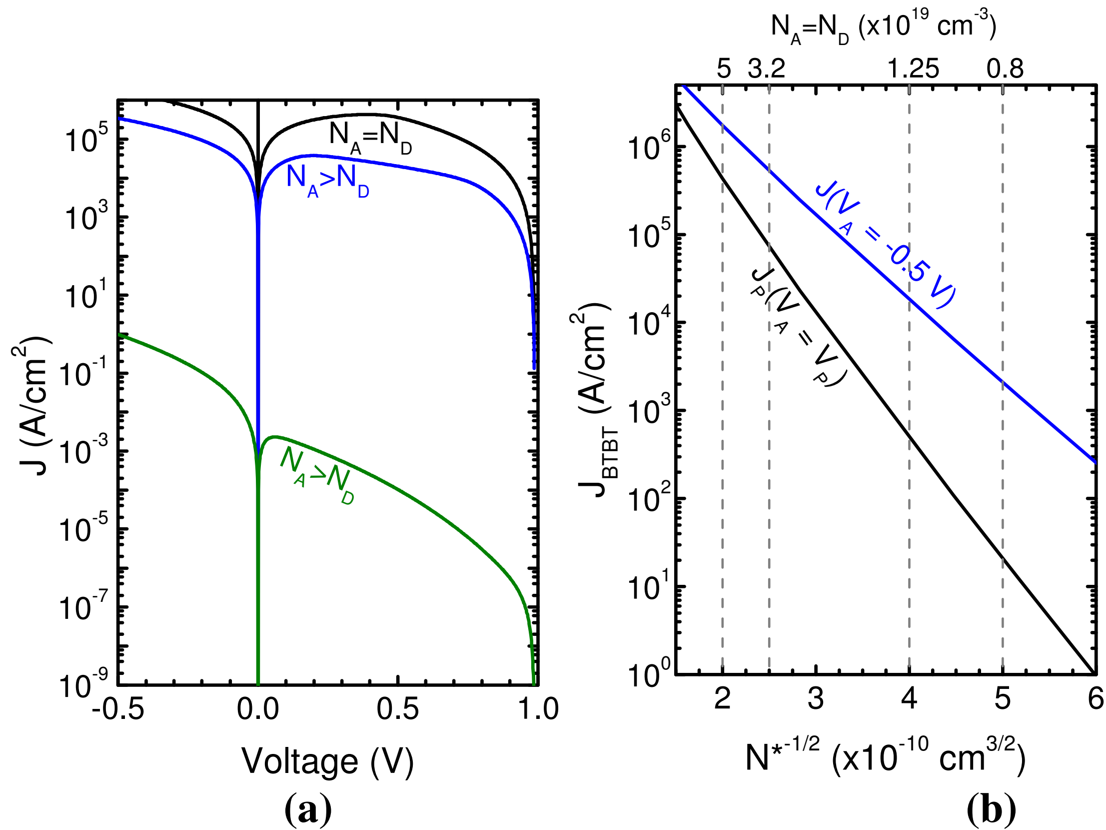

Fig. 3.12: Left (a), fully calculated BTBT J-V characteristics calculated using with KMP. Material and doping parameters are the same as those used for the detailed discussion on "*D*" (Section 3.2.3.1). Right (b), characteristic trendlines for the same fictitious material system. The doping sweep analysis was performed for J_P and V_A = -0.5 V.

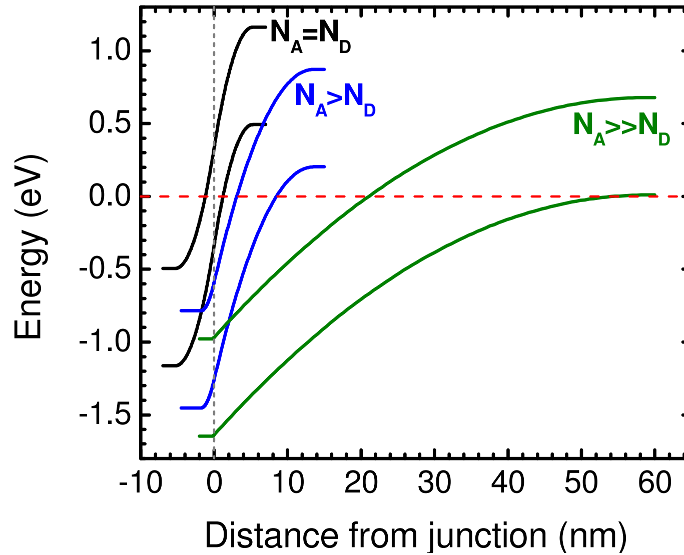

Fig. 3.13: Calculated band diagrams for the (i) cone, (ii) mesa, and (iii) complex mesa examples used in Section 3.2.3.1.

detail. This program was developed specifically for the work discussed in chapters 4, 5, and 6, using VB.net language and development environment. The KMP code can be found in Appendix A. Many material system parameters are stored within an Excel Workbook, as well as the E_F lookup table, and is directly used by the program. Materials can easily be modified and added by the user without modifying any code. In additional to (i) BTBT J-V characteristics, KMP can calculate (ii) doping sweeps for characteristic trendlines, (iii) basic band diagrams, and (iv) detailed *D'(E)* analysis.

Using the same fictitious material parameters and doping concentrations in Section 3.2.3.1 (detailed analysis of *D*), KMP was used to generate J-V curves (Fig. 3.12a) and trendlines (Fig. 3.12b). As will be seen in the following chapters, the modeled J-V characteristics have similar shapes to experimental measurements. J_P increases with N^*. V_P also increases however; this is mostly due to the shape of *D* (at what bias it begins to level off). There is clearly an exponential characteristic trendline (J_P vs. $N^{*-1/2}$). The ratio of zener current density to J_P decreases as N^* and J_P increases. The calculated band diagrams (Fig. 3.13) clearly shows the large increases in w_d, and hence BTBT barrier width, for each case. This increase in w_d is the

primary reason for the very large reduction in BTBT current density from (i) cone to (ii) mesa to (iii) complex mesa cases.

With the developed algorithms and KMP, the Kane model can be quickly and easily compared to experimental results. This includes full J-V characteristics, which previously has not been accomplished. Previously, only characteristic trendlines have been compared with the Kane model, and typically at low temperature in order to minimize phonon interactions [17]. If proven accurate, KMP can be easily distributed and used to provide useful insights into the operation of ETD structures. Additionally, the Kane model would be very useful for designing ETD structures with J_{BTBT} matched to the circuit specifications without many separate epitaxial growths and fabrications.

References for Chapter 3

[1] E. O. Kane, "Theory of Tunneling," *J. Appl. Phys.,* vol. 32, p. 83, 1961.

[2] S. M. Sze and K. K. Ng, "Physics of Semiconductor Devices," Third ed Hoboken, NJ: Wiley-Interscience, 2007, pp. 422-424.

[3] C. Rivas, R. Lake, G. Klimeck, W. R. Frensley, M. V. Fischetti, P. E. Thompson*, et al.*, "Full-Band Simulation of Indirect Phonon Assisted Tunneling in a Silicon Tunnel Diode With Delta-Doped Contacts," *Appl. Phys. Lett.,* vol. 78, p. 814, 02/05/ 2001.

[4] W. Bergner and R. Kircher, "Modeling of Band-to-Band Tunneling Mechanisms," *Jap. J. Appl. Phys.,* vol. 29, pp. L2304-L2306, Dec 1990.

[5] G. A. M. Hurkx, H. C. Degraaff, W. J. Kloosterman, and M. P. G. Knuvers, "A New Analytical Diode Model Including Tunneling and Avalanche Breakdown," *IEEE Trans. Elect. Dev.,* vol. 39, pp. 2090-2098, Sep 1992.

[6] V. Milovanovic and R. van der Toorn, "A Novel Physics-Based Compact Model of Band-to-Band Tunneling Current in p-n Junctions," *IEEE Trans. Elect. Dev.,* vol. 57, pp. 1583-1589, Jul 2010.

[7] A. Schenk, "Rigorous Theory and Simplified Model of the Band-to-Band Tunneling in Silicon," *Solid-State Electron.,* vol. 36, pp. 19-34, 1993.

[8] P. M. Solomon, J. Jopling, D. J. Frank, C. D'Emic, O. Dokumaci, P. Ronsheim*, et al.*, "Universal Tunneling Behavior in Technologically Relevant P/N Junction Diodes," *J. Appl. Phys.,* vol. 95, pp. 5800-5812, May 2004.

[9] K. Jandieri, W. Baronovskii, W. Stolz, and F. Gebhard, "Analytical Theory for Favorable Defects in Tunnel Diodes," *J. Appl. Phys.,* vol. 104, p. 114511, 2008.

[10] A. Luque and A. Marti, "Increasing the Efficiency of Ideal Solar Cells by Photon Induced Transitions at Intermediate Levels," *Phys. Rev. Lett.,* vol. 78, pp. 5014-5017, 1997.

[11] S. M. Hubbard, C. Bailey, S. Polly, C. Cress, J. Andersen, D. Forbes*, et al.*, "Nanostructured Photovoltaics for Space Power," *J. Nanophotonics,* vol. 3, 2009.

[12] S. M. Hubbard, C. Plourde, Z. Bittner, C. G. Bailey, M. Harris, T. Bald*, et al.*, "InAs Quantum Dot Enhancement of GaAs Solar Cells," in *IEEE Photovoltaic Spec. Conf.*, 2010, pp. 1217-1222.

[13] V. Siklitsky and A. Tolmatchev. (2001). *Physical Properties of Semiconductors (http://www.ioffe.ru/SVA/NSM/introduction.html ed.)*.

[14] L. Esaki, "New Phenomenon in Narrow Germanium p-n Junctions," *Physical Rev.,* vol. 109, p. 603, 1958.

[15] A. C. Seabaugh and Z. Qin, "Low-Voltage Tunnel Transistors for Beyond CMOS Logic," *Proc. IEEE,* vol. 98, pp. 2095-2110, 2010.

[16] G. Borgioli, G. Frosali, and P. F. Zweifel, "Wigner Approach to the Two-Band Kane Model for a Tunneling Diode," *Transport Theory and Stat. Phys.,* vol. 32, pp. 347-366, 2003.

[17] D. Meyerhofer, G. A. Brown, and H. S. Sommers, "Degenerate Germanium. I. Tunnel, Excess, and Thermal Current in Tunnel Diodes," *Physical Rev.,* vol. 126, p. 1329, 1962.

CHAPTER 4

Ge and III-V Tunnel Diodes on Si

In this chapter, a series of Ge and GaAs/InGaAs ETDs will be fabricated [1-4] and benchmarked against results from literature [5-18] to assess the quality non-traditional semiconductors on Si. This is a departure from traditional development performed by industry in order to meet the increasing demands of consumer electronics. To help satisfy the required continual improvement of integrated electronics, much effort has gone into the development of novel material systems [19], as well as alternate device structures [20-25]. Since its introduction as the main semiconductor, Si has remained the primary channel material. However, most other aspects of integrated circuits have been engineered with new materials; (i) high-*k* dielectrics, (ii) metal gates, (iii) Ge Source/Drains, (iv) straining liners, (v) low-k dielectrics, and (vi) refractory and low resistivity metals. This does not include dopant species and processing materials. Some of the modifications have modified the strain [26-29] and geometry of the Si channel [19, 30, 31] in order to improve mobility and gate control. However, the channel is still fundamentally limited by Si, which may be surpassed with new materials [19, 32-34]. The bulk of non-Si research is performed on substrates that are much more expensive and fragile than Si, and therefore unsuitable for mass manufacturing.

Previously, the majority of heterointegration of virtual substrates on Si involve thick graded buffers [35-37] or a surface transfer process [38-40]. While both of these processes have enabled limited research into the ability to fabricate non-traditional material systems on Si substrates, they are still viewed as non-manufacturable on a large scale. Therefore, the aspect ratio trapping (ART) [41-45] method discussed in Section 4.1.3, appears to provide high quality virtual substrates in a manufacturing friendly process. However, prior to this work there was no experimental result indicating the electrostatic properties of the ART virtual substrates [1-4].

This chapter investigates defect enabled leakage currents via high PVCR ETDs, which are known to be sensitive to such defects and require high quality crystalline semiconductors [46-51]. After verifying the electrostatic quality of ART substrates, the bulk of research and device optimization can proceed on standard III-V substrates. Optimized structures can be integrated on the still scarce heterointegrated virtual substrates to verify that minimal changes occur between substrate.

In this chapter, basic materials analysis techniques will be used to investigate the quality of the virtual substrate [41-44]. Quickly, the work will move towards verifying the electrical quality of the virtual substrate by investigating ETDs fabricated using an alloy junction process [1] and CVD based epitaxy [2-4]. Ge alloy junctions were fabricated and characterized as an initial study [1].

Afterwards, a series of five GaAs/InGaAs ETDs were grown on the Ge virtual substrates [1, 2]. Two companion GaAs/InGaAs ETDs were grown directly on Si and GaAs substrates, each. This investigated ETDs grown on the ART substrates, versus replicas grown directly on Si and GaAs substrates as nominally worst and best case scenarios. Furthermore, methodical changes to the baseline ETD structure looked at the effect of In concentration, In placement, graded In junctions, and *i*-layer thickness on ETD characteristics. A new fabrication process was developed, and served as the baseline process for all of the following device fabrication runs.

ETDs are also characterized over a large temperature range [3], to further elucidate the crystal quality. Finally, a new deep submicron process is developed from the original basic process [4]. As part of the process, a new e-beam lithography procedure is discussed.

4.1. Ge/III-V on Si Integration Methods

There are three basic issues regarding the integration of crystalline Ge and III-V semiconductors on Si substrates. The first is the large lattice constant difference between the various material systems. Ge and GaAs are the closest to Si, with a lattice mismatch (strain) of 4.1%. For thin epitaxial films, the mismatched layer will strain its lattice in order to conform to

the substrates dimensions. When the film exceeds a critical thickness the stress will become too large, and the film will relax by generating one dimensional misfit dislocations along the hetero-interface in [110] directions. Misfit dislocation must terminate at free surfaces (Eg. Sample edges or non-crystalline surfaces) or move away from the hetero-interface along (111) directions and form one dimensional threading dislocations. The threading dislocations act as non-radiative recombination centers and deep traps [52], increasing leakage currents (increasing J_V and decreasing PVCR). For Ge grown directly on Si a large threading dislocations density (TDD) of ~1.25×10^9 /cm^3 is generated.

The Second integration issue are thermal expansion differences. Typically, epitaxialy growths are performed at elevated temperatures (~400°C up to ~800$^{\circ C}$). Thermal energy is necessary to form regular crystalline lattice arrangements. As a result, crystal relaxation due to lattice mismatch occurs at these elevated temperatures. Further strain and relaxation may occur due to differences in thermal expansion rates as the samples cooled to room temperature. This is typically much smaller effects, no more than 0.26% for GaAs on Si.

Finally, fundamental differences in the crystalline structure may give rise to anti-phase domains. This is an issue of the ionic bonding in III-V semiconductors, which require an ideal cation-anion bonding arrangement. However, Si and Ge are covalently bonded, thereby lacking a portion of the growth template needed by compound semiconductors. A mis-alignment of the bonding phases may occur between two regions of growth, forming anion-anion and cation-cation bonds. These sites reduce minority carrier lifetimes and increase majority carrier scattering, but have not been shown to act as trap states [52]. Therefore, the effects of antiphase domains on BTBT may be small, especially compared to TDD.

Methods of minimizing, or even eliminating anti-phase domains have previously been developed and implemented by others [53, 54]. The effects of thermal expansion mismatch can be minimized by reducing growth temperatures. The main issue remaining is the formation of threading dislocations. Previously, heteroepitaxy of non-lattice matched substrates has utilized

relaxed graded buffers or substrate transfer processes. This work was among the first utilize aspect ratio trapping [1-4][41-45].

4.1.1. Relaxed, Compositionally Graded Buffers

In this method, the composition of the epitaxial growth is stepped in order to incrementally increase/decrease the lattice constant [35-37]. For instance, Ge virtual substrates on Si can be achieved by grading the $Si_{1-x}Ge_X$ content from 0% to 100% with 10 or more steps. At each step, the grow is performed in a way to allow the layer to relax. However, when done correctly, threading dislocations will be recycled at each step and move towards the sample edge, instead of generating new dislocations (Fig. 4.1a). Furthermore, the interface between compositional stepped layers help to suppress and terminate threading dislocations. This is clearly seen in Fig. 4.1b, where a defect free GaAs-virtual substrate is integrated on a Si substrate. First, $Si_{1-x}Ge_x$ is compositionaly graded from x = 0 to 100% (shown at the bottom of the figure).

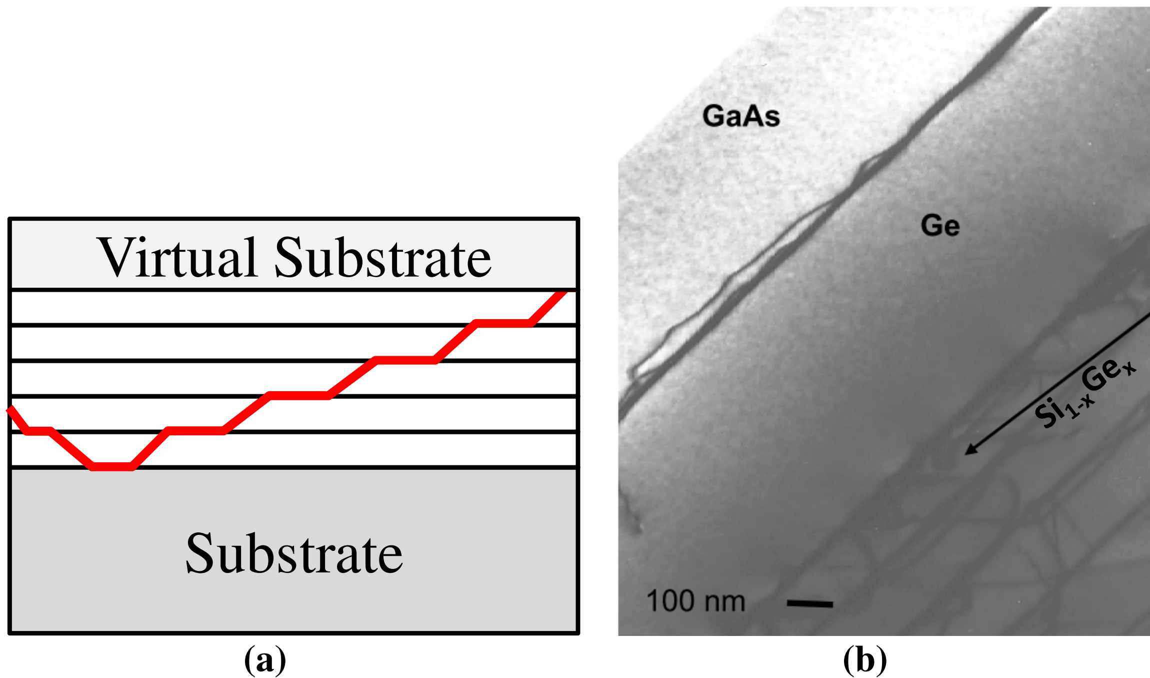

Fig. 4.1: Left (a), schematic diagram of graded buffer. Solid line shows a threading dislocation moving through the layers without generating new dislocations and terminating below the virtual-Ge substrate. Right (b) is a TEM of a $Si_{1-x}Ge_x$ graded buffer with defect free GaAs-on-Ge-virtual substrate integrated on a Si substrate (adopted from [36]).

Notice that each compositional step is clearly as dislocations are shunted horizontally. The final result is a defect free virtual-Ge substrate (middle of the image). On top of the Ge, GaAs is grown. Since there is only a 0.04% lattice mismatch between GaAs and Ge, no additional buffers are needed.

This method has produced virtual Ge substrates with TDD below 10^6 /cm^3. Furthermore, this method can be employed to generate virtual substrates on large Si wafers (depending on the epitaxial reactor). Additionally, a large variety of non-traditional electronics material systems and devices have been integrated on Si [35-37]. However, due to the complexity and expense of the epitaxial growth, this method has not been expanded to productions. Furthermore, the relaxed graded buffers needed are very thick (usually greater than ~1 μm), requiring extended growth times, thereby elevating the cost of this method.

4.1.2. Substrate Transfer Process

For this technique, desired epitaxial layers are prepared on an ideal, temporary substrate. Then, the temporary substrate is flipped upside down onto a Si substrate and chemically bonded to each other. Finally, the desired layers are released from the temporary substrate, leaving behind a high quality virtual substrate on Si. There are several ways to accomplish the previous steps. One method utilizes similar steps as the SmartCut^{tm} process [38] used for silicon-on-insulator (Fig. 4.2). First (a), the desired film stack is grown, starting with sacrificial InGaAs/InP layers. Then (b), H^+ implantation is done to desired depth (dashed line). Afterwards, (c) the epitaxial layers are bonded to a thin thermal oxide on top of a Si substrate. A (d) thermal step releases the temporary layer. Finally (e), the sacrificial InGaAs/InP layers are selectively etched, leaving behind a high quality III-V on insulator substrate.

Similar methods have been done without the H^+ implant. Instead, a selective etch to a sacrificial AlAs layer at the bottom of the structure (adjacent to the temporary substrate) is used to release the virtual substrate [39, 40]. Additionally, bonding has been done with metals (Mo,

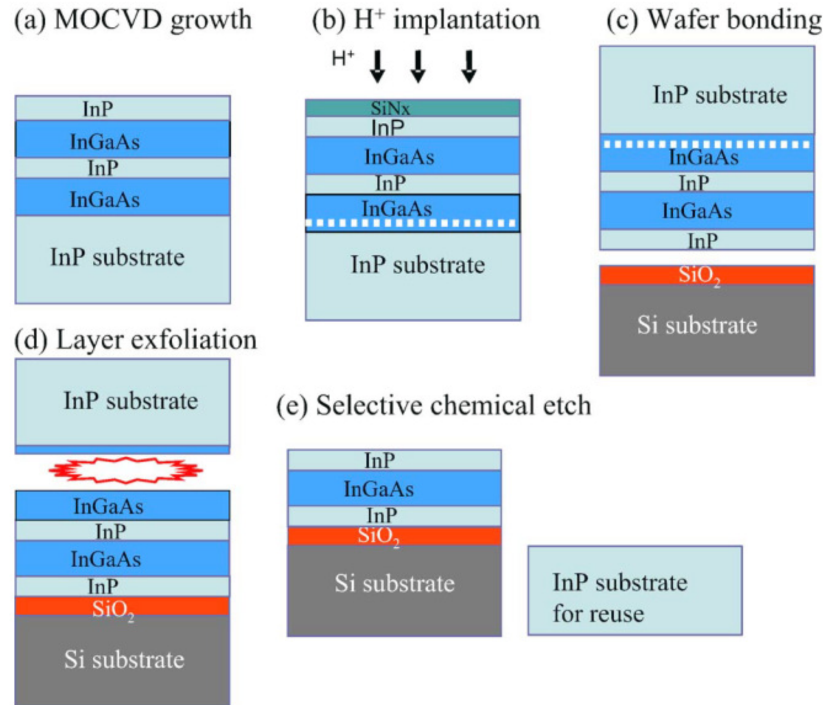

Fig. 4.2: SmartCut[tm] substrate transfer Process flow, adopted from [38]. Shows the (a) initial epitaxial layer start on temporary substrate, (b) H^+ implant, (c) wafer bonding, (d) layer exfoliation, and (e) surface preparation.

Au-Sn, Ge-Pd) [39, 40]. For that case, metal is deposited onto the epitaxial layers as the topmost layer. Then it is bonded onto a Si substrate with the same metal deposited on top.

There have been numerous variations to this method. However, there are several issues. There typically the yield is to low for manufacturing. It still requires the use of III-V substrates which are expensive, delicate, and limited in size to ~4 inch diameters. The bonding process requires good alignment, thermal steps, and sometimes mechanical pressure. The interface at the bonded surface is often mechanically unstable and prone to cracking and exfoliation. Additionally, it is not always appropriate to use an semiconductor on insulator or metal. In the end, this can be a fine method for research, but has yet to be demonstrated as manufacturable.

4.1.3. Aspect Ratio Trapping Hetero-Integration

In this method, vertical trenches are etched all of the way through an SiO_2 film, to the underlying Si substrate. A selective Ge epitaxial growth is performed, such that Ge only forms

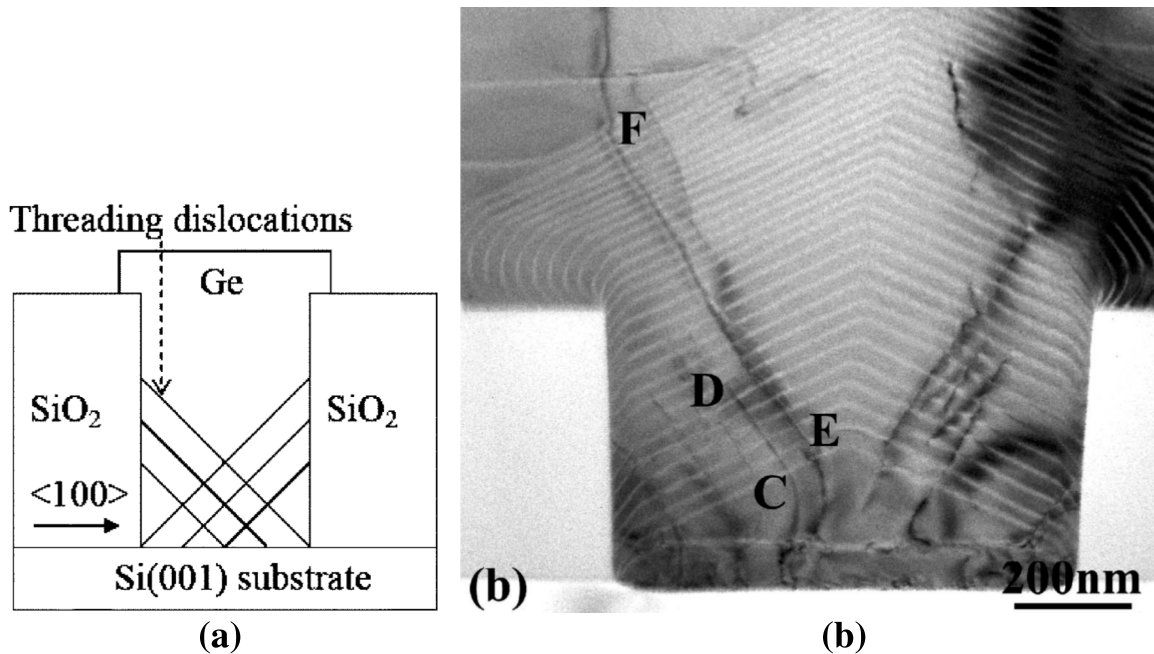

Fig. 4.3: (A) Schematic diagram of threading dislocations being trapped inside an ART trench (adopted from[43]). (b) TEM of overgrown Ge epitaxial growth inside a wide ART trench. White lines are thin layers of SiGe, showing the dynamics of growth inside and over the oxide barriers (adopted from [44]).

on crystalline semiconductors and not the amorphous structure of SiO_2. In this fashion, the Ge begins growing inside the oxide trenches, from the bottom up. The Threading dislocations formed move diagonally away from the Si surface, and towards the SiO_2 sidewalls, where they will terminate. Finally, Ge grown above the terminated threading dislocations will be a high quality virtual substrate.

In Fig. 4.3a, the Ge is grown slightly above the Oxide trenches. At the bottom of the trench, several threading dislocations form and terminate at the oxide interface, forming a "V" shape at the bottom of the trench. In this method, larger aspect ratios between the height and width of the trenches will trap greater numbers of defects. To form the virtual substrate, the oxide walls are overgrown until the growths from adjacent trenches are merged and a desired layer thickness is achieved. However, the progression of growth proceeds on approximately a [311] plane, which is not conducive for device fabrication. Even after full mergin of adjacent trenches, the Ge surface contains large hills and valleys (Fig. 4.3b). For a flat surface appropriate

for device fabrication, the virtual substrate process requires a CMP step at the end. Also, from Fig. 4.3b, notice that some of the threading dislocations escape due to the wide trench (small aspect ratio). Additional coalescent dislocations may form where two overgrown trenches merge (not shown here).

ART is an efficient method to reduce TDD by many orders of magnitude. The final film thickness can be a few 100 nm, including the virtual substrate, unlike grad buffers. This method has been shown to work with Ge [41-44], GaAs [42], and InP [45]. However, prior to this work there weren't any device results indicating the electrical quality of the ART substrates.

4.2. Materials Analysis of Ge on Si ART

High quality, crystalline, virtual Ge substrates were provided as part of a collaborative effort to investigate the effects of integrated semiconductors on device performance [41-44]. The virtual Ge substrates were integrated on [100] Si wafers using ART, which has been described in Section 4.1.3. After integration, Ge and GaAs tunnel diodes were fabricated using a variety of

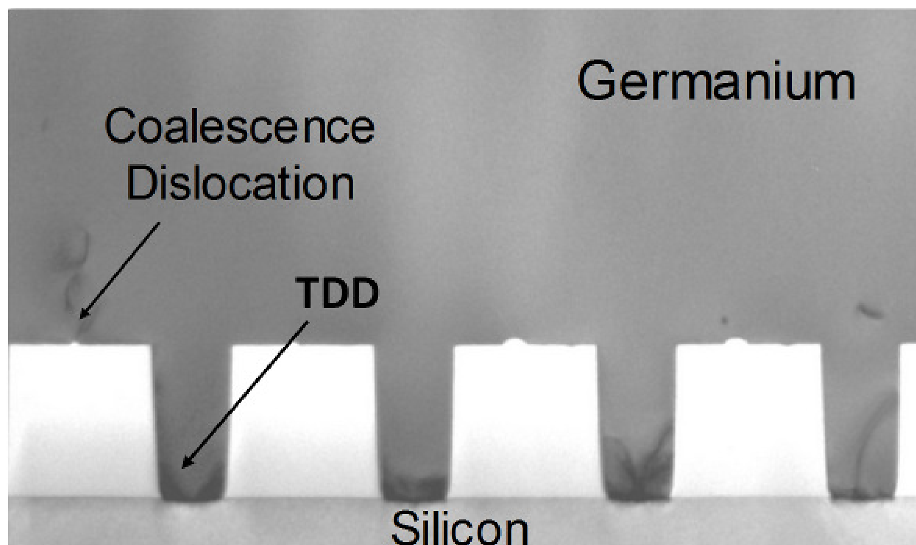

Fig. 4.4: TEM cross-section of coalesced Ge integrated on a Si substrate using ART. The majority of TDD resulting from the 4% lattice mismatch between Ge and Si is trapped by the oxide sidewalls within the trenches. A few extra dislocations are created around the coalescence planes.

processing techniques [1-4].

The Ge virtual substrate preparation began with 490 nm thermal oxide growth. Vertical trenches were etched into the oxide with various widths (100-400 nm) and pitches (250-500 nm). Ge epitaxial layer was selectively grown inside the trenches using reduced pressure chemical vapor deposition (RPCVD). Growth continued above the oxide trenches, until an 825 nm coalesced Ge layer formed. To provide a smooth and flat surface for optimal device fabrication, the Ge layer was planarized via chemical mechanical polishing (CMP).

As expected, a large threading dislocation density (TDD) was created at the Ge/Si interface, as seen in Fig. 4.4. However, the majority of TDD were trapped within the oxide trenches resulting in a high quality crystalline Ge layer only 200 nm above the substrate surface. A small number of coalescence dislocations were formed where the overgrown Ge from two adjacent trenches join together. Without ART, a blanket film of Ge forms a TDD of ~$2x10^9$ /cm^3, due to its 4% lattice mismatch with Si. Increasing the trench pitch (spacing) decreased TDD by greater than 10x (Fig. 4.5b). Increasing the trench aspect ratio (height to width ratio) decreased TDD by approximately 1,000x, down to ~$2x10^6$ /cm^3 (Fig. 4.5a). The visual and quantitative inspection indicates that a high quality virtual Ge substrate has been formed. This indicates that high quality electrical devices are achievable on ART substrates, but does not confirm this hypothesis.

4.3. Ge on Si Tunnel Junction

Initial experiments looked into directly testing the virtual Ge substrates by fabricating Esaki tunnel diodes (TDs). The device fabrication approach used in this study was adopted from Zhao, *et. al* [55]. The present approach differs in two minor ways. First, this study used a lower n-type doping concentration of $5x10^{20}$ cm^{-3} rather than $1x10^{21}$ cm^{-3}. Secondly, the Zhao study utilized evaporated Al rather than sputter deposited Al: 2% Si in the present study. It was

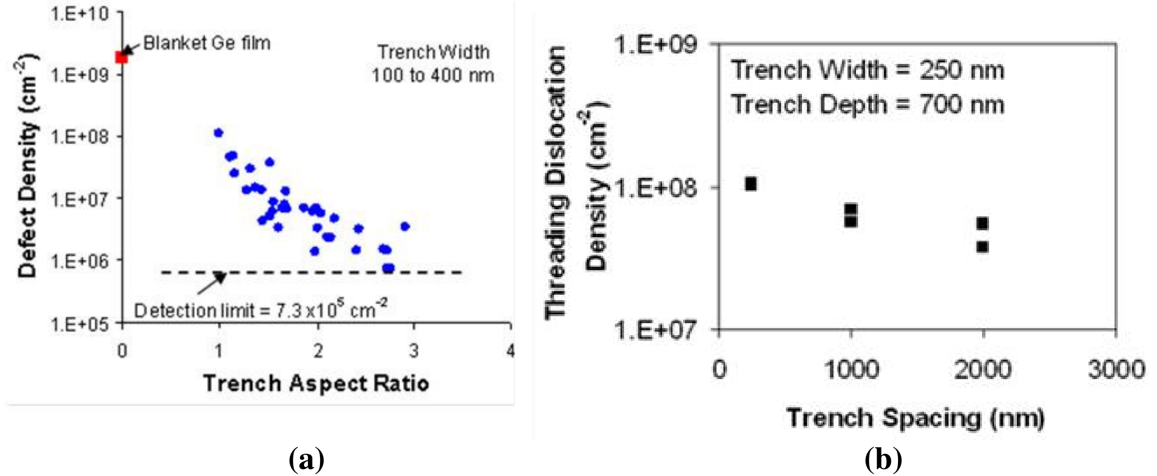

(a) **(b)**

Fig. 4.5: Defect density of virtual Ge substrate integrated on Si via ART. In general, (a) as the aspect ratio (height by width) of the oxide trenches increases TDD decreases. Additionally, (b) increasing the trench pitch (spacing) also decreases TDD. Optimal measured results reduced TDD from ~1.25×10^9 /cm^3 for a blanket film, down to ~1.25×10^6 /cm^3.

theorized that the addition of 2% Si may act to slow the reaction rate between Al and Ge resulting in a more abrupt alloy junction.

As grown, the Ge layer is undoped. Therefore fabrication began with the introduction of n-type dopants. The virtual substrates were coated with Emulsitone 5×10^{20} cm^{-3} phosphorosilica spin-on-glass (SOG), and baked at 800°C for five minutes under an N_2 ambient in an AG Associates Heat Pulse 610 Rapid Thermal Annealing (RTA) furnace. This step served to introduce a degenerate level of P into the Ge. The SOG was removed in a 10:1 DI water to HF bath for 25 seconds. A lift-off technique was used to define dots of a 140 nm thick Al: 2 %Si, film deposited via DC sputtering. Alloying of the p-type junction was performed via a spike RTA at 480 - 620°C at a target time of one second in an N_2 ambient. A ramp rate of 150°C/sec. was used for all samples. In practice, the chamber temperature was in the vicinity of the target temperature for three seconds, with some run to run variability. The fabrication procedure was applied to a substrate with coalesced Ge on Si. In this sample, the oxide openings had a width of 250 nm with a 1:1 pitch. Fig. 4.6 illustrates a schematic diagram of Ge on Si Esaki diodes.

4.3.1. Ge ETD Results and Analysis

For all process conditions, negative differential resistance or inflections were observed. Fig. 4.7 shows the dependence of the current voltage characteristics on the alloy temperature. In general a few trends were observed. First, elevating the anneal temperatures resulted in an increase in current density. An optimal fabrication window was found for a phosphorus diffusion at 825°C, five minutes. A maximum peak to valley current ratio (PVCR) of 1.1 with a current density of 4.1 kA/cm^2 was observed for an alloy temperature of 580°C, for one second. A 1.1 PVCR was also observed at 620°C, one second.

These results experimentally show a similar trend to Zhao [55] with lower peak to valley ratios. It should be noted that the overall current density in the Zhao study of 15 kA/cm^2 is roughly double the present reported value of 6 kA/cm^2 in both the control/ART diodes for a comparable anneal of 600°C, one second. This is attributed to a narrow depletion width in the Zhao et. al study due to the higher n-type doping levels. Based on recent publications of P-diffusion in Si, the junction is estimated to be 300 nm deep for these conditions [56].

For the Ge system, it is theorized that the Esaki diode performance can be greatly

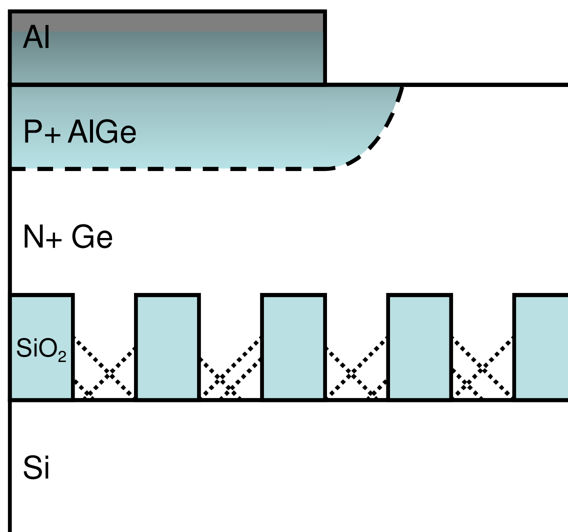

Fig. 4.6: Schematic cross-section of the Ge alloy junction TD.

improved by looking at alternative doping schemes. It should be noted that the highest reported PVCR for Ge Esaki tunnel diodes is about 10 [57]. Davis and Gibbons further point out that Al alloying typically resulted in lower PVCR values compared to other approaches as Al consumes Ge during alloying at a much faster rate compared to Sn or In [57, 58]. Chynoweth *et. al* also indicated that alloying Al in Ge results in backward diode performance [59]. Furthermore, it is speculated that it will be possible to realize a III-V on Si Esaki diode using similar techniques, which is expected to have substantially higher performance than either Si or Ge Esaki diodes.

In conclusion, it has been demonstrated Ge Esaki diodes on a Si substrate with a peak-to-valley ratio of 1.1. This result suggests the high quality of Ge epitaxy grown on trench-patterned Si substrate via ART defect-trapping technique. It demonstrates a viable technique for the integration of Ge and III-V materials on Si for devices such as resonant tunnelling diodes, HEMTs and MOSFETs. Furthermore, GaAs based structures may be directly grown on the Ge virtual substrates for improved device performance. In the following section a series of large PVCR GaAs ETDs are used to evaluate the ART substrates.

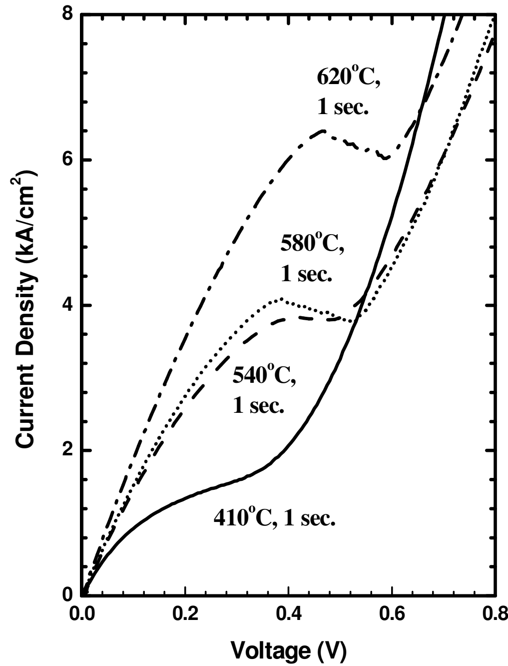

Fig. 4.7: I-V characteristics of Ge on Si ETDs for four separate anneal temperatures.

4.4. GaAs on Si Tunnel Junctions

The direct bandgap and low reduced effective mass of III-V semiconductors generally results in superior tunnel diodes compared to Si and Ge. Furthermore, the larger bandgap of GaAs, but not excessively so, results in tunnel diodes with large PVCRs in the range 21-25 [12, 13]. Whereas, the best Si and Ge tunnel diodes have PVCRs of 6 [8] and 10 [57], respectively. High PVCR in a given material system is a signature of low defect density resulting from low excess current. Therefore, large PVCR structures are more sensitive to crystal quality. The highest PVCR tunnel diodes have so far been produced by molecular beam epitaxy and attributed to the formation of abrupt heterojunctions and doping profiles and high activated impurity densities.

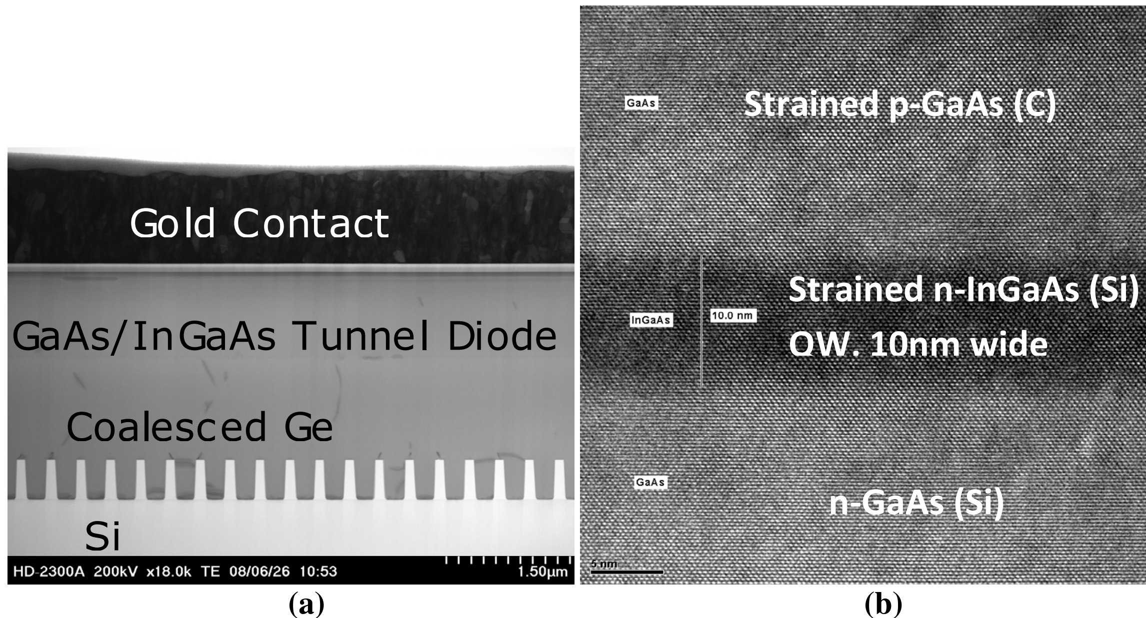

Fig. 4.8: TEM cross-sections of (a) entire GaAs TD on Ge ART layers and (b) a close-up of the TD junction itself. The bulk of the TDD is trapped within the ART structure, though a few defects remain present within the coalesced Ge. Visually, the Ge/GaAs interface traps more of the defects, providing a high quality GaAs virtual substrate. The high resolution micrograph shows a well defined junction with regular crystalline structure.

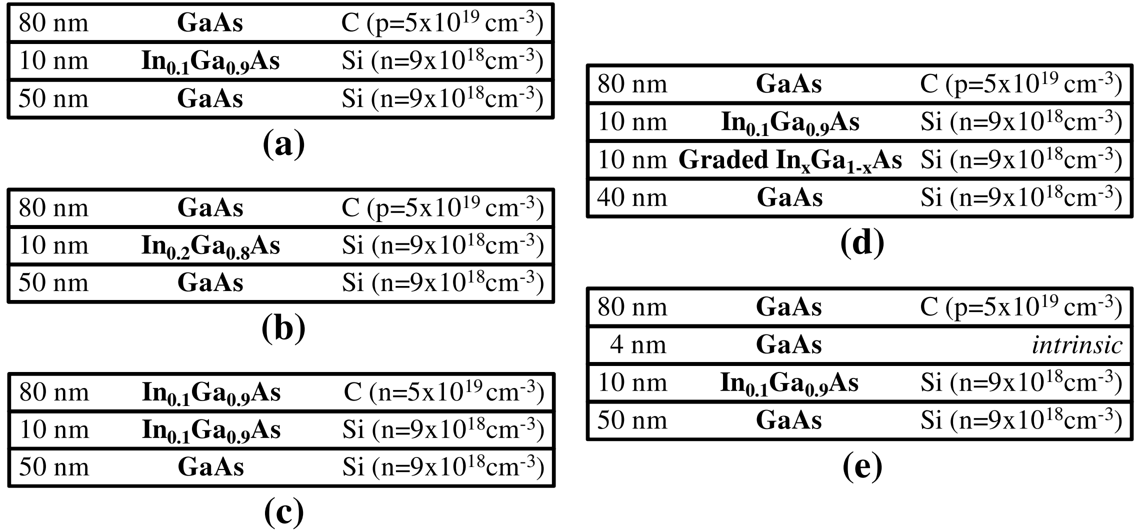

80 nm	**GaAs**	C (p=5x10^{19} cm^{-3})
10 nm	**$In_{0.1}Ga_{0.9}As$**	Si (n=9x10^{18}cm^{-3})
50 nm	**GaAs**	Si (n=9x10^{18}cm^{-3})

(a)

80 nm	**GaAs**	C (p=5x10^{19} cm^{-3})
10 nm	**$In_{0.2}Ga_{0.8}As$**	Si (n=9x10^{18}cm^{-3})
50 nm	**GaAs**	Si (n=9x10^{18}cm^{-3})

(b)

80 nm	**$In_{0.1}Ga_{0.9}As$**	C (n=5x10^{19} cm^{-3})
10 nm	**$In_{0.1}Ga_{0.9}As$**	Si (n=9x10^{18}cm^{-3})
50 nm	**GaAs**	Si (n=9x10^{18}cm^{-3})

(c)

80 nm	**GaAs**	C (p=5x10^{19} cm^{-3})
10 nm	**$In_{0.1}Ga_{0.9}As$**	Si (n=9x10^{18}cm^{-3})
10 nm	**Graded $In_xGa_{1-x}As$**	Si (n=9x10^{18}cm^{-3})
40 nm	**GaAs**	Si (n=9x10^{18}cm^{-3})

(d)

80 nm	**GaAs**	C (p=5x10^{19} cm^{-3})
4 nm	**GaAs**	*intrinsic*
10 nm	**$In_{0.1}Ga_{0.9}As$**	Si (n=9x10^{18}cm^{-3})
50 nm	**GaAs**	Si (n=9x10^{18}cm^{-3})

(e)

Fig. 4.9: Schematic diagrams of GaAs/InGaAs TDs. All four structures have the same nominal doping concentrations and film thicknesses. Each structure systematically varies material composition; (a) TD1 is a replica of Richard, *et al.* [13], (b) TD2 is a replica of TD1 but with 20% In mole fraction, (c) TD3 contains 10% In on both sides of the junction, (d) TD4 employs a graded heterojunction from 0% to 10% In, and (e) TD5 is a replica of TD1 with a nominally intrinsic GaAs layer inserted between the n- and p-type layers.

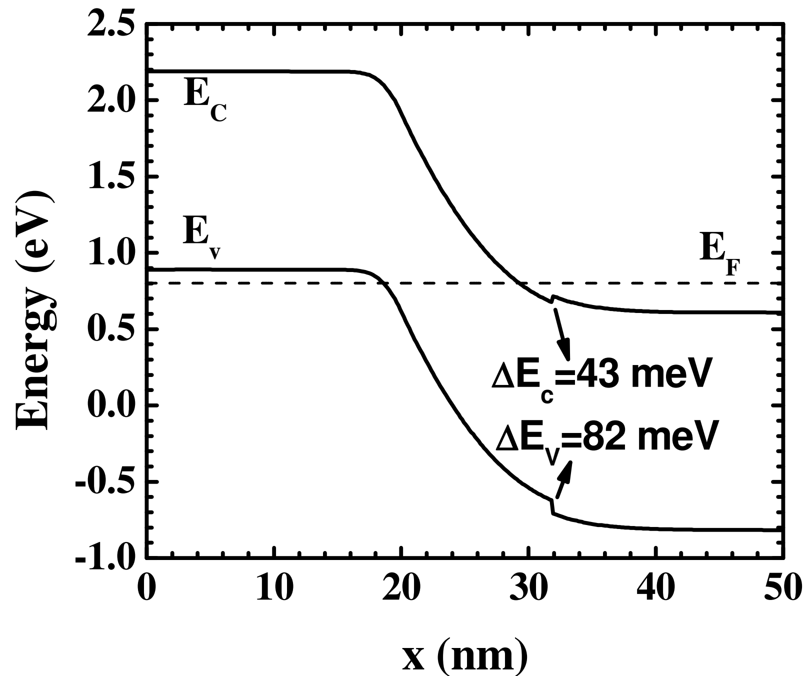

Fig. 4.10: Band diagram of TD3 calculated via OMEN, provided in collaboration with M. Luisier and G. Klimeck from Purdue University. The $In_{0.1}Ga_{0.9}As$ layer is assumed to be biaxially strained.

A series of five GaAs device structures adopted from Richard, *et al.* [13] were grown by MOCVD atop the previously described virtual-Ge substrate (~800 nm), with one example shown in Fig. 4.8. Recall that the virtual-Ge substrate is undoped, and therefore highly resistive. Therefore, a 500 nm thick, n-type GaAs layer was grown directly on top of the Ge providing a low resistivity layer which is used as a virtual ground for electrical measurements. Beneficially, additional dislocations were terminated at the hetero-interface (Fig. 4.8a). The tunnel junction itself (TD1: p-GaAs/n-$In_{0.1}Ga_{0.9}As$/n-GaAs) is shown in a high resolution TEM in Fig. 4.8b. As can be seen, the layers form a regular diamond crystal with smooth, well defined, sharp hetero-interfaces. From the TEM images, the epitaxial layers look like high quality crystalline semiconductors.

Five separate TD structures were grown, Fig. 4.9, and comprise a study centered around the effects of material composition and hetero-junctions on final device characteristics. All of the structures targeted the same dopant species (C and Si), concentrations ($5x10^{19}/cm^3$ and $9x10^{18}/cm^3$, respectively), and total layer thicknesses (80 nm and 60 nm, respectively). All five structures were grown on virtual-Ge substrates integrated on Si via ART. However, some of the structures were also grown directly on Si and GaAs substrates in order to compare electrical results of (i) highly defected epitaxy (directly on Si), (ii) high quality virtual substrates (ART), and (iii) lattice matched substrates (directly on GaAs). TD1 (Fig. 4.9a) is the base structure (duplicating T. A. Richard, *et al.* [13]), places a type I GaAs/InGaAs heterojunction at the tunnel junction. The second structure, TD2 (Fig. 4.9b), increases the In mole fraction to 20%. TD3 (Fig. 4.9c) incases the p/n junction entirely within an $In_{0.1}Ga_{0.9}As$ layer. TD4 (Fig. 4.9c) attempts to minimize the type I band alignments, and thus eliminate additional quantum wells and tunnel barriers, by gradually grading the In content from 0% to 10% over 10 nm. Finally, TD5 is a repeat of TD1 with a 4 nm nominally intrinsic layer inserted at the p-n junction.

A copy of TD1 and TD5 were grown directly on Si substrates (TD1-Si and TD5-Si), no ART or graded buffers. Due to the large lattice mismatch (~4%), the TDD is expected to be very high (≳$2\text{x}10^9$ /cm^3) providing extra leakage paths across the tunnel junction. As a result, it is

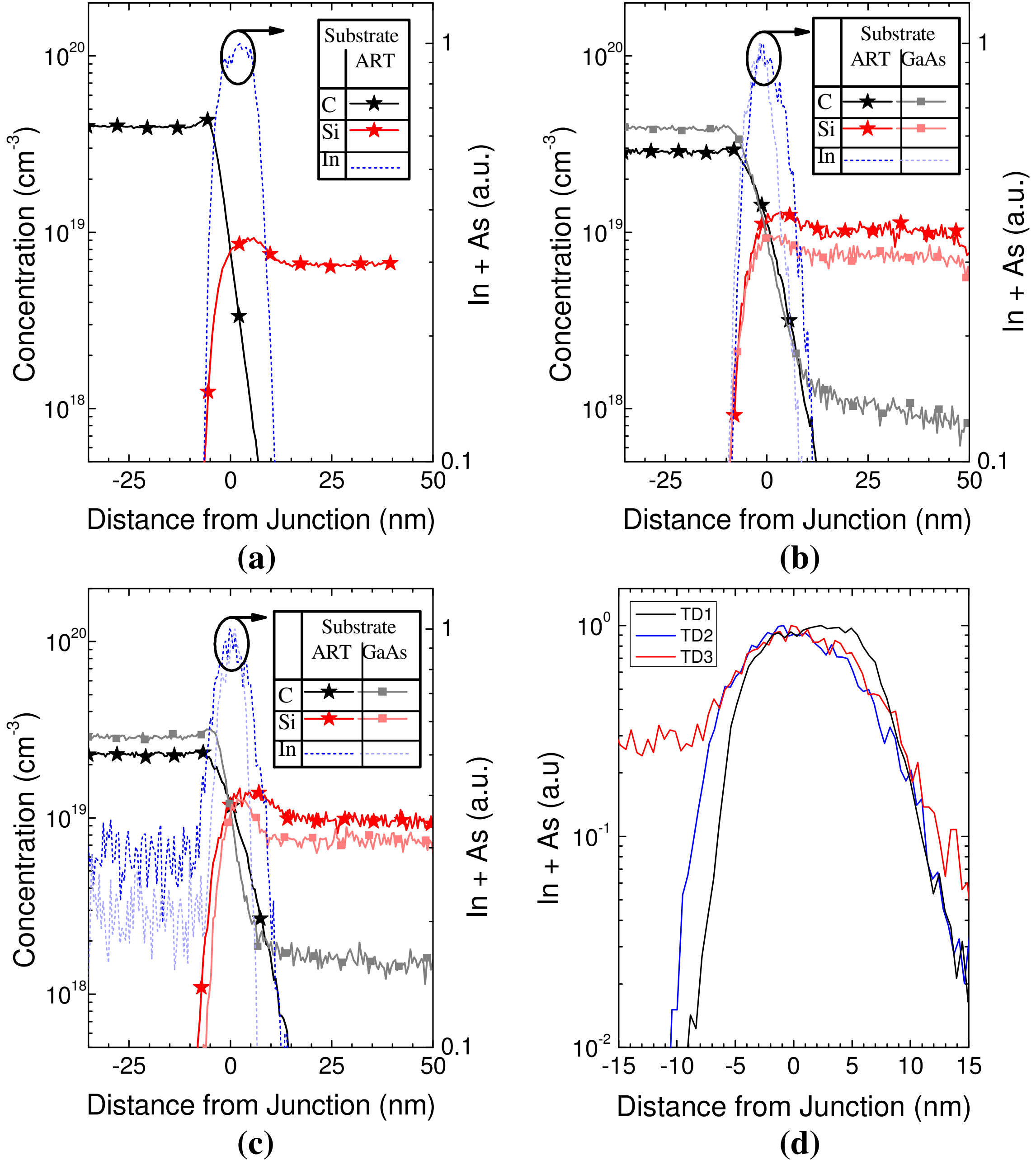

Fig. 4.11: SIMS analysis of C (p-type), Si (n-type) concentrations, and In/As normalized count. Includes results for (a) TD1, (b) TD2 and TD2-GaAs, and (c) TD3 and TD3-GaAs. Finally, (d) is included for direct comparison of In layer location.

expected that these devices will have poor electrical characteristics. Specifically, there should be a dramatic reduction in PVCR, if present at all, and similar or greater magnitude in J_P. Additionally, simultaneous growths of TD2 and TD3 were performed on directly GaAs substrates (TD2-GaAs and TD3-GaAs). Since GaAs substrates are the ideal starting substrates for these TDs, these TDs are expected to have similar, if not better, performance than their counterparts grown on ART substrates. Specifically, J_P should be approximately the same and potentially a lower J_V (increased PVCR) due to a smaller excess current resulting from few defects.

SIMS analysis was used to accurately assess dopant concentrations (Table 4.1 and Fig. 4.11) and the location of the InGaAs layer (Fig. 4.11). However, limitations in resources restricted the analysis to five of the nine structures grown: TD1, TD2, TD2-GaAs, TD3, and TD3-GaAs. The maximum measured doping concentrations adjacent to the tunnel junction (within ~7 nm) ranged approximately 1.7x for C (2.43 to 4.33 x10^{19} /cm^3) and Si (9.26 to 14.7 x10^{18} /cm^3), with the reduced average doping remaining fairly constant between 7.63 to 9.16 x10^{18} /cm^3 (~1.2x). For TD2-GaAs and TD3-GaAs, there is a residual C concentration in the bottom n-type layer, due to the trimethylgallium precursor. One would expect that there would be little variation in J_P due to doping concentrations. However, the magnitude of the minority dopant (providing the minority carriers) is less than, but comparable in magnitude to the primary dopant (providing the majority carriers) near the metallurgical junction. Therefore, counter

Table 4.1: Doping concentrations as measured by SIMS. Middle columns are maximum absolute values measured adjacent to the tunnel junction. Right hand columns are the maximum compensated values; |C-Si|.

Device	Max. Absolute Value			Max. Abs(Si-C) Value		
(x10^{18}/cm^3)	**C**	**Si**	**N***	**C**	**Si**	**N***
TD1	43.3	9.26	7.63	43.1	8.50	7.10
TD2	29.8	13.0	9.05	29.7	10.7	7.87
TD2-GaAs	40.4	9.71	7.83	40.0	6.80	5.81
TD3	24.3	14.7	9.16	23.6	11.4	7.69
TD3-GaAs	31.8	12.8	9.13	31.0	9.11	7.04

doping effects were taken into account by using the maximum |C-Si|. As a result the doping ranges were reduced to, 2.36 to 4.31 x10^{19} /cm^3 (~1.8x) for C, 6.80 to 11.4 x10^{18} /cm^3 (~1.7x) for C, and 5.81 to 7.87 x10^{18} /cm^3 (~1.4x) for N*. From the modeling results calculated in the previous chapter, J_P is expected to range about 10x, assuming no significant strain effects and homojunction behavior.

Also of interest is the thickness and location of the InGaAs layers. The SIMS analysis had no calibration standard for In. Therefore relative counts/sec. were reported instead of the mole fraction, indicating the location, if not the magnitude of the InGaAs layer. Clearly, the thickness of the InGaAs layer is thinner for the devices grown directly on GaAs substrates (Fig. 4.11b-c) by 3 nm and 6.5 nm for the TD2 and TD3 series, respectively. This indicates that there were a significant differences in the growth interactions between the virtual-GaAs and regular GaAs substrates. As a result, it is expected that TD2 and TD3 will have a larger J_P than TD2-GaAs and TD3-GaAs. However, it is not obvious the effects this will have on the PVCR, which is the main indicator being utilized in this study to qualify crystal quality of the epitaxial layers. Additionally, Fig. 4.11d shows that there is only ~2.5 nm difference in the thickness and location of the InGaAs layers for TD1, TD2, and TD3. This is surprising, since TD3 was design to maintain a 10% InGaAs throughout the entire 80 nm p-type layer. TD3 will still likely have a greater current density than TD1, due to its slightly larger doping density, somewhat thicker In layer, and a non-zero In content in the bulk p-type layer. TD2 should have the largest current densities due to its much larger, but unquantified, In content.

If the growth results are similar for rest of the samples, TD4 should have a current density between TD1 and TD2, thanks to its graded junction removing the extra tunnel barriers. TD5 may also see an increased current density due to the intrinsic layer separating the peak dopant concentrations, minimizing counter doping effects. However, it is extremely difficult to predict the effects that will be measured on PVCR.

4.4.1. Basic Fabrication Process

After the epitaxial layers are grown, the samples are prepared for thermal activation anneals, which are typically needed with CVD based growths. Thermal annealing helps to fully activate the dopants and remove H_2 from the crystal lattice. Increased dopant activation increases both J_P and PVCR, whereas H_2 removal only increases PVCR by reducing J_V. The anneals were performed using an AG 610 Rapid Thermal Processor (RTP), in an N_2 ambient. Temperature was ramped at ~100°C/sec. up to a target temperature, where it was help constant for five minutes, and finally air cooled back to room temperature.

After annealing, the samples were coated with a dual resist layer stack consisting of ~1.1 µm of photoresist (PR) on ~400 nm of LOR 5A (a non-photoactive lift-off resist). The LOR 5A was baked at 180°C for 60 sec., before the PR was coated. The PR was baked for 60 sec. at 90°C. Then, the samples were imaged using a Karl Suss MA150 contact aligner for approximately 25 sec. Finally, the resist stack was developed in CD26 developer for ~2 minutes, then rinsed in DI H_2O for ~60 seconds. At this point a series of contact holes are formed in the resist stack, with a large undercut present in the LOR 5A layer, as shown in Fig. 4.12a.

Immediately before metal deposition, the sample surface was cleaned using a HCl:H_2O (1:10) solution for 10 seconds. Blanket Au/Zn/Au (20nm/20nm/200nm) metal contacts were thermally evaporated. The shelf-like undercut profile of the resist stack was designed to act as a shadow mask (Fig. 4.12b). The excess contact metal (deposited on top of the PR) was lifted off by soaking the samples in a heated (~90°C) Remover PG bath until completion. After a one

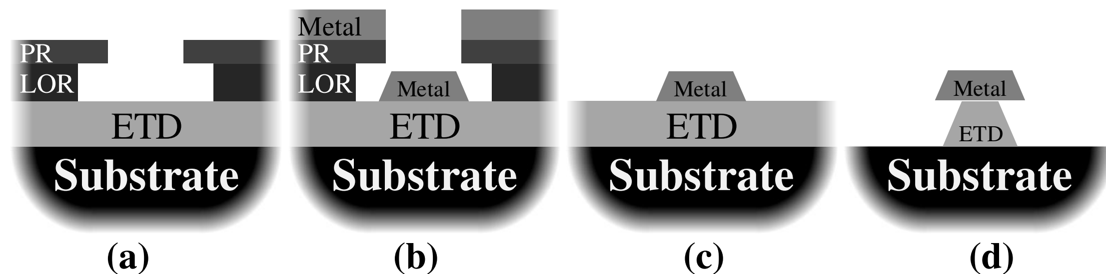

Fig. 4.12: Schematic diagrams showing the basic TD process flow; (a) lift-off resist profile past develop, (b) metal deposition, (c) post metal lift-off, and (d) mesa isolation etch.

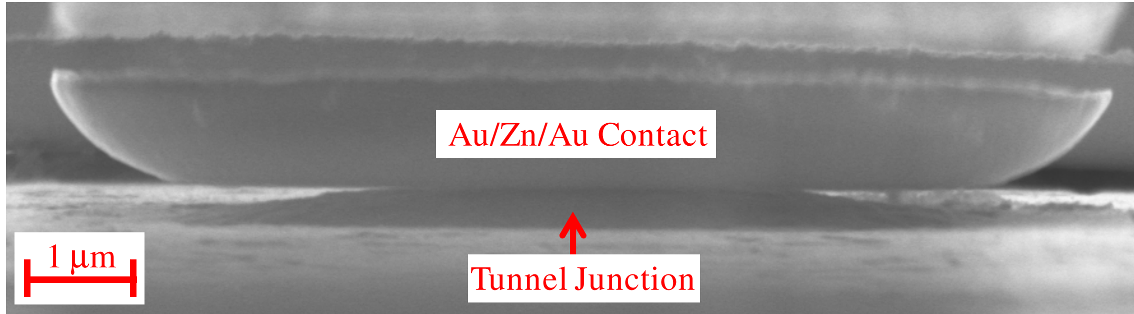

Fig. 4.13: High angle SEM image of GaAs TD on ART substrate. The large undercut (~2 μm on a side) clearly visible is due to the aggressive mesa isolation etch.

minute rinse in DI H_2O, only metal contacts remained on the surface (Fig. 4.12c). Finally, the contact metal was used as a self-aligned etch mask. An $H_2SO_4/H_2O_2/H_2O$ (1:8:80) acid bath was used to etch the GaAs/InGaAs layers in order to electrically isolate the tunnel junctions. The final result was a series of electrically isolated tunnel junctions (Fig. 4.12d), whose cross-sectional area is primarily determined by the metal contact geometry and etch time.

Given its aggressive nature, the tunnel junctions were substantially undercut, which was assessed with high angle SEM inspection (Fig. 4.12). The measured undercuts and device diameters were used to estimate junction areas for accurate current density calculations. Electrical characterization was performed with a Keithley 4200 semiconductor parameter analyzer. Very large area diodes (>100x) were used as virtual grounds for the device under test.

4.4.2. DC Electrical Results

First, an experiment was setup to determine the optimal thermal anneal temperature. Three TD1 samples were fabricated using the basic process previously described with (i) no anneal, (ii) 425°C anneal (following T. A. Richard, *et al.* [13]), and a 480°C anneal. Representative I-V characteristics for each sample is shown in Fig. 4.15. Each measurement was performed on the same size device for direct comparison. The PVCR made dramatic improvements from a minimum of 4, to a maximum of 24, back down to 18 for the "no anneal", 425°C, and 480°C annealed samples, respectively. These results nearly match the previous GaAs

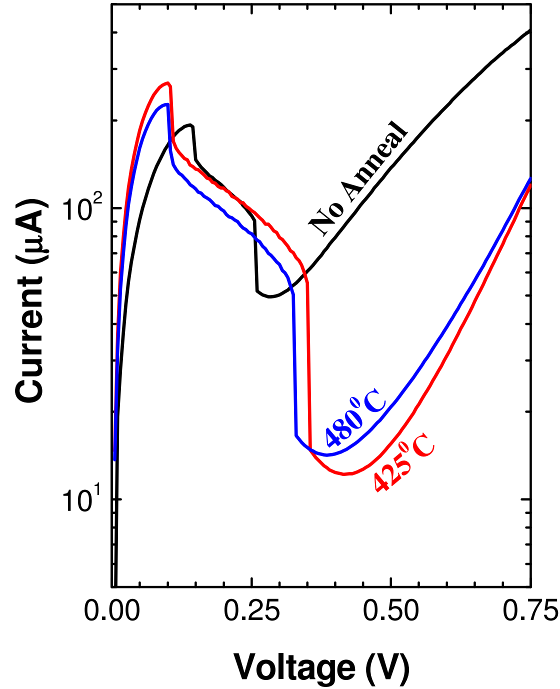

Fig. 4.14: Typical I-V characteristic of three TD1 samples with (i) no anneal (PVCR of 4), (ii) 425°**C** anneal (PVCR of 24), and (iii) 480°**C** anneal (PVCR of 18).

record PVCR of 25 [13], and surpassed the previous TD on Si record of 6 [8]. J_P follows a similar trend with the 425°C annealed sample exhibiting the largest current density. Therefore, of the tested conditions, 425°C was selected as the optimal anneal temperature. All of the following results use the optimized anneal temperature determined with this initial experiment.

Next, the effect of a 4 nm intrinsic layers (TD1 and TD5) and direct growth on Si (TD1-Si and TD5-Si) is examined. Shown in Fig. 4.15a are typical I-V characteristics for each device structures, all with similar device geometries. The on ART devices, TD1 and TD5, exhibit greater PVCRs of 24 and 11, respectively. The TDs grown directly on Si, TD1-Si and TD5-Si, have much smaller PVCRs of 3.9 and 4.4, respectively. These results indicate that there is a much greater density of defects for TDs grown on Si, as expected. This conclusion is additionally supported by the general trend of PVCR increasing when current density decreases (until $E_f \approx E_{C,V}$).

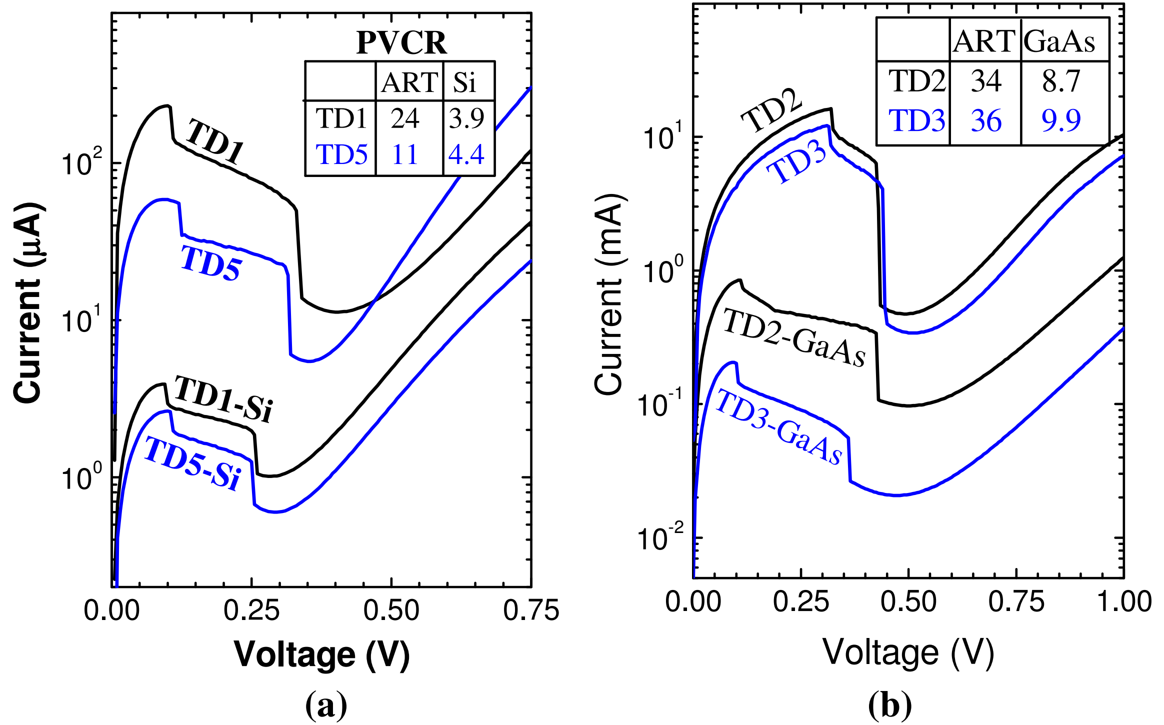

Fig. 4.15: Typical I-V characteristic of ~30 μm radii devices for (a) TD1, TD5, TD1-Si, TD5-Si, and (b) TD2, TD3, TD2-GaAs, TD3-GaAs. Devices grown on virtual ART substrates exhibit much greater PVCR and Current, indicating high quality material quality.

The on ART structures (TD1 and TD5) exhibit much larger current magnitudes than TD1-Si and TD5-Si. This is due to smaller BTBT efficiency, likely a result of lower active doping concentrations. Since the devices were grown simultaneously, and fabricated in parallel, it is likely that different growth interactions resulted in slightly different junction structures. This would be similar to the differences between TD grown on ART versus on GaAs substrates detailed in the SIMS results in Section 4.3.

TD1 and TD1-Si have a slightly larger current than TD5 and TD5-Si, which may only be a function of small variations in maximum doping concentrations. Conversely, TD1 has a much larger PVCR than TD5. In fact, the PVCR of TD1 is 4x greater than the previous on Si record [8], and nearly matches the previous GaAs record [13]. Therefore, it does not appear that the inserted intrinsic layer beneficially impacted the I-V characteristics. Furthermore, the virtual

ART substrates provide very high quality semiconductors on which to fabricate devices with highly competitive electrical characteristics.

The next set of experiments (Fig. 4.15b) look at changing the In mole fraction (TD2), the placement of InGaAs (TD3), as well as comparison with simultaneous growths on GaAs substrates (TD2-GaAs and TD3-GaAs). Again, it is immediately apparent that the on ART devices (TD2 and TD3) have much greater PVCRs (34 and 36, respectively) even though the comparison devices were grown directly on GaAs substrates (TD2-GaAs/8.7 and TD3-GaAs/9.9). The CVD epitaxy growth conditions were optimized for the ART substrates. As previously discussed, the SIMS results (Fig. 4.11) clearly show subtle but significant differences between the on ART and on GaAs growths. However, these results do not verify the quality of the epitaxy. In fact, the electrical results would indicate that ART optimized growths will yield poor epitaxial layers on other substrates. The results does not assert that the ART substrates are inherently better than GaAs substrates. That said, TD2 and TD3 surpass previous PVCR records for (i) Si substrates and separately for (ii) GaAs based TDs. Furthermore, this supports the claim that high quality semiconductors can be integrated on Si. Specifically, this has been shown here using ART as the integration method.

The current density in the on ART devices is much greater than in the on GaAs. From the SIMS results, Fig. 4.11, it is known that the doping concentrations are slightly reduced and the InGaAs layer is significantly smaller. It is reasonable that those features would significantly reduce the current density. Unexpectedly, TD2-GaAs has a much greater current density than TD3-GaAs even though the former has a much smaller average reduced doping, according to SIMS. This may be an indication of the effect of greater In content in the InGaAs layer. This is supported by a mildly large apparent current measured in TD2 versus TD3.

To better understand the relationship between J_P and doping, the measured values were plotted in Fig. 4.16, along with calculated trendlines for unstrained homojunction TDs using Kane's model [60] as discussed in the previous chapter. It will be shown in the following

chapters that the model accurately predicts InGaAs TD performance. Therefore, it is a good way to benchmark the performance of the fabricated devices.

First, it is apparent that the measured current densities are much greater than the predicted values. Recall that these TDs are under strain and have complex band alignments due to the heterojunction. Therefore they were expected to have larger than predicted current densities. However, TD2 and TD3 are on the 40% In line, with J_P nearly 100x greater than expected. Furthermore, the J_P for TD2 and TD3 are nearly the same, even though the calculated strain for TD2 is ~6.4%, more than 9x larger than TD3. In other words, it is not apparent what the tremendous boost in current density is due to. Secondly, the characteristic trendline encompassing TD1, TD2, TD3, TD2-GaAs, and TD3-GaAs is much steeper slope than predicted the trendlines predicted by the model. This would seem to indicate that these TDs are much more sensitive to doping variations than InGaAs homojunctions. In part, this is due to variations in the

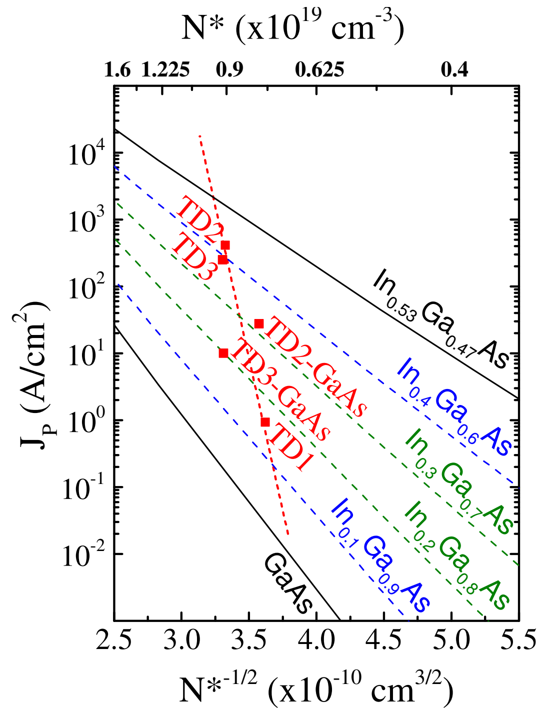

Fig. 4.16: Benchmarking of J_P vs. reduced doping (N^*) for TD1, TD2, TD3, TD2-GaAs, and TD3-GaAs. Measured data is plotted against unstrained InGaAs homojunction trendlines, calculated using Kane's [60] (discussed in the previous chapter, and shown to be accurate in the following chapter). Measured J_P is up to 100x predicted magnitude, with a much steeper trendline.

grown epitaxy layers. For each original TD structures, a much larger study consisting of at least three additional TD growths would be needed, wherein only the doping concentrations were varied. However, structures with steep trendlines may improve SS for TFETs.

High angle SEM inspection of the surface of mesa isolation etched samples revealed a large number of circular trenches, Fig. 4.17. These trenches are etch highlighted defects that propagated from the virtual substrates and through the epitaxy growths. Clearly, from Fig. 4.17, the epitaxial layers are not perfect. These defects will act as tiny shorts, mainly increasing valley currents, thereby reducing calculated PVCRs. However, scaling device geometries to smaller dimensions will reduce the number of defects present within the device. Eventually the devices will begin to "miss" the defects, and form between them, thereby maximizing the PVCR. Given resolution constraints of contact lithography, the smallest device junctions achieved were approximately 3.5 μm in diameter.

The I-V characteristics with the largest PVCRs for TD1, TD2, TD3, and TD4 all occurred with the smallest device sizes, and are shown in Fig. 4.18a. TD4, no previous electrical results discussed, has a maximum PVCR of 10. It is believed that the graded InGaAs junction successfully removed any additional tunnel barriers and quantum wells from the TD's band

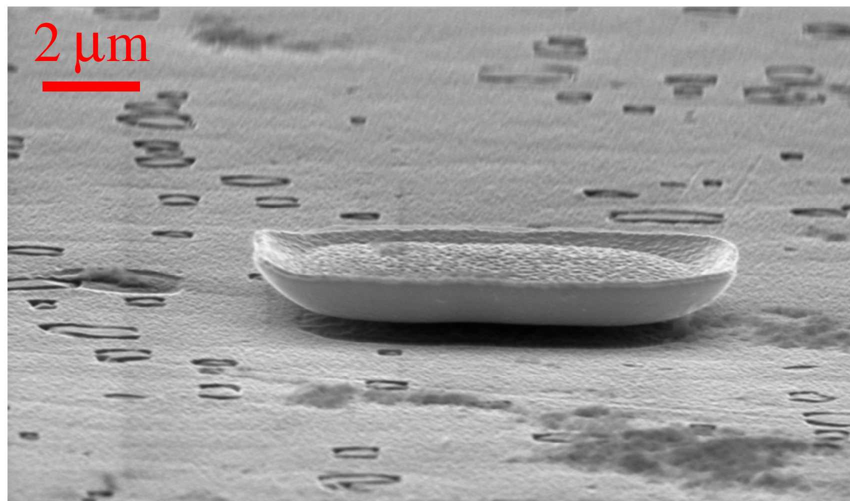

Fig. 4.17: High angle (82^0) SEM image of mesa isolation etched TD3. As highlighted by the wet chemical etch, the surface is marked by many large defects (there may be smaller ones not visible here). These defects would tend to degrade device performance.

structures. This did help maintain larger current densities. However, those extra band features tend to filter out excess valley current. As a result, the PVCR was negatively impacted.

Additionally, the TDs were benchmarked against of key TDs reported in literature, Fig. 4.18b and Table 4.2. As can be seen, the TDs fabricated for this study follow the typical trend of sacrificing current density for improved PVCR. The PVCR of TD1 improved by a few points to 27, which surpasses the previous GaAs record of 25 [13]. TD2 made a large improvement in PVCR up to 43 from its previous 34. However, the greatest improvement was measured in TD3 with a record PVCR of 56, which is a 56% improvement. Consequentially, TD3 is measured to have the largest PVCR of any previously reported (i) InGaAs TD or any (ii) TD fabricated on a Si substrate. Additionally, (iii) it is the 3rd largest PVCR ever reported [15, 17]. However, the measured PVCRs did not plateau, indicating that smaller device geometries could yield even larger values (see Section 4.6).

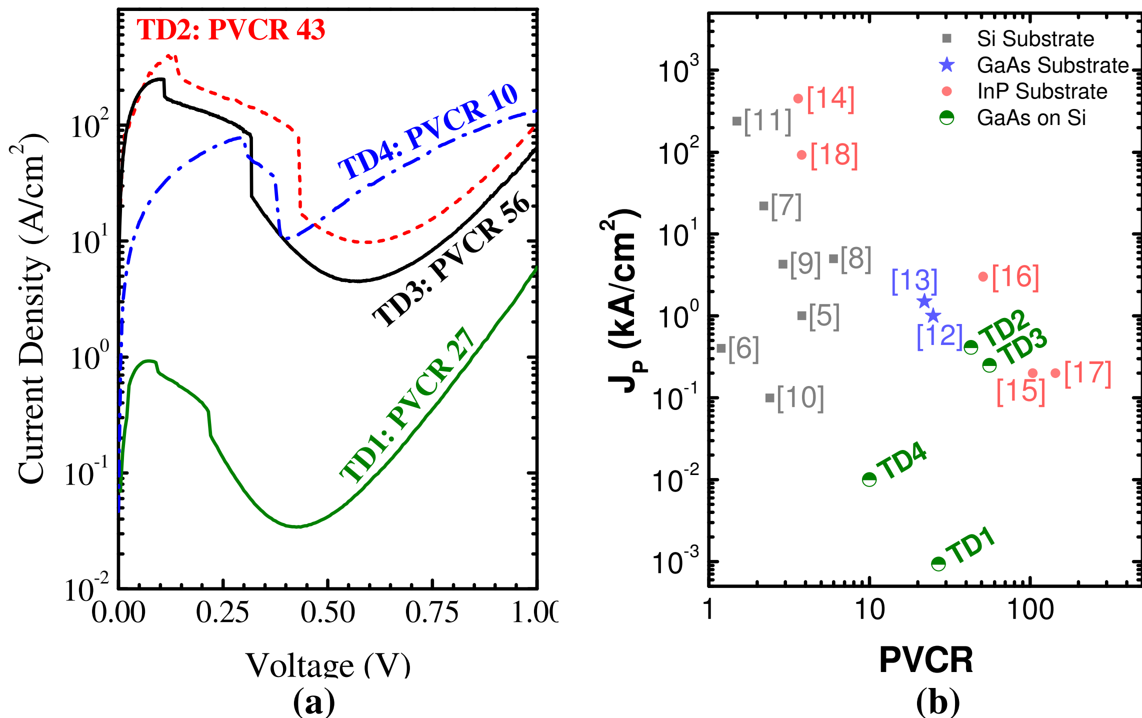

Fig. 4.18: (a) I-V characteristics with the best PVCR's measured for TD1, TD2, TD3, and TD4. (b) Benchmarking of TD1, TD2, TD3, and TD4 against key TDs in literature [5-18]. TD3 has the 3rd largest PVCR over all and the largest of all GaAs TD or TD on a Si substrate

Table 4.2: TD1, TD2, TD3, and TD4 parameters as well as the highest reported PVCR TDs fabricated on Si, GaAs, and InP substrates.

Type	Substrate	Tunnel Diode	Growth Technique	Jp (A/cm^2)	PVCR	Study
RITD	Si	Si/SiGe	MBE	5000	6	[8] Eberl, 2001
RTD	Si	Si/SiGe	MBE	218,000	3	[11] Chung, 2006
Esaki	GaAs	P^+/N^+ GaAs	Alloy	N/A	25	[12] Holonyak, 1960
Esaki	GaAs	GaAs/$In_{0.1}Ga_{0.9}As$	MOCVD	1500	22	[13] Richard, 1993
RITD	InP	InGaAs/InAlAs	MBE	200	104	[15] Day, 1993
RITD	InP	InGaAs/InAlAs	MBE	200	144	[17] Tsai, 1994
Esaki	**Si**	**GaAs(P^+) $In_{0.1}Ga_{0.9}As$(N^+)**	**UHVCVD/ MOCVD**	**9**	**27**	**[4] TD1**
Esaki	**Si**	**GaAs(P^+) $In_{0.2}Ga_{0.8}As$(N^+)**	**UHVCVD/ MOCVD**	**1000**	**43**	**[4] TD2**
Esaki	**Si**	**$In_{0.1}Ga_{0.9}As$**	**UHVCVD/ MOCVD**	**250**	**56**	**[4] TD3**
Esaki	**Si**	**GaAs(P^+) $In_{0.1}Ga_{0.9}As$(N^+)**	**UHVCVD/ MOCVD**	**65**	**8**	**[4] TD4**

4.4.3. Temperature Analysis

Many temperature studies of III-V Esaki diodes have been detailed since the 1960s [12, 61, 62]. These reports have focused on alloy junction devices, where localized liquid phase epitaxy is used to introduce a degenerate doping via a carrier metal to a host crystal sometimes resulting in a hump current due to the inclusion of the carrier metal [12, 61]. Devices doped by epitaxy as studied here are not expected to show this sort of defect. However, it was theorized that the integration of III-V on Si could result in unique defects not described in previous publications. In this study, the (i) temperature dependence of these devices, (ii) the insensitivity of tunnel current (forward and Zener) to temperature, and (iii) the absence of mid-gap states in the excess current have been reported.

From Kane's model [60], there is no direct temperature effect on the current density of direct bandgap TDs unlike standard diodes and the SS of CMOS. However, the bandgap and effective mass, both of which affect other material parameters, have a small dependence on

temperature. However, without knowing the rate of change for effective mass with temperature, the model predicts J_P will increase only ~40% per 100°C rise. A previous GaAs, alloy junction, TD reported by Holonyak, *et al.* [12], described a complicated relationship wherein J_P initial increased with temperature, and then began decreasing with temperature at approximately 300 K. At lower temperatures J_P is increasing due to the decrease in bandgap energy (tunnel barrier height). However, after the temperature is increased past some critical value mainly determined by doping concentrations, increases in the density of states will begin limiting E_F. This will make it appear as the diode is doped less at room temperature and therefore, it will have a smaller current density. On the other hand, J_V will always tend to increase with temperature. This is due to the excess current utilizing thermal/phonon energy to help "hop" into and then out of the bandgap, via defect states. Also, sidewall leakage currents will increase with temperature too.

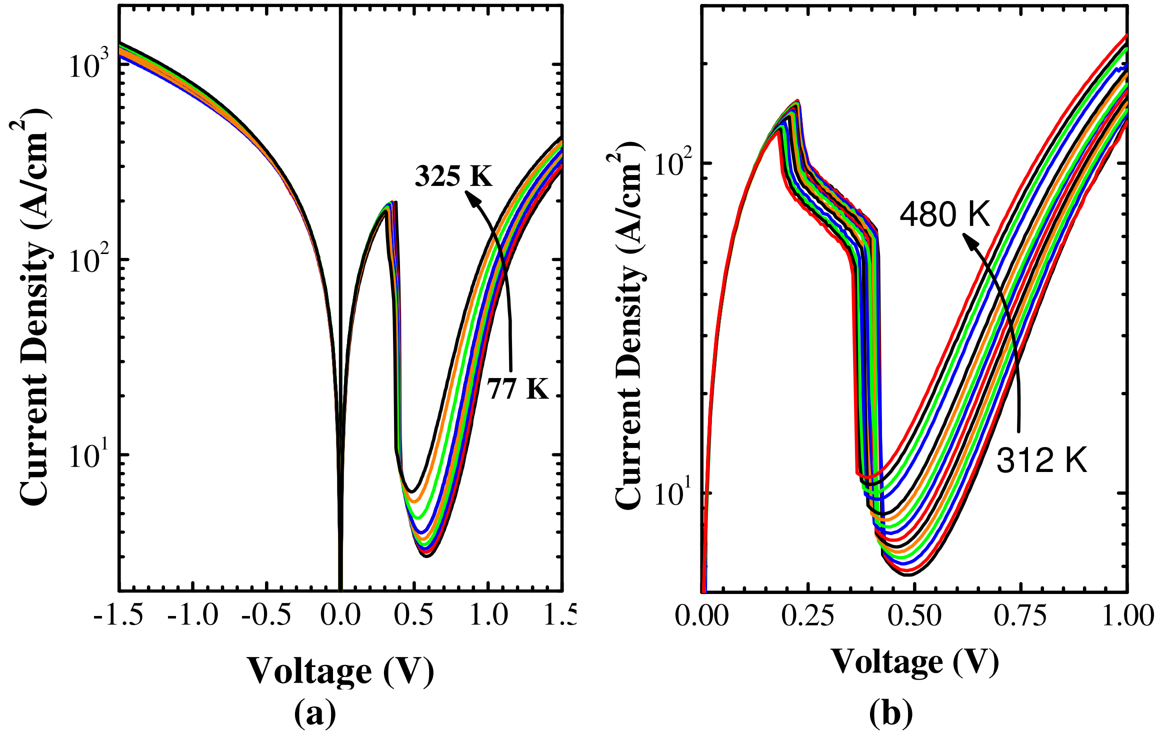

Fig. 4.19: Measured I-V characteristics of TD3 at (a) low temperatures (77 K to 325 K) and (b) high temperatures (312 K to 480 K). Contrary to the model prediction, J_P decreased with temperature. However, J_V increased and J_{Zener} remained fairly constant.

Due to temperature range constraints, two separate measurement setups were used. Low temperature measurements (room temperature down to ~77 K) were performed on an SPA system, whereas high temperature (up to ~200°C) measurements utilized a Keithley 4200

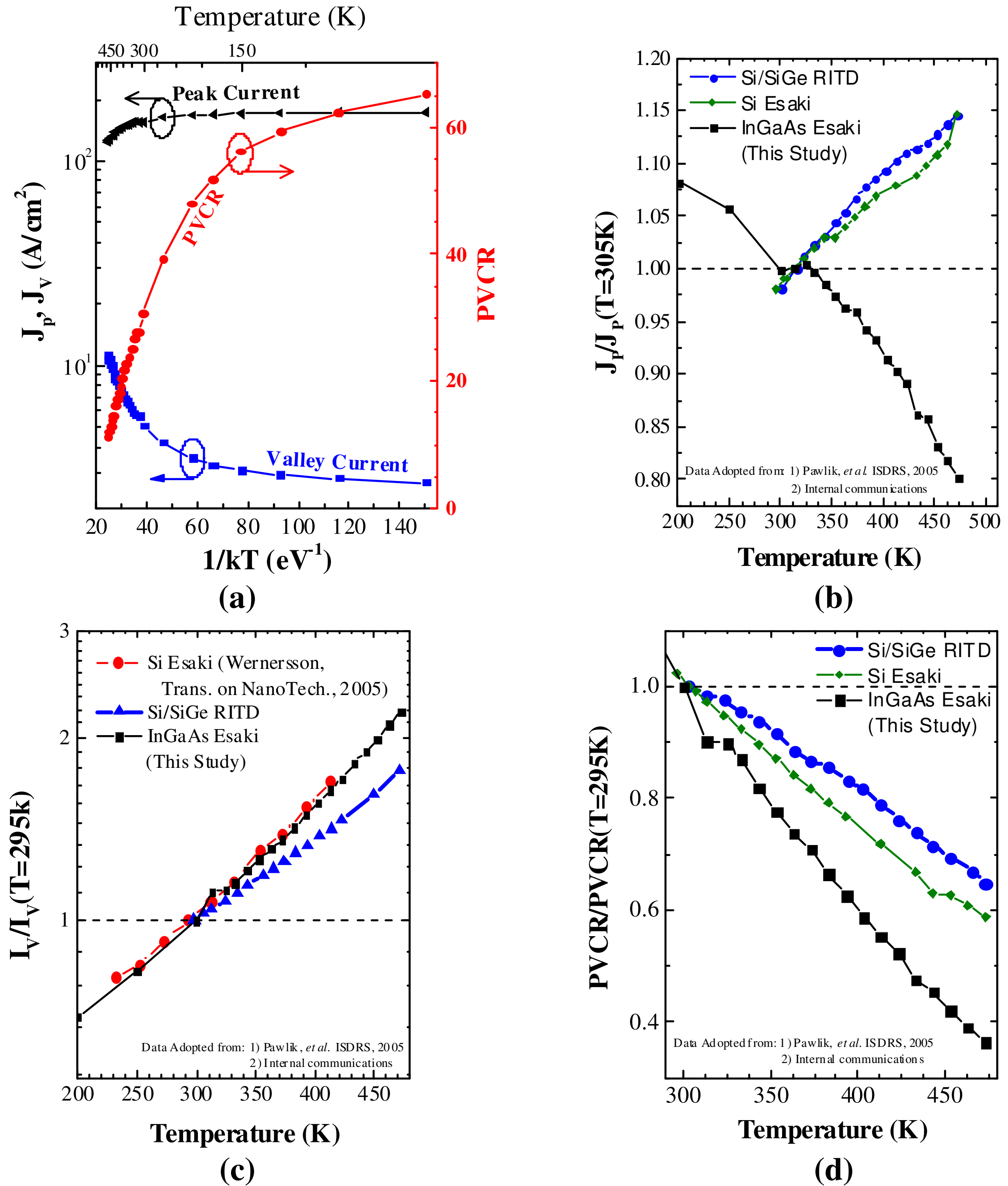

Fig. 4.20: (a) J_P, J_V, and PVCR versus $1/kT$ Most of the variation occurs at high temperatures with J_V. The other three graphs are normalized (b) J_P, (c) J_V, and (d) PVCR versus temperature for direct comparison with Si TD.

parameter analyzer. Due to constraints of the probe stations, large area devices (~32 μm diameter) were probed. As expected, the room temperature PVCR was limited to ~31, instead of the previous maximum value of 56.

The measured I-V characteristics for the (a) low and (b) high temperature measurements are shown in Fig. 4.19. Due to differences in the probe setup, the low temperature measurements have a larger series resistance. There is very little variation in the Zener current density (J_{Zener}). Interestingly, J_P decreased with temperature over the entire range, which went against the modeling prediction. Therefore, changes in the effective mass and density of states must be playing a dominant role. As expected, J_V increased with temperature. However, no hump current was observed in the post valley characteristics, indicating that there are few midgap states present [46].

To more clearly follow the trend of the key TD parameters J_P, J_V, and PVCR have been plotted against $1/kT$, Fig. 4.20a. A small kink in the data can be seen at the switch between low and high temperatures measurements, due to changing between the two separate measurement systems. The PVCR ranges from 11 to 65. The range for J_P and J_V was measured to be 125 A/cm^2 to 150 A/cm^2 and 11A/cm^2 to 2.7 A/cm^2, respectively. The majority of the variation occurred at temperatures above 300 K. However, the almost negligible change in current density over the 400 K temperature range indicates that J_P is nearly a pure BTBT current. On the other hand, J_V increased a substantial ~4x above 200 K. However, an Arrhenius extraction of the valley current taken at the valley voltage (V_V) exhibited an activation energy of 1.8 meV for low temperatures, indicative of a purely quantum mechanical tunneling mechanism.

The key TD parameters were normalized with its own value at room temperature, Fig. 4.20b-d, order to compare with Si and Si/SiGe TD measurements [63]. As expected, J_P for the Si based devices increases with temperature. The percent change is also less then that observed for TD3. Note, that the observed kink in GaAs is due to switching between measurement setups. The valley current for all of the Si and GaAs TDs increased and nearly at the same rate. This

result is another pointer at the high quality nature of the epitaxy grown on ART. Finally, as expected from the previous results, the PVCR of GaAs decreases more rapidly than the Si devices. This is mainly due to the inherent decrease in J_P over the temperature range.

As evidenced in Fig. 4.20, a thermally activated process is present in J_V. To further elucidate this process, the temperature dependent current was extracted for various voltages above the valley voltage (Fig. 4.21a). As indicated by J_P, J_{ZENER} does not show significant temperature dependence indicating high purity BTBT. However, at progressively larger biases beyond V_V, the current density increases more rapidly. Eventually, the current would be dominated by thermal processes.

$$J_{Excess} = J_0 \times \exp\left(\frac{V_a}{nkT}\right) \tag{4.1}$$

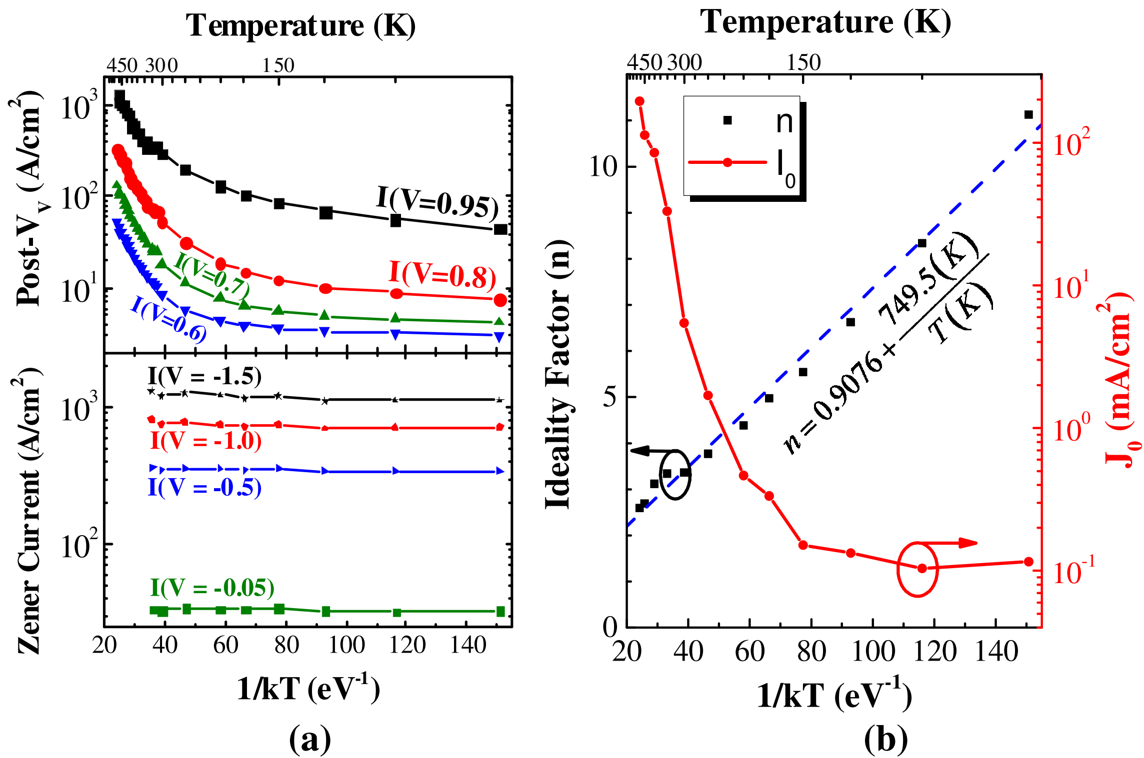

Fig. 4.21: Left (a) is measured current density versus temperature for various voltages. On the right (b) is extracted ideality factors and x-intercepts versus temperature.

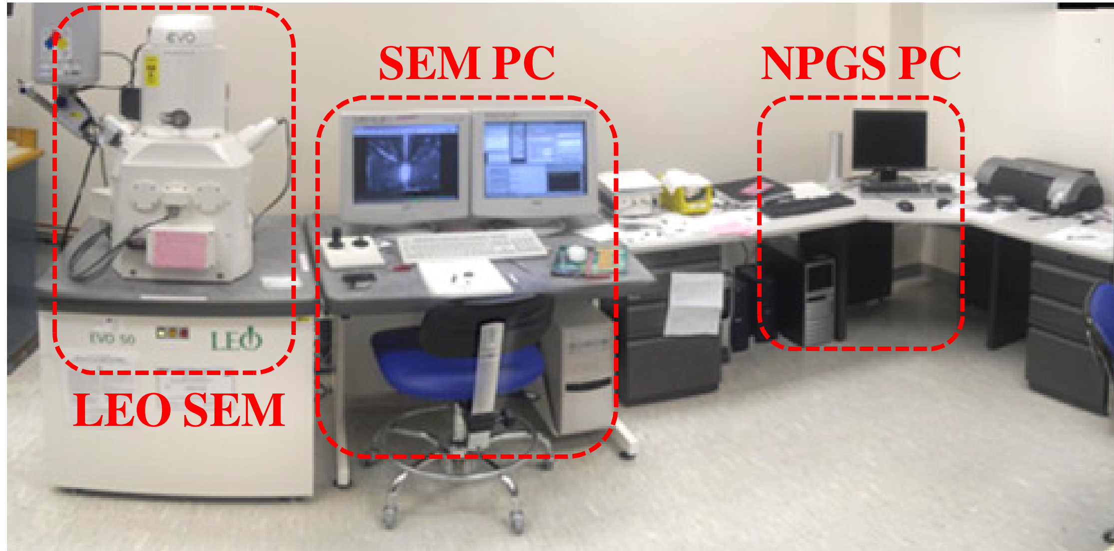

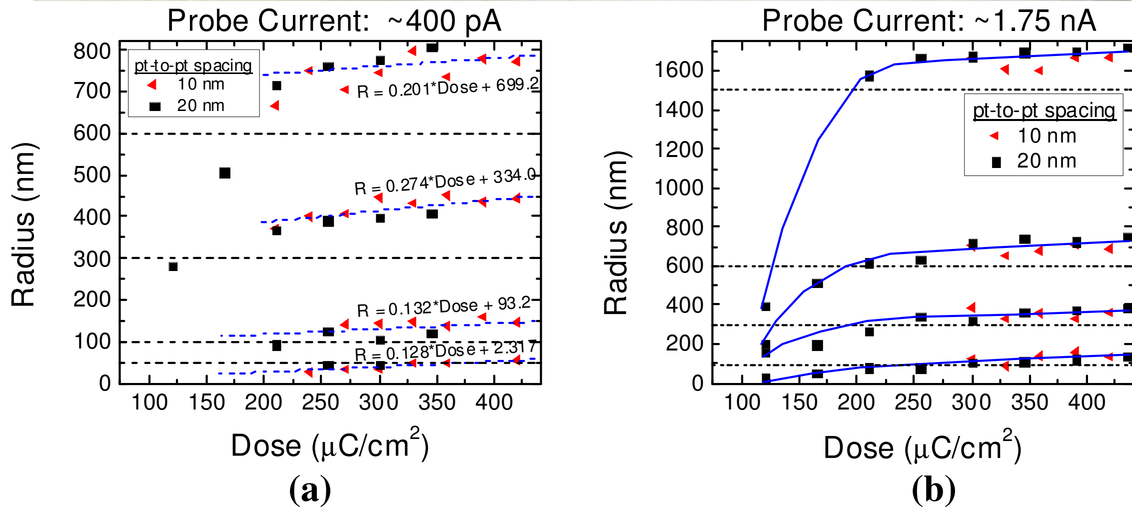

Fig. 4.22: The top picture of the Leo EVO 50 sample SEM and NPGS PC used for this work. On the bottom are measured feature size versus exposure dose for (a) low beam currents (~400 pA) and (b) large beam currents (~1.75 nA).

Using the standard excess current equation of a TD (4.1), ideality factors (n) and x-intercepts (J_0) were extracted and graphed in Fig. 4.21b. The ideality factor varies linearly from 2 to 12 via $n = 0.908+749.5/T$. Above ~150 K, the excess current mechanism is dominated by a series of thermal processes (e.g., thermionic hole and electron emission over the respective band offsets) which cannot be uniquely deconvolved from the present data. Furthermore, the data clearly reveals that the ART growth of the III-V diode on Si did not introduce mid-gap states as the data is consistent with prior reports of Si and GaAs Esaki diodes.

4.4.4. Deeply Scaled Tunnel Junctions

Up to this point, all of the TDs have been large with radii no smaller than 3 μm. It have already been shown that scaling the junction down have improved the characteristics. However, many have theorized that eventually sidewall leakage effects would begin to dominate the characteristics, and degrade performance. Additionaly, if tunnel junctions are to be used on commercial products, they will likely need to be scaled to similar dimensions as the transistor they are integrated with or replacing. To that end, the current fabrication process was expanded to fabricate and electrically test deeply scaled tunnel junctions.

The new fabrication process starts after the mesa isolation etch step from the original process. However, to achieve the ultra-small dimensions desired, electron beam (e-beam) lithography was developed and implemented for this work. To replace the standard PR, a positive e-beam resist (PMMA 950k) was used. A LEO Evo 50 sample SEM system (Fig. 4.22) was install with a Nano Pattern Generation System (NPGS), which controls the SEM in write mode and drives the e-beam to generate desired layout patterns. A series of test writes were initially performed in order to optimize the e-beam lithography process. The acceleration bias was held constant at 20 kV for all writes, a gold standard was used to tune the beam, and a faraday cup and pico-ammeter was used to measure probe currents. However, before tuning the beam, the system was warmed up for no less than 1 hour. After meticulously focusing onto the sample surface several exposure dose matrices were created, developed, and inspected. The first set used a low beam current (~400 pA) and looked at measured radii of 50nm, 100nm, 300nm, and 600nm versus exposure dose (Fig. 4.22a). The second set used a large beam current (~1.75 nA) for mask defined radii of 100nm, 300nm, 600nm, and 1500nm (Fig. 4.22). Each beam current used two different point-to-point spacing exposure settings; (i) 10 nm and (ii) 20 nm. There was no statistically significant difference between the two point-to-point settings, with the bulk of the noise in the data attributed to focus variations. Additionally, the rate in change of

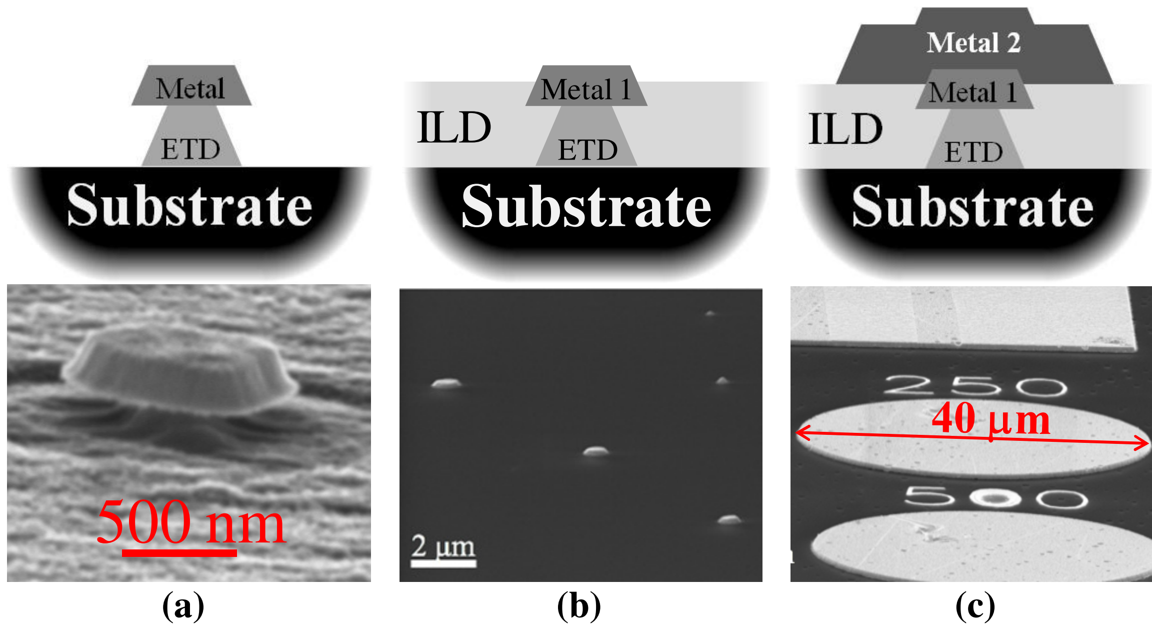

Fig. 4.23: Schematic diagram (top) and high angle SEM images (bottom) of the sub-micron fabrication process after (a) mesa isolation, (b) BCB planarization and etchback, and (c) metal 2 deposition and liftoff.

the measured radii leveled off at ~200 μC/cm^2, regardless of beam current. However, for added margin of error, typical exposure doses were set to 300 μC/cm^2.

As with the original fabrication process, metal 1 was used as the mesa isolation etch mask. Therefore, metal 1 was required to be scaled sub-micron dimensions so that the tunnel junction itself would achieve the desired size. One typical example is shown in Fig. 4.24a. However, it was not possible to directly probe the formed contact thus requiring a two metal layer process, with an inter-layer dielectric (ILD) in between.

After the mesa isolation etch, the sample was spin coated with bis-benzocyclobutene (BCB) which is a low-*K* spin on dielectric. The BCB was coated to a thickness of ~1.5 μm, encapsulating all features by more than 1 μm, and then baked at 140°C for five minute followed by a cure at 250°C for 60 min. in an N_2 ambient. The resultant sample surface was smooth and flat, with only gradual variations across the entire sample surface. To access the metal 1 contacts, the BCB was isotropically etched back using a 1:4 O_2:SF_6 dry plasma etch. Initialy, fast etches (high power) were used to get within a few 100 nm of the contact metal. Then, slow etches (low

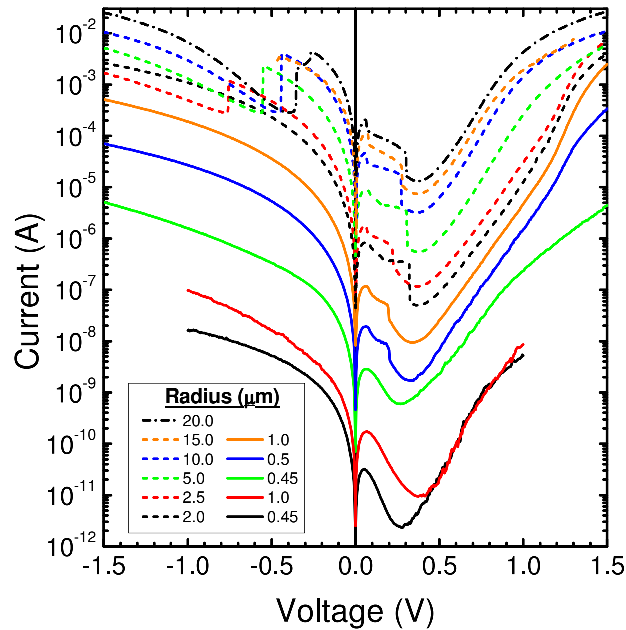

Fig. 4.24: Measured I-V characteristics of TD1 scaled to deep submicron dimensions. I_P ranged eight orders of magnitude, indicating a large range in device dimensions.

power) were used to precisely dial in the final BCB film thickness. Idealy, half of the contact metal thickness would be exposed, encapsulating the sample surface and tunnel junction within the insulative BCB (Fig. 4.24b). Finally, large (40 μm radii) probe pads were patterned and aligned to the metal 1 contact pads using a second e-beam lithography and metal deposition (Fig. 4.24c).

Electrical characterization proceeded using the Keithley 4200 parameter analyzer. Due to the very large area tunnel junction used as a virtual ground, NDR was measured in reverse bias for the larger tunnel junctions under test. Additionally, due to the aggressive nature of the mesa isolation etch, there is a large range in device dimension for each mask defined radii. Therefore, the measured I-V characteristics (Fig. 4.24) show I_P ranging eight orders of magnitude. Some of measured currents were much smaller than expected. The smallest I_P measured was 32 pA, which comes to a calculated radii of 16nm. This assumes that the 4 A/cm^2 J_P calculated from larger devices with known junction areas does not change over the wide range of currents.

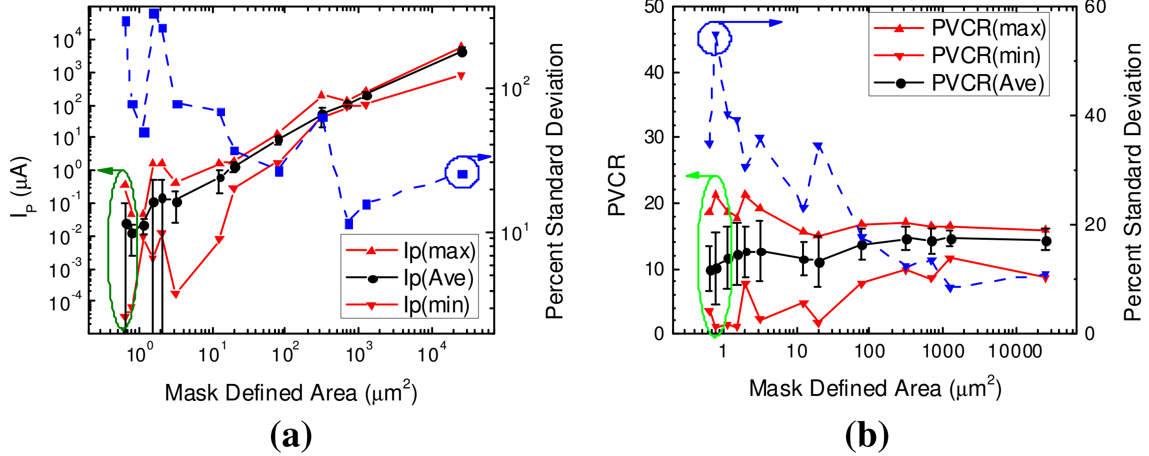

Fig. 4.25: Measured (a) I_P and (b) PVCR versus mask defined area for deep sub-micron scaled TD1 junctions. Due to noise in the actual junction areas, the maximum, average, minimum, and standard deviation of each size is shown.

Both I_P and PVCR were plotted versus mask defined area (Fig. 4.25) in order to quantify the scalability of the tunnel junctions. The average I_P trendline best represents how well the BTBT current scaled with area, and is mostly linear. The slope of the line yields a J_P of ~4 A/cm^2, slightly larger than previously estimated. The standard deviation in I_p increases as the junctions are scaled, which is due to variations in junctions areas being effected by lithography and mesa isolation etch deviations across the sample. In following studies, junction uncertainty is minimized by inspecting mesa undercuts and metal 1 dimensions with SEM imaging.

Contrary to previous studies, the average PVCR slightly degrades from 12 to 10 when the junctions are scaled, Fig. 4.25b. However, the maximum PVCR is a better measure of the ultimate capabilities achievable, and it shows a fairly steady improvement 16 to 21. The accumulated results from this study indicates that tunnel junctions can be scaled to ultra small dimension without significant degradation in performance. However, a robust fabrication process is needed in order to obtain consistent and reliable results. Furthermore, the development of the submicron process is critical for characterizing the ultra high BTBT current density ETDs discussed in Chapters 5 and 6.

4.5. Conclusions

Ge and GaAs semiconductor material systems were integrated on Si substrates via ART. Virtual substrates formed by ART have been shown to reduce TDD by over 1,000x, compared to direct epitaxial growth on Si substrates. However, those results do not confirm the electrical quality of the virtual substrates. As a new method for hetero-integration of high quality crystalline materials, a series ETD Structures were fabricated and electrically tested in

The first set of ETD devices utilized alloy junction formation. In a thermal anneal fabrication process, Al was alloyed with n^+-type Ge virtual substrates. Optimal annealing conditions were found to be 825°C for five minutes, resulting in a maximum PVCR of 1.1 and a J_P of 4.1 kA/cm^2. The results are commensurate with results on Ge substrates from literature [55, 64], and therefore indicate that the virtual substrates are of high quality.

Following the Ge ETD study, a series of five GaAs/$In_{1-x}Ga_xAs$ were grown on a GaAs-on-Ge ART virtual substrate. Two additional companion ETDs were grown directly on Si, with two more on a GaAs substrate for direct comparison of ideal and worst case results. A new fabrication process was developed for these structures, and serves as the foundation for all ETD structures afterwards. The optimal dopant activation anneal is 425°C for five minute anneal, and resulted in a maximum PVCR of 24 for TD1, which is just below the previous GaAs record of 25 for which this structure was designed after [13] and far beyond the on Si record of 6 [8].

The affect of a 4 nm *i*-layer was studied in TD1 and TD5, as well as direct growth on Si substrates with their companion pieces; TD1-Si and TD5-Si. There respective PVCRs were measured to be 24, 11, 3.9, and 4.4 respectively. The on ART devices had much large PVCR, adding more evidence to the high quality nature of the virtual substrates. Furthermore, TD1 (without *i*-layer) also had a large J_P than TD5 (with *i*-layer), for both the on ART and on Si substrate cases, indicating that the *i*-layer did not improve the ETD electrostatic properties.

The following study increased the In mole fraction to 20% (TD2) and surrounded the p-n junction entirely within a 10% InGaAs layer (TD3). The PVCR of these structures were greatly

improved to 34 and 36, respectively, surpassing the previous GaAs results. Interestingly, the control companion ETDs (TD2-GaAs and TD3-GaAs) exhibited much smaller PVCR of 8.7 and 9.9, respectively. It was determined from SIMS that there was a significant difference in the final device structure, which may have negatively impacted the PVCR, and certainly reduced the J_P for TD2-GaAs and TD3-GaAs. Interestingly, even though they had similar doping concentrations, TD2 had a large J_P than TD3 indicating that the increased In concentration improved BTBT efficiency. The introduction of a In concentration grading reduced PVCR to 10, but had a much larger J_P than TD1. In fact, TD2, TD3, and TD4 all had J_P much greater than predicted by Kane [60], when compared with characteristic homojunction trendlines calculated using the Kane model program discussed in Chapter 3. Finally, further testing revealed devices with PVCR of 43 and 56 for TD2 and TD3, respectively. The PVCR for TD3 is the third largest value reported in literature, strongly indicating that the ART virtual substrates are of very high quality.

High and low temperature (77 K up to 473 K) measurements was performed. J_P decreased slightly with temperature, indicating that it is an almost pure BTBT characteristics. J_V increased with temperature, at a slightly faster rate than J_P. An Arrhenius extraction of from the change in J_V with temperature yielded an activation energy of 1.8 meV, which is nearly negligible. Furthermore, the excess current exhibited a relatively small ideality factor of ~3.

The final study in this chapter developed a deep sub-micron fabrication process, based off of the basic fabrication process. The new process required the development and characterization of an e-beam lithography process, enabling the fabrication of devices down to 50 nm radii. With the new process, TD3 was scaled down to deep submicron dimensions in order to investigate the scaling properties of ETD structures. The average I_P versus junction area was linear, indicating negligible surface leakage currents. Furthermore, in this study the maximum PVCR increased from 16 to 21 as the junctions were scaled. The improvement in PVCR is largely due to improved (smaller) J_V, showing that the substrate is very high quality, but not perfect.

In general, the results from this chapter show that ART can be used to provide high quality virtual substrates on Si, without the need for large graded buffers or substrate transfer processes. Furthermore, defect related leakage currents were not directly observed in the high PVCR ETD structures, indicating that ART provides mechanically and electrically high quality virtual substrates. This conclusion is largely supported by the record high PVCR values achieved, and the small observed variations with temperature. Additionally, the deeply scaled ETD junctions showed no significant signs of surface leakage effects, and actually exhibited improved PVCR.

References for Chapter 4

[1] D. Pawlik, S. Sieg, S. K. Kurinec, S. L. Rommel, Z. Cheng, J. S. Park*, et al.*, "Alloyed Junction Ge Esaki Diodes on Si Substrates Realised by Aspect Ratio Trapping Technique," *Electron. Lett.,* vol. 44, pp. 930-932, Jul 2008.

[2] S. L. Rommel, D. Pawlik, P. Thomas, M. Barth, K. Johnson, S. K. Kurinec*, et al.*, "Record PVCR GaAs-based Tunnel Diodes Fabricated on Si Substrates using Aspect Ratio Trapping," *IEDM Tech. Digest,* pp. 739-742, 2008.

[3] D. J. Pawlik, P. Thomas, M. Barth, K. Johnson, S. L. Rommel, S. Mookerjea*, et al.*, "Indium Gallium Arsenide on Silicon Interband Tunnel Diodes for NDR-based Memory and Steep Subthreshold Slope Transistor Applications," in *Dev. Res. Conf.*, 2009, pp. 69-70.

[4] D. J. Pawlik, B. Romanczyk, E. Freeman, P. M. Thomas, M. Barth, S. L. Rommel*, et al.*, "Sub-micron Esaki Tunnel Diode Fabrication and Characterization," in *Int. Semicond. Dev. Res. Symp.*, 2009, pp. 1-2.

[5] V. M. Franks, K. F. Hulme, and J. R. Morgan, "An alloy process for making high current density silicon tunnel diode junctions," *Solid-State Electronics,* vol. 8, pp. 343-344, 1965.

[6] K. Ismail, B. S. Meyerson, and P. J. Wang, "Electron resonant tunneling in Si/SiGe double barrier diodes," *Applied Physics Letters,* vol. 59, p. 973, 08/19/ 1991.

[7] S. L. Rommel, T. E. Dillon, M. W. Dashiell, H. Feng, J. Kolodzey, P. R. Berger*, et al.*, "Room temperature operation of epitaxially grown Si/Si0.5Ge0.5/Si resonant interband tunneling diodes," *Applied Physics Letters,* vol. 73, pp. 2191-2193, 10/12/ 1998.

[8] K. Eberl, R. Duschl, O. G. Schmidt, U. Denker, and R. Haug, "Si-based resonant inter- and intraband tunneling diodes," *Journal of Crystal Growth,* vol. 227, pp. 770-776, Jul 2001.

[9] P. See, D. J. Paul, B. Hollander, S. Mantl, I. V. Zozoulenko, and K. F. Berggren, "High performance Si/Si1-Ge-x(x) resonant tunneling diodes," *IEEE Electron Device Letters,* vol. 22, pp. 182-184, Apr 2001.

[10] J. L. Wang, D. Wheeler, Y. Yan, J. L. Zhao, S. Howard, and A. Seabaugh, "Silicon tunnel diodes formed by proximity rapid thermal diffusion," *IEEE Electron Device Letters,* vol. 24, pp. 93-95, Feb 2003.

[11] S. Y. Chung, R. H. Yu, N. Jin, S. Y. Park, P. R. Berger, and P. E. Thompson, "Si/SiGe Resonant Interband Tunnel Diode With f(r0) 20.2 GHz and Peak Current Density 218

kA/cm(2) for K-band Mixed-Signal Applications," *IEEE Electron Device Lett.,* vol. 27, pp. 364-367, May 2006.
[12] N. Holonyak and I. A. Lesk, "Gallium-Arsenide Tunnel Diodes," *Proc. IRE,* vol. 48, pp. 1405-1409, 1960.
[13] T. A. Richard, E. I. Chen, A. R. Sugg, G. E. Hofler, and N. Holonyak, "High-Current Density Carbon-Doped Strained-Layer GaAs (P+)-InGaAs(N+)-GaAs(N+) P-N Tunnel-Diodes," *Appl. Phys. Lett.,* vol. 63, pp. 3613-3615, Dec 1993.
[14] T. P. E. Broekaert and C. G. Fonstad, "Extremely High Current Density, Low Peak Voltage, Pseudomorphic In 0.53Ga0.47As/AlAs/InAs Resonant Tunneling Diodes," 1989, pp. 559-562.
[15] D. J. Day, R. Q. Yang, L. Jian, and J. M. Xu, "Experimental demonstration of resonant interband tunnel diode with room temperature peak-to-valley current ratio over 100," *Journal of Applied Physics,* vol. 73, pp. 1542-4, 02/01 1993.
[16] J. H. Smet, T. P. E. Broekaert, and C. G. Fonstad, "Peak-to-valley current ratios as high as 50:1 at room temperature in pseudomorphic In0.53Ga0.47As/AlAs/InAs resonant tunneling diodes," *Journal of Applied Physics,* vol. 71, p. 2475, 03/01/ 1992.
[17] H. H. Tsai, Y. K. Su, H. H. Lin, R. L. Wang, and T. L. Lee, "P-N DOUBLE-QUANTUM-WELL RESONANT INTERBAND TUNNELING DIODE WITH PEAK-TO-VALLEY CURRENT RATIO OF 144 AT ROOM-TEMPERATURE," *IEEE Electron Device Letters,* vol. 15, pp. 357-359, Sep 1994.
[18] G. M. Cohen, D. Ritter, and C. Cytermann, "High peak tunnel current density Ga0.47In0.53As Esaki diodes," *Electronics Letters,* vol. 31, pp. 1511-1512, 1995.
[19] S. E. Thompson, R. S. Chau, T. Ghani, K. Mistry, S. Tyagi, and M. T. Bohr, "In Search of "Forever," Continued Transistor Scaling One New Material at a Time," *IEEE Trans. Semicond. Manuf.,* vol. 18, pp. 26-36, Feb 2005.
[20] J. Appenzeller, Y. M. Lin, J. Knoch, and P. Avouris, "Band-to-Band Tunneling in Carbon Nanotube Field-Effect Transistors," *Phys. Rev. Lett.,* vol. 93, pp. 196805-1-196805-4, 2004.
[21] T. Krishnamohan, D. Kim, S. Raghunathan, K. Saraswat, and Ieee, "Double-Gate Strained-Ge Heterostructure Tunneling FET (TFET) With Record High Drive Currents and < 60mV/dec Subthreshold Slope," in *IEEE IEDM Tech. Dig.*, ed, 2008, pp. 947-949.
[22] W.-Y. Loh, K. Jeon, C. Y. Kang, J. Oh, P. Patel, C. Smith*, et al.*, "Sub-60nm Si Tunnel Field Effect Transistors With Ion 100 mA/um," in *Proc. European Solid State Dev. Res. Conf.*, 2010, pp. 162-165.
[23] S. Mookerjea, D. Mohata, R. Krishnan, J. Singh, A. Vallett, A. Ali*, et al.*, "Experimental Demonstration of 100nm Channel Length In0.53Ga0.47As-Based Vertical Inter-band Tunnel Field Effect Transistors (TFETs) for Ultra Low-Power Logic and SRAM Applications," in *IEDM Tech. Dig.*, 2009, pp. 949-951.
[24] D. K. Mohata, R. Bijesh, S. Mujumdar, C. Eaton, R. Engel-Herbert, T. Mayer*, et al.*, "Demonstration of MOSFET-like on-current performance in arsenide/antimonide tunnel FETs with staggered hetero-junctions for 300mV logic applications," in *2011 IEDM Tech. Digest*, Piscataway, NJ, USA, 2011, pp. 33-5.
[25] G. Dewey, B. Chu-Kung, J. Boardman, J. M. Fastenau, J. Kavalieros, R. Kotlyar*, et al.*, "Fabrication, characterization, and physics of III-V heterojunction tunneling Field Effect Transistors (H-TFET) for steep sub-threshold swing," in *2011 IEEE International Electron Devices Meeting (IEDM 2011), 5-7 Dec. 2011*, Piscataway, NJ, USA, 2011, pp. 33-6.
[26] J. Welser, J. L. Hoyt, and J. F. Gibbons, "NMOS and PMOS Transistors Fabricated in Strained Silicon/Relaxed Silicon-Germanium Structures," in *IEEE IEDM*, 1992, pp. 1000-1002.

[27] J. Welser, J. L. Hoyt, and J. F. Gibbons, "Electron Mobility Enhancement in Strained-Si N-type Metal-Oxide-Semiconductor Field-Effect Transistors," *IEEE Electron Device Lett.,* vol. 15, pp. 100-102, 1994.

[28] J. Welser, J. L. Hoyt, S. Takagi, and J. F. Gibbons, "Strain Dependence of the Performance Enhancement in Strained-Si n-MOSFETs," in *IEEE IEDM*, 1994, pp. 373-376.

[29] D. K. Nayak, J. C. S. Woo, J. S. Park, K. L. Wang, and K. P. MacWilliams, "High-Mobility P-Channel Metal-Oxide-Semiconductor Field-Effect-Transistor on Strained Si," *Jap. J. Appl. Phys.,* vol. 33, pp. 2412-2414, 1994.

[30] X. Huang, W.-C. Lee, C. Kuo, D. Hisamoto, L. Chang, J. Kedzierski*, et al.*, "Sub 50-nm FinFET: PMOS," in *IEEE IEDM*, 1999, pp. 67-70.

[31] T. Numata, T. Irisawa, T. Tezuka, J. Koga, N. Hirashita, K. Usuda*, et al.*, "Performance Enhancement of Partially- and Fully-Depleted Strained-SOI MOSFETs and Characterization of Strained-Si Device Parameters," in *IEEE IEDM*, 2005, pp. 177-180.

[32] Y.-M. Lin, J. Appenzeller, Z. Chen, Z.-G. Chen, H.-M. Cheng, and P. Avouris, "High-Performance Dual-Gate Carbon Nanotube FETs With 40-nm Gate Length," *IEEE Electron Device Lett.,* vol. 26, pp. 823-825, 2005.

[33] K. Seyoung, N. Junghyo, J. Insun, D. Shahrjerdi, L. Colombo, Y. Zhen*, et al.*, "Realization of a High Mobility Dual-Gated Graphene Field-Effect Transistor With Al2O3 Dielectric," *Appl. Phys. Lette.,* vol. 94, p. 062107, 02/09 2009.

[34] M. Heyns, A. Alian, G. Brammertz, M. Caymax, Y. C. Chang, L. K. Chu*, et al.*, "Advancing CMOS Beyond the Si Roadmap With Ge and III/V Devices," in *IEEE IEDM*, 2011, pp. 13.1.1-13.1.4.

[35] S. Ting, M. Bulsara, V. Yang, M. Groenert, S. Samavedam, M. Currie*, et al.*, "Monolithic Integration of III-V Materials and Devices on Silicon," in *Silicon-based Optoelectronics*, 1999, pp. 19-28.

[36] M. E. Groenert, "Monolithic Heteroepitaxial Integration of III-V Semiconductor Lasers on Si Substrates," Ph.D., Materials Science and Engineering, Mass. Inst. of Tech., Mass. Inst. of Tech., 2002.

[37] M. E. Groenert, A. J. Pitera, R. J. Ram, and E. A. Fitzgerald, "Improved Room-Temperature Continuous Wave GaAs/AlGaAs and InGaAs/GaAs/AlGaAs Lasers Fabricated on Si Substrates Via Relaxed Graded GexSi1-x Buffer Layers," *J. Vac. Sci.,* vol. 21, pp. 1064-1079, 05/ 2003.

[38] C. Peng, J. Yi, S. S. Lau, X. Dapeng, L. Mawst, T. L. Alford*, et al.*, "High Crystalline-Quality III-V Layer Transfer onto Si Substrate," *App. Phys. Lett.,* vol. 92, pp. 092107-1, 03/03 2008.

[39] T. D. Chen, S. M. Spaziani, K. Vaccaro, J. P. Lorenzo, and N. M. Jokerst, "Epilayer Transfer for Integration of III-V Photodetectors onto a Silicon Platform Using Au-Sn and Pd-Ge Bonding," in *Int. Conf. Indium Phosphide and Related Materials*, 2000, pp. 502-505.

[40] T. Yu-Li, W. Chih-Hung, H. Jei-Li, and L. Chun-Ming, "Transfer of GaAs-Based Solar Cells onto Molybdenum and Silicon Substrates," in *Int. Conf. Concentrating Photovolt. Sys.*, 2012, pp. 61-64.

[41] J. S. Park, J. Bai, M. Curtin, B. Adekore, Z. Cheng, M. Carroll*, et al.*, "Defect Reduction and its Mechanism of Selective Ge Epitaxy in Trenches on Si(001) Substrates Using Aspect Ratio Trapping," in *Semicond. Defect Engineering - Mat., Synthetic Structures and Devices II*, 2007, pp. 315-320.

[42] J. Z. Li, J. Bai, J. S. Park, B. Adekore, K. Fox, M. Carroll*, et al.*, "Defect Reduction of GaAs Epitaxy on Si (001) Using Selective Aspect Ratio Trapping," *Appl. Phys. Lett.,* vol. 91, pp. 021114-021114, 2007.

[43] J. S. Park, J. Bai, M. Curtin, B. Adekore, M. Carroll, and A. Lochtefeld, "Defect Reduction of Selective Ge Epitaxy in Trenches on Si(001) Substrates Using Aspect Ratio Trapping," *Appl. Phys. Lett.,* vol. 90, p. 052113, 2007.

[44] J. Bai, J. S. Park, Z. Cheng, M. Curtin, B. Adekore, M. Carroll*, et al.*, "Study of the Defect Elimination Mechanisms in Aspect Ratio Trapping Ge Growth," *Appl. Phys. Lett.,* vol. 90, p. 101902, 2007.

[45] J. Z. Li, J. Bai, J. M. Hydrick, J. G. Fiorenza, C. Major, M. Carroll*, et al.*, "Thin Film InP Epitaxy on Si (001) Using Selective Aspect Ratio Trapping," in *ISTC/CSTIC 2009*, 2009, pp. 887-894.

[46] R. S. Claassen, "Excess and Hump Current in Esaki Diodes," *J. Appl. Phys.,* vol. 32, p. 2372, 1961.

[47] C. B. Pierce, H. H. Sander, and A. D. Kantz, "Radiation Induced Hump Structure in I-V Characteristics of Esaki Diodes," *J. of Appl. Phys.,* vol. 33, pp. 3108-3118, 1962.

[48] R. Swami and B. A. P. Tantry, "Excess Current in Tunnel Diodes in Presence of Lattice Defects," *Indian J. Pure Appl. Phys.,* vol. 7, pp. 556-558, 08/ 1969.

[49] A. M. Andrews, H. W. Korb, N. Holonyak, Jr., C. B. Duke, and G. C. Kleiman, "Photosensitive Impurity-Assisted Tunneling in Au-Ge-Doped Ga1-xAlxAs p-n Diodes," *Phys. Rev. B (Solid State),* vol. 5, pp. 4191-4194, 05/15 1972.

[50] Z. M. Alekseeva, V. N. Brudnyi, M. A. Krivov, and N. P. Krivorotov, "Effect of Intrinsic Lattice Defects on Excess Currents of Gallium Arsenide Tunnel Diodes," *Soviet Phys. J.,* vol. 19, pp. 1174-1177, 1976.

[51] Z. M. Alekseeva, V. N. Brudnyi, M. A. Krivov, and N. P. Krivorotov, "Influence of Intrinsic Lattice Defects on the Excess Currents in Gallium Arsenide Tunnel Diodes," *Soviet Phys. J.,* pp. 88-92, / 1976.

[52] K. Nauka, G. A. Reid, and Z. Liliental-Weber, "Electron Beam Induced Current and Cathodoluminescence Imaging of the Antiphase Domain Boundaries in GaAs Grown on Si," *Appl. Phys. Lett.,* vol. 56, pp. 376-378, 01/22 1990.

[53] M. Kawabe and T. Ueda, "Self-Annihilation of Antiphase Boundary in GaAs on Si(100) Grown by Molecular Beam Epitaxy," *Jap. J. Appl. Phys.,* vol. 26, pp. l944-l946, 1987.

[54] S. M. Ting and E. A. Fitzgerald, "Metal-Organic Chemical Vapor Deposition of Single Domain GaAs on Ge/GexSi1-x/Si and Ge Substrates," *J. Appl. Phys.,* vol. 87, pp. 2618-2618, 2000.

[55] J. Zhao, A. C. Seabaugh, and T. H. Kosel, "Rapid melt growth of germanium tunnel junctions," *Journal of the Electrochemical Society,* vol. 154, pp. 536-539, 2007.

[56] C. Chi On, K. Gopalakrishnan, P. B. Griffin, J. D. Plummer, and K. C. Saraswat, "Activation and diffusion studies of ion-implanted p and n dopants in germanium," *Applied Physics Letters,* vol. 83, p. 3275, 10/20/ 2003.

[57] R. E. Davis and G. Gibbons, "Design principles and construction of planar Ge Esaki diodes," *Solid-State Electronics,* vol. 10, pp. 461-466, 1967.

[58] D. Meyerhofer, G. A. Brown, and H. S. Sommers, "Degenerate Germanium. I. Tunnel, Excess, and Thermal Current in Tunnel Diodes," *Physical Review,* vol. 126, p. 1329, 1962.

[59] A. G. Chynoweth, R. A. Logan, and D. E. Thomas, "Phonon-Assisted Tunneling in Silicon and Germanium Esaki Junctions," *Physical Review,* vol. 125, p. 877, 1962.

[60] E. O. Kane, "Theory of Tunneling," *J. Appl. Phys.,* vol. 32, p. 83, 1961.

[61] A. M. Andrews, H. W. Korb, N. Holonyak, C. B. Duke, and G. G. Kleiman, "Tunnel Mechanisms and Junction Characterization in III-V Tunnel Diodes," *Physical Review B,* vol. 5, p. 2273, 1972.

[62] N. Holonyak, I. A. Lesk, R. N. Hall, J. J. Tiemann, and H. Ehrenreich, "Direct Observation of Phonons During Tunneling in Narrow Junction Diodes," *Physical Review Letters,* vol. 3, p. 167, 1959.

[63] D. J. Pawlik, S. Sudirgo, S. K. Kurinec, P. E. Thompson, P. R. Berger, and S. L. Rommel, "High Temperature Characterization of Si/SiGe Resonant Interband Tunnel Diodes," in *Int. Semicond. Dev. Res. Symp.*, 2005, pp. 153-154.

[64] Z. Qin, S. Sutar, T. Kosel, and A. Seabaugh, "Rapid melt growth of Ge tunnel junctions for interband tunnel transistors," Piscataway, NJ, USA, 2007, pp. 485-6.

CHAPTER 5

$In_{0.53}Ga_{0.47}As$ Esaki Tunnel Diodes

The previous chapter established that high quality virtual substrates can be integrated on Si via ART. Furthermore, the electrostatic qualities of the virtual substrates were verified with high PVCR GaAs/InGaAs ETDs [1-4] and directly benchmarked against a wide variety of ETDs from literature [5-18]. Because of the limited availability of ART virtual substrates, the following work will investigate $In_{0.53}Ga_{0.47}As$ ETDs [18-24], which were fabricated on lattice matched substrates (InP). Additionally, ETDs will be designed and grown as homojunctions to avoid the confounding effects of strain, heterojunction band alignments, and multiple effective masses. Standardizing ETD structures to a basic p^+-*i*-n^- diode with fixed layer thicknesses and nominally rectangular doping profiles enables direct mapping and modeling of BTBT behavior over a large design space. This methodology may then be used to design structures with targeted characteristics, such as maximizing BTBT current density (tunneling probability). In particular, this work is geared towards optimizing the Source/Body junction of a TFET for improved on-state current density. Therefore, it is important to learn how to maximize BTBT probabilities and current densities.

Additionally, device characteristics from ETDs based off of the standard layer structure are ideal for calibrating BTBT models, including the Kane model [25] discussed in Chapter 3. Typically, BTBT models are calibrated to no more than a couple specific devices covering a limited range device designs. Also, the models often use of various fitting parameters, which may change in a nonphysical way from structure to structure. However, with the guidelines and methods developed in this work, BTBT characteristics can be efficiently investigated over a large design space. The results of which will then be available for model calibrations, adding higher confidence to the quantitative predictions made by those same models.

In this chapter, $In_{0.53}Ga_{0.47}As$ homojunction ETDs will be grown on lattice matched InP substrates. $In_{0.53}Ga_{0.47}As$ was chosen for a multitude of reasons. (1) It is a direct bandgap semiconductor with very well known material parameters. (2) It has a small effective electron mass and moderate bandgap (~0.74 eV) which may allow it to achieve very large BTBT current densities while suppressing unwanted excess tunnel currents. Additionally, (3) there are many sources for $In_{0.53}Ga_{0.47}As$ epitaxy, with a large knowledge set and experience in growing very high quality layers with ultra-high doping concentrations ($\sim 10^{20}$ /cm^3) and sharp doping profiles. As such, $In_{0.53}Ga_{0.47}As$ is an ideal starting material system to (i) develop the initial experimental procedure, (ii) characterize a large design space using doping concentrations as the control variable, (iii) optimize and achieve greater BTBT current densities, and (iv) apply the Kane model for the entire experiment.

Additionally, there has been much discussion over the scalability of BTBT junctions. There are two main concerns. First, it is not known if surface leakage effects will increase and begin to dominate device characteristics the tunnel junctions are scaled to smaller dimensions. In an ETD, this would be seen as an increase in J_V and decrease in PVCR. If Fermi-level pinning is involved, J_P may also be affected. In a TFET, I_{Off} would increase and the gate would lose electrostatic control. The second concern is carrier quantization effects. A reduction in the standard 3D DOS when confined to 2D or 1D may substantially reduce, or alter, BTBT current densities.

Specifically in this chapter, fabrication and characterization of six distinct $In_{0.53}Ga_{0.47}As$ ETD structures is discussed. The low to medium J_P structures only required the standard fabrication process. However, two ultra-high J_P ETDs utilize an improved deep sub-micron process. As such, the scaling properties of $In_{0.53}Ga_{0.47}As$ BTBT are investigated on structures most appropriate for TFETs. Combining these results from other experimental results in literature [18-24], a characteristic trendline for $In_{0.53}Ga_{0.47}As$ ETDs is established, which relates J_P to doping concentration. Additionally, the Kane model is compared to each devices structure,

and the $In_{0.53}Ga_{0.47}As$ characteristic trendline. Ideal band diagrams are also examined for an improved understanding in the theory of operation for the ETD devices.

5.1. Ultra High Current Density $In_{0.53}Ga_{0.47}As$ Esaki Diodes

As before, the ETDs were designed with the p-type layer on top of the n-type layer. In order to improve the doping profiles a thin 3 nm intrinsic layer (*i*-layer) was inserted in the middle of the structure, forming a p-*i*-n diode (Fig. 5.1a). This spacer layer separates the two doping profiles, minimizing doping compensation at the metallurgical junction, thereby maximizing the effectiveness of N_A and N_D. Recall from Section 4.3 that the maximum compensated carrier concentrations adjacent to the tunnel junction was reduced by up to 30%. Additionally, the doping profiles at the p-n junction will be much shaper. The improved doping profiles and concentrations improve electrostatic characteristics of the ETD in two main ways. First, the improved non-compensated doping help increase the built-in voltage (V_{bi}) and decrease depletion widths. Unless the *i*-layer is too thick (typically ~3 nm in this work), the overall depletion width will be reduced, thereby increasing the BTBT current density. Second, there will be much fewer compensated, ionized, dopants near the tunnel junction providing additional

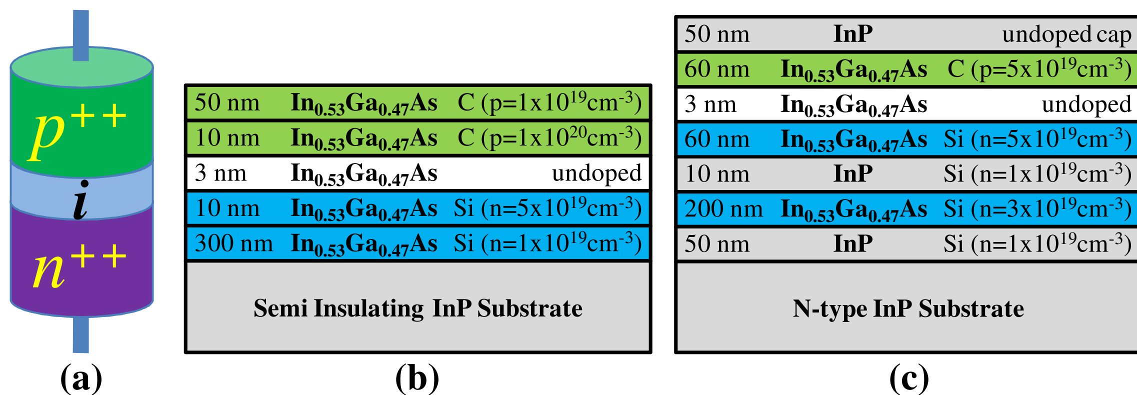

Fig. 5.1: Schematic diagrams of (a) basic p-*i*-n TD, (b) InGaAs-1, and (c) InGaAs-2. InGaAs-1 & -2 have same basic structure (p-i-n). To avoid growth defects for InGaAs-1 the maximum doping levels were kept within 10 nm of the junction. On InGaAs-2, a sacrificial InP capping layer protects the anode surface, and additional InP layers in the cathode act as etch stops.

recombination and scattering sites within the bandgap. With fewer defects in the tunnel junction, the excess current will be reduced, improving the ETD's PVCR. Achieving similar doping profile improvements in a TFET would enhance gate control, thereby improving I_{ON} and SS.

The highest doped sample, InGaAs-1 described in Fig. 5.1b, is expected to have the largest J_P. The structure was commercially grown at IQE using MBE, with C and Si as the p- and n-type dopants, respectively. The target doping concentrations for the tunnel junction itself was 10^{20} /cm^3 (C) and 5×10^{19} /cm^3 (Si). However, to avoid negatively impacting the quality of the epitaxy, those doping concentrations were limited to two separate 10 nm layers surrounding the *i*-layer. These three layers are approximately 23 nm thick and easily contain the predicted ~11 nm depletion width (see Section 5.1.2), and therefore should not impact J_P. The top anode (p-layer) was kept thin (~60 nm) in order to help reduce parasitic series resistances (R_{Series}) and minimize undercut during mesa isolation etch for improved control over junction areas. Conversely, a thick (300 nm) cathode layer (n-type) was grown to help minimize R_{Series}. This was especially important since the structure was grown on a semi insulating (S.I.) InP substrate.

The second sample, InGaAs-2 illustrated in Fig. 5.1c, was grown by metal-organic MBE at Technion, Israel Institute of Technology, by Prof. D. Ritter [23]. The maximum achievable doping for the ETD was slightly less InGaAs-1. Therefore, the target C (5×10^{19} /cm^3) and Si (5×10^{19} /cm^3) concentrations were not limited to two small 10 nm layers. This helped to simplify the p-*i*-n junction and reduce R_{Series}. Additional measures to minimize R_P include an n-type substrate and a 200 nm thick $In_{0.53}Ga_{0.47}As$ layer below the cathode. Three additional InP layers were included in the layer designed. The growth began with a doped InP layer in order to improve the quality of the following epitixay layers. The second InP layer is placed as an etch stop, to help prevent over etching the ETDs. Finally, the top InP layer is a sacrificial cap which protects the anode surface during storage and is to be removed at the start of fabrication.

SIMS measurements were taken on both InGaAs-1 and InGaAs-2 for accurate assessment of the doping profile slope and maximum concentrations. Contrary to the targets, the C doping concentrations were comparable in magnitude at 9.8×10^{19} /cm^3 (InGaAs-1) and 8.6×10^{19} /cm^3 (InGaAs-2). Whereas the Si measured in InGaAs-1 was much larger than in InGaAs-2, at 7.4×10^{19} /cm^3 and 4.5×10^{19} /cm^3, respectively. From the SIMS data, it is also plain that InGaAs-1 has a much sharper doping profile than InGaAs-2, with C/Si slopes of 5.7/2.3 nm/dec and 8.1/15.4 nm/dec, respectively. Given the doping concentrations and junction profiles (to a lesser extent), InGaAs-1 should have a much greater J_P.

Because of the expected magnitude of current densities, and to continue studying the effect of scaling tunnel junction, InGaAs-1 and InGaAs-2 were fabricated using the deep submicron process discussed in Section 4.3.4. However, there were a few minor alterations made to the process. First, no dopant activation anneal was performed since they are rarely needed for MBE grown epitaxy. Therefore, processing began with a simple surface clean (10 seconds in a

	InGaAs-1	**InGaAs-2**
	Doping	
	cm^{-3}	**cm^{-3}**
C	9.8×10^{19}	8.6×10^{19}
Si	7.4×10^{19}	4.5×10^{19}
N*	4.2×10^{19}	3.0×10^{19}
	Slope	
	nm/dec.	**nm/dec.**
C	5.7	8.1
Si	2.3	15.4

(a)

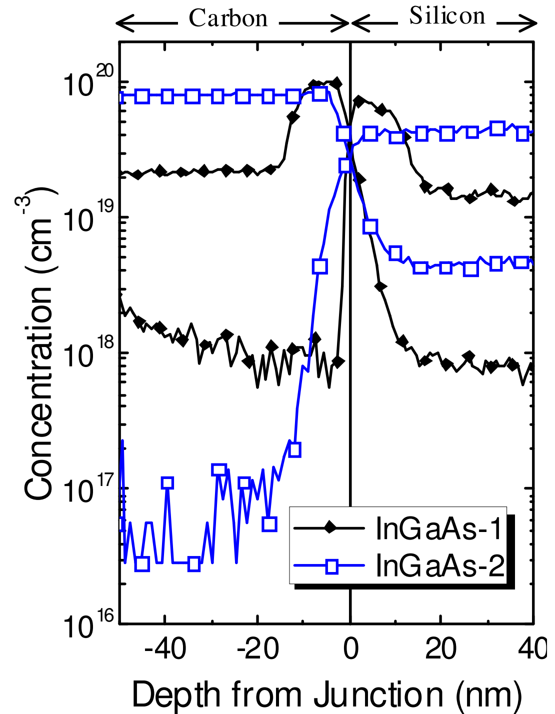

(b)

Fig. 5.2: (a) Maximum doping concentrations and profile slopes acquired from (b) SIMS measurements of InGaAs-1 and InGaAs-2.

10:1, HCl:H_2O mixture), followed by lithography level 1. However, InGaAs-2 first requires an InP cap etch in HCl:H_2O (1:1) for 60 seconds. Second, the mesa isolation etch used a citric Acid:H_2O:H_2O_2 acid bath, which is much slower (~1nm/minute) and more controllable. The acid bath itself is mixed in two steps. First, the citric acid:H_2O is mixed 1:1 by weight until the anhydrous citric acid crystals are fully dissolved, and the solution is back to room temperature. Then, immediately before needed, the citric acid/water solution is mixed with H_2O_2 at a 20:1 ratio by volume. This etch is also highly selective against InP.

The final alteration to the process is a tunnel junction area characterization step for improved accuracy when calculating current density. This step also utilized the LEO EVO 50 sample SEM. First, device cross-sections were analyzed with the sample tilted at least to ~87^0 (Fig. 5.3), thus negating the need to destructively cleave the sample. As is usually the case when chemically etching compound semiconductors, there are different etch profiles depending on the cross-section angle. For the case shown here (Fig. 5.3a), a vertical cut-line shows a cross-section with angled sidewalls (Fig. 5.3b). On the other hand, when looking at a horizontal cut-line, the cross-section the mesa sidewalls are nearly vertical (Fig. 5.3c). The mesa undercut values are taken from the bottom edge of the metal contact, to the mesa tunnel junction edge, located ~60 nm below the bottom of the metal. Using about a dozen measurements, average undercut

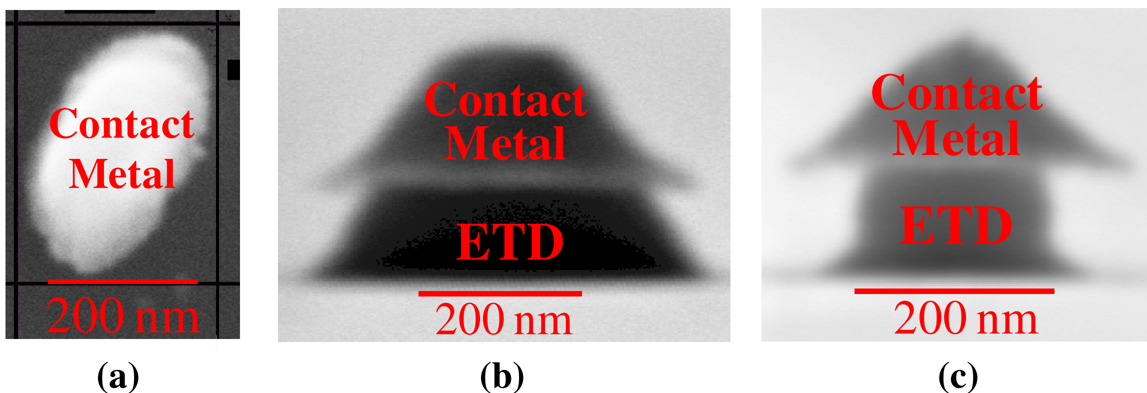

Fig. 5.3: SEM images of ETD after mesa isolation from a (a) top-down, (b) vertical cross-section, and (c) horizontal cross-section view points. Undercut values measured from bottom of contact metal to edge of mesa, 60 nm below contact metal (location of the metallurgical junction.

values are calculated for both the horizontal and vertical cutline cross-sections. The undercut values are used to adjust the measured metal contact radii, which require a much more extensive analysis.

Due to process variations (such as drifting beam focus and beam current), each pattern size may have a large variation in printed dimensions across the sample surface. Therefore, the top down areas of each metal contact (below ~2 μm radii) was measured in at least six different locations. With ~16 device sizes, this required at least ~100 images. An ImageJ macro (See

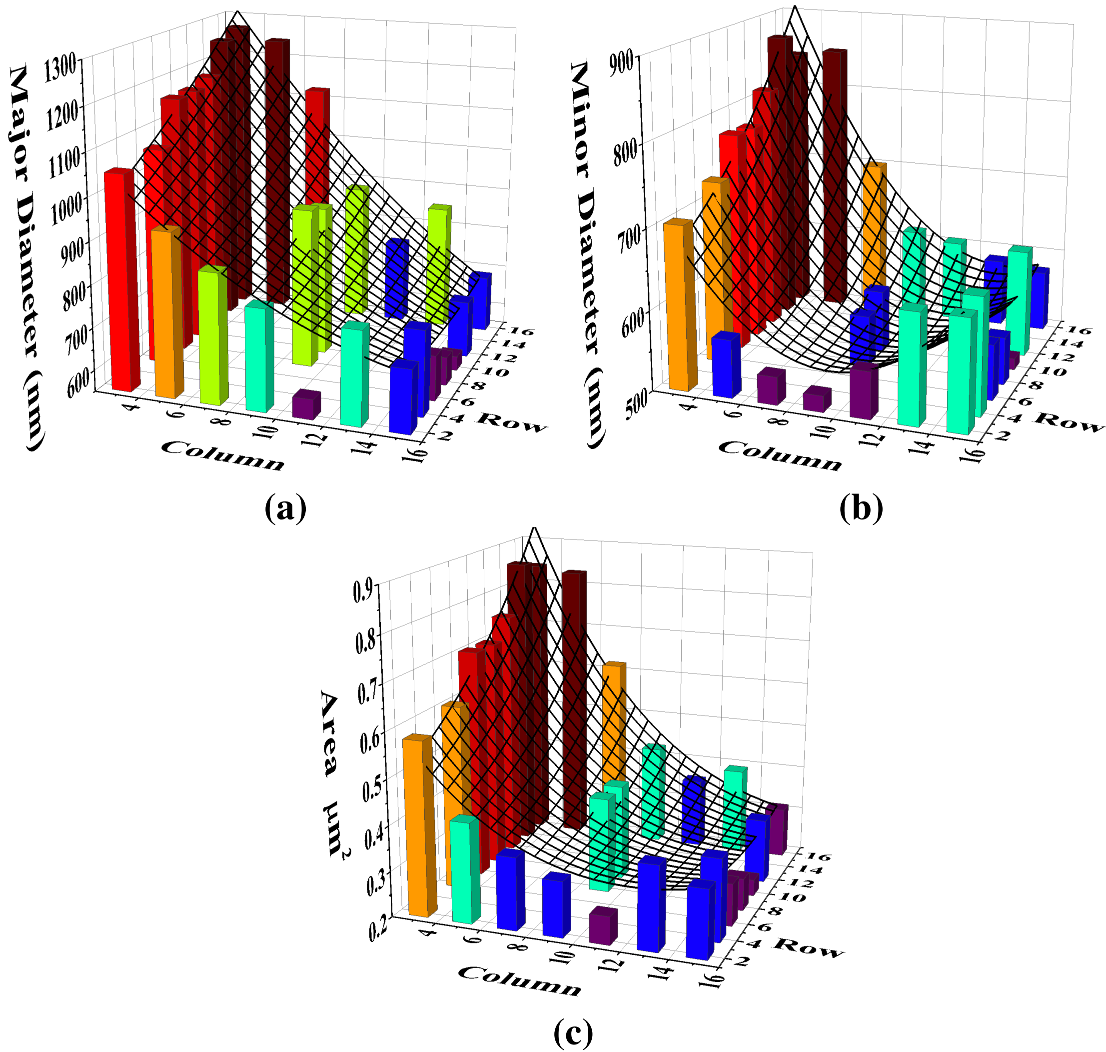

Fig. 5.4: Metal contact (a) major diameters, (b) minor diameters, and (c) areas across InGaAs-1 for 400 nm radii patterns. Major and Minor axis used a surface fit. Area surface was calculated from the surface fits.

appendix) was developed to semi-automate image analysis of the device dimensions. The program output is the major axis, minor axis, and angle of the least squares ellipse fit to the metal contacts. 3D bar plots of the measured major and minor axis (Fig. 5.4a, b) were used to visualize the systematic variations as well as generate a non-linear surface fits (5.1). The surface fits were used to calculate the metal contact areas, which were then compared with the measured areas (Fig. 5.4c) in order to confirm accuracy. Finally, the tunnel junction area of each device was calculated using (5.2). Even with all of the above area analysis, there is still some statistical variation in the junction areas. Therefore, large numbers of electrical measurements (usually more than 200) are needed for high confidence and accuracy.

$$Z = Z_0 + ax + by + cx^2 + dy^2 + fxy \tag{5.1}$$

$$Area = \pi\left(r_{Major} - \Delta r_{Undercut}\right)\times\left(r_{Minor} - \Delta r_{Undercut}\right) \tag{5.2}$$

5.1.1. Electrical Characterization of High Current Density $In_{0.53}Ga_{0.47}As$ ETDs

Like the GaAs-based devices from Chapter 4, electrical measurements were performed using a Keithley 4200 semiconductor parameter analyzer. A set of I-V characteristic curves, covering a wide range of devices sizes, are shown in Fig. 5.5 for (a) InGaAs-1 and (b) InGaAs-2. The dimensions listed are average radii calculated from the area analysis performed after mesa isolation etch (described in Section 5.1). For InGaAs-1, device dimensions ranged from 47 nm up to 1.53 μm radii, with I_P covering three orders of magnitude. For InGaAs-2, devices ranged from 84 nm to 2.5 μm radii, with I_P covering a similar range as InGaAs-1. Larger size junctions for both ETDs could not be measured due to the 100 mA current limit on the Keithley 4200. In past literature, large J_P became difficult to measure due to (i) localized heating requiring pulsed measurements, (ii) large device areas, and/or (iii) uncertainties in the junction area [11, 14]. These issues are circumvented by scaling the junctions to deep submicron dimensions. This enabled the direct measurement of the TD's DC characteristics by reducing parasitic resistances to negligible

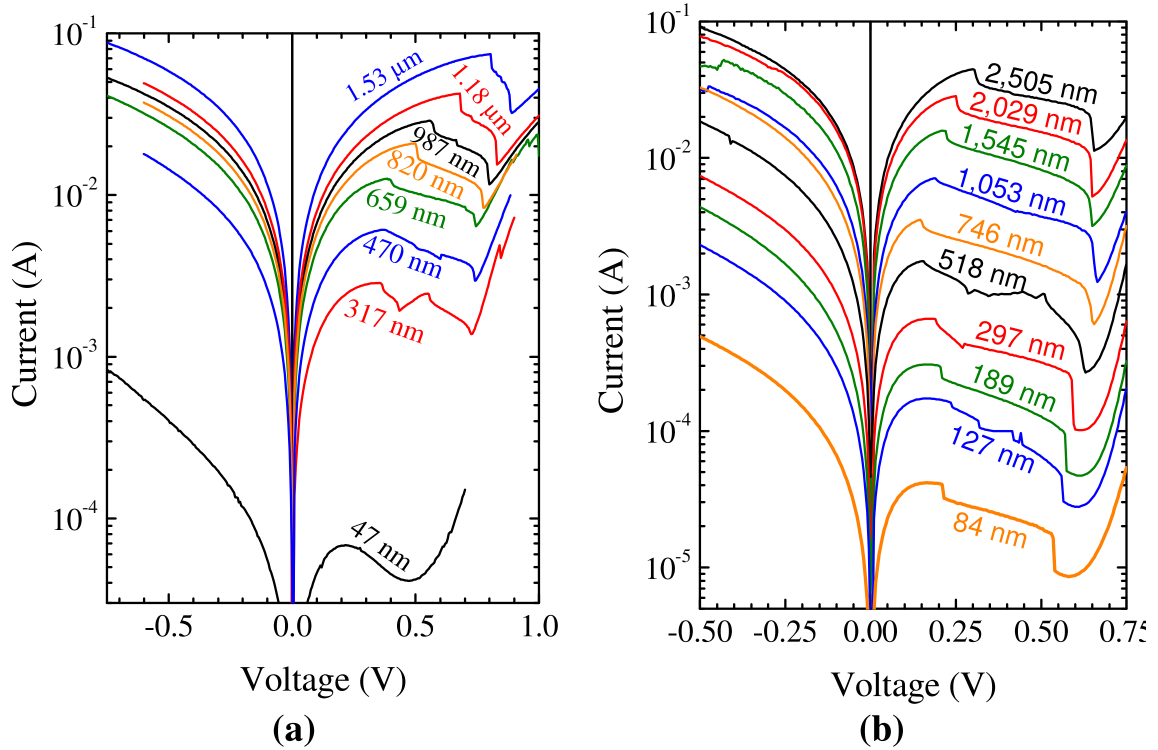

Fig. 5.5: Measured I-V characteristics for (a) InGaAs-1 and (b) InGaAs-2 over a wide range of sizes. Each curve is labeled with its average estimated radius.

levels. Subsequently, the process of calibrating BTBT models to experimental results is simplified.

For comparable sizes, the I_P for InGaAs-1 is significantly larger than InGaAs-2, indicating a larger BTBT current density. The combination of ultra-high current density and soft metal contacts/pads created an uncommon problem during electrical testing. Due to localized heating, occasionally the Au metal above the device would blow apart (Fig. 5.6). This would diminish the electrical connection between the semiconductor and metal, causing noise and increased R_{Series} in the measurements. If care was not taken to minimize the voltage sweep appropriately, a full open would occur. Smaller junctions tended to be more susceptible to this issue. It is also important to understand that reliability few devices smaller than 300 nm radii survived fabrication. There was also less available information for area characterization.

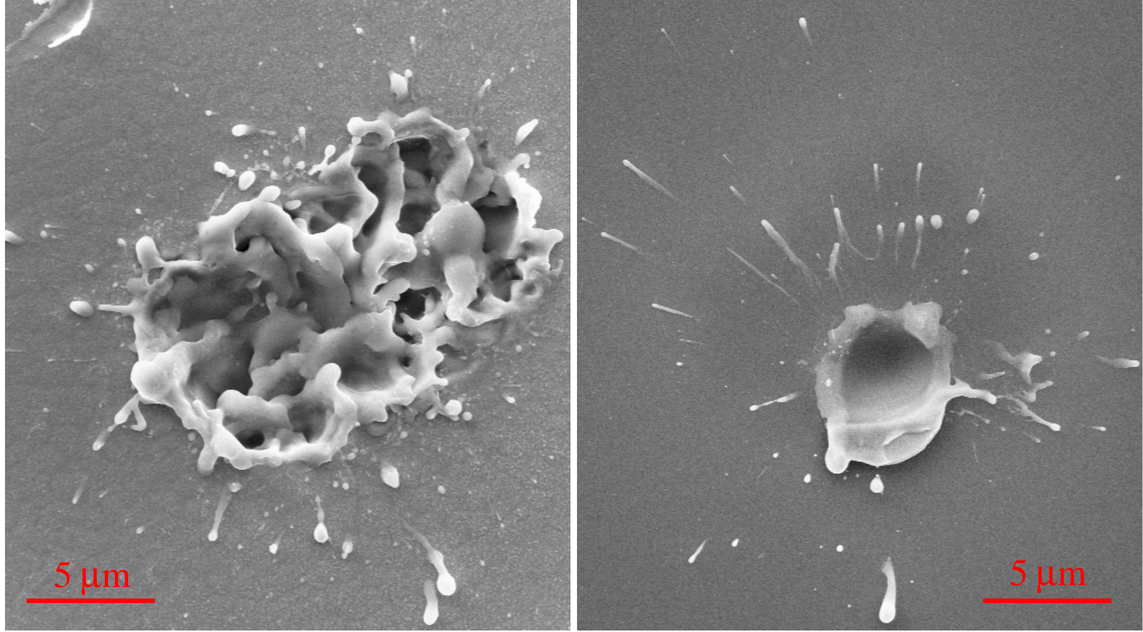

Fig. 5.6: SEM images of Au probe pad blow out due to localized heating This does not kill the device, but causes problems with measurements (noise and opens).

Resulting in large uncertainty for the calculated areas for the ultra small junctions. Furthermore, there aren't many clean measurements for improved statistical analysis.

In addition to comparing current densities, it is clearly visible from Fig. 5.5 that InGaAs-2 is affected by R_{Series} less than InGaAs-1. This is clearly visible in the I-V characteristics as a positive shift in V_P and V_V, as I_P and I_V increases. R_{Series} clearly becomes significant for device sizes of ~300 nm and 1 μm for InGaAs-1 and InGaAs-2, respectively. Eventually, if the voltage drop across the R_{Seires} becomes too large (larger junction areas or R_{Series}), than the ETD/R_{Series} circuit will behave like a latch and prevent accurate ETD measurements.

Plotting measured I_P versus I_P is very useful for quantifying R_{Series}, and determining the intrinsic V_P of the ETD structures. Equation (5.3) relates measured V_P to the instrinsic V_P of the ETD plus a voltage drop across a constant resistance (R_{Series}) and an area dependent resistance (ρ_{Area}) such as contact resistance, and resistance of the semiconductor mesa. Rearranging (5.3), and a linear equation (5.4) can be formed, where R_{Series} is the slope, and the product $J_P \times \rho_{Area} \times V_P$ is the y-intercept (minimum measurable V_P). Typically, ρ_{Area} is very small and therefore is

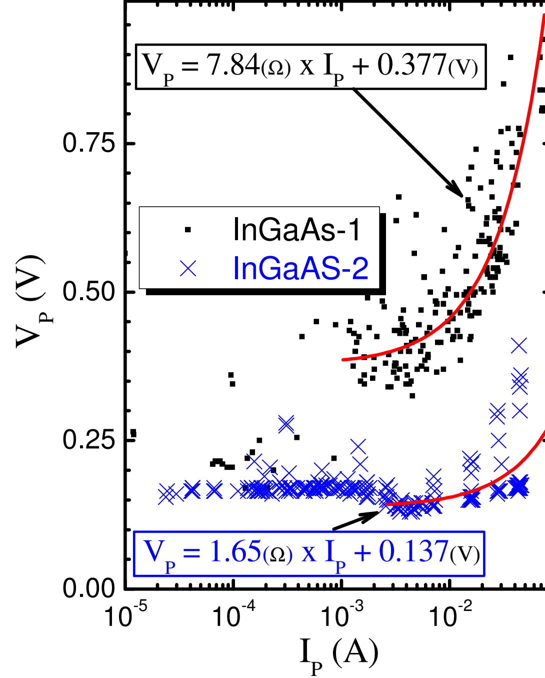

Fig. 5.7: Variation of V_P versus I_P. Slope of the line fit provides average R_{Series}. Y-intercept is the average minimum measureable V_P, which is usually the intrinsic V_P.

negligible. Therefore, the x-intercept of the line fits to Fig. 5.7 are typically the intrinsic V_P. From the line fits, InGaAs-1 has a larger R_{Series} of 7.8 Ω compared to 1.7 Ω for InGaAs-2. Additionaly, the intrinsic V_P for InGaAs-1 is estimated to be a much greater 0.38 V versus 0.14 V for InGaAs-2. However, there are many InGaAs-1 devices with much smaller V_P, around 0.2 V. There may be some additional sources of parasitic resistances present in most devices, elevating the y-intercept.

$$V_P(measured) = V_P + I_P \times \left(R_{Series} + \rho_{Area} / Area \right) \tag{5.3}$$

$$V_{P(measured)} = R_{Series} \times I_P + \left(J_P \times \rho_{Area} + V_P \right) \tag{5.4}$$

There is a very large spread in PVCR values measured, with an average of 1.9 and 5.1 for InGaAs-1 and InGaAs-2, respectively. Similarly to the GaAs based ETDs from Chapter 4, the average PVCR decreases as junction area is scaled (Fig. 5.8a). However, the maximum PVCR

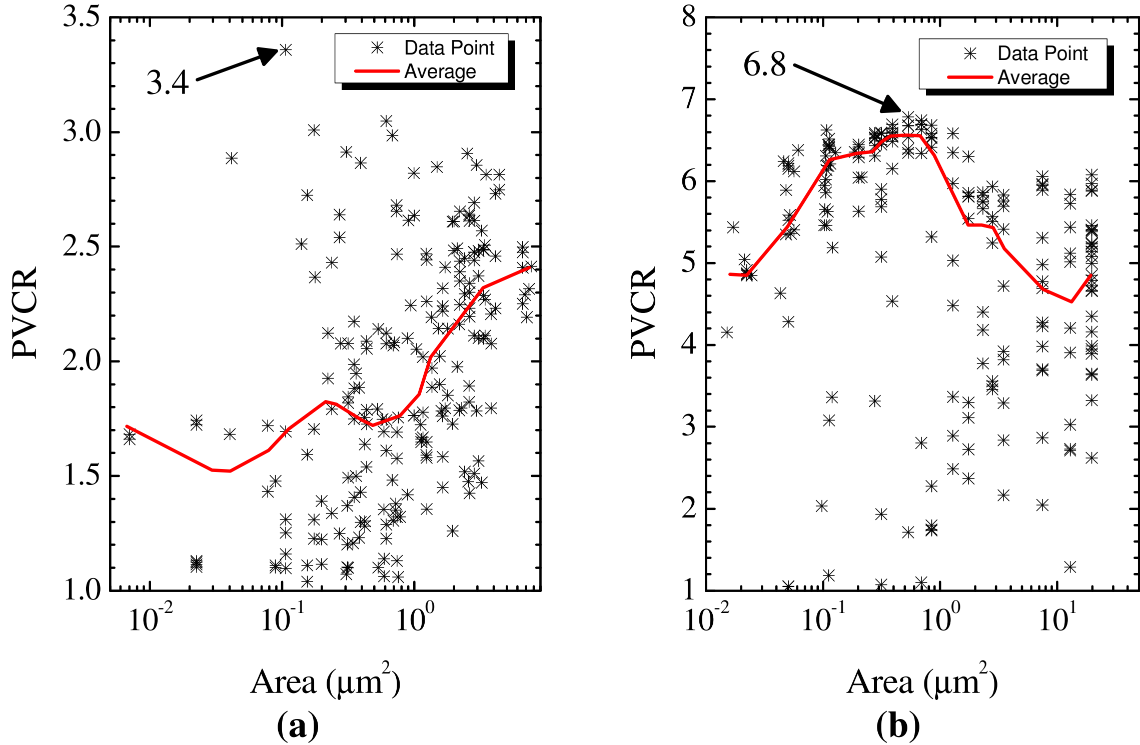

Fig. 5.8: Scaling properties of PVCR for (a) InGaAs-1 and (b) InGaAs-2. The solid lines indicate smoothed averages of the dataset. The maximum PVCR improved a small amount as the junctions were scaled.

increases to 3.4, for a 180 nm radii device. On the other hand, InGaAs-2 had a much smaller statistical variation and a much higher average PVCR of 5.1 (Fig. 5.8b). Unlike InGaAs-1, the average PVCR increases down to ~500 nm Radii, and then flattens out. The maximum PVCR follows the same trend as the average, reaching 6.8 for a 410 nm Radii. For complete analysis of PVCR versus junction area, a much larger data set is needed.

It is evident from Fig. 5.9a that I_P is linearly related to the junction area and therefore is not dominated by surface leakage currents. The main exceptions are the result of statistical deviations in the smallest junction areas, which are due to known fabrication variations. This is especially apparent for InGaAs-1, where very few area characterization measurements were taken for the smallest printed features (it was thought that only a few survived fabrication). From these results it is conclusive that BTBT junctions are scalable to deep sub-micron dimensions, a necessary structural requirement for high performance TFETs. Additionally, it is clear the J_P for

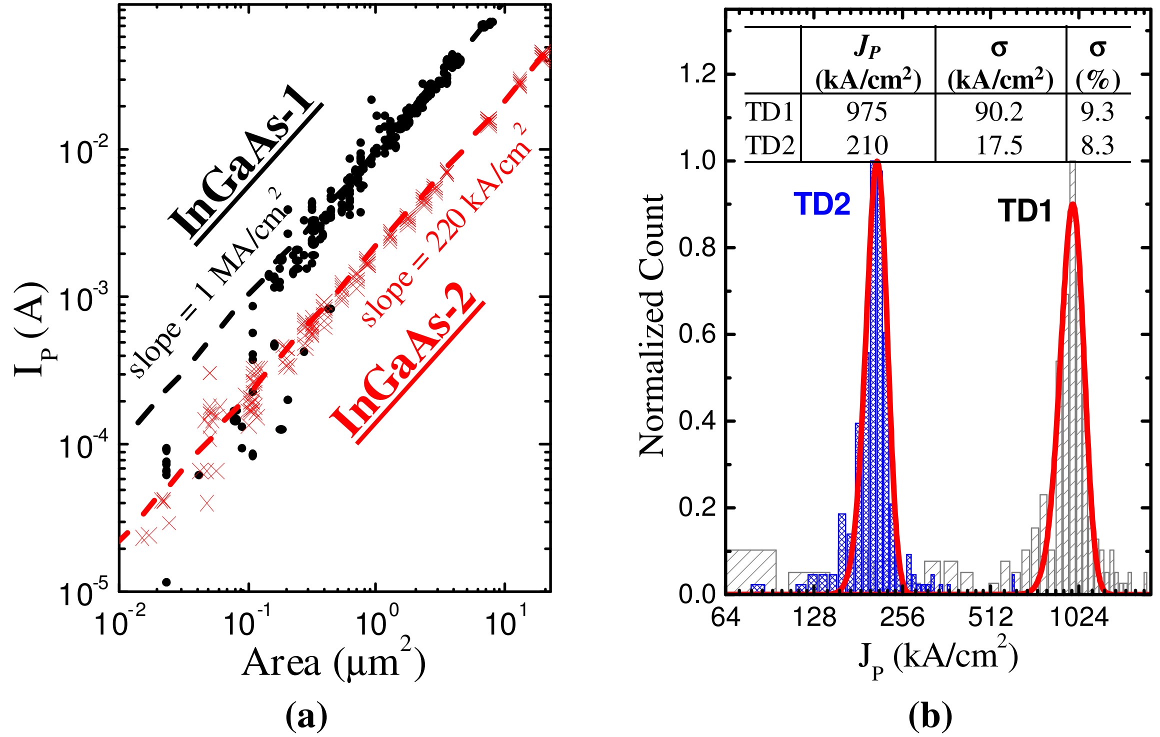

Fig. 5.9: On the left is the (a) scaling properties of I_P for InGaAs-1 and InGaAs-2. On the right are the J_P histograms for both ETDs. The Gaussian fits were used to calculate the average J_P and standard deviation (table inset).

InGaAs-1 is greater than InGaAs-2, which is certainly due to the differences in doping concentrations. The slope of the least squares line fit (dashed lines) to each dataset yields preliminary J_P of 1 MA/cm^2 and 220 kA/cm^2 for InGaAs-1 and InGaAs-2, respectively.

To calculate a statistically accurate J_P, a histogram from the 200+ measured devices for each structure was used, Fig. 5.9b. From the Gaussian fit to each data set J_P is 975 kA/cm^2 and 210 kA/cm^2 for TD1 and TD2, respectively. The J_P of TD2 is comparable to the highest Si/SiGe ETD current density [11], with a much greater PVCR. TD1 has the largest experimentally observed J_P of any homojunction ETD, and the second largest over-all [23, 24]. Zener current densities of 8 MA/cm^2 (TD1) and 3 MA/cm^2 (TD2) were measured at a bias of -0.5 V. It is clear from these results that $In_{0.53}Ga_{0.47}As$ is capable of generating ultra-high BTBT current densities at low applied biases. It is necessary to have large active doping concentrations with fairly sharp doping profiles.

5.1.2. Modeling InGaAs-1 and InGaAs-2

Band diagrams (Fig. 5.10) were calculated using the doping concentrations determined from SIMS (Fig. 5.2a). Fermi energies were calculated using the algorithms developed for the Kane model program discussed in Chapter 3, which assumes a simplified two band theory (only the Γ-valley for electrons). However, an extra option was added for $In_{0.53}Ga_{0.47}As$, which includes the L- and X-valleys for calculating $E_{F,n}$. Also, bandgap narrowing (BGN) effects were also calculated using (5.5) and (5.6), from [26]. Where $\Delta E_{G,Majority}$ and $\Delta E_{G,Minority}$ are the changes in E_C and E_V, depending on the majority doping type. The constants – a, b, c, d – can be found in Table 5.1. The final bandgap used is calculated as the average ΔE_G for the n- and p-sides of the junction. This is obviously a first order approximation, by ignoring band edge alignments.

$$\Delta E_{G,Majority} = a\left(\frac{N_{A,D}}{10^{19}}\right)^{1/3} - b\left(\frac{N_{A,D}}{10^{19}}\right)^{1/2} \tag{5.5}$$

$$\Delta E_{G,Minority} = c\left(\frac{N_{A,D}}{10^{19}}\right)^{1/4} - d\left(\frac{N_{A,D}}{10^{19}}\right)^{1/2} \tag{5.6}$$

At equilibrium, three band diagrams are shown for both InGaAs-1 (Fig. 5.10a) and InGaAs-2 (Fig. 5.10b). All of the calculations assume that the doping profiles are perfectly square, full depletion approximation, and all bands are parabolic (constant effective mass). The basic band structure assumes the *i*-layer (d) is 0 nm thick and only the Γ-valley is relevant. The second set of band diagrams inserts a perfect 3 nm *i*-layer. Finally, E_F is calculated using four bands (Γ, L, and X) and *d* is was setto 0 nm. A fourth set of band structures were calculated

Table 5.1 Constants for calculating bandgap narrowing (BNG).

	a	b	c	d	Units
N_A	9.2	3.4	11.3	0.23	meV
N_D	47.6	0	3.2	0	meV

Table 5.2 Modeling results for InGaAs-1 and InGaAs-2. The Kane model is not setup to include an *i*-layer (d), and therefore all J-V results assume d is 0 nm.

	d (nm)	Model Parameters	E_G (eV)	w_d (nm)	Barrier Width (nm)	J_P (kA/cm^2)	$E_{F,n}$-E_C (eV)	E_V-$E_{F,p}$ (eV)	V_P (V)	n
InGaAs-1	0	2 Band	0.736	10.6	2.53	683	2.18	0.162	0.196	1.31
InGaAs-1	3	2 Band	0.736	11.0	2.63					
InGaAs-1	0	4 Band	0.736	9.06	2.96	343	1.36	0.162	0.177	0.58
InGaAs-1	0	4 Band/BGN	0.662	8.76	2.75	480	1.28	0.162	0.178	0.62
InGaAs-2	0	2 Band	0.736	11.8	3.26	262	1.77	0.148	0.174	1.00
InGaAs-2	3	2 Band	0.736	12.1	3.36					
InGaAs-2	0	4 Band	0.736	10.7	3.59	153	1.31	0.148	0.162	0.54
InGaAs-2	0	4 Band/BGN	0.670	10.4	3.37	218	1.25	0.148	0.163	0.58

using 4-bands, *d* equal to 0 nm, and bandgap narrowing. Those results are tabulated, along with the others, in Table 5.2 but not shown in Fig. 5.10. For easy comparison, the x-axis is centered at the middle of the *i*-layer, with the shaded region indicating the *i*-layer itself. As can be seen, the largest change from the basic model, is the use of 4-bands to calculate $E_{F,n}$. The insertion of a small *i*-layer has minimal effects.

The numerical results for all eight band diagram calculations are listed in Table 5.2. As can be seen, the 3 nm *i*-layer only increases the depletion width (w_d) by only ~0.35 nm, increasing the tunnel barrier width a negligible ~0.1 nm. Therefore, it is reasonable to ignore the *i*-layer for the J-V modeling. The largest effect comes from using 4-bands to calculate $E_{F,n}$, which reduces w_d from 10.6/11.8 nm (InGaAs-1/InGaAs-2) to 9.06/10.7 nm. Furthermore, the tunnel barrier widths are reduced from 2.53/3.26 nm to 2.63/3.59 for InGaAs-1/InGaAs-2. This is a large reduction of approximately ~40%, and certainly effects the calculated BTBT current. Finally adding the effects of BNG narrows w_d by an additional ~0.2 nm, and shrinks the bandgap (tunnel barrier height) by 74 meV and 66 meV for InGaAs-1 and InGaAs-2, respectively. From here, simulations will include (i) 2-bands only, (ii) 4-bands, and (iii) 4-bands with BNG.

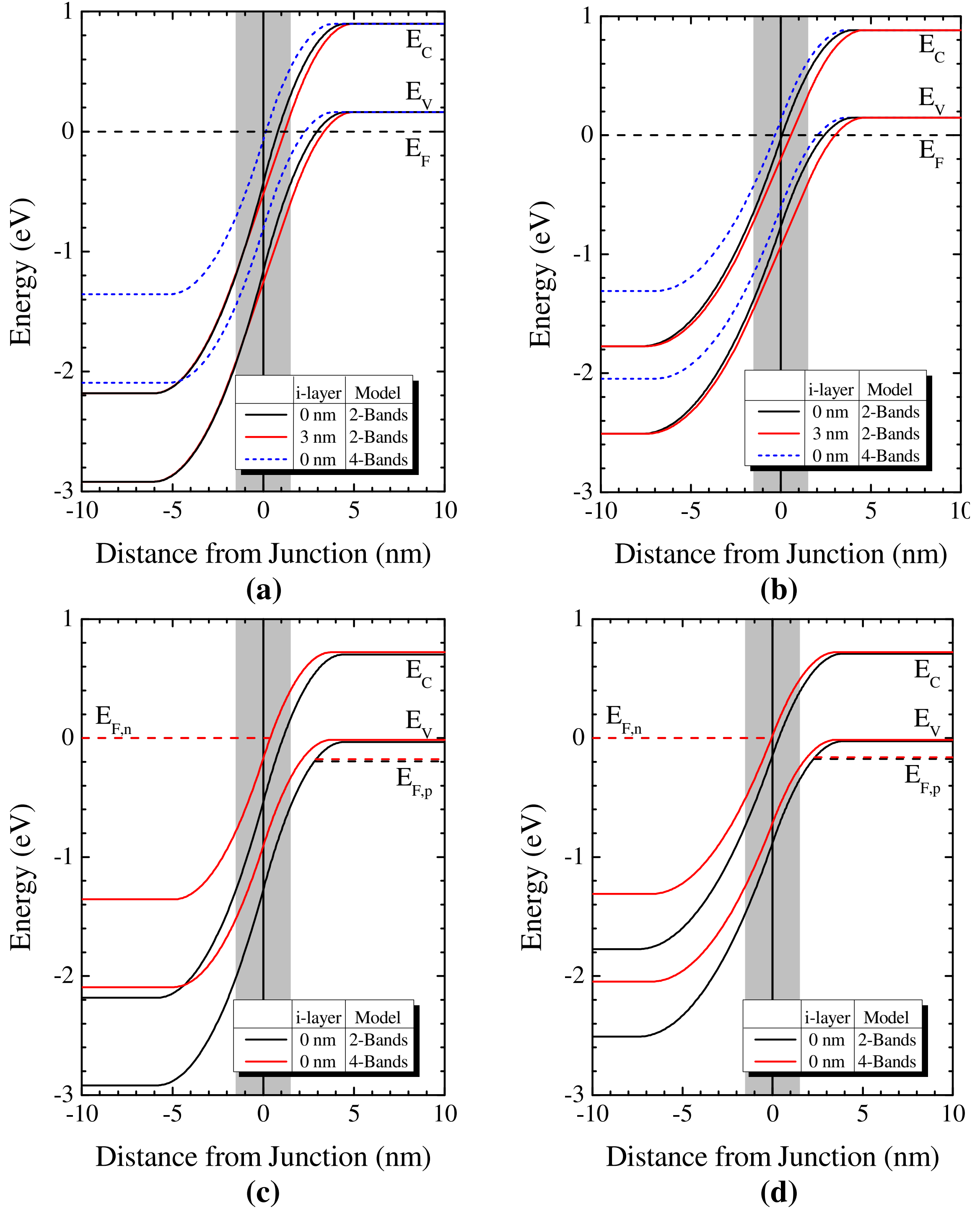

Fig. 5.10: Calculated band diagrams assuming 2-band approximation, abrupt junctions, and full depletion approximation. Top row are at equilibrium for (a) InGaAs-1 and (b) InGaAs-2. The 3 nm *i*-layer has a minimal effect on the tunnel barrier. The Bottom row is biased at the calculated V_P for (a) InGaAs-1 and (b) InGaAs-2. V_P is largely dependent on $E_{F,p}$.

The non-equilibrium band diagrams at the V_P are shown for InGaAs-1 (Fig. 5.10c) and InGaAs-2 (Fig. 5.10d). Notice that V_P occurs when $E_{V,p}$ is shifted just below $E_{F,n}$ for all cases. Additionally, $E_{F,p}$ is nearly the same for all cases, and therefore so is V_P. This is because $E_{F,p}$ is much smaller than $E_{F,n}$, due to their respective density of states and doping concentrations. If $E_{F,n}$ was much larger than $E_{F,p}$, than V_P would closely follow $E_{F,n}$. V_P may be predicted by (5.7). $E_{F,minor}$ is the smaller of the two Fermi potentials, kT is the thermal energy present, and n is some constants (typically less than two). When the two Fermi energies are close to each other, than V_P would be an average of $E_{F,n}$ and $E_{F,p}$, which has been described elsewhere [27].

$$V_P = E_{F,\text{minor}} + n \times kT \tag{5.7}$$

From the Kane model, Table 5.2 predicts that J_P will be ~500 kA/cm^2 and ~200 kA/cm^2 for InGaAs-1 and InGaAs-2, respectively. The specific value depends on which parameters are used. The greater values are predicted with the simplest 2-band model. The 4-band model reduces the prediction by ~55%. Finally adding in BNG brings J_P band to ~75% of the original value. There is only a small variation in V_P, since it is dominated by $E_{F,P}$. Typical values of "n" range between 0.5 and 1.3, with an average of 0.8. In general, "n" follows $0.83 \times E_{F,p} + 0.5$.

The calculated J-V results are compared with InGaAs-1 (left) and InGaAs-2 (right) using the 2-bands (Fig. 5.11a, d), 4-bands (Fig. 5.11b, e), and 4-bands and BGN (Fig. 5.11c, f) models. For each curve, a simple exponential line is fitted to the post-valley characteristic as a simple J_{Excess} model. The basic 2-bands model best estimated J_P and the pre-peak BTBT current densities. However, the slope of the NDR region is way too shallow and extended due to the over-estimated V_{bi} prolonging the mesa-like portion of the overlap integral. When J_{Excess} is added to J_{Model}, the PVCR is nearly non-existent for InGaAs-1, and very small for InGaAs-2.

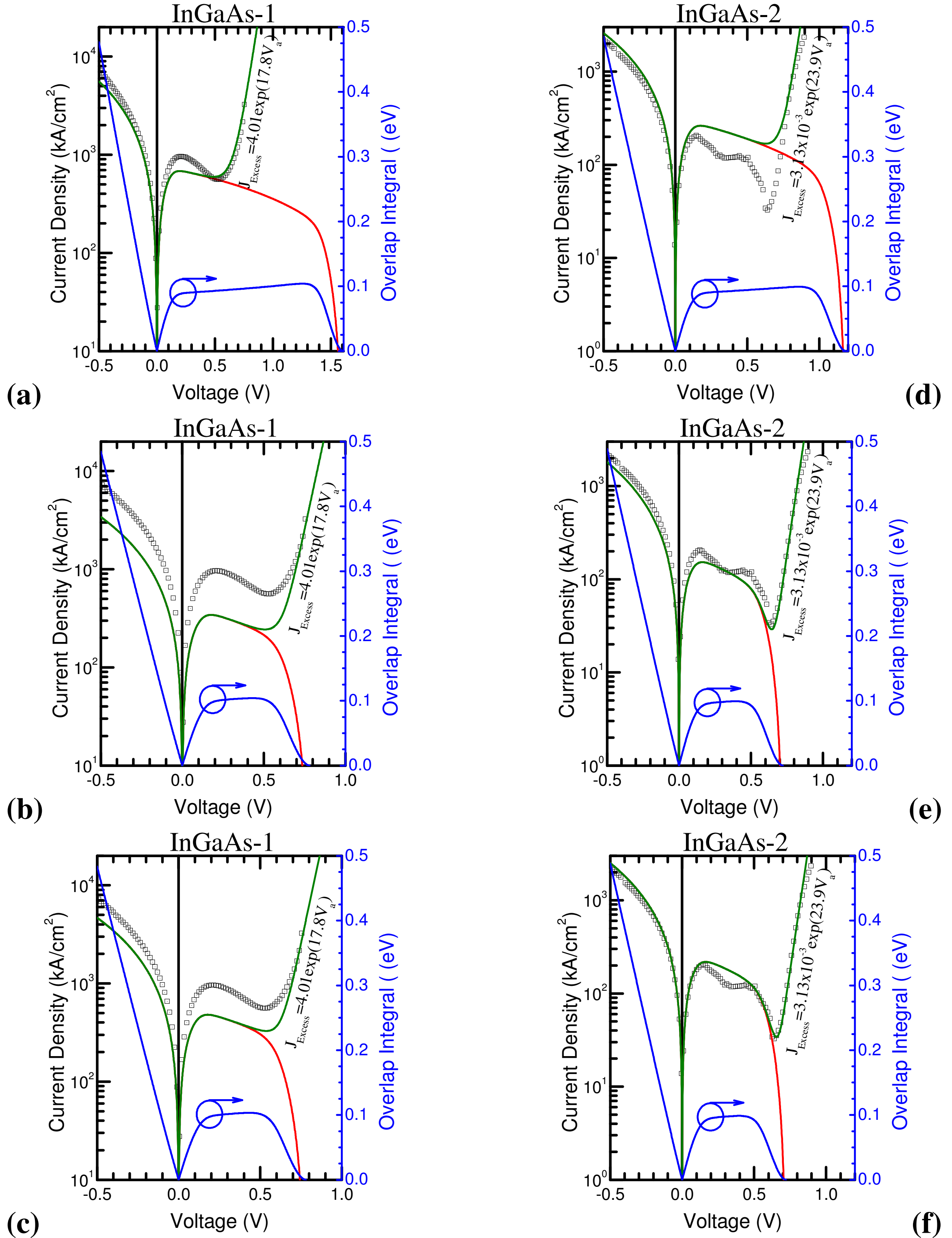

Fig. 5.11: Calculated BTBT J-V characteristics vs. measured for (left) InGaAs-1 and (right) InGaAs-2. Top row (a, d) are 2-band, middle row (b, e) are 4-band, and the bottom row (c & f) are the 4-bands & BGN results. The 2-band model gave the best pre-J_P current densities. Whereas, the 4-band & BGN model gave the best post-J_P results.

Calculating $E_{F,n}$ using the 4-bands model fixes the issue with the NDR region. By using all three electron valleys (Γ, L, and X), the $E_{F,n}$ became substantially smaller, as described in Fig. 5.10, and Table 5.2. As a result, the overlap integral (D) is much shorter in forward bias, which greatly improves the final PVCR close to the measured value. However, the 4-bands model also increased the tunnel barrier width. As a result, the calculated BTBT current density was significantly reduced. The calculated values are still within the same magnitude the measured data.

Adding in BGN to the calculations reduced the tunnel barrier width and height. As a result, the BTBT current densities increased, but not back to their original values. For InGaAs-1, the model still underestimated the current density. For InGaAs-2 the model predicted the same current density as was measured in the fabricated devices. Additionally, with the fitted J_{Excess}, the

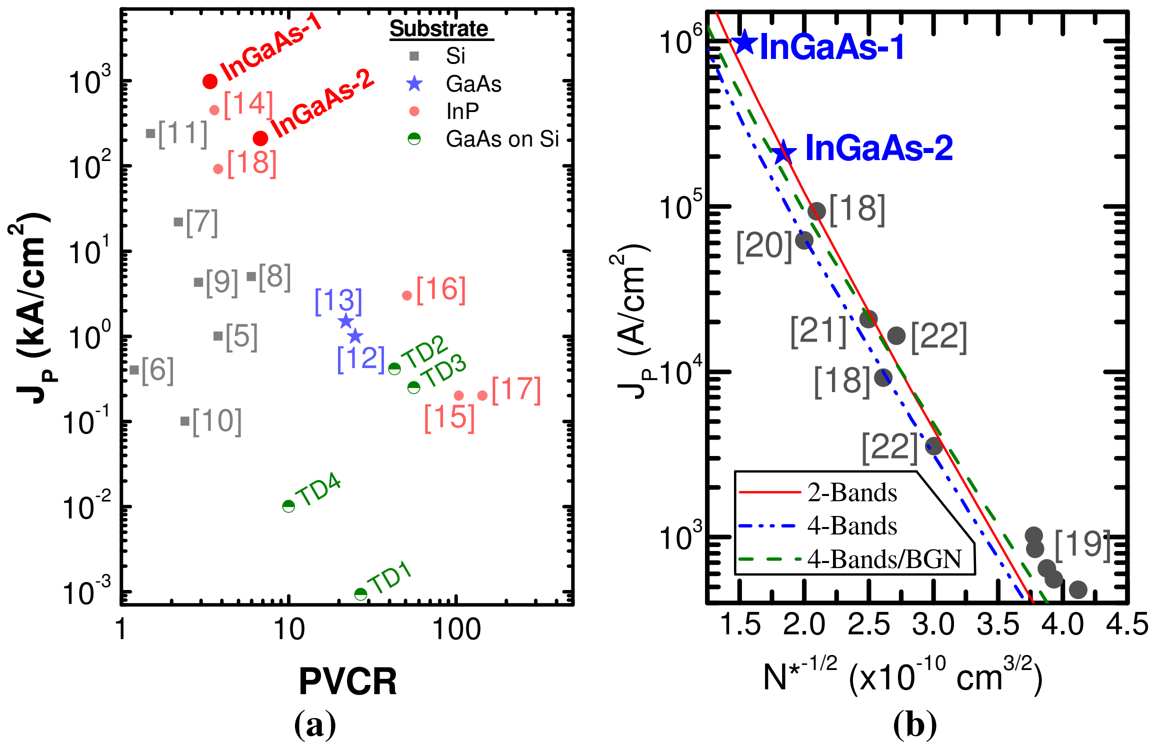

Fig. 5.12: Contrasting InGaAs-1 and InGaAs-2 with previous results and other ETDs from literature by compare J_P versus (a) PVCR [4-18] and (b) reduced average doping (N^*) [18-23]. Solid and Dashed lines are Kane model predictions using 2-bands, 4-bands, and 4-Bands/BGN.

NDR and valley regions are also accurate. Also, notice that J_{Excess} becomes significant as "D" and J_{Model} sharply descend. A small change in J_{Excess}, would cause a very large shift in J_V (minimal change in V_V), thereby causing a large change in PVCR. If J_{Excess} is increased too much, as is the case for the InGaAs-1 device shown above, J_V and the PVCR will only have minor changes due to the mesa-like shape of "D". Conversely, V_V will shift more dramatically.

Even though the current density magnitude for InGaAs-1 is low, the shape of the cure is very accurate. If the magnitude of the calculated curve is matched to the measurements, the model will accurate predict the J-V characteristics for the bias conditions used here. Therefore, if J_P is known, J_{Model} may be used to predict the rest of the J-V characteristic. Furthermore, given that the primary concern is J_P and pre-peak characteristics, the simple 2-band model is the most accurate for predictions.

5.1.3. Benchmarking $In_{0.53}Ga_{0.47}As$ ETDs

As introduced in Chapter 4, InGaAs-1 and InGaAs-2 are benchmarked against ETDs from literature. First, J_P is plotted again PVCR (Fig. 5.12a). As can be seen, InGaAs-1 has the largest current density shown, and InGaAs-2 is tied for 3rd with a Si/SiGe beased device [11]. However, the InGaAs based structure have much greater PVCR than the Si based structures. Therefore, it is reasonable to predict that InGaAs is a better material system for BTBT based devices. However, this does not take doping into consideration.

It has already been established that doping has a large impact on J_P. In Fig. 5.12b, J_P is plotted against the inverse square root of the reduced average doping (N^*) for 11 ETDs in literature as well as InGaAs-1 and InGaAs-2. Even though there are a great number of $In_{0.53}Ga_{0.47}As$ ETDs reported in literature, only those reports that follow the following restrictions were included. These restriction guarantees that the final list is a homogeneous set, with doping being the only significant variable. First, the entire tunnel junction must be $In_{0.53}Ga_{0.47}As$ without any strain. The *i*-layer, if present, may not exceed ~4 nm. There must be a representative I-V

curve present with clear NDR. There needs be high confidence in the value measured and calculated for J_P. Finally, there must be clear a SIMS plot which may be used to extract the appropriate doping concentrations.

It is clear from Fig. 5.12b, that all of the collected InGaAs ETDs form an exponential line. Also included are trendlines from the Kane more using (i) 2-bands, (ii) 4-bands, and (iii) 4-bands & BGN modeling parameters as discussed in sections 5.1.2. All three lines are very close to each other, with only fairly small differences in slope and magnitude. However, the basic 2-bands line (solid) does the best job over-all of predicting J_P. It is also the closest to a least squares exponential fit to the data (not shown here). Therefore, to simplify the calculations and analysis, the more accurate 2-bands $E_{F,n}$ model will be used for the remaining modeling work.

5.2. Low Current Density $In_{0.53}Ga_{0.47}As$ ETD

The third $In_{0.53}Ga_{0.47}As$ ETD (InGaAs-3 shown in Fig. 5.13a) was designed to be a medium level current density grown by MBE from a 3rd source; Texas State University. A major difference for this design was flipping the structure upside down, and placing the n-type layer on top. The growth began with a 300 nm p-type $In_{0.52}Al_{0.48}As$, then is switch over to 300 nm of p-type $In_{0.53}Ga_{0.47}As$. Furthermore, due to constraints in the epitaxy reactor, Be was used as the dopant species instead of C. Similar to InGaAs-1, the maximum N_A concentration is targeted to $5x10^{19}$ /cm^3, and is contained within a 10nm layer adjacent to the 3 nm *i*-layer. Finally, the entire 60 nm n-type cathode had a target concentration of 4. $5x10^{19}$ /cm^3. Using the Kane model, verified for the InGaAs system in the previous Section (5.1.3), J_P is calculated to be approximately 10 kA/cm^2.

The fabrication began with the deep sub-micron process used for InGaAs-1 and InGaAs-2. However, processing was halted after mesa isolation etch in order to perform preliminary electrical testing of the ETDs. Additionally, Mo was sputtered as the contact metal, instead of the Au/Zn/Au film stack used for all previous samples. As a refractory metal, Mo is a much cleaner

metal (Au contamination can be a huge issue on Si clean rooms), has a work function more appropriate for n-type semiconductors, and there is the potential for patterning with a dry plasma. Since this was the first time working with Mo, several transfer length method (TLM) features were added to the layout. The TLMs were aligned horizontally and vertically to the wafer flat.

5.2.1. Electrical Results for InGaAs-3

Electrical measurements began with the TLM structures. From the results shown in Fig. 5.13b, both sets of TLMs resulted in a straight line, with the Horizontal having the least noise. The results of both TLMs were very close to each other, which one would expect. The average contact resistance (R_{Cotact}), sheet resistance (R_{Sheet}), transfer length ($L_{Transfer}$), and contact resistivity ($\rho_{Contact}$) measured were 0.37 (Ω), 37 (Ω/sq.), 1.28 (μm), and 6.0x10^{-7} (Ω-cm^2), respectively. The contact resistivity is sufficient for these ETD structures.

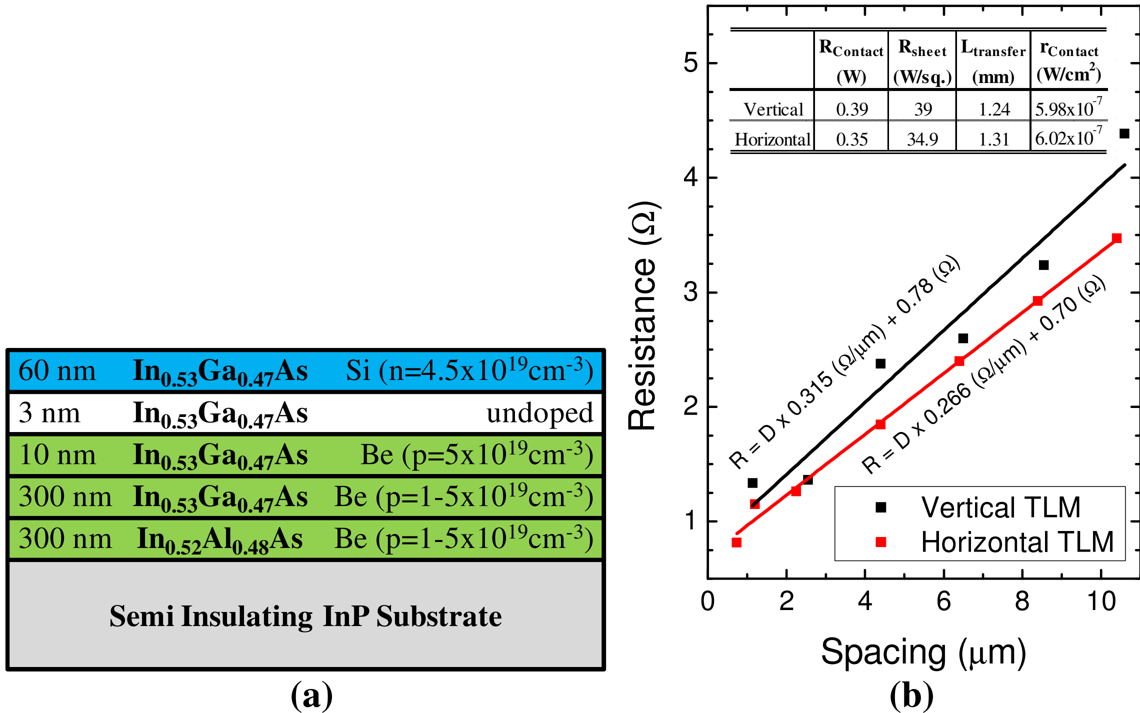

Fig. 5.13: Left, (a) Schematic diagram of InGaAs-3 with original target doping concentrations. Right, (b) vertically and horizontally oriented TLM results for Mo contacts on n-type $In_{0.53}Ga_{0.47}As$.

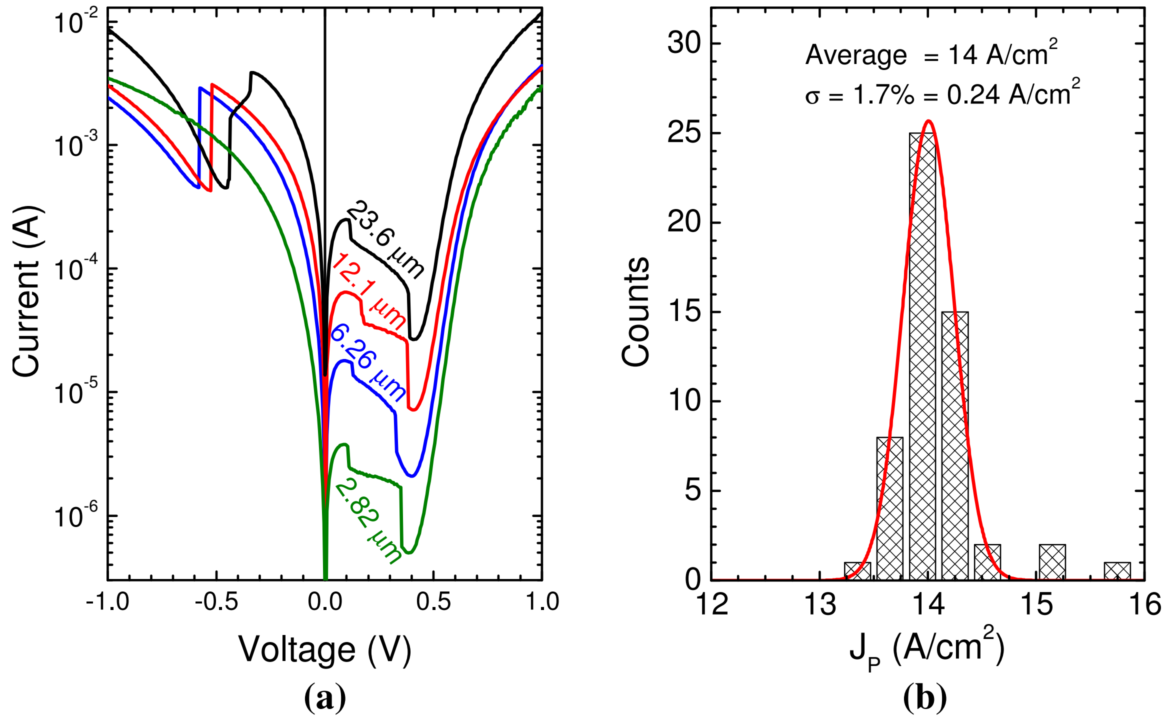

Fig. 5.14: Left, (a) I-V characteristics for InGaAs-3. NDR in reverse bias is from the device used as a virtual short to ground. Right, (b) J_P histogram with Gaussian fit. J_P is much smaller than predicted.

The electrical results of the large area, post-mesa etched ETDs can be found in Fig. 5.14a. The measured I_P ranged two orders of magnitude, and was primarily limited by the (i) largest printed devices and (ii) probe tips diameter (~2.5 μm). Smaller features were printed, but without going through the entire sub-micron process, they could not be tested. At larger biases (~0.65 V), an external R_{Series} began dominating the I-V characteristics. In reverse bias, the NDR of the device used as a virtual ground is clearly present. Reverse NDR is not visible for the smallest ETD (2.82 μm radii), because its reverse bias current does not achieve I_P for the virtual ground device.

Since the virtual ground device structure is at least 15x greater than the device under test, this indicates that the current density of InGaAs-3 is much less than the previous two ETDs, as expected. For a high confidence level assessment of J_P, another histogram was formed. The Gaussian fit to the distribution gave an average J_P of 14 A/cm^2, with a very small standard

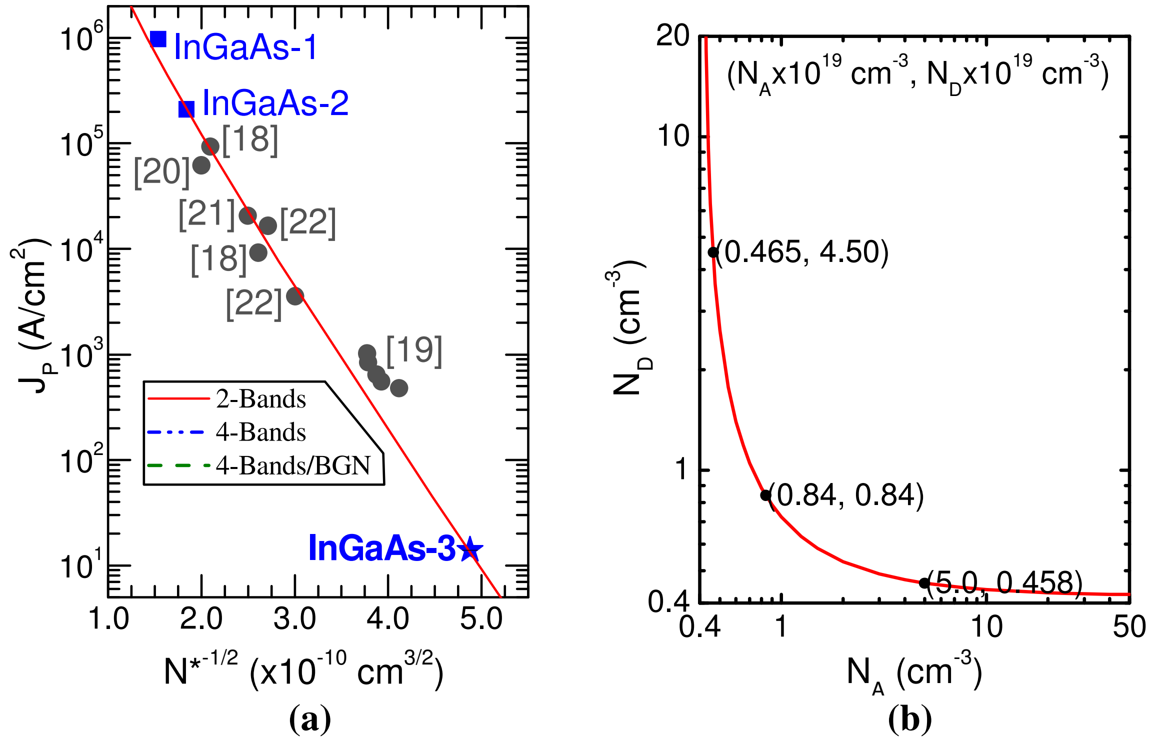

Fig. 5.15: Left, (a) $In_{0.53}Ga_{0.47}As$ trendline including predicted placement of InGaAs-3 (measured J_P of 14 A/cm^2). Right, (b) isometric reduced doping curve for an $N^* = 4.2\text{x}10^{18}/\text{cm}^3$. Labeled points assume (i)N_A is off target, (ii) N_A=N_D, or (iii) N_D is off target.

deviation of 1.7% (0.24 A/cm^2). This result is three orders of magnitude smaller than the predicted value.

5.2.2. Investigating the Low J_P of InGaAs-3

Assuming that the $In_{0.53}Ga_{0.47}As$ trendline is still valid for the low J_P measured, there are two main reasons that the structure was so far off in its current density. First, the doping concentration may be much smaller than expected. Second, the *i*-layer may have been grown to large. Both issues could be easily clarified with SIMS. However, the $In_{0.53}Ga_{0.47}As$ trendline was first used to predict the N^* needed to achieve the measured J_P. As labeled in Fig. 5.15a, InGaAs-3 is far removed from all other devices, with an expected N^* of 4.2x10^{18} /cm^3. A curve was generated for all possible (within reason) combinations N_A and N_D doping concentrations. The curve assompotically approaches *x*= and *y*= 4.2x10^{18} /cm^3. It is not uncommon for the

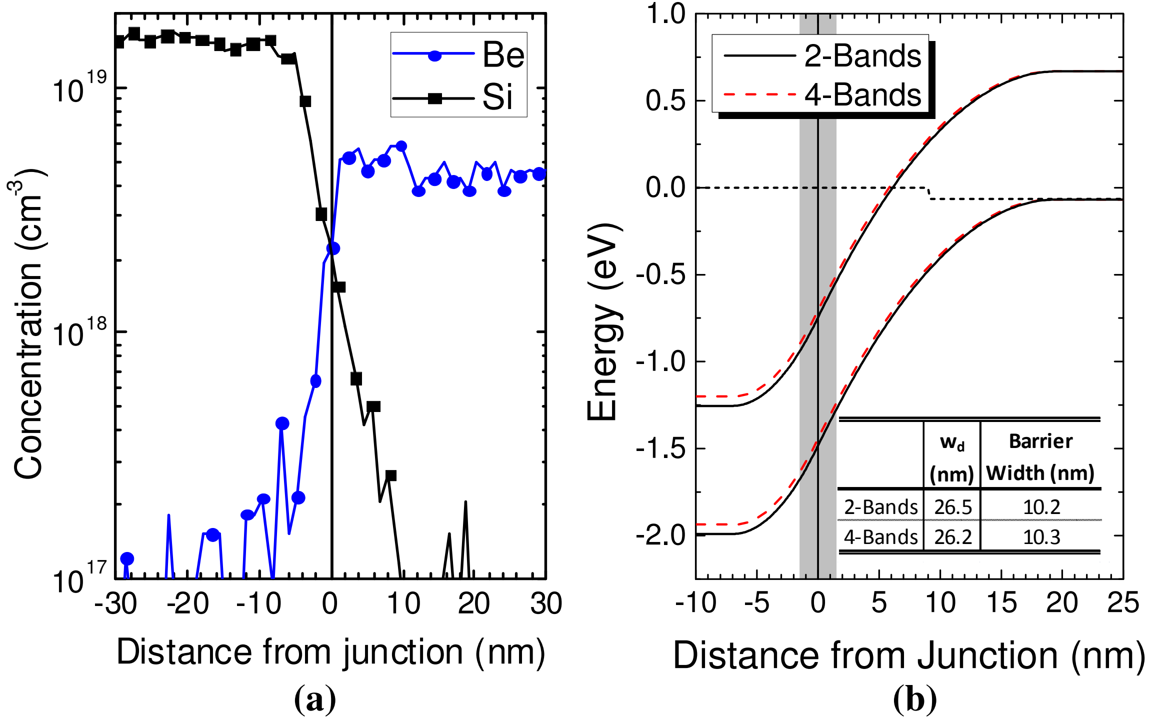

	w_d (nm)	Barrier Width (nm)
2-Bands	26.5	10.2
4-Bands	26.2	10.3

Fig. 5.16: Left, (a) SIMS results for InGaAs-3. Be concentration if much smaller than targeted. Right, (b) calculated band diagram biased at V_P using 2-bands and 4-bands E_F model.

temperature setting an effusion cell to be set for the wrong doping concentration. Therefore, two data points are labeled assuming only one of the target concentrations was achieved. Also included was $N_A = N_D$.

The SIMS results are shown in Fig. 5.16a. The Si doping concentration is a little smaller (36%) than the target, maxing out at 1.59×10^{19} /cm^3 near the tunnel junction. However, the bigger error is the Be, which only achieved 5.70×10^{18} /cm^3, which is one order of magnitude off of the target. In fact, the Be doping concentration is the same in the 300 nm and 10 nm layers. The measured N^* for InGaAs-3 is exactly equal to the predicted value of 4.2×10^{18} /cm^3. Therefore, the $In_{0.53}Ga_{0.47}As$ is accurate for a current range of nearly five orders of magnitude, and is useful for predictions.

5.2.3. Simulation Results for InGaAs-3

It is clear that J_P is very small because of thebe doping concentration. The calculated band diagram, Fig. 5.16b, shows a large w_d and tunnel barrier width of ~26 nm and ~10 nm, respectively. Additionally, N_A is less than the DOS for holes (~8.1x10^{18} /cm^3), severely limiting the number of open states (holes) for electrons to tunnel into. There is only a small difference between the 2-bands and 4-bands model, indicating that most of the electrons are populating the Γ-valley.

The J-V characteristics of InGaAs-3 were calculated using 2-bands and 4-bands $E_{F,n}$ modeling, Fig. 5.17. BGN was excluded for its vast overestimation of J_P. An exponential line fit to the post-valley characteristic was used as the J_{Excess}, and added to J_{model}. Additionally, measured from the high voltage rang in forward bias, a 96.2 Ω series resistance was included. Otherwise, as can be seen, the basic model begins to overestimate the current density at moderate voltages. As can be seen, both calculated curves are very close to the measured values. In

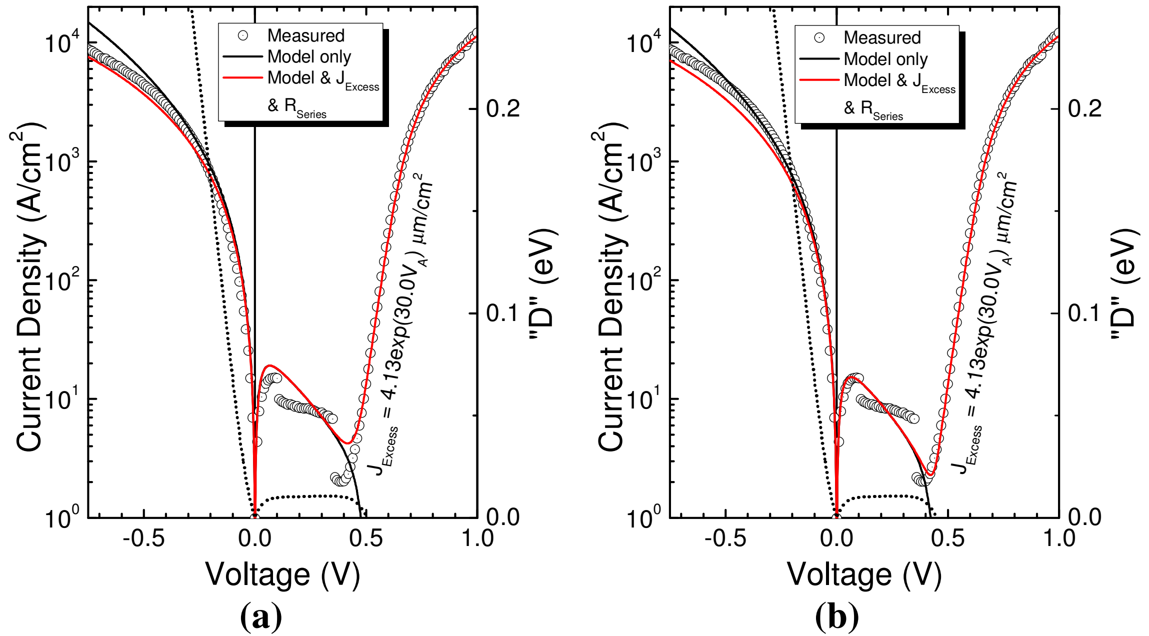

Fig. 5.17: Calculated J-V characteristics using (a) 2-bands and (b) 4-bands. For improved accuracy post valley, J_{Excess} was added via an exponential line fit. Additionally, a 96.2 Ω R_{Series} was added to improve the fit at high current magnitudes.

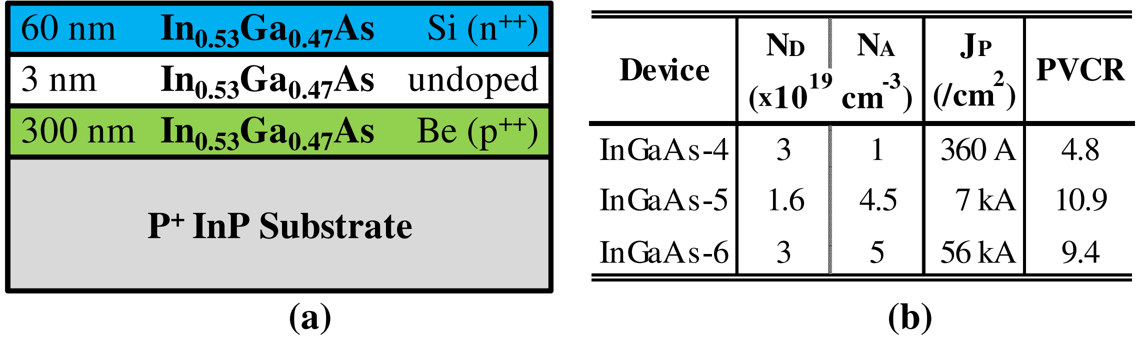

Device	N_D ($x10^{19}$	N_A cm^{-3})	J_P ($/cm^2$)	PVCR
InGaAs-4	3	1	360 A	4.8
InGaAs-5	1.6	4.5	7 kA	10.9
InGaAs-6	3	5	56 kA	9.4

Fig. 5.18: (a) Schematic diagram of medium current density $In_{0.53}Ga_{0.47}As$ ETD with (b) coping concentrations, measured J_P, and PVCR for InGaAs-4, InGaAs-5, and InGaAs-6.

reverse bias the 2-bands model (Fig. 5.17) is the most accurate. However, in forward bias, the 4-bands model (Fig. 5.17b) is more accurate. The Kane model has been shown to accurately predict $In_{0.53}Ga_{0.47}As$ J-V characteristics for high (InGaAs-1 and InGaAs-2) and low (InGaAs-3) current densities. Therefore, one can be confident in its ability to perform well over the entire range. To verify this hypothesis, three medium current density $In_{0.53}Ga_{0.47}As$ ETD structures were also fabricated.

5.3. Medium Current Density $In_{0.53}Ga_{0.47}As$ ETDs

To help fill out the middle current density range of the $In_{0.53}Ga_{0.47}As$ trendline, three additional ETD structure were grown. The structure for (i) InGaAs-4, (ii) InGaAs-5, and (iii) InGaAs-6, shown in Fig. 5.18a, is similar to InGaAs-3. However, structure was grown on a p-type InP substrate, the $In_{0.52}Al_{0.48}As$ layer was skipped, and the entire anode (p^{++}) layer was targeted with the maximum doping. The target doping concentrations are listed in Fig. 5.18b. Due to limited resources and improved growth calibrations, SIMS analysis was not performed on these structures. It was assumed that the actually doping concentration was very close to the target values. From the $In_{0.53}Ga_{0.47}As$ trendline, J_P was expected range from approximately ~600 A/cm^2 to ~50 kA/cm^2.

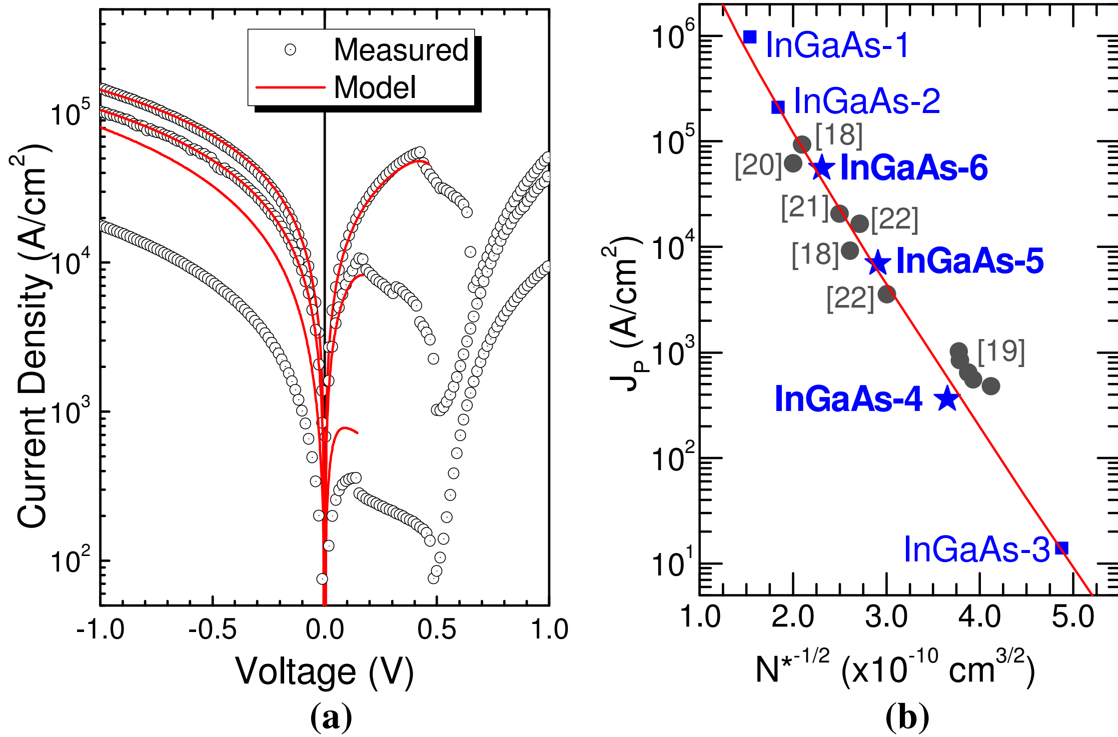

Fig. 5.19: (a) Typical J-V characteristics for InGaAs-4, InGaAs-5, and InGaAs-6. Solid lines are calculated using the basic 2-bands model, cut-off at the measured V_P. A ~6 μΩ-cm^2 R_{Series} was added to the model. (b) Characteristic trendline for $In_{0.53}Ga_{0.47}As$, covering five orders of magnitude, including the three additional data points added.

These structure were grown by MBE at Texas State University, the same as InGaAs-3. Since it was known that the current density will not exceed 100 kA/cm^2, the basic fabrication process was used. Sub-micron devices are only necessary for high current density structures and investigating the scaling properties of tunnel junctions. Additionally, only a few measurements of contact areas are needed for high confidence in the current densities calculated. Furthermore, these measurements area easily performed within one hour using an optical microscope, versus an entire day needed for the deep-submicron process.

As before, no activation anneals were performed, and Mo was used as the contact metal. However, instead of a lift-off lithography process, Mo was first deposited over the entire sample surface. Then contact lithography was performed. Finally, using an O_2:SF_6 plasma etch, the

exposed Mo was removed, leaving behind Mo contact pads. The subtractive Mo etch resulted in better sidewall morphology, and improved device dimension control versus the lift-off process.

5.3.1. Results for Medium Current Density ETDs

The typical J-V characteristics InGaAs-4, InGaAs-5, and InGaAs-6 are shown in Fig. 5.19a. As J_P increased, V_P also significantly increased. This is a clear indication that there is a relatively large R_{Series} present, which also limits this apparent Zener current density. Using a linear fit to the Zener and forward current at large biases gives a ~6 μΩ-cm^2 resistivity, which may be largely due to the Mo contacts. The PVCRs for InGaAs-5 and InGaAs-6 (10.9, and 9.4 listed in Fig. 5.18b) are comparable to InGaAs-2 and InGaAs-3. However, the PVCR of InGaAs-4 is only 4.8, similar to InGaAs-1. It is not evident why the PVCR of InGaAs-4 is much smaller.

The modeled J-V characteristics for all three structures, with the measured R_{Series}, are also shown in Fig. 5.19a. For clarity, the model was only plotted up to the measured V_P. There is very close agreement between the modeled and measured results for InGaAs-5 and InGaAs-6. Because of the magnitude of R_{Series}, the Zener current density for InGaAs-6 is only slightly larger than InGaAs-5. If R_{Series} was smaller there would be a much larger disparity between the two curves. There is a large difference between the measured characteristic and the model for InGaAs-4, with the predicted/measured J_P of 780/360 A/cm^2. This is most likely due to the doping concentration of the device structure. If the actually doping concentrations differed from the target value by only ±10% (±5% change in N^*), the predicted J_P varies from 430 A/cm^2 up to 1.3 kA/cm^2. Whereas the predicted J_P only ranges 2.6x and 2.2x for InGaAs-5 and InGaAs-6, respectively.

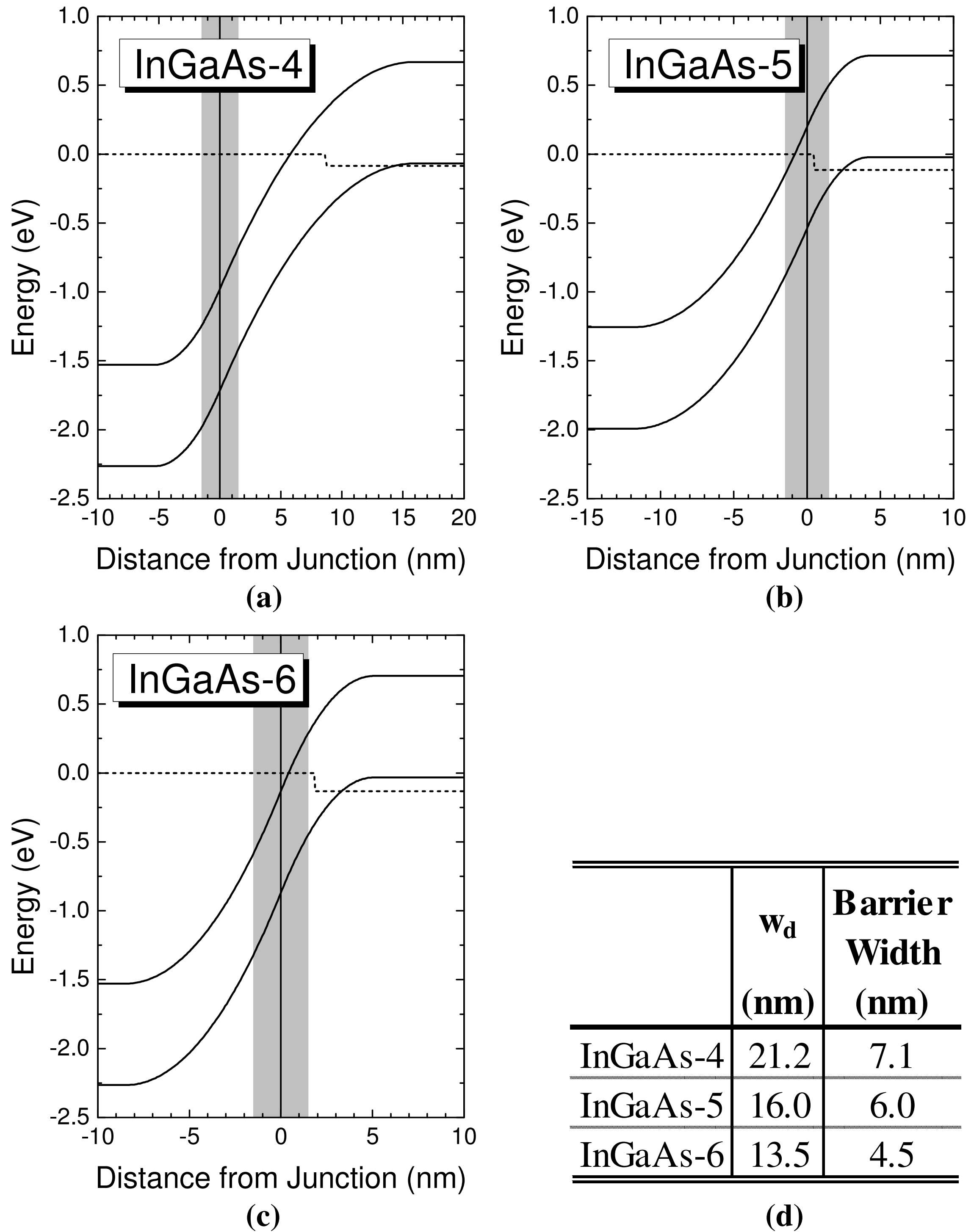

	w_d (nm)	Barrier Width (nm)
InGaAs-4	21.2	7.1
InGaAs-5	16.0	6.0
InGaAs-6	13.5	4.5

Fig. 5.20: Calculated band diagrams for (a) InGaAs-4, (b) InGaAs-5, and (c) InGaAs-6. The bands were calculated with a 0 nm *i*-layer and an applied bias of V_P as predicted by the Kane model. For easy reference, the quasi-Fermi levels were extended into the bandgap. Bottom right, (d) the depletion and tunnel barrier widths are listed.

In Fig. 5.19b, InGaAs-4, InGaAs-5, and InGaAs-6 are added to the $In_{0.53}Ga_{0.47}As$ trendline. As expected, InGaAs-5 and InGaAs-6 appear very close to the trendline. Recall from Chapter 3, material system trendlines are generated with $N_A = N_D$. As a result, there is a small but significant range in J_P for different ratios of N_A/N_D, of the same reduced average (N*). Because of that difference, and the slope of the trendline, the InGaAs-4 data point appears much closer to the model than expected.

Calculated band diagrams are shown for each ETD in Fig. 5.20a-c. The bands were calculated using the target doping concentrations, but with an *i*-layer of 0 nm. The applied bias was set to V_P from the Kane model, and E_f was calculated using the basic 2-bands (Γ-valley only). The quasi Fermi energies ($E_{F,n}$ and $E_{F,p}$) were extended into the middle of the bandgap, for easy reference as to the magnitude of V_A (and hence, V_P). As with the previous $In_{0.53}Ga_{0.47}As$ ETDs, V_P approximately $nkT + E_{F,p}$. Where n is some number, less than two. When $E_{F,p}$ is very close to E_V, V_P seems to decouple from $E_{F,p}$ and becomes constant. The depletion and tunnel barrier widths are listed in Fig. 5.20d. There is a fairly wide range in tunnel barrier widths (7.1 nm down to 4.5 nm), which follows the large range in J_P (from 360 A/cm^2 up to 56 kA/cm^2).

5.4. Conclusions

In this chapter, the deep submicron process developed in Chapter 4 was improved with an extensive area characterization step performed post mesa-isolation etch. This characterization improves estimated junction areas over the entire sample, enabling accurate analysis of BTBT current scaling properties and current densities.

The two ultra-high current density $In_{0.53}Ga_{0.47}As$ ETDs (InGaAs-1 and InGaAs-2) were fabricated with the deep submicron process. For each sample, about 100 area measurements and over 200 I-V measurements were used in the analysis. Line fits to V_P versus I_P plots indicated that the intrinsic V_P for InGaAs-1 and InGaAs-2 is 0.377 V and 0.137 V, respectively. I_P scaled linearly with junction area, for both device structures. The smallest InGaAs-1 devices did fall off

of the trendline, but this was due to a lack of measured junction areas and not non-idealities in the electrostatics. Therefore, there were no observed defects in the scaling properties of the tunnel junctions, down to 47 nm radii. Gaussian fits to J_P histograms yielded average J_P of 975 kA/cm^2 (InGaAs-1) and 210 kA/cm^2 (InGaAs-2). InGaAs-1 is the largest reported homojunction J_P, and second largest overall. This was accomplished not only because of the epitaxial quality and material parameters, but also the magnitude of doping concentration achieved during growth.

Band diagram calculations showed that the 3 nm *i*-layer adds a negligible width to the tunnel barrier. However, BNG and additional electron valleys (Γ- and X-) can drastically alter $E_{F,n}$ and tunnel barrier widths. Comparing the Kane model to experimental results, the basic 2-band model best matches pre-peak BTBT current density for both devices. However, 4-band $E_{F,n}$ modeling is needed to match the shape of the NDR region. Furthermore, a nearly perfect match between the model and experimental results was achieved for InGaAs-2 with BNG was also included. A more appropriate BNG model may result in an improved output for InGaAs-1. Comparing with results form literature, J_P versus N^* plot shows a clear exponential trendline for $In_{0.53}Ga_{0.47}As$, with the basic 2-band Kane model accurately fitting the trendline.

The modeled trendline was used to diagnose and predict the actual doping concentration present in InGaAs-3, which was fabricated using the basic process. The basic process was updated with a Mo, a refractory metal more appropriate for manufacturing. A J_P of 14 A/cm^2 was measured. As predicted from the $In_{0.53}Ga_{0.47}As$ trendline, SIMS analysis confirmed that the reduced average doping of the structure was 4.2×10^{18} /cm^3, resulting from ~1/10 targeted Be incorporation. For this device, the basic Kane model was very accurate in predicting the J-V characteristics. However, the 4-bands model made some small improvements in the forward direction.

The last $In_{0.53}Ga_{0.47}As$ fabricated and characterized were of medium to large current density ETDs. InGaAs-4, InGaAs-5, and InGaAs-6 were found to have J_P of 380 A/cm^2, 7 kA/cm^2, and 56 kA/cm^2, respectively. Unlike the previous devices, SIMS analysis was not

performed to confirm doping concentrations. However, the Kane model accurately predicted the J-V characteristics of InGaAs-5 and InGaAs-6. The model small overestimation for InGaAs-4 may be a mostly due inaccurately assumed doping concentration. All of the experimental results fit on the characteristic trendline for $In_{0.53}Ga_{0.47}As$, which covers five orders of magnitude in current density.

Finally, the results from this chapter show that ultra-high current density ETDs can be fabricated and retain good characteristics when scaled down to deep submicron dimensions. The $In_{0.53}Ga_{0.47}As$ material system follows a simple exponential trendline, which accurately predicts J_P over five orders of magnitude. The Kane model fits the trendline as well as J-V characteristics without any additional fitting parameters. The Kane model has been shown to accurately predict both J_P and J-V characteristics. Therefore, with a given J_P, which is unaffected by R_{Series}, the entire J-V characteristic may be calculated.

References for Chapter 5

[1] D. Pawlik, S. Sieg, S. K. Kurinec, S. L. Rommel, Z. Cheng, J. S. Park, *et al.*, "Alloyed Junction Ge Esaki Diodes on Si Substrates Realised by Aspect Ratio Trapping Technique," *Electron. Lett.,* vol. 44, pp. 930-932, Jul 2008.

[2] D. J. Pawlik, B. Romanczyk, E. Freeman, P. M. Thomas, M. Barth, S. L. Rommel*, et al.*, "Sub-micron Esaki Tunnel Diode Fabrication and Characterization," in *Int. Semicond. Dev. Res. Symp.*, 2009, pp. 1-2.

[3] D. J. Pawlik, P. Thomas, M. Barth, K. Johnson, S. L. Rommel, S. Mookerjea*, et al.*, "Indium Gallium Arsenide on Silicon Interband Tunnel Diodes for NDR-based Memory and Steep Subthreshold Slope Transistor Applications," in *Dev. Res. Conf.*, 2009, pp. 69-70.

[4] S. L. Rommel, D. Pawlik, P. Thomas, M. Barth, K. Johnson, S. K. Kurinec*, et al.*, "Record PVCR GaAs-based Tunnel Diodes Fabricated on Si Substrates using Aspect Ratio Trapping," *IEDM Tech. Digest,* pp. 739-742, 2008.

[5] V. M. Franks, K. F. Hulme, and J. R. Morgan, "An alloy process for making high current density silicon tunnel diode junctions," *Solid-State Electronics,* vol. 8, pp. 343-344, 1965.

[6] K. Ismail, B. S. Meyerson, and P. J. Wang, "Electron resonant tunneling in Si/SiGe double barrier diodes," *Applied Physics Letters,* vol. 59, p. 973, 08/19/ 1991.

[7] S. L. Rommel, T. E. Dillon, M. W. Dashiell, H. Feng, J. Kolodzey, P. R. Berger*, et al.*, "Room temperature operation of epitaxially grown Si/Si0.5Ge0.5/Si resonant interband tunneling diodes," *Applied Physics Letters,* vol. 73, pp. 2191-2193, 10/12/ 1998.

[8] K. Eberl, R. Duschl, O. G. Schmidt, U. Denker, and R. Haug, "Si-based resonant inter- and intraband tunneling diodes," *Journal of Crystal Growth,* vol. 227, pp. 770-776, Jul 2001.

[9] P. See, D. J. Paul, B. Hollander, S. Mantl, I. V. Zozoulenko, and K. F. Berggren, "High performance Si/Si1-Ge-x(x) resonant tunneling diodes," *IEEE Electron Device Letters,* vol. 22, pp. 182-184, Apr 2001.

[10] J. L. Wang, D. Wheeler, Y. Yan, J. L. Zhao, S. Howard, and A. Seabaugh, "Silicon tunnel diodes formed by proximity rapid thermal diffusion," *IEEE Electron Device Letters,* vol. 24, pp. 93-95, Feb 2003.

[11] S. Y. Chung, R. H. Yu, N. Jin, S. Y. Park, P. R. Berger, and P. E. Thompson, "Si/SiGe Resonant Interband Tunnel Diode With f(r0) 20.2 GHz and Peak Current Density 218 kA/cm(2) for K-band Mixed-Signal Applications," *IEEE Electron Device Lett.,* vol. 27, pp. 364-367, May 2006.

[12] N. Holonyak and I. A. Lesk, "Gallium-Arsenide Tunnel Diodes," *Proc. IRE,* vol. 48, pp. 1405-1409, 1960.

[13] T. A. Richard, E. I. Chen, A. R. Sugg, G. E. Hofler, and N. Holonyak, "High-Current Density Carbon-Doped Strained-Layer GaAs (P+)-InGaAs(N+)-GaAs(N+) P-N Tunnel-Diodes," *Appl. Phys. Lett.,* vol. 63, pp. 3613-3615, Dec 1993.

[14] T. P. E. Broekaert and C. G. Fonstad, "Extremely High Current Density, Low Peak Voltage, Pseudomorphic In 0.53Ga0.47As/AlAs/InAs Resonant Tunneling Diodes," 1989, pp. 559-562.

[15] D. J. Day, R. Q. Yang, L. Jian, and J. M. Xu, "Experimental demonstration of resonant interband tunnel diode with room temperature peak-to-valley current ratio over 100," *Journal of Applied Physics,* vol. 73, pp. 1542-4, 02/01 1993.

[16] J. H. Smet, T. P. E. Broekaert, and C. G. Fonstad, "Peak-to-valley current ratios as high as 50:1 at room temperature in pseudomorphic In0.53Ga0.47As/AlAs/InAs resonant tunneling diodes," *Journal of Applied Physics,* vol. 71, p. 2475, 03/01/ 1992.

[17] H. H. Tsai, Y. K. Su, H. H. Lin, R. L. Wang, and T. L. Lee, "P-N DOUBLE-QUANTUM-WELL RESONANT INTERBAND TUNNELING DIODE WITH PEAK-TO-VALLEY CURRENT RATIO OF 144 AT ROOM-TEMPERATURE," *IEEE Electron Device Letters,* vol. 15, pp. 357-359, Sep 1994.

[18] G. M. Cohen, D. Ritter, and C. Cytermann, "High peak tunnel current density Ga0.47In0.53As Esaki diodes," *Electronics Letters,* vol. 31, pp. 1511-1512, 1995.

[19] M. F. Vilela, A. Freundlich, A. Bensaoula, and N. Medelci, "High Performance In0.47Ga0.53As Tunnel Junctions Grown by Chemical Beam Epitaxy on InP and GaAs and Si Substrates," in *IEEE Int. Symp. Circ. Sys.*, 1993, pp. 227-230.

[20] W. L. Chen, G. O. Munns, X. Wang, and G. I. Haddad, "Co-integration of high speed heterojunction bipolar transistors (HBTs) and tunnel diodes," in *High Speed Semiconductor Devices and Circuits, 1995. Proceedings., IEEE/Cornell Conference on Advanced Concepts in*, 1995, pp. 465-474.

[21] N. Shamir, D. Ritter, and C. Cytermann, "Tunnel diode collector contact in InP based PNP heterojunction bipolar transistors," *Solid-State Electronics,* vol. 46, pp. 785-789, 2002.

[22] N. Shamir and D. Ritter, "Reducing the current crowding effect in bipolar transistors by tunnel diode emitter design," *Solid-State Electronics,* vol. 47, pp. 127-130, 2003.

[23] D. Pawlik, M. Barth, P. Thomas, S. Kurinec, S. Mookerjea, D. Mohata*, et al.*, "Sub-micron InGaAs Esaki Diodes With Record High Peak Current Density," in *Dev. Res. Conf.*, 2010, pp. 163-164.

[24] D. Pawlik, B. Romanczyk, P. Thomas, S. Rommel, M. Edirisooriya, R. Contreras-Guerrero*, et al.*, "Benchmarking and Improving III-V Esaki Diode Performance with a Record 2.2 MA/cm2 Peak Current Density to Enhance TFET Drive Current," in *IEEE IEDM Tech. Digest*, 2012, pp. 27.1.1-27.1.3.

[25] E. O. Kane, "Theory of Tunneling," *J. Appl. Phys.,* vol. 32, p. 83, 1961.

[26] W.-S. Cho, M. Luisier, D. Mohata, S. Datta, D. Pawlik, S. L. Rommel, *et al.*, "Full Band Atomistic Modeling of Homo-Junction InGaAs Band-to-Band Tunneling Diodes Including Band Gap Narrowing," *Appl. Phys. Lett.,* vol. 100, p. 063504, 2012.

[27] S. M. Sze and K. K. Ng, "Physics of Semiconductor Devices," Third ed Hoboken, NJ: Wiley-Interscience, 2007, pp. 422-424.

CHAPTER 6

GaAs and InAs Esaki Tunnel Diodes

Previously, the PVCR and J_P of fabricated ETDs [1-4] were directly benchmarked against reports from literature [5-18]. In the last chapter, a characteristic trendline for the $In_{0.53}Ga_{0.47}As$ material system was created with experimental results from literature [18-22] as well as six ETDs from this work [23, 24]. The key results included (i) record high J_P (975 kA/cm^2), (ii) tunnel junctions scaled to deep submicron dimensions (46 nm radii) without any surface leakage or Fermi-level pinning effects observed, (iii) determination of $In_{0.53}Ga_{0.47}As$ characteristic trendline via experimental results and the Kane model, and (iv) accurate modeling of J-V characteristics covering a J_P range of 5 orders of magnitude. [18-27]

This chapter expands on the previous results by expanding the mapping efforts to GaAs and InAs ETDs [24-27]. With its large bandgap (1.4 eV), GaAs will have smaller BTBT current density as compared to $In_{0.53}Ga_{0.47}As$. However, it is another material system with well known material parameters, a readily available source of experienced epitaxial growers, and can be grown as an unstrained homojunction ETD with similar quality as $In_{0.53}Ga_{0.47}As$. Additionally, are part of the ternary $In_{1-x}Ga_xAs$ system, GaAs will represent the BTBT current density floor. Three separate GaAs ETD structures, fabricated with the basic process due to the small J_P expected, will be discussed. Results will be compared with data from literature in order to general a GaAs trendline. Finally, the Kane model will be compared to the experimental results.

InAs has a much smaller bandgap (0.35 eV), enabling much larger BTBT current densities. As such, its characteristic trendline will be shown to represent the ceiling for the $In_{1-x}Ga_xAs$ system. Three InAs ETD structure, fabricated initially using both the basic and deep submicron process, will be discussed. None of the few reports of InAs ETDs from literate [28-30] are appropriate for this work. Therefore, the InAs characteristic trendline is only matched to

the ETDs in this study. As before, the Kane model will be compared with the experimental results. When combined with the GaAs and $In_{0.53}Ga_{0.47}As$ results, the BTBT characteristics for the entire $In_{1-x}Ga_xAs$ system can be interpolated. This makes the entire data set and model very powerful for a large range of homojunction ETD structures.

Finally, a unique result observed with the smallest J_P InAs ETDs will be discussed. Specifically, an observed NDR that is due to Mo and Ta contacts to p^{++} InAs. This is the first room temperature report of this phenomenon, and was only observed after the initial fabrication runs. It is proposed that Fermi pinning due to an undesirable interfacial oxide at the InAs surface is the main cause.

6.1. GaAs Esaki Diodes

The GaAs ETDs (Fig. 6.1a) follow a similar structure as the medium current density $In_{0.53}Ga_{0.47}As$ ETDs from Section 5.3. The anode was only 50 nm thick, since these structures were grown directly on P^+ GaAs substrates to help minimize R_{Series}. Additionally, the GaAs ETDs were expected to have low current density, reducing the sensitivity to R_{Series}. As before, a 3 nm *i*-layer preceded the 60 nm cathode. All three GaAs ETDs targeted the same N_D (Be) concentration of 3×10^{19} /cm^3. The N_A (Si) concentration was systematically increased from 5×10^{18} /cm^3, to 1×10^{19} /cm^3, to 5×10^{19} /cm^3 for GaAs-1, GaAs-2, and GaAs-3 (Fig. 6.1b),

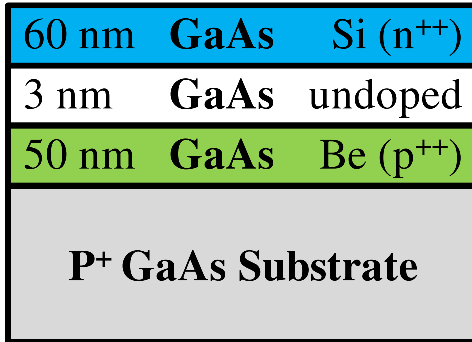

(a)

Device	N_D ($\times10^{19}$ cm^{-3})	N_A ($\times10^{19}$ cm^{-3})	J_P (/cm^2)	PVCR
GaAs-1	3	0.5	11 μA	1.1
GaAs-2	3	1	45 mA	7.5
GaAs-3	3	5	56 A	16

(b)

Fig. 6.1: Left, (a) Schematic diagram of GaAs ETD structures. Right, (b) table of target doping concentrations, as well as measured J_P and PVCR for GaAs-1, GaAs-2, and GaAs-3.

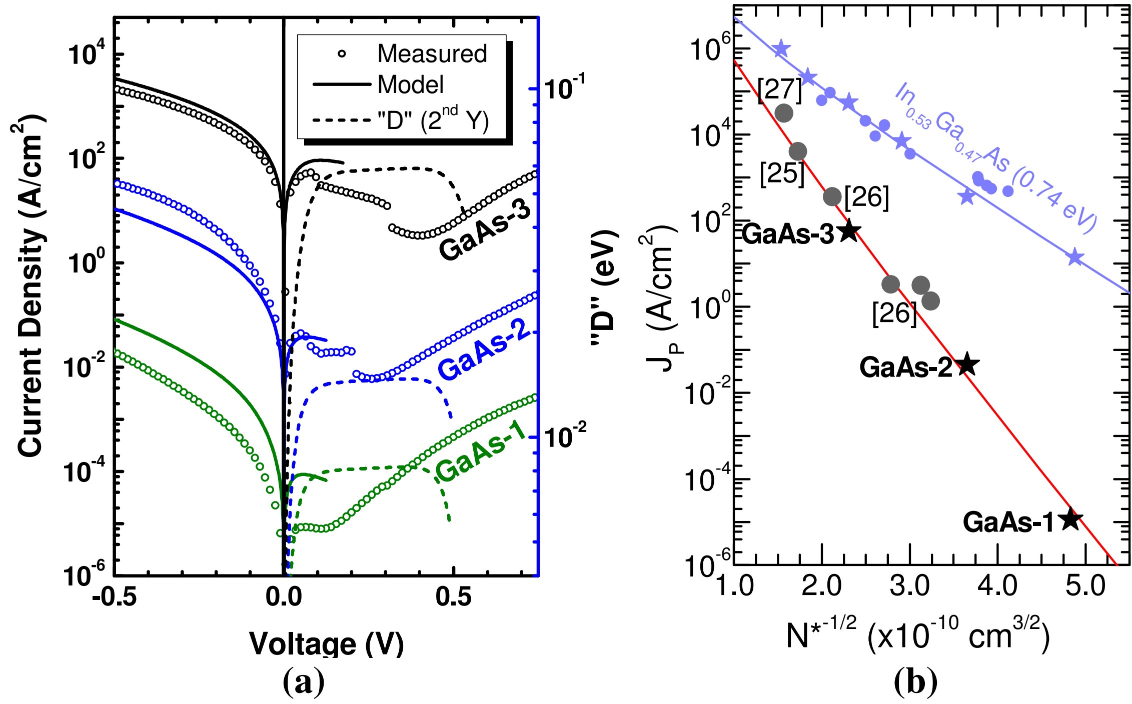

Fig. 6.2: Left, (a) typical J-V characteristics (symbols), modeling results (solid line), and "D" (dashed line; right y-axis) for GaAs-1, GaAs-2, and GaAs-3. Right, (b) GaAs trendling (solid line) including data points from literature (circles) and this work (stars) [18-27]. $In_{0.53}Ga_{047}As$ ETD trendline included as reference.

respectively.

Fabrication followed the basic process, similar to the medium current density $In_{0.53}Ga_{0.47}As$ ETDs. That is, there was no activation anneal. Blanket Mo was deposited via sputtering as the contact metal. Contact lithography and plasma etch defined metal 1 contact, followed by mesa isolation etch. Limited optical microscope inspection was used to quickly assess junction areas. With its large bandgap (1.42 eV), it was known that the current density of the GaAs ETDs would be small, potentially much smaller than any other ETDs fabricated for this work. Therefore, large junction areas were needed to prevent current magnitudes from becoming too small.

Table 6.1: Modeling results for all three GaAs ETDs. As expected, w_d, tunnel barrier width, $E_{F,p}$, E_V, and J_P proportionately increase with each other. $E_{F,p}$ for GaAs-1 is greater than E_V, and therefore lies within the bandgap.

	w_d (nm)	Barrier Width (nm)	$E_{F,n}$-E_C (eV)	E_V-$E_{F,p}$ (eV)	n	J_P (/cm^2)	V_P (V)
GaAs-1	25.2	18.8	0.558	-0.0125	2.68	88.1 uA	0.057
GaAs-2	19.1	14.1	0.558	0.0100	2.20	37.9 mA	0.067
GaAs-3	12.2	8.9	0.558	0.0864	0.835	92.2 A	0.108

6.1.1. Results for GaAs ETDs

Typical J-V characteristics for GaAs-1, GaAs-2, and GaAs-3 are shown in Fig. 6.2a. There is negligible R_{Series} present in the measurements, with V_P remaining less than 0.1 V for all ETDs. The magnitude of current density is very small, ranging seven orders of magnitude, and is largely attributed to the large bandgap (large tunnel barrier results in small tunneling probabilities) and low p-type concentration. From Fig. 6.1b, average measured J_P is 11μA/cm^2, 45 mA/cm^2 and 56 A/cm^2, for GaAs-1, GaAs-2, and GaAs-3, respectively. The maximum PVCR increases with J_P, from 1.1, to 7.5, to 16. The increase in PVCR is largely attributed to the ratio of $E_{F,p}/E_{F,n}$, discussed below.

The characteristic trendline for GaAs (Fig. 6.2b) is below and much steeper than the previously established $In_{0.53}Ga_{0.47}As$ trendline. Several GaAs ETDs from literature [25-27] achieved much higher J_P, because of the doping concentrations they were able to obtain. In a departure from using SIMS to establish doping concentrations, Oh *et al.* [26] used capacitance measurements to extract depletion widths. For this work, the depletion widths were used to back out N^* for accurate placement in the figure. The trendline calculated from the is practically the same as the least squares exponential line fit to the data points (not shown here). Furthermore, the trendline accurately predicts J_P over 9.5 orders of magnitude, from a medium J_P of 31 kA/cm^2 [27] down an ultra small 14.5 μA/cm^2 from GaAs-1. This occurs over the same approximate doping range as for the $In_{0.53}Ga_{0.47}As$ ETDs.

$$V_P = E_{F,\mathrm{minor}} + n \times kT \quad (6.1)$$

Key model results are listed in Table 6.1 and calculated band diagrams shown in Fig. 6.3. The calculated depletion (w_d) and tunnel barrier widths rapidly decrease as N_A increases, resulting

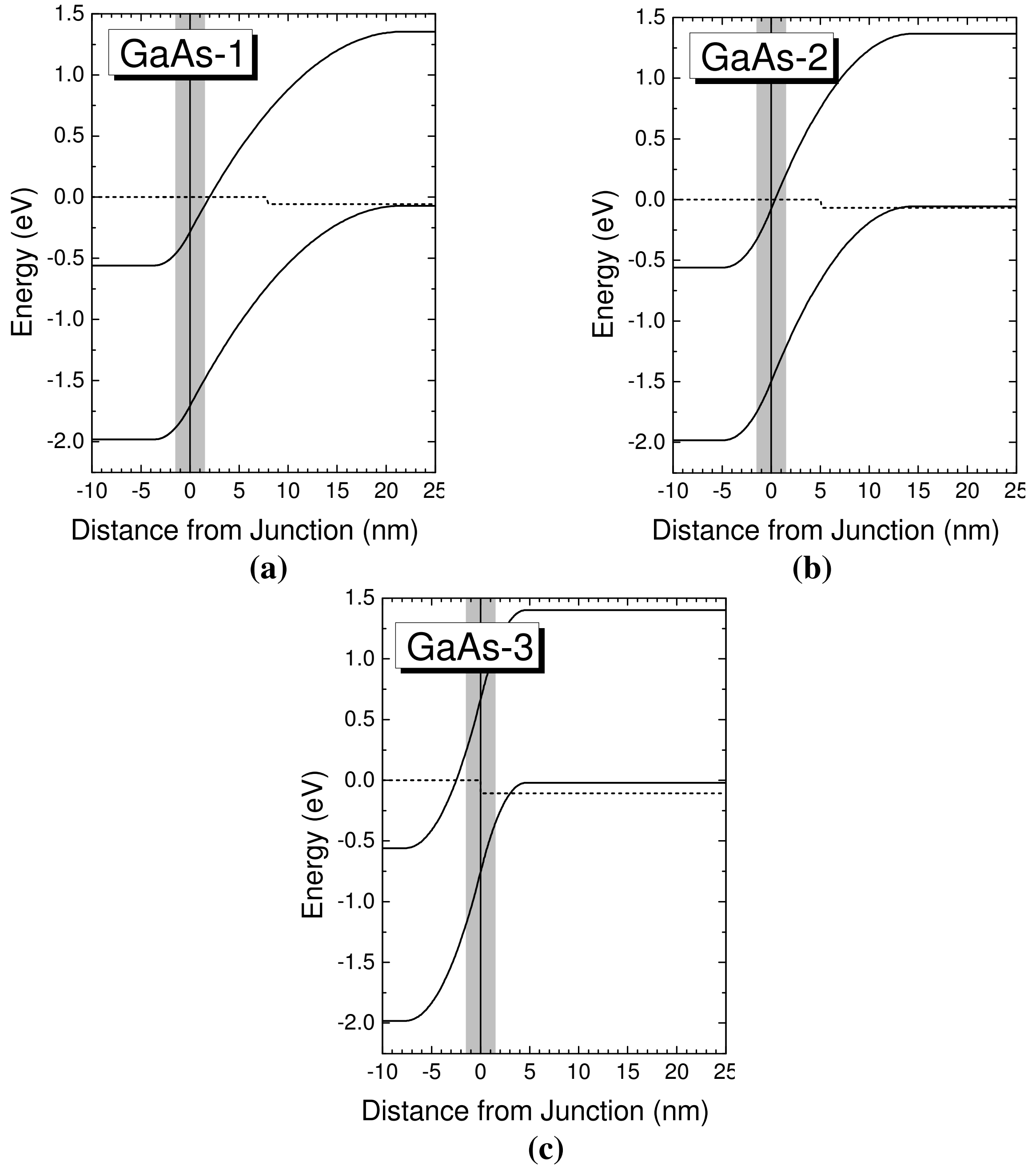

Fig. 6.3: Calculated band diagrams at a bias of V_P for (a) GaAs-1, (b) GaAs-2, and (c) GaAs-3. Only 2-bands $E_{F,n}$ (Γ-valley) calculations were available. Quasi Fermi energies were extended into the bandgap for easy reference. Shaded region is the *i*-layer.

in exponentially larger increases in J_P. Due to its large DOS for holes (~9.7×10^{18} /cm^3), $E_{F,p}$ is 12.5 meV above E_V for GaAs-1, and only 10 meV below E_V for GaAs-2. Consequentially, V_P is small, nearly constant, decoupled from $E_{F,p}$, and n becomes large (6.1). Since N_A for GaAs-3 is relatively large, E_V - $E_{F,p}$ is big enough to control V_P, reducing n to ~0.8.

The modeled J-V characteristics for the GaAs ETDs (Fig. 6.2a) are shown for reverse bias, and a little beyond V_P in forward. As with the band diagram calculations, the model assumes 2-bands only (Γ-valley). The model accurately predicts the current density for GaAs-2 and GaAs-3, up to V_P. There is a large discrepancy between the model and measurements for GaAs-3. For these ultra low current densities, the differences are likely due to the unknown active doping concentrations. A ±10% doping variation (±5% N*) in GaAs-1 results in a 17x range in J_P. Even the uncertainty associated with SIMS may not sufficiently characterize the doping profile. However, the model will predict the BTBT current density over the region of interest if J_P is matched to the measured value.

The model does not accurately predict the NDR region. With the small DOS for electrons (~4×10^{18} /cm^3), $E_{F,n}$ (0.56eV) is large enough to start filling the second valley (L-valley) which is ~0.5 eV above the Γ-valley. As a result, the modeled NDR is much longer than the measured NDR. Additionally, $E_{F,n}$ is much greater than $E_{F,p}$, causing the overlap integral (D, shown in Fig. 6.2a) to quickly plateau in forward bias, and remain there for almost the entire

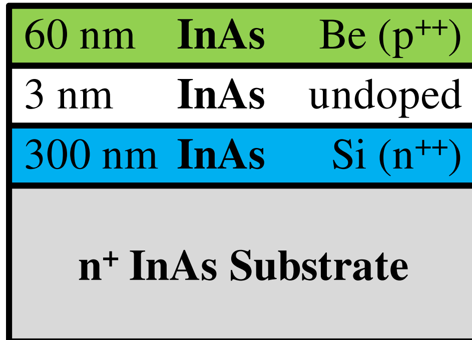

(a)

Device	N_D (x10^{19}	N_A cm^{-3})	J_P (/cm^2)	PVCR
InAs-1	0.3	1.8	2.3 kA	2.0
InAs-2	1	1.8	38 kA*	NA
InAs-3	3	1.8		

(b)

Fig. 6.4: Left, (a) Schematic diagram of InAs ETD structures. Right, (b) table of target doping concentrations, as well as measured J_P and PVCR for InAs-1, InAs-2, and InAs-3.

range. Consequentially, in GaAs-1 the BTBT current density post-peak does not have much "time" to drop off before J_{Excess} dominates. As a result, the measured PVCR is very smaller and likely cannot be improved without increasing N_A. For GaAs-2, J_{Excess} did not increase as quickly as J_P, shifting V_P to the right and causing a large increase in PVCR. The PVCR would be increased (and potentially maximized) when $E_{F,n} = E_{F,p}$. Because for that situation, D will consistently rise to $V_P = E_{F,n}$, and then immediately drop off.

6.2. InAs Esaki Diodes

Unlike the previous ETDs, InAs-1, InAs-2, and InAs-3 (Fig. 6.4a) were grown with the p-type layer (anode) on top of the n-type (cathode) layer, in order to help maintain sharp junction profiles. Furthermore, only n-type InAs substrates were available (p-type GaSb has a small lattice mismatched). The p-type dopant species, Be, has relatively large surface segregation. If it

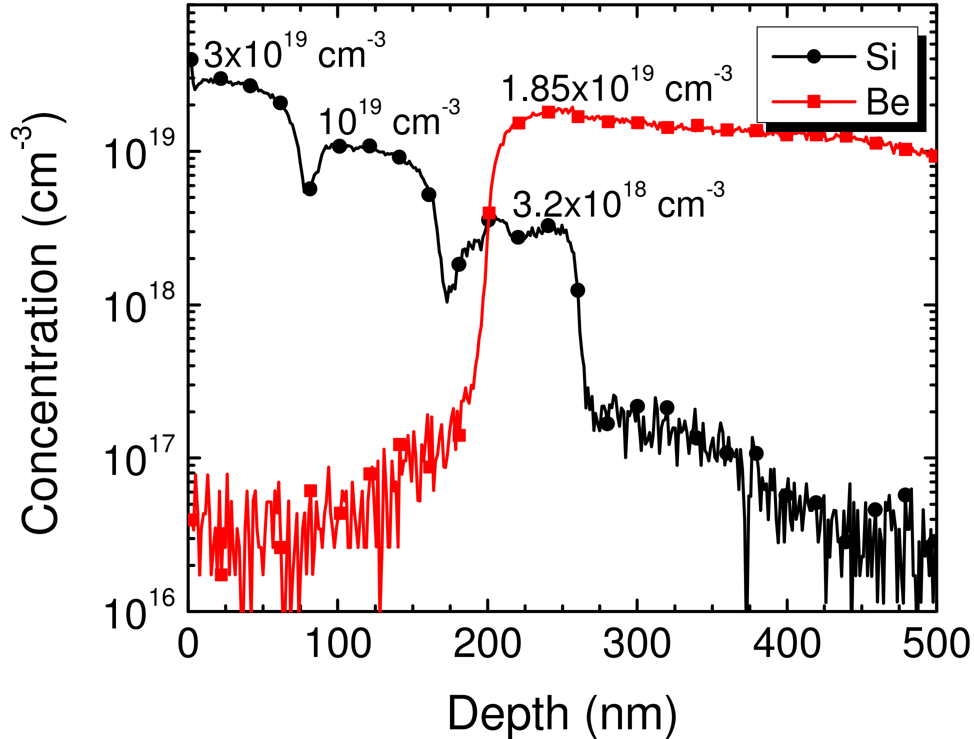

Fig. 6.5: SIMS results of the doping calibration growth for the InAs ETDs. Three Si steps and one Be mesa indicate the doping concentrations for all three InAs ETDs.

were placed in the bottom layer, it may have significantly segregated through the *i*-layer and into the cathode. This could have negatively impacted the I-V characteristics. Since it was expected that InAs would have poor results due to its small bandgap (0.35 eV), it was even more important to consider dopant surface segregation effects.

With the cathode on the bottom, the InAs ETDs were grown by MBE on top of n^+ InAs substrate. The cathode was grown with three separate doping concentrations using Si (Fig. 6.4b); (i) 3×10^{18} /cm^3 (InAs-1), (ii) 1×10^{19} /cm^3 (InAs-2), and (iii) 3×10^{19} /cm^3 (InAs-3). The anode was grown to 60 nm thick and doped with Be at a concentration of 1.8×10^{19} /cm^3 for all InAs ETDs. Additionally, Be concentration was held constant because of concerns over the DOS for holes (6.7×10^{18} /cm^3) and the maximum achievable Be (1.8×10^{19} /cm^3) concentration. Under these conditions, E_V-$E_{F,p}$ will only be ~50 meV, which does not leave a lot of room for change. Therefore, in order to see the largest spread n J_P, Be was maximized. As with the previous homojunction ETDs, a 3 nm *i*-layer was inserted between the anode and cathode.

A doping calibration growth was used to accurately estimate the average doping concentrations that will be present in the final InAs ETD structures. All four targeted coping

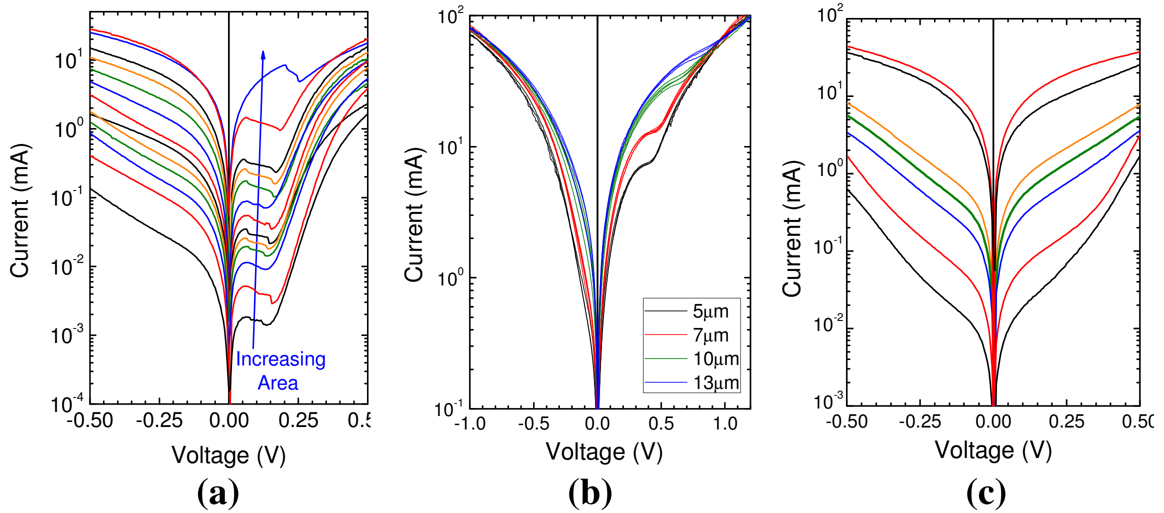

Fig. 6.6: I-V characteristics for (a) InAs-1, (b) InAs-2, and (c) InAs-3. InAs-1 shows clear NDR and I_P scaling with area. InAs-2 shows strong kinks, indicating the location an magnitude of the pure BTBT J_P. InAs-3 mostly looks ohmic.

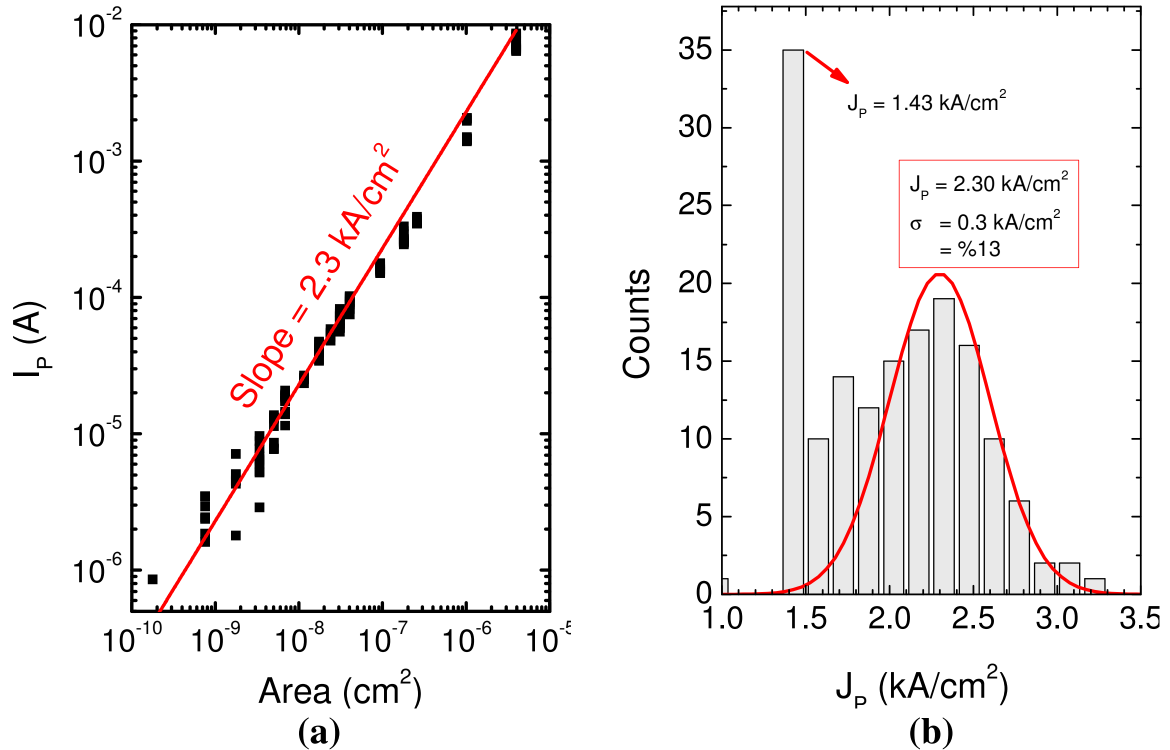

Fig. 6.7: Left, (a) measured I_P versus junction area. Right, (b) histogram of J_P (167 measurements), with Gaussian fit indicating average J_P of 2.3 kA/cm^2.

concentrations were grown in a 300 nm InAs layer. SIMS analysis was used to verify the doping concentrations (Fig. 6.5). However, junction profile information cannot be extracted from the calibration growth.

All InAs ETDs were fabricated using the basic process, similar to the GaAs ETDs. That is, there was no activation anneal. Blanket Mo was deposited as the contact metal, via sputtering. Contact lithography and plasma etch defined metal 1 contact, followed by mesa isolation etch. Limited optical microscope inspection was used to quickly assess junction areas. Even though InAs has a small bandgap (0.35 eV), the relatively small reduced doping average (N^*), from the small doping concentrations, will limit current densities below 200 kA/cm^2. Therefore, deeply scaled junction areas were not needed. However, a companion InAs-1 piece was fabricated using the deep submicron process.

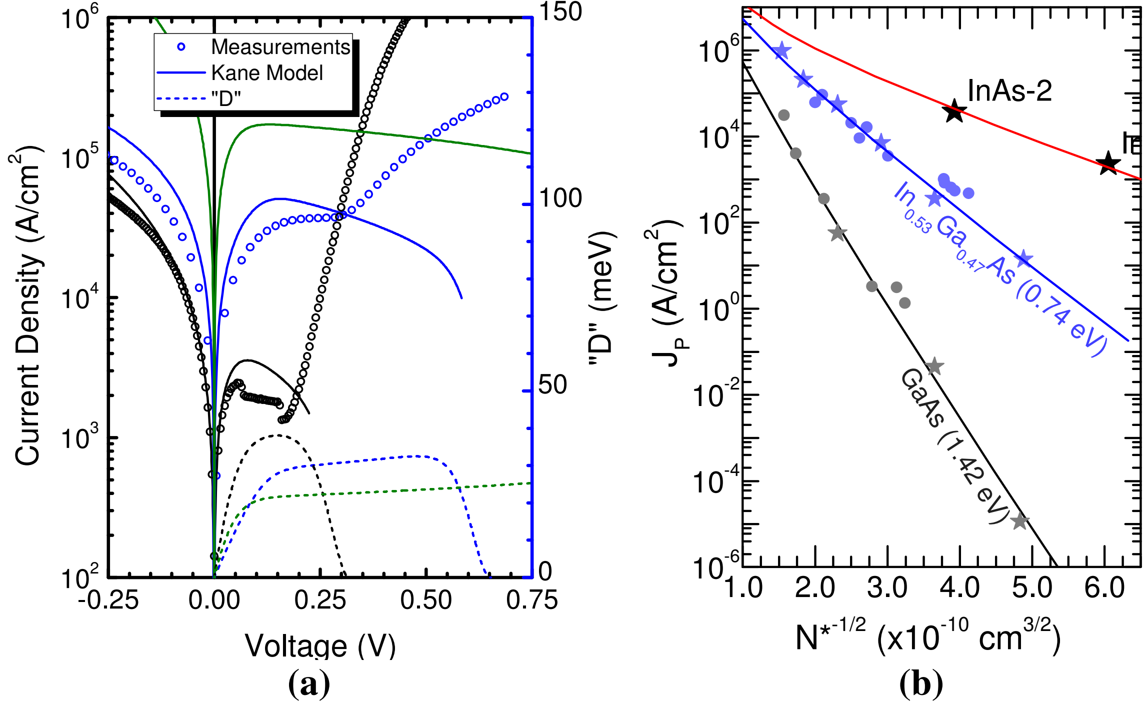

Fig. 6.8: Left, (a) measured J-V characteristics (symbols) as well as modeled characteristics (solid line) and "D" (dashed line). Right, (b) characteristic trendlines for GaAs, $In_{0.53}As_{0.47}As$, and InAs [18-27]. The InAs trendline, calculated from the Kane model, is greater than the previous trendlines.

6.2.1. InAs ETD Electrical Results

The DC I-V electrical characteristics measured for (a) InAs-1, (b) InAs-2, and (c) InAs-3 are shown in Fig. 6.6. In forward bias, InAs-1 shows clear NDR with PVCR up to 2.0 and I_P that appears to scale well with just area. The R_{Series} becomes significant above ~1 mA of current, and shifted V_P for the largest devices only. InAs-2 exhibits clear "kinks", similar to backward diodes. The current magnitude of the kink increases linearly with junction area, indicating that this is an ETD with large I_{Excess} masking, or overtaking, the I_P and I_V. The magnitude of the kink is indicative of the BTBT J_P, but not a precise measurement since it also includes parasitic. There is a significant amount of R_{Series} present, shifting the kink voltage to the right as the junction area (and current) increases. The kink becomes less pronounced as the shift increases. Therefore, the smallest devices show the best characteristics. Finally, InAs-3 did not exhibit any NDR or kink-like behavior. As a result, the BTBT current density for InAs-3 could not be characterized.

From Fig. 6.7a, I_P does in fact scaling linearly with junction area. The slope of the line fit gives a preliminary indication of the average J_P. The Gaussian fit to the histogram in Fig. 6.7b gives a J_P of 2.3 kA/cm^2, with a standard deviation of 300 A/cm^2 (13%). There is a second peak in the histogram centered at 1.43 kA/cm^2. This peak is from a second set of InAs-1 samples whose areas were not corrected for, and therefore the current densities calculated from this set is suspect. However, these samples did provide interesting characteristics in reverse bias, which is discussed in Section 6.2.2. From the position of the kinks, the approximate J_P of InAs-2 is calculated to be 38 kA/cm^2.

In Fig. 6.8a are two representative J-V curves for InAs-1 and InAs-2 (symbols). From the figure, it is clear that InAs-2 has greater BTBT current density and R_{Series}. There are very few reports of InAs ETDs in literature [28-30], none of which fit the criteria for inclusion in this analysis. Therefore, there only two data points to assess the trendline (Fig. 6.8b), and any line fit would be superfluous. The characteristic InAs trendline as calculated by the Kane model (solid line) is shown in Fig. 6.8b, and clearly fits the InAs-1 and InAs-2 data points. Due largely to its small bandgap, the InAs trendline is greater than both the GaAs and $In_{0.53}Ga_{0.47}As$ trendlines. However, InAs has the shallowest slope, indicating a smaller sensitivity to doping variation. In other words, only small doping concentrations are needed to achieve medium BTBT current densities. However, it only possible to increase J_P by a few orders of magnitude, even with maximized doping concentrations.

Table 6.2: Modeling results for all three InAs ETDs. As expected, w_d and tunnel barrier width decrease as doping, $E_{F,n}$, and J_P increase. Interestingly, V_P and "n" significantly increases, even though $E_{F,p}$ remains constant.

	w_d (nm)	Barrier Width (nm)	$E_{F,n}$-E_C (eV)	E_V-$E_{F,p}$ (eV)	n	J_P (/cm^2)	V_P (V)
InAs-1	19.6	11.6	0.269	0.0493	1.11	3.57 kA	0.078
InAs-2	15.3	6.0	0.604	0.0493	2.15	50.7 kA	0.105
InAs-3	15.1	3.5	1.260	0.0493	3.120	172 kA	0.130

Modeled J-V characteristics for all three InAs ETDs are shown in Fig. 6.7a, with the final results listed in Table 6.2. A 150 μΩ-cm^2 R_{Series} was added to InAs-2, for improved matching with the measured data. As can be seen, the modeled J-V characteristics for InAs-1 and InAs-2 is greater than the measurements. However, due to its shallow slope, both devices lie much closer to the InAs trendline (Fig. 6.8b) than is apparent from the modeled J-V characteristics. Furthermore, a 10% doping variation for InAs-1 and InAs-2 outputs a low/high J_P of 2.3/5.6 kA/cm^2 and 38/71 kA/cm^2, respectively. It is likely that the actual doping concentration in the ETDs is approximately 10% lower than the target values.

As with GaAs, $E_{F,n}$ was calculated with only 2-bands (Γ-valley only). The L-valley is ~0.7 eV above the direct bandgap, and therefore initially one would expect that it would not play a large role in the Fermi energy calculations. However, because of its small DOS for electrons (1.2×10^{17} /cm^3), the L-valley will start to limit $E_{F,n}$ starting with N_D of ~3.5×10^{18} /cm^3. Therefore, the predicted NDR for InAs-1 looks to be reasonable. However, for InAs-2 and InAs-3, the NDR region is drawn-out due to the extended mesa-like overlap integral (D) associated with the calculated Fermi energies. Regardless, except at low current densities (N_D concentrations), $E_{F,n}$ will be much greater than $E_{F,p}$, causing "D" to be mesa-like in shape. Combined with a naturally

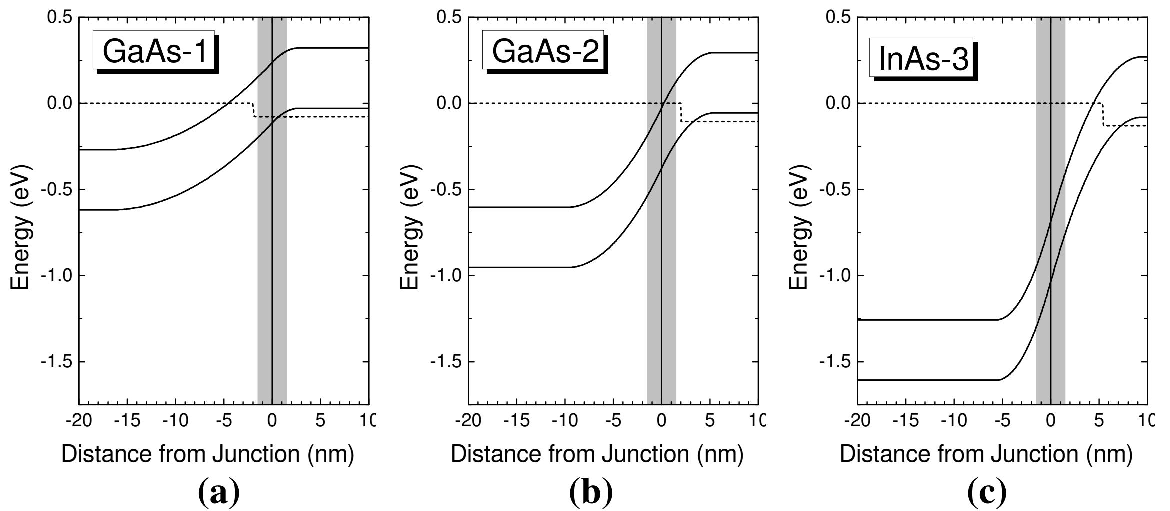

Fig. 6.9: Calculated band structure for (a) InAs-1, (b) InAs-2, and (c) InAs-3. $E_{F,n}$ was calculated using only the Γ-valley.

larger V_P due to the small bandgap of InAs, and any reasonable magnitude in J_{Excess} will begin to swamp out J_V, negating the NDR and forming a "kink" in the characteristic. Additionally, J_{Excess} will typically be relatively large due to InAs small bandgap. Therefore, as a homojunction ETD, is unlikely that InAs can exhibit large J_P.

Contrary to previous ETDs, the maximum "D" value decreased with increasing doping concentration. Recall from Chapter 3, the overlap integral has an inverse dependence on ξ_{ave}/E_G in addition to the direct dependence on $E_{F,smaller}$. Previously, N_A was the main species varied. Due to large DOS for holes on the systems under investigation, the change in $E_{F,p}$ was more significant than the relatively small increase in ξ_{ave}/E_G. However, for the InAs ETDs, the similar increases in $E_{F,n}$ caused very large increases in ξ_{ave}/E_G, as can be seen in the calculated band diagrams in Fig. 6.9. Consequentially, the maximum "D" value decreased with increasing N_D.

Additionally, because of the small bandgap and relatively large $E_{F,n}$, the average electric field (ξ) does not change as rapidly for InAs, then in the previous systems. Consequentially, the tunnel barrier thickness does not change much with V_A. Therefore, V_P shifts to larger than expected biases where Fermi-Dirac statistics requires that greater percentages of available states are filled with electrons in the cathode.

6.2.2. NDR from Metal on P$^+$ InAs Contacts

The first couple iterations of InAs-1 fabrication looked at (i) Ta, (ii) Mo, and (iii) Al contacts using the basic fabrication process. The ideal metal workfunction (ϕ_m) for Ta (4.2 eV), Mo (4.6 eV), and Al (4.2 eV) indicates that these metals should form Schottky contacts. Unexpectedly, NDR was observed in reverse bias during electrical characterization of the Mo and Al contacts (Fig. 6.11). As can be seen, the reverse bias peak scales with the area of the ETD under test with a smaller J_P. Therefore, is clear that the observed NDR is related to the InAs mesa and contact metal of the forward biased ETD structure. Otherwise, the I_P would be constant

or scaling independent of the device under test (DUT), such as the forward bias characteristic of the ETD used as the virtual short to ground.

The Mo contact had a much larger J_P of 720 A/cm^2 versus the Al contact, with 160 A/cm^2 J_P. It is believed that the metal-semiconductor interface is to the root source of this NDR. Several past reports [31-35] have observed this phenomenon at cryogenic temperatures, but never before has it been reported with room temperature measurements. It has been proposed that the key to forming NDR at the metal-InAs interface is due to the unusual level of Fermi pinning for InAs. Unlike most other III-V semiconductors, the surface E_F will be pinned near the conduction band. Thus, with contact to p-type InAs, a surface inversion channel is formed (Fig. 6.10a). Generally it is believed that the Fermi pinning is due to thin dielectrics, on the order of mono-layers, forming on the InAs surface. After fabrication of these samples, it was discovered that a small leak was present in the system. Consequently, a low base pressure was not achieved (~5 μTorr), and therefore that was a lot of O_2 in the chamber during deposition. This was likely the source of a non-ideal interfacial layer, providing Fermi pinning of the InAs surface. Subsequent InAs ETD fabrication had very low base pressures (<1 μTorr), much less O_2 present,

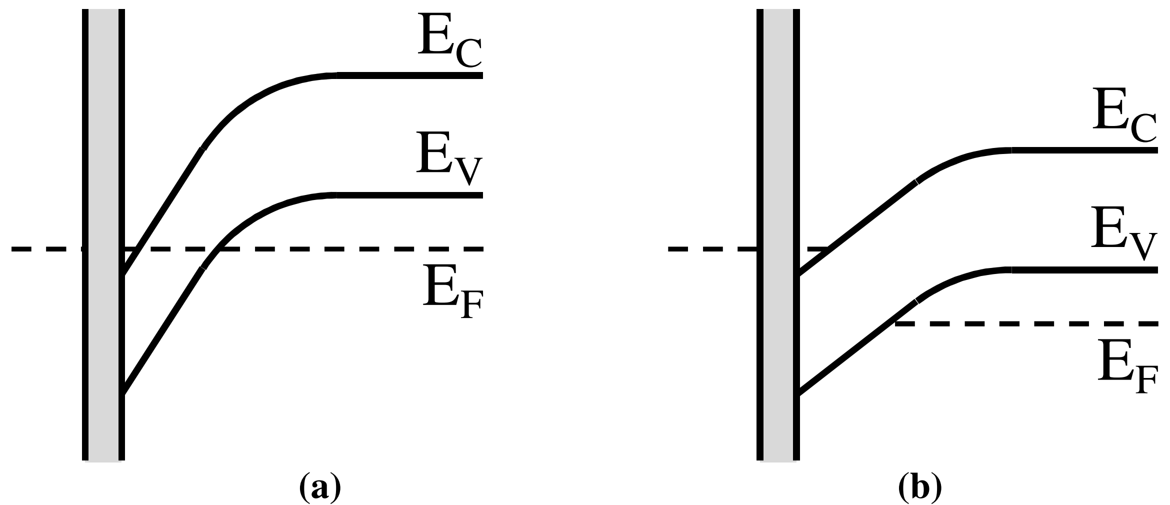

Fig. 6.10: Proposed band diagrams of the metal-InAs interface at (a) equilibrium and (b) with an applied bias. Between the metal and InAs is an ultra thin insolative layer providing an additional tunnel barrier, and Fermi level pinning at the interface.

and therefore a better metal-InAs interface, with less Fermi pinning.

When the metal-InAs junction is under a small positive bias (the ETD is reverse biased), electrons in the metal contact can tunnel into the surface channel, and then through the bandgap, into the hole states present below E_V and above E_F. Therefore, as expected, an immediate rise in current would be measured. Biasing a little further aligns the InAs bandgap with the E_F in the metal region, significantly blocking current flow from the metal to InAs (Fig. 6.10b). As with basic ETDs, one would expect that increased Fermi energies (below E_V in the p^+ InAs bulk, and above E_C at the pinned surface) would increase J_P. The doping in this study is 20x to 200x greater than in those from literature [31-35]. At the concentrations used in the papers, $E_{F,p}$ is not even below E_V. However, cooling to cryogenic temperatures would increase $E_{F,p}$ and reduce I_{Excess}, making an NDR visible. Whereas, in this study $E_{F,p}$ is already shifted bellow E_V, enabling the observance of NDR at room temperature.

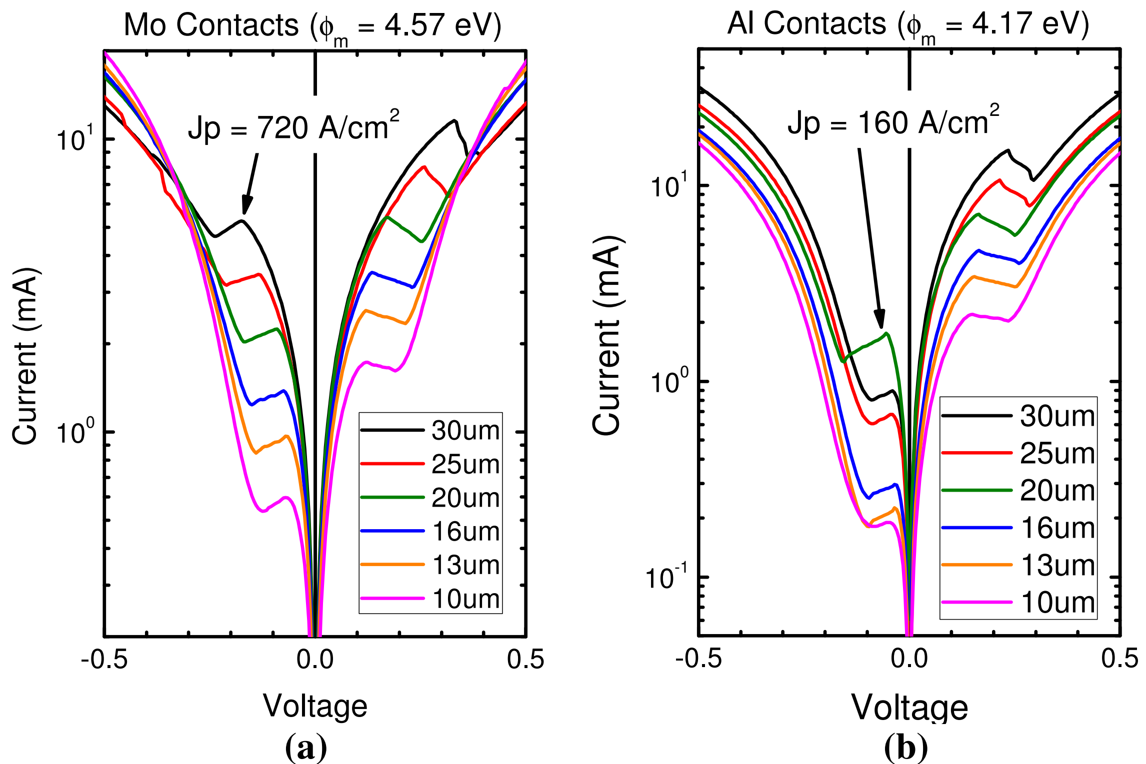

Fig. 6.11: Measured I-V characteristics displaying NDR in reverse bias due to the (a) Mo and (b) Al metal contacts to p^{++} InAs.

6.3. Conclusions

The BTBT characteristics of GaAs and InAs were investigated. With these result, and those for $In_{0.53}Ga_{0.47}As$ from Chapter 5, the entire $In_{1-x}Ga_xAs$ ternary system is known. The GaAs ETDs represent the BTBT floor, whereas InAs has a greater trendline than the other two. However, due to the material properties and maximum achievable doping for InAs, it cannot achieve J_P as high as $In_{0.53}Ga_{0.47}As$. Therefore, $In_{0.53}Ga_{0.47}As$ would be the best candidate for an unstrained homojunction TFET. On the other hand, one is not concerned about turning off the BTBT (leakage currents), than InAs may still be beneficial. Conversely, it low BTBT current densities are needed, then GaAs is an ideal material system.

Three GaAs ETDs were fabricated with measured J_P of 11 μA/cm^2, 45 mA/cm^2, and 56 A/cm^2 for GaAs-1, GaAs-2, and GaAs-3, respectively. Over 6.5 orders of magnitude in J_P were covered, ranging from the ultra low current density (GaAs-1) to moderately low (GaAs-3). A few devices from literature achieved moderate to high current density [25-27]. Ultimately, the maximum achievable doping concentration combined with the bandgap of GaAs (1.42 eV) limits J_P to less than 100 kA/cm^2. As expected, the characteristic trendline of GaAs was less than $In_{0.53}Ga_{0.47}As$. However, it is a much steeper slope, covering 10.5 orders of magnitude compared to five for $In_{0.53}Ga_{0.47}As$. This clearly shows that GaAs is much more sensitive to doping variation. Additionally, the Kane model accurately predicts the GaAs characteristic trendline and J-V characteristics.

Three InAs ETDs were fabricated. However, InAs-3, which had the largest doping, did not exhibit any NDR or characteristic "kinks" indicating the presence of J_P, most likely a result of very large excess currents. InAs-2 behaved more like a backwards diode, due to a sever "kink" at approximately the location of its BTBT J_P at ~38 kA/cm^2. InAs-1 was the only device to clearly show a peak, worth a J_P of 2.3 kA/cm^2 and maximum PVCR of 2.0. Without any extra data points from literature, only InAs-1 and InAs-2 were used to verify the characteristic trendline

predicted by the Kane model. The Kane model matched fairly close to the experimental results, validating the model's accuracy for InAs. In addition to the InAs homojunction results, NDR in reverse bias was observed for the initial InAs-1 runs using Mo and Al contacts. The was explained as a surface inversion channel due to Fermi pinning, a phenomenon that is so far unique to InAs. This is the first report of metal to p^+ InAs NDR at room temperature. The measured J_P values were 720 A/cm^2 and 160 A/cm^2 for Mo and Al, respectively. Further experimentation would need to be performed in order to determine the controllability of the characteristic.

Finally, this chapter completes the comprehensive mapping of the $In_{1-x}Ga_xAs$ ternary system. Experimental results were the basis of determining the range of achievable J_P, and characteristic trendlines. The Kane model was shown to accurately fit the system and predict device characteristics. The results from this work may be used to design homojunction ETDs with specific device characteristics, or judge the suitability of a particular $In_{1-x}Ga_xAs$ system for a particular application. Furthermore, the experimental results may be used to calibrate finite element BTBT models in order to improve their ability to quantitatively predict the behavior of more complicated and potentially useful device structures.

References for Chapter 6

[1] D. Pawlik, S. Sieg, S. K. Kurinec, S. L. Rommel, Z. Cheng, J. S. Park, *et al.*, "Alloyed Junction Ge Esaki Diodes on Si Substrates Realised by Aspect Ratio Trapping Technique," *Electron. Lett.,* vol. 44, pp. 930-932, Jul 2008.

[2] D. J. Pawlik, B. Romanczyk, E. Freeman, P. M. Thomas, M. Barth, S. L. Rommel, *et al.*, "Sub-micron Esaki Tunnel Diode Fabrication and Characterization," in *Int. Semicond. Dev. Res. Symp.*, 2009, pp. 1-2.

[3] D. J. Pawlik, P. Thomas, M. Barth, K. Johnson, S. L. Rommel, S. Mookerjea, *et al.*, "Indium Gallium Arsenide on Silicon Interband Tunnel Diodes for NDR-based Memory and Steep Subthreshold Slope Transistor Applications," in *Dev. Res. Conf.*, 2009, pp. 69-70.

[4] S. L. Rommel, D. Pawlik, P. Thomas, M. Barth, K. Johnson, S. K. Kurinec, *et al.*, "Record PVCR GaAs-based Tunnel Diodes Fabricated on Si Substrates using Aspect Ratio Trapping," *IEDM Tech. Digest,* pp. 739-742, 2008.

[5] V. M. Franks, K. F. Hulme, and J. R. Morgan, "An alloy process for making high current density silicon tunnel diode junctions," *Solid-State Electronics,* vol. 8, pp. 343-344, 1965.

[6] K. Ismail, B. S. Meyerson, and P. J. Wang, "Electron resonant tunneling in Si/SiGe double barrier diodes," *Applied Physics Letters,* vol. 59, p. 973, 08/19/ 1991.

[7] S. L. Rommel, T. E. Dillon, M. W. Dashiell, H. Feng, J. Kolodzey, P. R. Berger*, et al.*, "Room temperature operation of epitaxially grown Si/Si0.5Ge0.5/Si resonant interband tunneling diodes," *Applied Physics Letters,* vol. 73, pp. 2191-2193, 10/12/ 1998.

[8] K. Eberl, R. Duschl, O. G. Schmidt, U. Denker, and R. Haug, "Si-based resonant inter- and intraband tunneling diodes," *Journal of Crystal Growth,* vol. 227, pp. 770-776, Jul 2001.

[9] P. See, D. J. Paul, B. Hollander, S. Mantl, I. V. Zozoulenko, and K. F. Berggren, "High performance Si/Si1-Ge-x(x) resonant tunneling diodes," *IEEE Electron Device Letters,* vol. 22, pp. 182-184, Apr 2001.

[10] J. L. Wang, D. Wheeler, Y. Yan, J. L. Zhao, S. Howard, and A. Seabaugh, "Silicon tunnel diodes formed by proximity rapid thermal diffusion," *IEEE Electron Device Letters,* vol. 24, pp. 93-95, Feb 2003.

[11] S. Y. Chung, R. H. Yu, N. Jin, S. Y. Park, P. R. Berger, and P. E. Thompson, "Si/SiGe Resonant Interband Tunnel Diode With f(r0) 20.2 GHz and Peak Current Density 218 kA/cm(2) for K-band Mixed-Signal Applications," *IEEE Electron Device Lett.,* vol. 27, pp. 364-367, May 2006.

[12] N. Holonyak and I. A. Lesk, "Gallium-Arsenide Tunnel Diodes," *Proc. IRE,* vol. 48, pp. 1405-1409, 1960.

[13] T. A. Richard, E. I. Chen, A. R. Sugg, G. E. Hofler, and N. Holonyak, "High-Current Density Carbon-Doped Strained-Layer GaAs (P+)-InGaAs(N+)-GaAs(N+) P-N Tunnel-Diodes," *Appl. Phys. Lett.,* vol. 63, pp. 3613-3615, Dec 1993.

[14] T. P. E. Broekaert and C. G. Fonstad, "Extremely High Current Density, Low Peak Voltage, Pseudomorphic In 0.53Ga0.47As/AlAs/InAs Resonant Tunneling Diodes," 1989, pp. 559-562.

[15] D. J. Day, R. Q. Yang, L. Jian, and J. M. Xu, "Experimental demonstration of resonant interband tunnel diode with room temperature peak-to-valley current ratio over 100," *Journal of Applied Physics,* vol. 73, pp. 1542-4, 02/01 1993.

[16] J. H. Smet, T. P. E. Broekaert, and C. G. Fonstad, "Peak-to-valley current ratios as high as 50:1 at room temperature in pseudomorphic In0.53Ga0.47As/AlAs/InAs resonant tunneling diodes," *Journal of Applied Physics,* vol. 71, p. 2475, 03/01/ 1992.

[17] H. H. Tsai, Y. K. Su, H. H. Lin, R. L. Wang, and T. L. Lee, "P-N DOUBLE-QUANTUM-WELL RESONANT INTERBAND TUNNELING DIODE WITH PEAK-TO-VALLEY CURRENT RATIO OF 144 AT ROOM-TEMPERATURE," *IEEE Electron Device Letters,* vol. 15, pp. 357-359, Sep 1994.

[18] G. M. Cohen, D. Ritter, and C. Cytermann, "High peak tunnel current density Ga0.47In0.53As Esaki diodes," *Electronics Letters,* vol. 31, pp. 1511-1512, 1995.

[19] M. F. Vilela, A. Freundlich, A. Bensaoula, and N. Medelci, "High Performance In0.47Ga0.53As Tunnel Junctions Grown by Chemical Beam Epitaxy on InP and GaAs and Si Substrates," in *IEEE Int. Symp. Circ. Sys.*, 1993, pp. 227-230.

[20] W. L. Chen, G. O. Munns, X. Wang, and G. I. Haddad, "Co-integration of high speed heterojunction bipolar transistors (HBTs) and tunnel diodes," in *High Speed Semiconductor Devices and Circuits, 1995. Proceedings., IEEE/Cornell Conference on Advanced Concepts in*, 1995, pp. 465-474.

[21] N. Shamir, D. Ritter, and C. Cytermann, "Tunnel diode collector contact in InP based PNP heterojunction bipolar transistors," *Solid-State Electronics,* vol. 46, pp. 785-789, 2002.

[22] N. Shamir and D. Ritter, "Reducing the current crowding effect in bipolar transistors by tunnel diode emitter design," *Solid-State Electronics,* vol. 47, pp. 127-130, 2003.

[23] D. Pawlik, M. Barth, P. Thomas, S. Kurinec, S. Mookerjea, D. Mohata, *et al.*, "Sub-micron InGaAs Esaki Diodes With Record High Peak Current Density," in *Dev. Res. Conf.*, 2010, pp. 163-164.

[24] D. Pawlik, B. Romanczyk, P. Thomas, S. Rommel, M. Edirisooriya, R. Contreras-Guerrero, *et al.*, "Benchmarking and Improving III-V Esaki Diode Performance with a Record 2.2 MA/cm2 Peak Current Density to Enhance TFET Drive Current," in *IEEE IEDM Tech. Digest*, 2012, pp. 27.1.1-27.1.3.

[25] H. Satoh and T. Imai, "Degradation of Ge-Doped and Zn-Doped GaAs Tunnel Diodes," *Jap. J. Appl. Phys.,* vol. 7, pp. 875-880, 08/ 1968.

[26] J.-H. Oh, N. Hayakawa, and M. Konagai, "Carbon Diffusion Behavior in a GaAs Tunnel Junction With a Heavily Carbon Doped p+-Layer by Metalorganic Molecular Beam Epitaxy," *Jap. J. Appl. Phys.,* vol. 36, pp. 6300-6301, 1997.

[27] Y. Oyama, T. Ohno, K. Suto, and J.-I. Nishizawa, "Ultra Shallow Sidewall GaAs Tunnel Junctions Prepared by Low-Temperature Area-Selective Epitaxial Re-growth Method," in *J. Crys. Growth*, 2005, pp. e1085-e1089.

[28] H. P. Kleinknecht, "Indium arsenide tunnel diodes," *Solid-State Electronics,* vol. 2, pp. 133-140, 1961.

[29] H. Ghoneim, P. Mensch, H. Schmid, C. D. Bessire, R. Rhyner, A. Schenk, *et al.*, "In Situ Doping of Catalyst-Free InAs Nanowires," *Nanotechnology,* vol. 23, 2012.

[30] J. C. Ho, A. C. Ford, C. Yu-Lun, P. W. Leu, O. Ergen, K. Takei, *et al.*, "Nanoscale Doping of InAs via Sulfur Monolayers," *Appl. Phys. Lett.,* vol. 95, p. 072108, 08/17 2009.

[31] C. A. Mead and W. G. Spitzer, "Fermi Level Position at Metal-Semiconductor Interfaces," *Phys. Rev.,* vol. 134, pp. 713-716, 1964.

[32] G. H. Parker and C. A. Mead, "Energy-Momentum Relationship in InAs," *Phys. Rev. Lett.,* vol. 21, pp. 605-607, 1968.

[33] A. V. Kalameitsev, D. A. Romanov, A. P. Kovchavtsev, G. L. Kuryshev, K. O. Postnikov, and I. M. Subbotin, "Negative Differential Resistivity of a Nonideal Schottky Barrier Based on Indium Arsenide," *Semicond.,* vol. 31, pp. 308-314, 03/ 1997.

[34] D. A. Romanov, A. V. Kalameitsev, A. P. Kovchavtsev, and I. M. Subbotin, "Conversion Tunneling in Non-ideal Schottky Barriers: Virtual Resonance Manifestation and Interface States Influence," in *Mat. Res. Soc. Symp.*, 1997, pp. 443-448.

[35] M. F. Millea, M. McColl, and A. H. Silver, "Electrical Characterization of Metal/InAs Contacts," *J. Electron. Mat.,* vol. 5, pp. 321-340, 06/ 1976.

CHAPTER 7

Universal BTBT Model

In this chapter the composite $In_{1-x}Ga_xAs$ characteristic BTBT map is presented. The full mapping utilizes two plots, which related J_P with (i) doping concentration and (ii) bandgap (tunnel barrier height). From the $In_{1-x}Ga_xAs$ map, it is determined that the maximum J_P measured in this work (975 kA/cm^2 from InGaAs-1) can be improved by no more than ~3x. From the final $In_{1-x}Ga_xAs$ characteristic BTBT map, a new universal BTBT model (UBM) will be presented, discussed, and compared with the Kane model as well as the homojunction experimental results. The new model utilizes two fitting parameters, but provides a closed form analytical equation for the computation of J_P over a wide range of materials and doping conditions. There are no other reports of such a model in literature, including a similar approach by Solomon, *et al.* [1]. Furthermore, it is believed that physical meaning can be attributed to the fitted parameters with the help of the Kane model [2] for reference.

7.1. Final Mapping of $In_{1-x}Ga_xAs$ BTBT Characteristics

The comprehensive map of J_P for the $In_{1-x}Ga_xAs$ ternary system is shown in Fig. 7.1. On the left (Fig. 7.1a) is the familiar plot of J_P versus $N^{*-1/2}$ for (i) GaAs, (ii) $In_{0.53}Ga_{0.47}As$, and (iii) InAs. The solid data points are experimental results from this work, open points are from literature, and the solid lines are calculated using Kane's model [2]. Those three material systems show the minimum, central, and maximum characteristic trendlines – respectively - for the capabilities of $In_{1-x}Ga_xAs$. The trendlines themselves are exponential by nature, except for a small upward bend at very large doping and small bandgaps. The experimental results reside close to the theoretical trendlines (within a 10% margin of error in doping concentration). Largely due to its E_G (1.42 eV), GaAs achieved ultra-low J_P of 11 (µA/cm^2) and ΔJ_P range of

~9.5 orders of magnitude which is much larger than the other systems. InAs has the largest trendlines, however ΔJ_P only ranges one order of magnitude due to its small bandgap (0.35 eV) and DOS (N_C/N_V of 0.12/6.7 x 10^{18} /cm^3). In fact, this limited the maximum J_P to 38 kA/cm^2, which is approximately the same value as the maximum GaAs ETD. The $In_{0.53}Ga_{0.47}As$ trendline is nearly halfway between GaAs and InAs, covering five orders of magnitude. Even with its larger bandgap (0.74 eV) than InAs, $In_{0.53}Ga_{0.47}As$ achieved the largest J_P of 975 MA/cm^2.

Concerning homojunction TFET structures, $In_{0.53}Ga_{0.47}As$ would be a better option than InAs or GaAs. It can achieve very large and small BTBT currents. In other words, it is the most promising at achieving desirable I_{On} as well as I_{On}/I_{Off} ratios. InAs would provide large I_{On}, but low I_{On}/I_{Off} ratios, which would result in unacceptable noise margins and off-state power consumption. GaAs would likely provide a much larger I_{On}/I_{Off} ratio, as well as better SS.

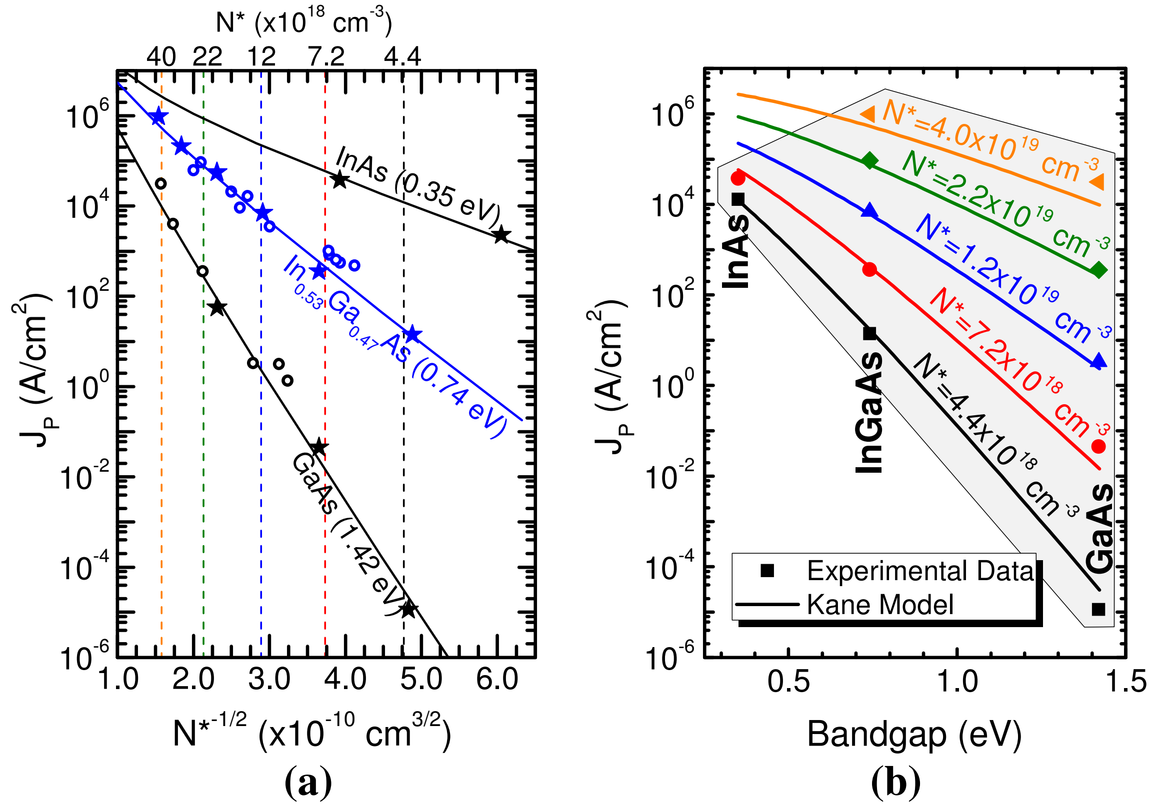

Fig. 7.1: Left (a), standard J_P versus doping for GaAs, $In_{0.53}Ga_{0.47}As$, and InAs ETDs. Vertical cutlines indicate N^* values used for the right hand plot. (b) Shows the relationship between J_P and E_G for various N^*. Solid lines are calculation results from the KMP.

However, its large bandgap prevents very large BTBT currents, limiting its ability to supply current densities necessary to drive large integrated circuits and thereby negating its attractiveness as a material system for TFETs. However, in circuit applications that are driven primarily by voltage without the need for large drive current densities, GaAs may be an excellent choice.

The characteristic trendlines in Fig. 7.1a quantify the relationship between J_P versus doping, and show a general relationship with E_G ($J_P \propto 1/E_G$). The exact relationship between J_P and E_G, which represents the tunnel barrier height, is shown in Fig. 7.1b. Specifically, the composition of $In_{1-x}Ga_xAs$ is stepped from x = 1 (InAs) to 0 (GaAs) and evaluated at a specific N^*. Thus, each line quantifies the relationship between E_G and J_P, for a given N^*. The data points are experimental results closest to the vertical cut-lines in Fig. 7.1a. The lowest InAs point is taken as the logarithmic average between InAs-1 and InAs-2, since the target N^* is roughly in the middle of the two experimental results. Typically there is a small deviation between the target N^* and experimental N^* value, resulting in a small deviation between the data points and model. Excepting a small deviation, there is generally an exponential relationship between J_P and E_G (tunnel barrier height), which was expected. The slope of each trend decreases as doping increases. In general, J_P changes less rapidly as (less sensitive to) N^* increases and E_G decreases. Furthermore, J_P appears to approach a common value beyond the plotted values and well beyond what is physically achievable with ($In_{1-x}Ga_xAs$). However, additional material systems with smaller bandgaps, or heterojunction ETDs of Type II and III band alignments may have effective bandgaps less than InAs, and continue the trends established in this work.

The shaded region in Fig. 7.1b covers that area where experimental results exist. In other words, within this design space an appropriately designed and fabricated ETD is likely to exhibit NDR in forward bias and have J_P close to the predicted value. As it stands, it is less likely structures designed outside of the shaded region will operate as well. Therefore, the maximum J_P that can be reliably achieved are $In_{1-x}Ga_xAs$ ETDs with %In mole fractions of 50% to 65%. Higher doping concentrations are needed to significantly surpass 1 MA/cm^2 for $In_{1-x}Ga_xAs$ ETDs.

However, even by increasing the doping concentrations to reasonable maximum levels (~10^{20} /cm^3) the greatest achievable J_P is ~2 MA/cm^2, a fairly small improvement in on the results reported in this work.

The comprehensive BTBT mapping of the $In_{1-x}Ga_xAs$ system (Fig. 7.1) is a powerfull tool. The example above clearly shows that the maximum J_P cannot be extended much beyond the current record of 975 kA/cm^2. This can be used to determine the optimal achievable drive current that an unstrained, homojunction $In_{1-x}Ga_xAs$ TFET can achieve. More importantly, this work provides extensive , self-consistent, experimental results that is already being used for the calibration of TCAD BTBT models. Furthermore, the models can be calibrated not only for a single material system, but specifically for (i) GaAs, (ii) $In_{0.53}Ga_{0.47}As$, and (ii) InAs and the ability to interpolate the remainder of the ternary system. Additionally, the $In_{1-x}Ga_xAs$ map can be used to design ETDs by designating a desired J_P and determining the requisite In composition and doping concentration, or vice versus. There may be the need for a few iterations in device design to fine tune the results, but this is far more efficient than approximations from previous experiments. Finally, the method of fabrication, testing, analysis, and mapping may be extended to any number of additional materials systems, including heterojunction ETDs.

7.2. Universal BTBT Model

At the start of Chapter 3 four desirable features for an analytical BTBT model were listed. Ultimately, the best convergence of those features would be a so called universal BTBT model (UBM). Ideally, the UBM would be a (i) closed form analytical expression, without any complex functions (the four basic arithmetic functions, exponents, and exponentials). There would (ii) not be any fitting parameters, with only standard (iii) material constants used to delineate the output of various material systems. Finally, it would be equally applicable in (iv) forward and reverse bias.

In 2004, Solomon, *et al.* [1] presented a universal model developed for Si to account for tunneling leakage current in p-n junctions associated with MOSFETs. After the appropriate transformations are made, the model is compact and easy to work with. It is likely that the procedure can be adapted to work with other material systems. However, a different set of approximations, transformations, and fitting parameters may be needed, which does not conform to the goal equally applicable across material systems (feature (iii)). It is also not obvious if it would work in forward bias at all, let alone predict J_P, which is a key parameter that enables to computation of the BTBT J-V characteristics.

Largely through directed trial and error, it was discovered that there does exist a very simple exponential relationship between J_P, depletion width (w_d), E_G, and relative tunneling effect mass (m_r), as described by (7.1) and (7.2). Fig. 7.2a shows a plot of J_P versus $T_{material}$ for a wide

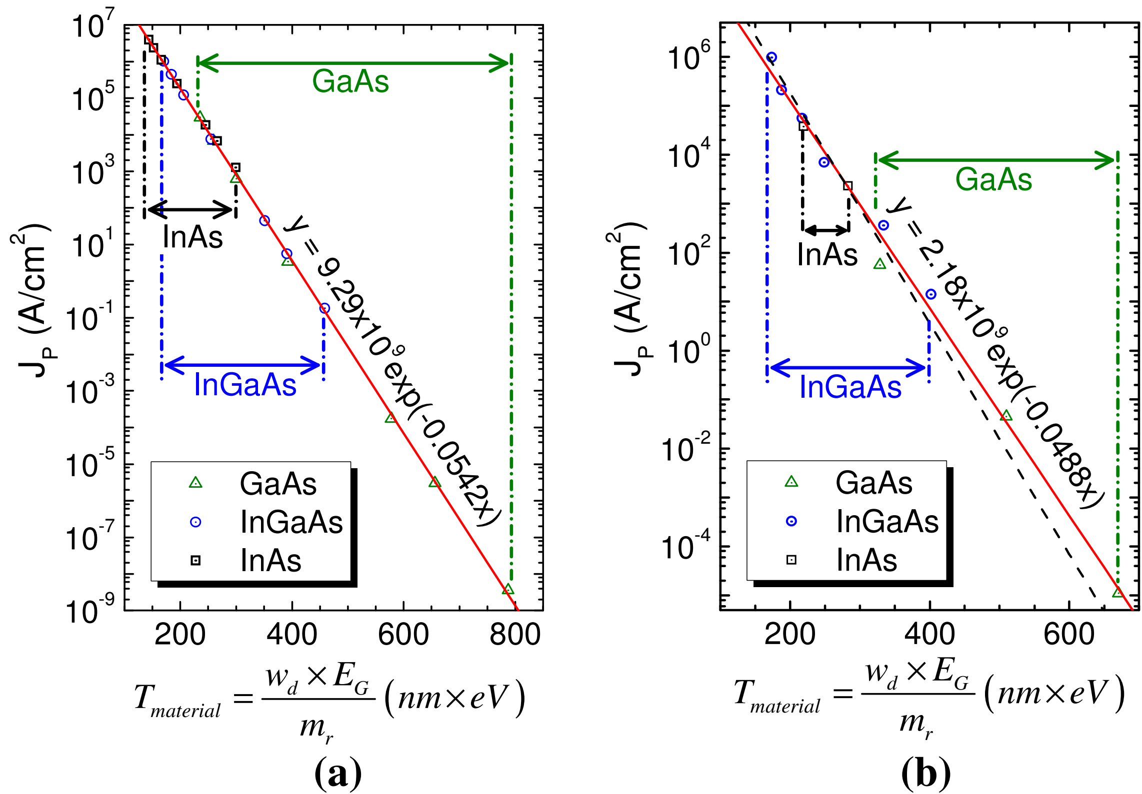

Fig. 7.2: Universal model transformation applied to the (a) Kane model ($N_A = N_D$), as well as, (b) experimental results from this work. The dashed line in (b) is the exponential fit from (a). Most deviations in the experimental data are a result of $N_A \neq N_D$.

range of N^* values for (i) GaAs, (ii) $In_{1-x}Ga_xAs$, and (iii) InAs as predicted by the Kane model. Those three material systems were chosen because this work has already shown that the model agrees well with the experimental results. In Fig. 7.2a, there are only very small deviations between the calculated data points from KMP and the exponential line fit, some of which is likely due to the use of w_d at a V_A of 0 V. Even though the UBM uses fitted parameters, they are constant over the three material systems used in Fig. 7.2.

$$J_P = A\exp\left(\beta \times T_{material}\right) \tag{7.1}$$

$$T_{material} = \frac{w_d \times E_G}{m_r} \tag{7.2}$$

Fig. 7.2b shows the UBM applied to the experimental results reported in Chapter 5 and 6. As can be seen, there the data forms another exponential line. The exponential fit to the experimental data has a slightly shallower slope (solid line) as compared to the exponential line from Fig. 7.2a (dashed line). A significant amount of the deviation present is due to $N_A \neq N_D$. Additionally, notice that the range on $In_{0.53}Ga_{0.47}As$ fully encompasses InAs, and the maximum GaAs shifted to the right, which conforms to the mapping analysis performed in Section 7.1.

In (7.2), E_G and m_r are simple material parameters, but w_d is a structure parameter. It helps to provide intuitive insight, but requires additional computation. Using standard the standard depletion approximation, $T_{material}$ becomes (7.3), which requires the built in bias (V_{bi}) and N^* (a supplied device design parameter). The super-degenerate approximation for E_f can be used to derive an appropriate equation for V_{bi}, (7.4). This results in a simplified closed form, analytical model, that is accurate across multiple material systems without modifying any parameters. Notice that N_D and N_A cannot be combined as N^*. Therefore, different ratios of N_A/N_D but with the same N^* will have some minor variations in J_P, which is observable in Fig. 7.2b. However, the model can be further simplified for the case of $N_A = N_D$. The built in bias can

be rewritten in the form of $V_{bi} \approx E_G + \gamma N^{*2/3}$, where γ is defined in (7.5). Notice that V_{bi} has no direct dependence on temperature ($N_{C/V}^{2/3}$ is proportional to *kT*), which is a result of using super-degeneracy. Consequently, the only temperature variation visible from the output of UBM are the result of E_G, ε_s, and m_r changing with temperature. Generally, those parameters do not change rapidly with temperature and some of the changes will compensate for each other, thereby causing only small changes in the models output. This conforms with the temperature analysis performed in Chapter 4, and conventional theory.

$$T_{material} = \frac{\sqrt{2\varepsilon_s} E_G}{\sqrt{q m_r}} \sqrt{\frac{V_{bi}}{N^*}} \tag{7.3}$$

$$V_{bi} \approx E_G + (kT)\left(\frac{3\sqrt{\pi}}{4}\right)^{2/3}\left[\left(\frac{N_D}{N_C}\right)^{2/3} + \left(\frac{N_A}{N_V}\right)^{2/3}\right] \tag{7.4}$$

$$\gamma = (kT)\left(\frac{3\sqrt{\pi}}{4}\right)^{2/3}\left[N_C^{-2/3} + N_V^{-2/3}\right] \tag{7.5}$$

Characteristic terndlines versus N^* were recreated for (i) GaAs, (ii) InGaAs, (iii) GaSb, (iv) InAs, and (v) InSb using KMP (solid lines) and UBM (data points). However, a small multiplicative correction factor was added to the intercept/slope of the exponential line fit for InAs (1.1/0.45), GaSb (1/4.3), and InSb (1.165/1.165). With further analysis and comparison to the Kane model, it is expected that the constants to the exponential line fit can be related to physical parameters. This would negate the need for fitted parameters and explaining the small changes needed to improve accuracy. In Fig. 7.3a, the solid points use the unaltered constants. As can be seen, the correction factor for InAs only made small improvements to the fit. Notice that the UBM is able to accurately account for the small upward curvature to the characteristic trendlines that is clearly visible for InAs and InSb.

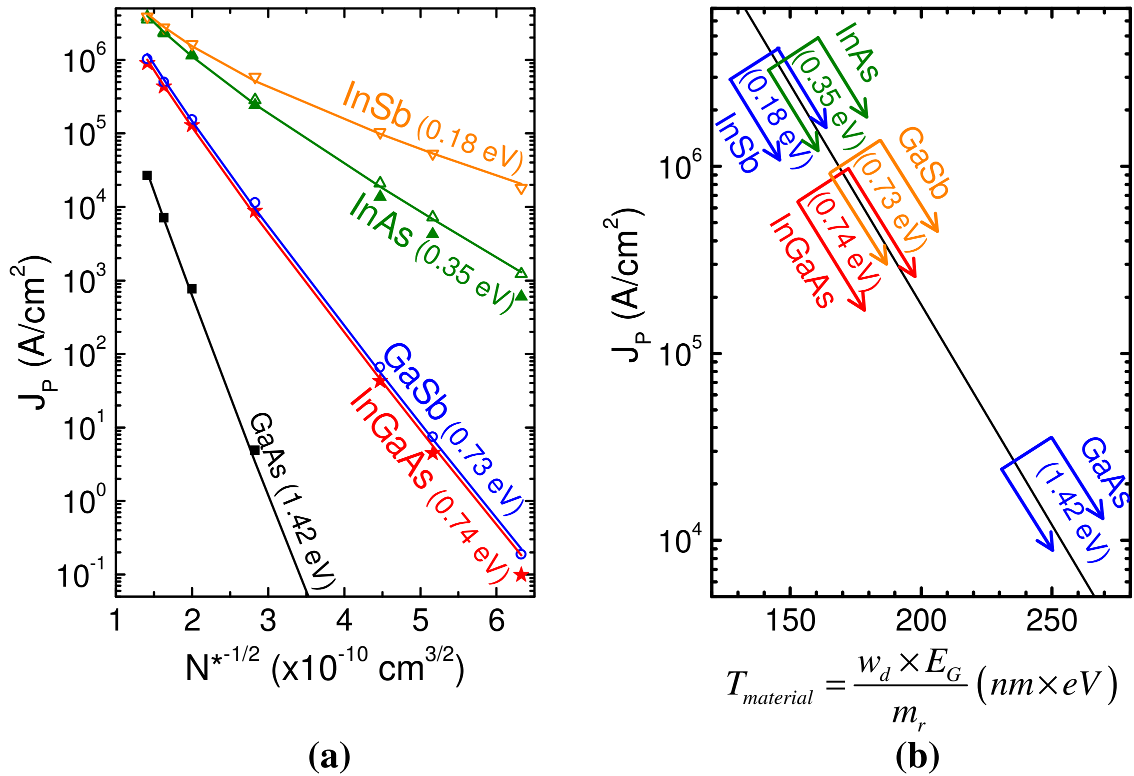

Fig. 7.3: Left (a), characteristic trendlines for (i) GaAs, (ii) $In_{0.53}Ga_{0.47}As$, (iii) GaSb, (iv) InAs, (v) InSb calculated by Kane (solid) and UBM (data points). The solid points use the base-line UBM, where the open points use correction factors. Right (b), UBM trendline (solid) marked with the predicted maximum J_P.

Finally, Fig. 7.3b plots J_P versus $T_{material}$, with the approximate maximum achievable J_P, ignoring non-idealities. It was assumed that the maximum achievable doping concentration is ~10^{20} /cm^3, which is reasonable for most material systems. Notice that as E_G becomes smaller, the effect on J_P decreases, which was previously observed in Section 7.1. In generally, UBM is in very good agreement with Kane model, whose accuracy for several of the material systems has been verified with experimental in this work. UBM is a closed form analytical equation, that does not use any complex functions. It currently uses two fitted parameters, which work across multiple material systems. Its applicability has not been applied to other biasing conditions. Therefore, the UBM presented here is much closer to the ideal universal tunneling model then Solomon [1], and some additional development in order to appropriately relate the fitted parameters to physical constants and parameters. Regardless, as it currently stands, UBM is another powerful tool for mapping ETD characteristics, and designing ETD structures.

7.2.1. Model Limitations

As with any model, the UBM is only accurate for some range of conditions. Since this model is matched to Kane's BTBT model, one can expect similar limitations. That is, unstrained homojunction ETDs made with direct bandgap material systems. Additionally, the doping profiles should be approximately square with a negligible *i*-layer. Furthermore, the final form of the model uses super degeneracy to calculate Fermi energies. Therefore, it is reason able to expect greater deviations at lower doping concentrations. On the other hand, significant deviations may occur at ultra high doping concentrations due to the position and curvature (for effect mass considerations) of the "L" and "X" valleys.

Specifically, the model has only been fitted to the experimental results discussed in this work: $In_{1-x}Ga_xAs$. There may be a different form needed for other material systems if the shapes of their characteristic trendlines are significantly different. For instance, strained and heterojunction ETDs will likely exhibit unique trendline shapes. Furthermore, there may be no simple UBM modification to correct for the unique tunneling barriers formed in heterojunction ETDs.

References for Chapter 7

[1] P. M. Solomon, J. Jopling, D. J. Frank, C. D'Emic, O. Dokumaci, P. Ronsheim, *et al.*, "Universal Tunneling Behavior in Technologically Relevant P/N Junction Diodes," *J. Appl. Phys.,* vol. 95, pp. 5800-5812, May 2004.

[2] E. O. Kane, "Theory of Tunneling," *J. Appl. Phys.,* vol. 32, p. 83, 1961.

CHAPTER 8

Conclusions

Previously, is was determined from the characteristic BTBT map that the maximum J_P measured in this work (975 kA/cm^2 from InGaAs-1) can only be improved upon by ~3x for the $In_{1-x}Ga_xAs$ ternary system. For dramatic improvements to the maximum current density the basic ETD structures must be modified using (i) δ-doping, (ii) strain, (ii) Type II band alignment, and/or (iv) Type III band alignments. This chapter will begin with discussing the four basic methods for increasing BTBT current density.

In its current form, the Kane model program (KMP) is ready for distribution and use by other groups, which has always been part of the intent for KMP. However, there are many improvements that can be made. (1) The UBM can be added as an additional BTBT model. (2) A tool for comparing and matching experimental and modeled characteristics within KMP. (3) Graphical analysis of I-V, band diagram, carrier distribution, and overlap integral structure. Finally, (4) modifications and improvements to the Kane model for improved accuracy to a larger range of device structures.

Finally, an overview of the work completed in this dissertation will be discussed as two separate groups. The first group discusses Tools and procedures developed for the completion of this work and continued development of the field. The second group relates to the experimental results and how they advanced the field of BTBT devices.

8.1. Beyond Unstrained Homojunction Esaki Diodes

There are four structural adaptations that can be made to the basic ETD in order to improve BTBT current densities beyond the mapped design space in this work without resorting solely to semiconductors with smaller E_G or higher doping capabilities. Specifically, (i)

δ-doping, (ii) strain, (iii), Type II band alignments, and (iv) Type III band alignments. These variations, and combinations thereof, have dominated efforts in literature to optimize BTBT current density and/or PVCR. However, the experiments typically involve no more than a few ETD structures which ultimately cannot be used to generate a characteristic trendline as described in this work. Additionally, a lack of compiled baseline data in literature has made it difficult to determine the effectiveness of the variations described below.

The simplest adaptations are δ-doping layers (Fig. 8.1a). This method is credited as one major enhancement enabling Si/SiGe ETDs to achieve J_P and PVCR up to ~200 kA/cm^2 [1] and 6 [2], respectively. In this method, epitaxial growth is halted on one, or both, sides of the *i*-layer. However, deposition of the dopants is continued, ideally forming a monolayer of dopant atoms at the surface. In practice, the dopants will continue to segregate and diffuse. Nonetheless, extremely large doping concentrations are achievable for an ultra thin layer. Consequentially, the

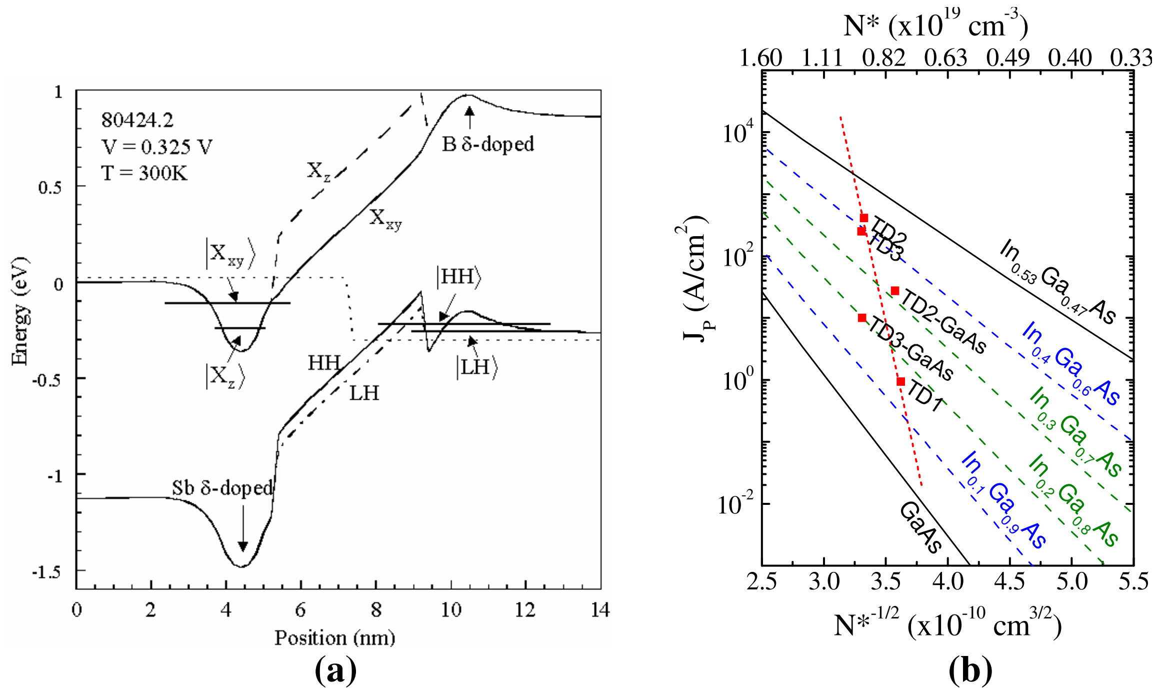

Fig. 8.1: Left (a), Si/SiGe resonant interband ETD band diagram illustrating (adopted from [1]) **δ**-doping and Type II band alignment. Right (b), GaAs/InGaAs heterojunction ETDs. The measured J_P for each structures far exceeds the 10% (TD1, TD3, and TD3-GaAs) and 20% (TD2 and TD2-GaAs) $In_xGa_{1-x}As$ characteristic trendlines.

depletion region can be confined mostly within the *i*-layer. The BTBT current density is thereby dominated by the *i*-layer thickness instead of doping concentration, which typically is more controllable and can result in enhanced BTBT characteristics [3].

Strain has been beneficially used to enhance MOSFET characteristics by improving carrier mobilities and increasing drive currents [4-7]. Similarly, E_G and m_r can be manipulated by strain. Recall, from Chapter 4, the GaAs/InGaAs heterojunction ETDs produced J_P far greater than the predicted 10% and 20% In content characteristic trendlines (Fig. 8.1b). This enhancement is largely due to the insertion of a thin, strained, $In_xGa_{1-x}As$ layer near the tunnel junction. The band alignment at the hetero-interface is very small (< 100 meV) and of type I. In other words, a standard homojunction $In_xGa_{1-x}As$ ETD would provide similar, if not better BTBT probabilities. Therefore, the effect of strain on various material parameters was enough to enhance the tunnel characteristics.

Heterojunctions may also be used to engineer an improved tunnel barrier, enhancing BTBT without strain. If the heterojunction ETD results in a type II band alignment (Fig. 8.2a) [8], the energy region with BTBT ($E_{V,p} – E_{C,n}$) has a much smaller tunnel barrier width than either material by itself. The smallest barrier width occurs in a small region indicated by the shaded circle and quantified as ΔE = 80 meV in Fig. 8.2a. This staggered bandgap results in a characteristic trendline greater than either material involved, included InAs. However, notice that the tunnel barrier height remains equal to E_G on their respective sides of the junctions. As a result, J_{Excess} is reduced by the larger bandgap material, improving PVCR (or I_{Off} in a TFET).

The Staggered gap ETD can be improved upon by increasing the band offset until a broken gap (Type III) heterojunction is formed (Fig. 8.2b) [8]. In this case, the shaded circle indicates a region (ΔE = -70 meV) where the tunnel barrier width is ideally 0 nm. In other words, the band structure forms more of a pipeline in which carriers are free to move from one side to

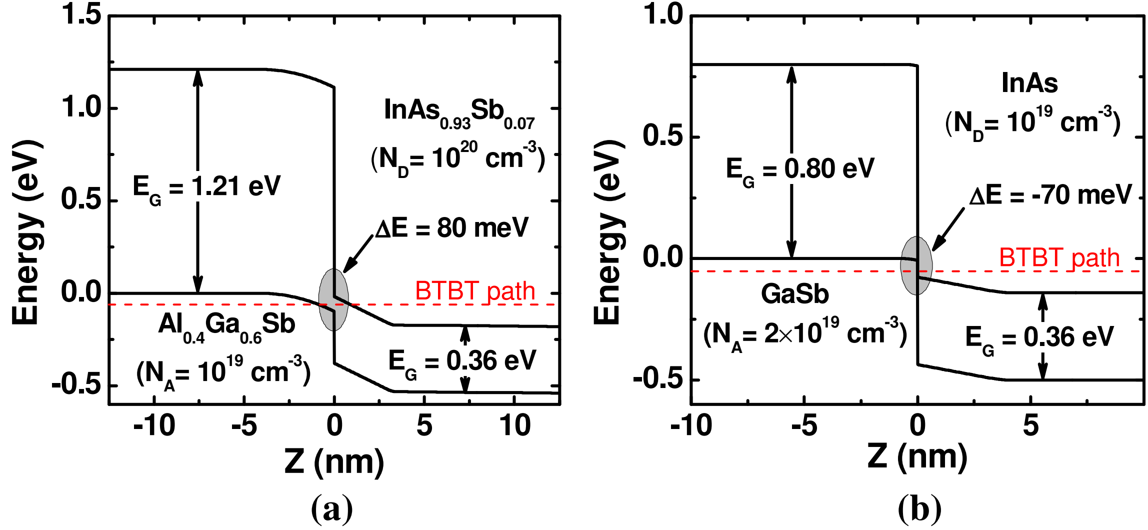

Fig. 7.2: Band diagrams showing the improved tunneling barrier widths for a (a) type II staggered gap and (b) type III broken gap heterojunction ETDs (adopted from [8]).

the other with very little effort. Consequentially, very large BTBT current densities are achievable [8] while maintaining relatively large PVCR.

Implementing one or more of the above ETD structure adaptations can greatly enhance BTBT characteristics, and greatly increases the number of structure designs. However, by following the device mapping procedure developed in this work, the behavior of any particular system can be systematically characterized with a limited number of fabrication runs. All that remains is choosing the structure design to implement, which can be narrowed down by considering (i) application, (ii) available material systems, (iii) maximum desired complexity, (iv) realistic band diagrams, and (v) material parameters as well as their dependence on strain.

8.2. Enhancements to the Kane Model Program

The Kane model program (KMP) developed for this work provides a straight forward GUI for operation. The KMP provides many useful tools including (i) J-V calculation, (ii) N^* sweep, (iii) basic band diagrams, and (iv) overlap integral structures, which are all described in Chapter 3. The program can be distributed for use by other research groups. There are several additions that can be made to KMP for improved analysis and modeling capabilities. (1) The

easiest to implement would be the addition of UBM calculations. Whenever the standard Kane model is ran, the program can also calculate UBM for quick and easy comparison between the two models and experimental results. Additionally, a new function can be added to sweep E_G, $N_{A/D}$, and m_r. If UBM is verified for variable temperature or applied bias, than that functionality can also be added to the tool.

(2) A matching tool for directly comparing an input J-V characteristic (Ex. Experimental measurement) to the Kane mode. KMP can be programmed to automatically match the biasing conditions of the input data, and compute an r-square fit with the Kane model. Additionally, an empirical fit to the J_{Excess} and user defined R_{Series} may be added for enhanced matching capabilities. A 3rd generation evolution may include some automated fitting procedures.

(3) Another tool would combine the J-V plotting feature with (i) band diagram, (ii) carrier distribution, and (iii) overlap integral structure ($D'(E)$ from Section 3.2.3). Each plot of the additional plots could be turned on or off as desired by the user. The carrier distribution plots would be drawn directly on the band diagram for greater impact and easier analysis. Ideally, the user would adjust a slider bar on the J-V plot in order to designate V_A for the other plots, which will be updated automatically. If the refresh/calculation rate is fast enough, the updates can be live, allowing the user to see the changes occurring in a smooth "movie-like" fashion.

(4) There are a couple adaptations to the Kane model that would potential provide added accuracy or functionality. First, (i) a user designated *i*-layer can be added to the model parameters (w_d and ξ), more closely mimicking the ETD designs. Second, (ii) graded doping profiles. First iteration would most likely assume exponential decay. Additional functions, or even generic user profiles may be implemented afterwards. The third addition would be (iii) enabling BNG and multi-band E_F functional to any material system. Finally, (iv) the greatest challenge would be expanding the model to work with heterojunctions. It is not known if this can be done without making unreasonable assumptions and approximations, or restrictions on appropriate heterojunctions. However, from this work it is evident that hetrojunction ETDs are

Table 8.1: Breakdown of the different ETD structures fabricated and characterized for this work.

Ge	GaAs/InGaAs				Homojunctions			
On ART	On ART	On GaAs	On Si	Total	GaAs	InGaAs	InAs	Total
1	5	2	2	9	3	6	3	12
Total Device Count = 22								

needed to make large enhancements to BTBT current densities. Therefore, adopting the model to heterojunctions would enable to continued usefulness of the Kane model, and KMP, into the next generation of ETD structures.

As indicated, some of the suggested modification would not require much effort (#1, parts of #2, #4-i & iii). Some of the additions may not be easy to implement, but there is a clear path to do so (#2, remainder of #3, and #4-ii). However, it is not clear the path to modifying the Kane mode for heterojunction ETD structures. It may be no more difficult than using material parameters "a" and "b" on the p- and n- side of the junction, respectively. But modify the bandgap to the ΔE band alignment at the hetero-interface. The calculation may need to be piece-wise depending on doping concentrations, V_A, and tunneling energy. It is likely that a much more sophisticated adaptation may be needed, beyond the scope of KMP. In which case it may be best to move onto a TCAP platform. Regardless, KMP is a great tool for modeling, predicting, and understanding the operation of homojunction ETDs. This is the first step to engineering heterojunctions with enhanced characteristics.

8.3. Summation of Work Completed

Many tools and procedures were developed in order to complete this work. Some of the tools and procedures were novel for the location the work was completed. Others are novel to the field and provide a great advancement for the BTBT community. In either case, these tools and procedures are, and will be, the foundation for continued BTBT development. Similarly, the results of the work completed add a great deal to the knowledge base of the community. The developed theoretical knowledge will shape the design and understanding of future experiments.

On the other hand, the experimental results will be used for model calibration, device design and optimization, and determination of material limitations

8.3.1. Developed Tools and Procedures

The Ge-Al alloy process for Ge ETDs was a new process. In particular, the use of spin-on-glass for introducing n-type dopants in to the Ge, and the thermal process for forming the p-type Al-Ge alloy junction. Junction alloying was the original and primary method of ETD fabrication [9-11]. However, after the development of epitaxial growth methods, it fell out of favor and became a lost art. This method should continually be looked into as a replacement to standard forms of doping. It is known that alloy junction can form high quality and sharp doping profiles for high quality ETD characteristics. Additionally, it is conceivable that this method can be used to provide horizontally tunnel junctions, instead of purely vertical structure which epitaxial methods are generally limited too. Furthermore, the alloyed junction is fundamentally a heterojunction with unique material qualities.

For the homojunction ETD structures, a novel deep sub-micron fabrication process was developed off of a baseline, self-aligned procedure. (1) Within the sub-micron process, E-Beam lithography was developed. This included the (i) operation of the SEM system and the NPGS software, (ii) chemicals involved with the process, (iii) layout design and implementation, and (iv) determination of optimal E-beam conditions. (2) The ILD planarization and etch back step utilizing BCB required the development of appropriate coating, etching, and metrology procedures. (3) Finally, the key to accurately scaling and current density analysis was the development of appropriate area characterization. The development of the deep submicron fabrication process enables the measurement of ultra-high current density ETDs (i) by reducing the effects of R_{Series}, (ii) minimizing uncertainty in junction areas, and (iii) negating the need for pulsed measurements to reduce the effects of localized heating. Additionally, this enables the study of scaling junction areas from very large areas down to deep sub-micron dimensions. Such

analysis is useful for determining changes in (i) BTBT current density, (ii) surface leakage effects, (iii) and electrically active defects. Future developments may be able to scale devices down to dimensions where the DOS start to follow 2D and 1D confinement, which may provide significantly different BTBT characteristics. Ultimately, TFETs will operate with 2D and 1D confinement. To date there is no experimental study that clearly identifies the effect of quantum confinement on BTBT.

Proper characterization and analysis procedures were developed. The material characterization procedures is this work were primarily limited to SIMS analysis to verify layer thicknesses, and quantify doping profiles. Future work should expand upon materials analysis techniques to include, but not limited by, EDX, XRD, and AFM. This will become extremely important for heterojunction systems. Other methods of determine active or present doping profiles may also become necessary. This work developed the techniques for characterizing the DC electrical characteristics of ETDs. These methods enable parameters such as J_P and PVCR to be reported with high confidence. It also enables the use of junction characteristics and scaling properties for materials analysis. The BTBT mapping techniques presented here is a powerful method of efficiently and consistently assessing the capabilities of a given material system, as well as benchmarking with other materials. Additionally, the mapped trendlines can be used by device and circuit designers for predicting or determining optimal device characteristics and limit the number of development runs needed.

There was no modifications made to the original Kane model [13]. However, a VB.net program was developed to automate the (i) material parameter retrieval, (ii) E_F calculations, (iii) Kane model calculation, (iv) band diagram calculations, and (v) overlap integral analysis. In general, KMP is a powerful tool for understanding the operation of and project the behavior of homojunction ETDs. This can be done on a qualitative and quantitative level, including the production of material BTBT maps. The development of UBM is a novel model, which provides a simple equation for "back-of-the-envelope" type calculations as well as a more direct method of

benchmarking and comparing various ETD structures and materials systems with each other. Further developments of the model may provide physical meaning the fitted parameters and enable full I-V characteristics. It is likely that the model will follow a form similar to some of the empirical models reported in literature [14].

8.3.2. Experimental Results

For this work, 22 unique ETD structure were designed, fabricated, and electrically tested. 10 of the devices were a part of the virtual substrate integration on Si. These ETDs were used to verify the electrical quality of the ART integrated virtual substrates. The remaining 12 ETDs were used to mapping and characterizing the BTBT behavior of the $In_{1-x}Ga_xAs$ ternary system. Finally, The Kane [13] and UBM models were compared and calibrated to the experimental results.

The first diode, an Al-Ge alloy junction had comparable PVCR to similar device fabricated on Ge substrates. The difficulty of the alloy process, and availability of epitxial growths shifted the efforts towards GaAs/InGaAs ETDs. Five structures were grown on ART virtual substrates, with two companion pieces grown on GaAs, two grown on Si. The PVCR of the on ART ETDs (up to 56 for TD-3) were greater than their on Si and GaAs companions. Additionally, the PVCR of TD1-,2,3, and 4 surpasses the previous GaAs record of 24. Furthermore, a 1.8 meV activation energy was extracted from the low-to-high temperature measurements. This all indicates that the ART virtual substrates are of a high quality, with few electrically active defects present. The deep submicron scaling experiment showed that ETD device characteristics do not necessarily degrade with as the sidewall surface area to junction cross-sectional area increases. In fact, the device characteristics improved.

Mapping of the $In_{1-x}Ga_xAs$ ternary system, which utilized 12 ETD structures, began with the fabrication of two ultra-high current density $In_{0.53}Ga_{0.47}As$ ETDs. These two structures directly indicate the maximum J_P (~1 MA/cm^2) achievable. Furthermore, the deep submicron

scaling conclusively show that the BTBT characteristics do not degrade down to dimensions of at least 50 nm radii. However, there is currently not conclusive experiment indicating the effects of scaling down to 2D and 1D quantum confinement. InGaAs-3 (J_P = 14 A/cm^2) showed that the Kane model and characteristic trendlines can be used to accurately predict doping concentrations after J_P is measured and before SIMS analysis. The final InGaAs ETDs filled in the middle of the characteristic trendline, showing that it is a consistent exponential line.

The three GaAs ETDs were enough to fill it's characteristic trendline. The GaAs characteristic trendline is less than $In_{1-x}Ga_xAs$, which was expected due to their respective bandgaps (1.42 eV and 0.74 eV). GaAs-1 provided the smallest J_P (11 μA/cm^2), with the system covering the largest range of values (9.5 orders of magnitude). The GaAs trendline indicates that GaAs ETDs are limited to J_P less than 100 kA/cm^2, well below what is needed for TFETs.

Only two of the three InAs ETDs could be used to provide data points for a trendline. The InAs characteristic trendline is greater than the previous two. However, because of its small bandgap (0.35 eV), J_{Excess} limited observable J_P to ~40 kA/cm^2, which is well below the maximum $In_{0.53}Ga_{0.47}As$ ETD value. An unexpected result with InAs was the observation of NDR due to the metal-p$^+$ InAs junction. This is the first room temperature report of this phenomenon, and is theorized to be due Fermi level pinning at the InAs surface, forming a thin n$^+$ surface channel.

Finally, the Kane model and UBM were matched to the experimental results. Both models accurately predict J_P for the $In_{1-x}Ga_xAs$ ternary system, can be used to interpolate between the experimental results. Additionally, the Kane model accurately predicts full BTBT J-V characteristics, which can be used to device and circuit designers.

References for Chapter 8

[1] S. L. Rommel, T. E. Dillon, P. R. Berger, R. Lake, P. E. Thompson, K. D. Hobart, *et al.*, "Si-based interband tunneling devices for high-speed logic and low power memory applications," in *1998 IEEE IEDM Tech. Digest*, San Francisco, CA, 1998, pp. 1035-1037.

[2] K. Eberl, R. Duschl, O. G. Schmidt, U. Denker, and R. Haug, "Si-based resonant inter- and intraband tunneling diodes," *Journal of Crystal Growth,* vol. 227, pp. 770-776, Jul 2001.

[3] N. Jin, S. Y. Chung, R. H. Yu, R. M. Heyns, P. R. Berger, and P. E. Thompson, "The effect of spacer thicknesses on Si-based resonant interband tunneling diode performance and their application to low-power tunneling diode SRAM circuits," *IEEE Transactions on Electron Devices,* vol. 53, pp. 2243-2249, Sep 2006.

[4] J. Welser, J. L. Hoyt, and J. F. Gibbons, "NMOS and PMOS Transistors Fabricated in Strained Silicon/Relaxed Silicon-Germanium Structures," in *IEEE IEDM*, 1992, pp. 1000-1002.

[5] J. Welser, J. L. Hoyt, and J. F. Gibbons, "Electron Mobility Enhancement in Strained-Si N-type Metal-Oxide-Semiconductor Field-Effect Transistors," *IEEE Electron Device Lett.,* vol. 15, pp. 100-102, 1994.

[6] J. Welser, J. L. Hoyt, S. Takagi, and J. F. Gibbons, "Strain Dependence of the Performance Enhancement in Strained-Si n-MOSFETs," in *IEEE IEDM*, 1994, pp. 373-376.

[7] D. K. Nayak, J. C. S. Woo, J. S. Park, K. L. Wang, and K. P. MacWilliams, "High-Mobility P-Channel Metal-Oxide-Semiconductor Field-Effect-Transistor on Strained Si," *Jap. J. Appl. Phys.,* vol. 33, pp. 2412-2414, 1994.

[9] D. Pawlik, B. Romanczyk, P. Thomas, S. Rommel, M. Edirisooriya, R. Contreras-Guerrero*, et al.*, "Benchmarking and Improving III-V Esaki Diode Performance with a Record 2.2 MA/cm2 Peak Current Density to Enhance TFET Drive Current," in *IEEE IEDM Tech. Digest*, 2012, pp. 27.1.1-27.1.3.

[10] L. Esaki, "New Phenomenon in Narrow Germanium p-n Junctions," *Physical Rev.,* vol. 109, p. 603, 1958.

[11] R. H. Rediker and T. M. Quist, "Properties of GaAs alloy diodes," *Solid-State Electronics,* vol. 6, pp. 657-665, 1963.

[12] V. M. Franks, K. F. Hulme, and J. R. Morgan, "An alloy process for making high current density silicon tunnel diode junctions," *Solid-State Electronics,* vol. 8, pp. 343-344, 1965.

[13] E. O. Kane, "Theory of Tunneling," *J. Appl. Phys.,* vol. 32, p. 83, 1961.

[14] S. M. Sze and K. K. Ng, "Physics of Semiconductor Devices," Third ed Hoboken, NJ: Wiley-Interscience, 2007, pp. 422-424.

APPENDIX A

Kane Model Program

Appendix A.1: Main window for PIVET.

The following is the main body code for the Kane model program (KMP), 0. The program is written with VB.net, using the Microsoft Visual Studio development environment. Description of the programs operation and function can be found in Section 3.5.

```
Imports System.Math

Public Class Form1
    Dim xApp As New
Microsoft.Office.Interop.Excel.Application
    Dim xBook As
Microsoft.Office.Interop.Excel.Workbook =
xApp.Workbooks.Open(System.IO.Directory.Get
CurrentDirectory() &
"\ETD_Calculations.xlsx")

    Private Sub Form1_Load(ByVal sender As
System.Object, ByVal e As System.EventArgs)
Handles MyBase.Load
        Dim path(1) As String
        Dim xsheet As
Microsoft.Office.Interop.Excel.Worksheet
```

```
        Dim SheetCount, Mat_Count, i As
Integer
        Dim SheetExists(1) As Boolean

        path(0) =
System.IO.Directory.GetCurrentDirectory() &
"\ETD_Calculations.xlsx"

        If System.IO.File.Exists(path(0)) =
True Then
        Else
            xBook = xApp.Workbooks.Add
            xBook.SaveAs(path(0))
        End If

        SheetCount = xBook.Worksheets.Count
        If SheetCount > 0 Then
            For i = 1 To SheetCount Step 1
                If xBook.Worksheets(i).name
= "Fermi_Integral" Then
                    SheetExists(0) = True
                End If

                If xBook.Worksheets(i).name
= "Mat_Systems" Then
                    SheetExists(1) = True
                End If
            Next

        Else
            SheetExists(0) = False
        End If

        Me.Visible = True
        If SheetExists(0) = False Then
            Me.Refresh()
            xBook.Worksheets.Add.name =
"Fermi_Integral"

xBook.Worksheets("Fermi_Integral").cells(1,
1).value = "Y"

xBook.Worksheets("Fermi_Integral").cells(1,
2).value = "Fermi Integral"

Calculate_Integral(xBook.Worksheets("Fermi_I
ntegral"), 6, -8.13)
        End If

        Me.Visible = True
        If SheetExists(0) = False Then
            Me.Refresh()
            xBook.Worksheets.Add.name =
"Fermi_Integral"

xBook.Worksheets("Fermi_Integral").cells(1,
1).value = "Y"

xBook.Worksheets("Fermi_Integral").cells(1,
2).value = "Fermi Integral"

Calculate_Integral(xBook.Worksheets("Fermi_I
ntegral"), 6, -8.13)
        End If

        If SheetExists(0) = True Then
            xsheet =
xBook.Worksheets("Mat_Systems")
            Mat_Count =
xsheet.Application.WorksheetFunction.CountA(
xsheet.Range("A:A"))
            For i = 1 To Mat_Count Step 1

Mat_Sys.Items.Add(xsheet.Cells(i, 1).text)
            Next

            Mat_Sys.SelectedText = "Si"
        End If

        xBook.Save()
        For i = 1 To 6 Step 1
            DGrid1.Rows.Add()
        Next

        For i = 1 To 4 Step 1
            DGrid2.Rows.Add()
        Next

'********************************************
********
        DGrid1.Item(0, 0).Value = "Material"
        DGrid1.Item(0, 1).Value =
"Temperature"
        DGrid1.Item(0, 2).Value = "Eg(300
K)"
        DGrid1.Item(0, 3).Value = "er"
        DGrid1.Item(0, 4).Value = "m*/m0
(tunneling)"
        DGrid1.Item(0, 5).Value = "Vp"
        DGrid1.Item(0, 6).Value = "Jp"

        DGrid1.Item(1, 0).Value = "Si"
        DGrid1.Item(1, 1).Value = "300"
        DGrid1.Item(1, 2).Value = "1.12"
        DGrid1.Item(1, 3).Value = "11.68"
        DGrid1.Item(1, 4).Value = "0.16"

        DGrid1.Item(2, 0).Value = ""
        DGrid1.Item(2, 1).Value = "K"
        DGrid1.Item(2, 2).Value = "eV"
        DGrid1.Item(2, 5).Value = "V"
        DGrid1.Item(2, 6).Value = "A/cm^2"

'********************************************
********
        DGrid2.Item(0, 0).Value = "m*/m0"
        DGrid2.Item(0, 1).Value = "Nc,v"
        DGrid2.Item(0, 2).Value =
"n,p(target)"
        DGrid2.Item(0, 3).Value =
"n,p(calculated)"
        DGrid2.Item(0, 4).Value = "Efn,p-Ev"

        DGrid2.Item(1, 0).Value = "1.08"
        DGrid2.Item(1, 1).Value = ""
        DGrid2.Item(1, 2).Value = "5e19"
        DGrid2.Item(1, 3).Value = ""
        DGrid2.Item(1, 4).Value = ""
        DGrid2.Item(2, 0).Value = "0.81"
        DGrid2.Item(2, 1).Value = ""
        DGrid2.Item(2, 2).Value = "5e19"
        DGrid2.Item(2, 3).Value = ""
        DGrid2.Item(2, 4).Value = ""

        DGrid2.Item(3, 0).Value = ""
        DGrid2.Item(3, 1).Value = "cm^-3"
        DGrid2.Item(3, 2).Value = "cm^-3"
        DGrid2.Item(3, 3).Value = "cm^-3"
        DGrid2.Item(3, 4).Value = "eV"
```

```
        For i = 0 To 154 Step 1
            DGrid3.Rows.Add()
            DGrid3.Item(0, i).Value = i /
1000
        Next
        DGrid3.Item(3, 0).Value = "Va = 0 V"
        DGrid3.Item(4, 0).Value = "Va = Vp"
        DGrid3.Item(3, 1).Value = "Vbi-Va
(V)"
        DGrid3.Item(3, 3).Value = "Wd (nm)"
        DGrid3.Item(3, 5).Value = "Wn (nm)"
        DGrid3.Item(3, 7).Value = "Wp (nm)"
        DGrid3.Item(3, 9).Value = "E-field
(V/cm)"
        DGrid3.Item(3, 11).Value = "Pre-
factor (1/ohm-cm/eV)"
        DGrid3.Item(4, 11).Value = "Arg.
(cm/V)"
        DGrid3.Item(3, 13).Value = "Efn
(eV)"
        DGrid3.Item(4, 13).Value = "Efp
(eV)"
        DGrid3.Item(3, 15).Value = "Nd (cm^-
3)"
        DGrid3.Item(4, 15).Value = "Na (cm^-
3)"
        DGrid3.Item(3, 17).Value = "Vp (V)"
        DGrid3.Item(4, 17).Value = "Jp
(A/cm^2)"
        DGrid3.Item(3, 20).Value = "D (eV)"

        DataGridView1.Rows.Add(203)
        DataGridView1.Item(4, 0).Value = "i-
layer (nm)"
        DataGridView1.Item(5, 0).Value = 0
        DataGridView1.Item(4, 1).Value = "Wd
(nm)"
        DataGridView1.Item(4, 2).Value = "TB
Width (nm)"
        DataGridView1.Item(4, 3).Value =
"Ave. E-Field (V/cm)"
        DataGridView1.Item(4, 4).Value =
"Efn-Ec (eV)"
        DataGridView1.Item(4, 5).Value =
"Ev-Efp (eV)"
        DataGridView1.Item(4, 6).Value =
"'n'"

        DofE.Rows.Add(500)

    End Sub

    Private Sub Button1_Click(ByVal sender
As System.Object, ByVal e As
System.EventArgs) Handles Button1.Click
        Select Case Bands.SelectedTab.Name
            Case "tab1"
                IV_Sweep()
            Case "tab2"
                N_Sweep_Jp()
            Case "tab3"
                N_Sweep_Va()
            Case "tab4"
                Calc_Bands()
            Case "tab5"
                Calc_DofE()
        End Select
    End Sub

    Private Sub IV_Sweep()
        Dim xSheet As
Microsoft.Office.Interop.Excel.Worksheet
        Dim path As String
        Dim i, j, steps, rows As Integer
        Dim pi, q, m0, h_bar, c, e0, k, T,
kT As Double
        Dim er, Eg, mr(2), m_eff(2), Nc(1),
Nv(1), es As Double
        Dim Na, Nd, Efn, Efp, Vbi As Double
        Dim Va, X, E_bar, eV, Edel, Estep,
D, tempD, terms(2), Vp, Jp As Double

        path =
System.IO.Directory.GetCurrentDirectory() &
"\ETD_Calculations.xlsx"
        xSheet =
xBook.Worksheets("Fermi_Integral")

        pi = 3.1415926536
        q = 1.602176E-19 'C
        m0 = 510998.91 'eV
        h_bar = 0.000000000000000658211899
'eV*Sec
        c = 299792000.0 'm/Sec
        e0 = 0.000000000000008854188 'F/cm
        k = 0.00008617343 'eV/K
        T = DGrid1.Item(1, 1).Value 'K
        kT = k * T 'eV

        er = DGrid1.Item(1, 3).Value
        Eg = DGrid1.Item(1, 2).Value 'eV
        mr(0) = DGrid2.Item(1, 0).Value 'N-
type
        mr(1) = DGrid2.Item(2, 0).Value 'P-
type
        mr(2) = DGrid1.Item(1, 4).Value
'Tunneling

        es = e0 * er 'F/cm
        m_eff(0) = mr(0) * m0 / c ^ 2 'eV
(N-type)
        m_eff(1) = mr(1) * m0 / c ^ 2 'eV
(P-type)
        m_eff(2) = mr(2) * m0 / (c ^ 2) 'eV
(Tunneling)
        Nc(0) = 0.000001 * Sqrt(1 / 2) *
(m_eff(0) / (pi * h_bar ^ 2)) ^ 1.5 'cm^-
3/eV
        Nc(1) = (kT ^ 1.5) * Nc(0) 'cm^-3
        Nv(0) = 0.000001 * Sqrt(1 / 2) *
(m_eff(1) / (pi * h_bar ^ 2)) ^ 1.5 'cm^-
3/eV
        Nv(1) = (kT ^ 1.5) * Nv(0) 'cm^-3
        DGrid2.Item(1, 1).Value =
Nc(1).ToString("0.###e0") 'N-type
        DGrid2.Item(2, 1).Value =
Nv(1).ToString("0.###e0") 'P-type

        Nd = DGrid2.Item(1, 2).Value 'N-type
        Na = DGrid2.Item(2, 2).Value 'P-type

        Eg = BNG(Nd, Na, Eg)

        If CheckBox1.Checked = True Then
            Efn = Firmi_Levels2(xSheet, Nd,
Nc(1)) 'Only accurate for InGaAs (53/47)
        Else
```

```
            Efn = Firmi_Levels(xSheet, Nd,
Nc(1)) ', Nc(0))
        End If

        Efn = Eg - Efn * kT
        DGrid2.Item(1, 4).Value =
Efn.ToString("0.####")

        'P-type region
        Efp = Firmi_Levels(xSheet, Na,
Nv(1)) ', Nv(1))
        Efp = Efp * kT
        DGrid2.Item(2, 4).Value =
Efp.ToString("0.####")

        DGrid1.Refresh()
        DGrid2.Refresh()
        DGrid3.Refresh()

        Vp = 0
        Jp = 0
        Vbi = Efn - Efp 'eV
        Dim temp(1) As Double
        Vapplied(Efn, Efp, Eg)
        steps = DGrid3.RowCount - 2
        For j = 0 To steps Step 1
            Va = DGrid3.Item(0, j).Value
'(Efn + Efp - Eg) / 2 'eV
            X = 100 * Sqrt(q * (Vbi - Va) *
Na * Nd / (2 * es * (Na + Nd))) 'V/m
            E_bar = h_bar * X * Sqrt(2) /
(pi * Sqrt(m_eff(2) * Eg)) 'eV
            Estep = (Vbi - Va - Eg) / 500
            D = 0
            For i = 0 To 500 Step 1
                eV = Estep * i
                If eV < Vbi - Eg - Va - eV
Then
                    Edel = eV
                Else
                    Edel = Vbi - Eg - Va -
eV
                End If
                temp(0) = eV + Eg
                temp(1) = -Vbi + Va + Eg +
eV
                D = D + (Fcv(temp(0), Efn,
kT) - Fcv(temp(1), Efp, kT)) * (1 - Exp(-2 *
Edel / E_bar)) * Estep
            Next
            terms(0) = (q * X / (36 * pi *
h_bar ^ 2)) * Sqrt(2 * m_eff(2) / Eg) /
10000
            terms(1) = Exp(-pi *
Sqrt(m_eff(2)) * (Eg ^ 1.5) / (2 * Sqrt(2) *
h_bar * X))

            DGrid3.Item(1, j).Value = (D *
terms(0) * terms(1)).ToString("0.#####e0")
            DGrid3.Item(2, j).Value =
D.ToString("0.#####e0")

            If DGrid3.Item(1, j).Value > Jp
Then
                Jp = DGrid3.Item(1, j).Value
                Vp = DGrid3.Item(0, j).Value
                tempD = D
            End If
        Next

        rows = DGrid3.RowCount
        If rows < 21 Then
            For i = 1 To 21 - rows Step 1
                DGrid3.Rows.Add()
            Next
        End If
        DGrid3.Item(3, 0).Value = "Va = 0 V"
        DGrid3.Item(4, 0).Value = "Va = Vp"
        DGrid3.Item(3, 1).Value = "Vbi-Va
(V)"
        DGrid3.Item(3, 3).Value = "Wd (nm)"
        DGrid3.Item(3, 5).Value = "Wn (nm)"
        DGrid3.Item(3, 7).Value = "Wp (nm)"
        DGrid3.Item(3, 9).Value = "E-field
(V/cm)"
        DGrid3.Item(3, 11).Value = "Pre-
factor (1/ohm-cm)"
        DGrid3.Item(4, 11).Value = "Arg.
(cm/V)"
        DGrid3.Item(3, 13).Value = "Efn
(eV)"
        DGrid3.Item(4, 13).Value = "Efp
(eV)"
        DGrid3.Item(3, 15).Value = "Nd (cm^-
3)"
        DGrid3.Item(4, 15).Value = "Na (cm^-
3)"
        DGrid3.Item(3, 17).Value = "Vp (V)"
        DGrid3.Item(4, 17).Value = "Jp
(A/cm^2)"
        DGrid3.Item(3, 20).Value = "D (eV)"

        X = 10000000 * Sqrt(2 * es * (Nd +
Na) * (Efn - Efp) / (q * Nd * Na))
        DGrid3.Item(3, 2).Value = (Efn -
Efp).ToString("0.#####e0")
        DGrid3.Item(3, 4).Value =
X.ToString("0.#####e0") '"Wd (nm)"
        DGrid3.Item(3, 6).Value = (X * Na /
(Na + Nd)).ToString("0.#####e0") '"Wn (nm)"
        DGrid3.Item(3, 8).Value = (X * Nd /
(Na + Nd)).ToString("0.#####e0") '"Wp (nm)"
        DGrid3.Item(3, 10).Value = (Sqrt(q *
(Efn - Efp) * Na * Nd / (2 * es * (Na +
Nd)))).ToString("0.#####e0") '"E-field
(V/cm)"

        X = 10000000 * Sqrt(2 * es * (Nd +
Na) * (Efn - Efp - Vp) / (q * Nd * Na))
        DGrid3.Item(4, 2).Value = ((Efn -
Efp) - Vp).ToString("0.#####e0") '"Vbi-Vp
(V)"
        DGrid3.Item(4, 4).Value =
X.ToString("0.#####e0") '"Wd (nm)"
        DGrid3.Item(4, 6).Value = (X * Na /
(Na + Nd)).ToString("0.#####e0") '"Wn (nm)"
        DGrid3.Item(4, 8).Value = (X * Nd /
(Na + Nd)).ToString("0.#####e0") '"Wp (nm)"
        DGrid3.Item(4, 10).Value = (Sqrt(q *
(Efn - Efp - Vp) * Na * Nd / (2 * es * (Na +
Nd)))).ToString("0.#####e0") '"E-field
(V/cm)"

        DGrid3.Item(3, 12).Value = (q *
Sqrt(2 * m_eff(2) / Eg) / (100 * 36 * pi *
h_bar ^ 2)).ToString("0.#####e0")  '"Pre-
factor (1/ohm-cm/eV)"
        DGrid3.Item(4, 12).Value = (-pi *
Sqrt(m_eff(2)) * (Eg ^ 1.5) / (100 * 2 *
```

```
Sqrt(2) * h_bar)).ToString("0.#####e0")
'"Arg. (cm/V)"

        DGrid3.Item(3, 14).Value =
Efn.ToString("0.####") '"Efn (eV)"
        DGrid3.Item(4, 14).Value =
Efp.ToString("0.####") '"Efp (eV)"
        DGrid3.Item(3, 16).Value = Nd '"Nd
(cm^-3)"
        DGrid3.Item(4, 16).Value = Na '"Na
(cm^-3)"
        DGrid3.Item(3, 18).Value = Vp '"Vp
(V)"
        DGrid3.Item(4, 18).Value =
Jp.ToString("0.#####e0") '"Jp (A/cm^2)"
        DGrid3.Item(4, 20).Value =
tempD.ToString("0.#####e0") '"D (eV)"

        If DGrid3.Item(0, steps).Value <>
Efn - Efp - Eg Then
            DGrid3.Item(0, steps + 1).Value
= Efn - Efp - Eg
            Va = DGrid3.Item(0, steps +
1).Value '(Efn + Efp - Eg) / 2 'eV
            X = 100 * Sqrt(q * (Vbi - Va) *
Na * Nd / (2 * es * (Na + Nd))) 'V/m
            E_bar = 100 * h_bar * X *
Sqrt(2) / (pi * Sqrt(m_eff(2) * Eg / (c ^
2))) 'eV

            Estep = (Vbi - Va - Eg) / 10
            D = 0
            For i = 0 To 10 Step 1
                eV = Estep * i
                If eV < Vbi - Eg - Va - eV
Then
                    Edel = eV
                Else
                    Edel = Vbi - Eg - Va -
eV
                End If
                D = D + (Fcv(eV + Eg, Efn,
kT) - Fcv(-eV, Efp, kT)) * (1 - Exp(-2 *
Edel / E_bar)) * Estep
            Next
            terms(0) = (q * X / (36 * pi *
h_bar ^ 2)) * Sqrt(2 * m_eff(2) / Eg) /
10000
            terms(1) = Exp(-pi *
Sqrt(m_eff(2)) * (Eg ^ 1.5) / (2 * Sqrt(2) *
h_bar * X))

            DGrid3.Item(1, steps + 1).Value
= (D * terms(0) *
terms(1)).ToString("0.#####e0")
            DGrid3.Item(2, steps + 1).Value
= D.ToString("0.#####e0")
        End If

        DGrid1.Item(1, 5).Value = Vp
        DGrid1.Item(1, 6).Value =
Jp.ToString("0.#####e0")

    End Sub

    Private Function Fcv(ByVal E As Double,
ByVal Ef As Double, ByVal kT As Double) As
Double
        If (E - Ef) < 10 * kT Then
            Fcv = 1 / (1 + Exp((E - Ef) /
kT))
        Else
            Fcv = Exp(-(E - Ef) / kT)
        End If
    End Function

    Private Sub Vapplied(ByVal Efn As
Double, ByVal Efp As Double, ByVal Eg As
Double)
        Dim rows, i As Integer
        Dim Vstart, Vend, dV As Double

        rows = DGrid3.RowCount
        Vstart = TextBox1.Text
        dV = TextBox2.Text
        Vend = Efn - Efp - Eg

        For i = rows - 2 To 0 Step -1
            DGrid3.Rows.RemoveAt(i)
        Next
        DGrid3.Rows.Clear()
        rows = Int((Vend - Vstart) / dV)
        For i = 0 To rows Step 1
            DGrid3.Rows.Add()
            DGrid3.Item(0, i).Value = Vstart
+ i * dV
        Next

    End Sub

    Public Function Firmi_Levels(ByVal
xSheet As
Microsoft.Office.Interop.Excel.Worksheet,
ByVal n_target As Double, ByVal Ncv As
Double) ', ByVal Ncv0 As Double)
        'This provides something
        Dim y, Fintegral, temp(), Alpha As
Double

        Fintegral = n_target * Sqrt(PI) / (4
* Ncv)
        y = -Log(n_target / Ncv)

        'If the doping is small enough, the
sample is not degenerate
        'Therefore, the standard equation is
good
        If y >= 6 Then
            GoTo TheEnd
        End If



        Dim i, row(2), RowCount, steps As
Integer
        Dim Table(,) As Object
        Dim starty As Double

        RowCount =
xSheet.Application.WorksheetFunction.Count(x
Sheet.Range("A:A")) + 1

        'Initial guess using modified Eq 26a
(pp. 19 in Sze 3rd edition)

        'Initial guess using degenerate Ef
statistics.
```

```
        Alpha = (3 * Sqrt(PI) / (4 * Ncv)) ^
(2 / 3)
        y = -Alpha * n_target ^ (2 / 3)
        row(1) = Int((6 - y) * 100) + 3 'row
closest to this result

        If Fintegral >
xSheet.Cells(RowCount, 2).value Then
            Do While Fintegral >
xSheet.Cells(RowCount, 2).value
                starty =
xSheet.Cells(RowCount, 1).value
                Calculate_Integral(xSheet,
starty - 0.01, starty - 1)
                RowCount =
xSheet.Application.WorksheetFunction.Count(x
Sheet.Range("A:A")) + 1
            Loop
            row(2) = RowCount
            row(0) = RowCount - 100
            GoTo SearchPoint
        End If

        If row(1) > RowCount Then
            row(1) = RowCount
        End If

        'y(0) to low; y(1) current; y(2) to
high
        If xSheet.Cells(row(1), 2).value >
Fintegral Then
            '-------------------------------
--------------------------------------------
------------
            row(2) = row(1)
            steps = Int((row(1) - 2) / 100)
+ 1
            For i = 1 To steps Step 1

                'Make sure the row to check
is not below the minimum of "2"
                If row(1) - 100 > 1 Then
                    row(1) = row(1) - 100
                Else
                    row(1) = 2
                End If

                'Check if Fint(check) - Fint
at row(1) - is greater than target Fint
                If xSheet.Cells(row(1),
2).value > Fintegral Then
                    'Update upper bound
                    row(2) = row(1)
                Else
                    'Lower bound for
Fint(check) found.  Update row and exit for
loop
                    row(0) = row(1)
                    i = 100000000.0
                End If
            Next
            '-------------------------------
--------------------------------------------
------------

        Else
            '-------------------------------
--------------------------------------------
------------
            row(0) = row(1)
            steps = Int((RowCount - row(1))
/ 100) + 1
            For i = 1 To steps Step 1

                'Make sure the row to check
is not above RowCount
                If row(1) + 100 < RowCount
Then
                    row(1) = row(1) + 100
                Else
                    row(1) = RowCount
                End If

                'Check if Fint(check) - Fint
at row(1) - is less than target Fint
                If xSheet.Cells(row(1),
2).value < Fintegral Then
                    'Update lower bound
                    row(0) = row(1)
                Else
                    'Upper bound for
Fint(check) found.  Update row and exit for
loop
                    row(2) = row(1)
                    i = 100000000.0
                End If
            Next
            '-------------------------------
--------------------------------------------
------------

        End If

SearchPoint:
        ReDim Table(row(2) - row(0) + 1, 2)
        Table = xSheet.Cells(row(0),
1).Resize(row(2) - row(0) + 1, 2).Value

        For i = 1 To row(2) - row(0) + 1
Step 1
            If Table(i, 2) < Fintegral Then
                row(0) = i
            ElseIf Table(i, 2) > Fintegral
Then
                row(2) = i
                i = 200
            Else
                row(0) = i
                row(2) = i
            End If
        Next

        'Interpolate to find "y_target"
        y = Table(row(0), 1) + (Fintegral -
Table(row(0), 2)) * (Table(row(2), 1) -
Table(row(0), 1)) / (Table(row(2), 2) -
Table(row(0), 2))

TheEnd:


        '***Note:  Ef = Eg - y * kT
        Firmi_Levels = y


    End Function

    Public Function Firmi_Levels2(ByVal
xSheet As
Microsoft.Office.Interop.Excel.Worksheet,
ByVal N As Double, ByVal Nc As Double)
```

```
        Dim dy(3), y(3), m(3), F(5), Ec(3),
kT As Double
        Dim dRow(3), row(3), i, RowCount As
Integer
        kT = 0.00008617343 * DGrid1.Item(1,
1).Value 'eV
        RowCount =
xSheet.Application.WorksheetFunction.Count(x
Sheet.Range("A:A")) + 1

        m(1) = 0.052
        m(2) = 0.29
        m(3) = 0.68

        m(2) = (m(2) / m(1)) ^ 1.5
        m(3) = (m(3) / m(1)) ^ 1.5
        m(1) = m(1) / m(1)

        Ec(1) = 0
        Ec(2) = 0.464
        Ec(3) = 0.594

        dy(2) = Ec(2) / kT
        dy(3) = Ec(3) / kT

        dRow(2) = Int(dy(2) * 100)
        dRow(3) = Int(dy(3) * 100)

        'Target F_integral
        F(0) = (Sqrt(PI) / 4) * (N / Nc)
'(DGrid2.Item(1, 2).Value / Nc)
        y(1) = 6

        For i = 2 To Int(RowCount / 100)
Step 1
            y(2) = y(1) + dy(2)
            y(3) = y(1) + dy(3)

            row(1) = Int(-y(1) * 100 + 600 +
2)

            row(2) = row(1) - dRow(2)
            row(3) = row(1) - dRow(3)

            If y(1) < 6 Then
                F(1) = xSheet.Cells(row(1),
2).value
            Else
                F(1) = (Sqrt(PI) / 4) *
Exp(-y(1))
            End If

            If y(2) < 6 Then
                F(2) = xSheet.Cells(row(2),
2).value
            Else
                F(2) = (Sqrt(PI) / 4) *
Exp(-y(2))
            End If

            If y(3) < 6 Then
                F(3) = xSheet.Cells(row(3),
2).value
            Else
                F(3) = (Sqrt(PI) / 4) *
Exp(-y(3))
            End If

            F(4) = F(1) + m(2) * F(2) + m(3)
* F(3)

            If F(4) < F(0) Then
                y(1) = Round(y(1) - 1)
            Else
                i = RowCount
            End If
        Next

        y(1) = Round(y(1) + 1)
        For i = 1 To 100 Step 1
            y(2) = y(1) + dy(2)
            y(3) = y(1) + dy(3)

            row(1) = Int(-y(1) * 100) + 600
+ 2

            row(2) = row(1) - dRow(2)
            row(3) = row(1) - dRow(3)

            If y(1) < 6 Then
                F(1) = xSheet.Cells(row(1),
2).value
            Else
                F(1) = (Sqrt(PI) / 4) *
Exp(-y(1))
            End If

            If y(2) < 6 Then
                F(2) = xSheet.Cells(row(2),
2).value
            Else
                F(2) = (Sqrt(PI) / 4) *
Exp(-y(2))
            End If

            If y(3) < 6 Then
                F(3) = xSheet.Cells(row(3),
2).value
            Else
                F(3) = (Sqrt(PI) / 4) *
Exp(-y(3))
            End If

            F(4) = F(1) + m(2) * F(2) + m(3)
* F(3)

            If F(4) < F(0) Then
                y(1) = Round(100 * (y(1) -
0.01)) / 100
            Else
                i = RowCount
            End If
        Next

        row(1) = Int(-y(1) * 100 + 1) + 600
        row(2) = row(1) - dRow(2)
        row(3) = row(1) - dRow(3)
        If y(1) < 6 Then
            F(1) = xSheet.Cells(row(1),
2).value
        Else
            F(1) = (Sqrt(PI) / 4) * Exp(-
y(1))
        End If

        If y(2) < 6 Then
            F(2) = xSheet.Cells(row(2),
2).value
        Else
            F(2) = (Sqrt(PI) / 4) * Exp(-
y(2))
        End If
```

```
        If y(3) < 6 Then
            F(3) = xSheet.Cells(row(3),
2).value
        Else
            F(3) = (Sqrt(PI) / 4) * Exp(-
y(3))
        End If

        F(4) = F(1) + m(2) * F(2) + m(3) *
F(3)

        row(1) = row(1) + 1
        row(2) = row(2) + 1
        row(3) = row(3) + 1
        If y(1) < 6 Then
            F(1) = xSheet.Cells(row(1),
2).value
        Else
            F(1) = (Sqrt(PI) / 4) * Exp(-
y(1))
        End If

        If y(2) < 6 Then
            F(2) = xSheet.Cells(row(2),
2).value
        Else
            F(2) = (Sqrt(PI) / 4) * Exp(-
y(2))
        End If

        If y(3) < 6 Then
            F(3) = xSheet.Cells(row(3),
2).value
        Else
            F(3) = (Sqrt(PI) / 4) * Exp(-
y(3))
        End If

        F(5) = F(1) + m(2) * F(2) + m(3) *
F(3)

        y(0) = y(1) - 0.01 * (F(0) - F(4)) /
(F(5) - F(4))
        y(1) = y(0)
        y(2) = y(1) + dy(2)
        y(3) = y(1) + dy(3)

        Return y(0)

    End Function

    Public Function BNG(ByVal Nd As Double,
ByVal Na As Double, ByVal Eg As Double)
        Dim ABCD(1, 3), dEmaj(1), dEmin(1),
dEg(1) As Double

        'Constants for Na
        ABCD(1, 0) = 0.0092
        ABCD(1, 1) = 0.0034
        ABCD(1, 2) = 0.0113
        ABCD(1, 3) = 0.00023

        'Constants for Nd
        ABCD(0, 0) = 0.0476
        ABCD(0, 1) = 0
        ABCD(0, 2) = 0.0032
        ABCD(0, 3) = 0



        dEmaj(0) = ABCD(0, 0) * (Nd /
1.0E+19) ^ (1 / 3) + ABCD(0, 1) * (Nd /
1.0E+19) ^ 0.5
        dEmin(0) = ABCD(0, 2) * (Nd /
1.0E+19) ^ 0.25 + ABCD(0, 3) * (Nd /
1.0E+19) ^ 0.5

        dEmaj(1) = ABCD(1, 0) * (Na /
1.0E+19) ^ (1 / 3) + ABCD(1, 1) * (Na /
1.0E+19) ^ 0.5
        dEmin(1) = ABCD(1, 2) * (Na /
1.0E+19) ^ 0.25 + ABCD(1, 3) * (Na /
1.0E+19) ^ 0.5

        dEg(0) = dEmaj(0) + dEmin(0)
        dEg(1) = dEmaj(1) + dEmin(1)

        If CheckBox2.Checked = True Then
            Return (Eg - (dEg(0) + dEg(1)) /
2)
        Else
            Return Eg
        End If

    End Function

    Public Sub Calculate_Integral(ByVal
xSheet As
Microsoft.Office.Interop.Excel.Worksheet,
ByVal StartY As Double, ByVal EndY As
Double)
        Dim i, j, StartRow, row As Integer

        Dim sum, y, Dx3 As Double
        sum = xSheet.Cells(2, 1).value
        StartRow =
xSheet.Application.WorksheetFunction.Count(x
Sheet.Range("A:A")) + 2
        Dx3 = 0.001 / 3
        For i = 0 To ((StartY - EndY) * 100)
Step 1
            row = StartRow + i
            y = StartY - i / 100
            xSheet.Cells(row, 1).value = y
            sum = 0
            For j = 1 To 10000 Step 2
                sum = sum + Dx3 *
(Integrand(y, 0.001 * (j - 1)) + 4 *
Integrand(y, 0.001 * j) + Integrand(y, 0.001
* (j + 1)))
            Next
            If y < -90 Then
                For j = 10001 To 20000 Step
2
                    sum = sum + Dx3 *
(Integrand(y, 0.001 * (j - 1)) + 4 *
Integrand(y, 0.001 * j) + Integrand(y, 0.001
* (j + 1)))
                Next
            End If
            TextBox3.Text = "Populating
Fermi-integral Table (" & y & "/" & EndY &
")"
            TextBox3.Refresh()
            xSheet.Cells(row, 2).value = sum
        Next

    End Sub

    Public Function Integrand(ByVal y As
Double, ByVal x As Double) As Double
```

```
        Integrand = (x ^ 2) / (1 + Exp(y + x
^ 2))
    End Function

    Private Sub Button2_Click(ByVal sender
As System.Object, ByVal e As
System.EventArgs) Handles Button2.Click
        Dim xSheet As
Microsoft.Office.Interop.Excel.Worksheet
        Dim path As String
        Dim k, T, h_bar, pi, m0, c As Double
        Dim mr(1), m_eff(1), Eg, Ef(2), kT
As Double
        Dim n_target, p_target, Nc, Nv As
Double

        path =
System.IO.Directory.GetCurrentDirectory() &
"\ETD_Calculations.xlsx"
        xSheet =
xBook.Worksheets("Fermi_Integral")

        pi = 3.1415926536
        m0 = 510998.91 'eV
        h_bar = 0.000000000000000658211899
'eV*Sec
        c = 299792000.0 'm/Sec
        k = 0.00008617343 'eV/K
        T = DGrid1.Item(1, 1).Value 'K

        kT = k * T 'eV
        Eg = DGrid1.Item(1, 2).Value 'eV
        mr(0) = DGrid2.Item(1, 0).Value 'N-
type
        mr(1) = DGrid2.Item(2, 0).Value 'P-
type
        m_eff(0) = mr(0) * m0 / c ^ 2 'eV
(N-type)
        m_eff(1) = mr(1) * m0 / c ^ 2 'eV
(P-type)
        Nc = 0.000001 * Sqrt(1 / 2) * (kT *
m_eff(0) / (pi * h_bar ^ 2)) ^ 1.5 'cm^-3
        Nv = 0.000001 * Sqrt(1 / 2) * (kT *
m_eff(1) / (pi * h_bar ^ 2)) ^ 1.5 'cm^-3

        n_target = DGrid2.Item(1, 2).Value
'N-type
        p_target = DGrid2.Item(2, 2).Value
'P-type
        DGrid2.Item(1, 1).Value =
Nc.ToString("0.###e0") 'N-type
        DGrid2.Item(2, 1).Value =
Nv.ToString("0.###e0") 'P-type

        'N-type region
        Ef(2) = Firmi_Levels(xSheet,
n_target, Nc)
        Ef(2) = Eg - Ef(2) * kT
        DGrid2.Item(1, 4).Value =
Ef(2).ToString("0.####")

        'P-type region
        Ef(2) = Firmi_Levels(xSheet,
p_target, Nv)
        Ef(2) = Ef(2) * kT
        DGrid2.Item(2, 4).Value =
Ef(2).ToString("0.####")

        DGrid1.Refresh()
        DGrid2.Refresh()
        DGrid3.Refresh()


    End Sub

    Private Sub Calc_Bands()
        Dim xSheet As
Microsoft.Office.Interop.Excel.Worksheet
        Dim path As String
        Dim i, j, steps, rows As Integer
        Dim pi, q, m0, h_bar, c, e0, k, T,
kT As Double
        Dim er, Eg, mr(2), m_eff(2), Nc(1),
Nv(1), es As Double
        Dim Na, Nd, Efn, Efp, Vbi As Double
        Dim Va, X, Xn, Xp, Cn, Cp, dX,
Xstep, V(2), i_layer, E_bar, eV, Edel,
Estep, D, tempD, terms(2), Vp, Jp As Double

        path =
System.IO.Directory.GetCurrentDirectory() &
"\ETD_Calculations.xlsx"
        xSheet =
xBook.Worksheets("Fermi_Integral")

        pi = 3.1415926536
        q = 1.602176E-19 'C
        m0 = 510998.91 'eV
        h_bar = 0.000000000000000658211899
'eV*Sec
        c = 299792000.0 'm/Sec
        e0 = 0.0000000000000088541 88 'F/cm
        k = 0.00008617343 'eV/K
        T = DGrid1.Item(1, 1).Value 'K
        kT = k * T 'eV
        i_layer = DataGridView1.Item(5,
0).Value / 10000000.0

        er = DGrid1.Item(1, 3).Value
        Eg = DGrid1.Item(1, 2).Value 'eV
        mr(0) = DGrid2.Item(1, 0).Value 'N-
type
        mr(1) = DGrid2.Item(2, 0).Value 'P-
type
        mr(2) = DGrid1.Item(1, 4).Value
'Tunneling


        es = e0 * er 'F/cm
        m_eff(0) = mr(0) * m0 / c ^ 2 'eV
(N-type)
        m_eff(1) = mr(1) * m0 / c ^ 2 'eV
(P-type)
        m_eff(2) = mr(2) * m0 / (c ^ 2) 'eV
(Tunneling)
        Nc(0) = 0.000001 * Sqrt(1 / 2) *
(m_eff(0) / (pi * h_bar ^ 2)) ^ 1.5 'cm^-
3/eV
        Nc(1) = (kT ^ 1.5) * Nc(0) 'cm^-3
        Nv(0) = 0.000001 * Sqrt(1 / 2) *
(m_eff(1) / (pi * h_bar ^ 2)) ^ 1.5 'cm^-
3/eV
        Nv(1) = (kT ^ 1.5) * Nv(0) 'cm^-3
        DGrid2.Item(1, 1).Value =
Nc(1).ToString("0.###e0") 'N-type
        DGrid2.Item(2, 1).Value =
Nv(1).ToString("0.###e0") 'P-type

        Nd = DGrid2.Item(1, 2).Value 'N-type
        Na = DGrid2.Item(2, 2).Value 'P-type
        Va = TextBox1.Text
```

```
        Eg = BNG(Nd, Na, Eg)

        'Firmi_Levels1()
        'N-type region
        If CheckBox1.Checked = True Then
            Efn = Firmi_Levels2(xSheet, Nd,
Nc(1)) 'Only accurate for InGaAs (53/47)
        Else
            Efn = Firmi_Levels(xSheet, Nd,
Nc(1)) ', Nc(0))
        End If

        Efn = Eg - Efn * kT
        DGrid2.Item(1, 4).Value =
Efn.ToString("0.####")

        'P-type region
        Efp = Firmi_Levels(xSheet, Na,
Nv(1)) ', Nv(1))
        Efp = Efp * kT
        DGrid2.Item(2, 4).Value =
Efp.ToString("0.####")

        Vbi = Efn - Efp
        X = Sqrt(i_layer ^ 2 + 2 * es * (Vbi
- Va) * (Na + Nd) / (q * (Na * Nd))) -
i_layer 'cm
        Xn = X * (Na / (Na + Nd))
        Xp = X * (Nd / (Nd + Na))

        DataGridView1.Item(5, 1).Value = (X
+ i_layer) * 10000000.0
        DataGridView1.Item(5, 2).Value = Eg
* 10000000.0 / ((Vbi - Va) / (X + i_layer))
'"TB Width (nm)"
        DataGridView1.Item(5, 3).Value =
(Vbi - Va) / (X + i_layer)
        DataGridView1.Item(5, 4).Value = Efn
- Eg
        DataGridView1.Item(5, 5).Value = Efp
        If Efn - Eg < -Efp Then
            DataGridView1.Item(5, 6).Value =
(Efn - Eg) / 0.0259
        Else
            DataGridView1.Item(5, 6).Value =
Efp / 0.0259
        End If

        Cp = q * Na / (2 * es)
        Cn = q * Nd / (2 * es)

        dX = Xn / 100
        For i = 0 To 100 Step 1
            Xstep = dX * i - Xn - i_layer /
2
            V(0) = Cn * (Xn + Xstep +
i_layer / 2) ^ 2 - Efn + Eg
            DataGridView1.Item(0, i).Value =
(Xstep) * 10000000
            DataGridView1.Item(1, i).Value =
V(0) - Eg
            DataGridView1.Item(2, i).Value =
V(0)
            DataGridView1.Item(3, i).Value =
0
        Next

        For i = 0 To 1 Step 1
            Xstep = (i * i_layer) - i_layer
/ 2
            V(0) = Cn * Xn * (2 * Xstep + Xn
+ i_layer) - Efn + Eg
            DataGridView1.Item(0, 101 +
i).Value = (Xstep) * 10000000
            DataGridView1.Item(1, 101 +
i).Value = V(0) - Eg
            DataGridView1.Item(2, 101 +
i).Value = V(0)
            DataGridView1.Item(3, 101 +
i).Value = 0
        Next

        dX = Xp / 100
        For i = 0 To 100 Step 1
            Xstep = dX * i + i_layer / 2
            V(0) = (Vbi - Va) - Cp * (Xstep
- Xp - i_layer / 2) ^ 2 - Efn + Eg
            DataGridView1.Item(0, 103 +
i).Value = (Xstep) * 10000000.0
            DataGridView1.Item(1, 103 +
i).Value = V(0) - Eg
            DataGridView1.Item(2, 103 +
i).Value = V(0)
            DataGridView1.Item(3, 103 +
i).Value = -Va
        Next

    End Sub

    Private Sub Calc_DofE()
        Dim xSheet As
Microsoft.Office.Interop.Excel.Worksheet
        Dim path As String
        Dim i, j, steps, rows As Integer
        Dim pi, q, m0, h_bar, c, e0, k, T,
kT As Double
        Dim er, Eg, mr(2), m_eff(2), Nc(1),
Nv(1), es As Double
        Dim Na, Nd, Efn, Efp, Fnp(2), Vbi As
Double
        Dim Va, X, E_bar, eV, Edel, Estep,
D, tempD, terms(2), Vp, Jp As Double

        path =
System.IO.Directory.GetCurrentDirectory() &
"\ETD_Calculations.xlsx"
        xSheet =
xBook.Worksheets("Fermi_Integral")

        pi = 3.1415926536
        q = 1.602176E-19 'C
        m0 = 510998.91 'eV
        h_bar = 0.000000000000000658211899
'eV*Sec
        c = 299792000.0 'm/Sec
        e0 = 0.00000000000008854188 'F/cm
        k = 0.00008617343 'eV/K
        T = DGrid1.Item(1, 1).Value 'K
        kT = k * T 'eV

        er = DGrid1.Item(1, 3).Value
        Eg = DGrid1.Item(1, 2).Value 'eV
        mr(0) = DGrid2.Item(1, 0).Value 'N-
type
        mr(1) = DGrid2.Item(2, 0).Value 'P-
type
        mr(2) = DGrid1.Item(1, 4).Value
'Tunneling
```

```
        es = e0 * er 'F/cm
        m_eff(0) = mr(0) * m0 / c ^ 2 'eV
(N-type)
        m_eff(1) = mr(1) * m0 / c ^ 2 'eV
(P-type)
        m_eff(2) = mr(2) * m0 / (c ^ 2) 'eV
(Tunneling)
        Nc(0) = 0.000001 * Sqrt(1 / 2) *
(m_eff(0) / (pi * h_bar ^ 2)) ^ 1.5 'cm^-
3/eV
        Nc(1) = (kT ^ 1.5) * Nc(0) 'cm^-3
        Nv(0) = 0.000001 * Sqrt(1 / 2) *
(m_eff(1) / (pi * h_bar ^ 2)) ^ 1.5 'cm^-
3/eV
        Nv(1) = (kT ^ 1.5) * Nv(0) 'cm^-3
        DGrid2.Item(1, 1).Value =
Nc(1).ToString("0.###e0") 'N-type
        DGrid2.Item(2, 1).Value =
Nv(1).ToString("0.###e0") 'P-type

        Nd = DGrid2.Item(1, 2).Value 'N-type
        Na = DGrid2.Item(2, 2).Value 'P-type

        Eg = BNG(Nd, Na, Eg)

        'Firmi_Levels1()
        'N-type region
        If CheckBox1.Checked = True Then
            Efn = Firmi_Levels2(xSheet, Nd,
Nc(1)) 'Only accurate for InGaAs (53/47)
        Else
            Efn = Firmi_Levels(xSheet, Nd,
Nc(1)) ', Nc(0))
        End If

        Efn = Eg - Efn * kT
        DGrid2.Item(1, 4).Value =
Efn.ToString("0.####")

        'P-type region
        Efp = Firmi_Levels(xSheet, Na,
Nv(1)) ', Nv(1))
        Efp = Efp * kT
        DGrid2.Item(2, 4).Value =
Efp.ToString("0.####")

        DGrid1.Refresh()
        DGrid2.Refresh()
        DGrid3.Refresh()

        Vp = 0
        Jp = 0
        Vbi = Efn - Efp 'eV
        Dim temp(1) As Double
        Va = TextBox1.Text
        X = 100 * Sqrt(q * (Vbi - Va) * Na *
Nd / (2 * es * (Na + Nd))) 'V/m
        E_bar = h_bar * X * Sqrt(2) / (pi *
Sqrt(m_eff(2) * Eg)) 'eV

        Estep = (Vbi - Va - Eg) / 500
        D = 0
        For i = 0 To 500 Step 1
            eV = Estep * i
            If eV < Vbi - Eg - Va - eV Then
                Edel = eV
            Else
                Edel = Vbi - Eg - Va - eV
            End If
            temp(0) = eV + Eg
            temp(1) = -Vbi + Va + Eg + eV

            Fnp(0) = Fcv(temp(0), Efn, kT)
            Fnp(1) = Fcv(temp(1), Efp, kT)
            Fnp(2) = (Fnp(0) - Fnp(1))
            tempD = (1 - Exp(-2 * Edel /
E_bar))

            D = Fnp(2) * tempD

            DofE.Item(0, i).Value = eV
            DofE.Item(1, i).Value = Fnp(0)
            DofE.Item(2, i).Value = Fnp(1)
            DofE.Item(3, i).Value = Fnp(2)
            DofE.Item(4, i).Value = tempD
            DofE.Item(5, i).Value = D

        Next

    End Sub

    Private Sub
Mat_Sys_SelectedIndexChanged(ByVal sender As
System.Object, ByVal e As System.EventArgs)
Handles Mat_Sys.SelectedIndexChanged
        Changed_Material(False)
    End Sub

    Private Sub Temp_KeyDown(ByVal sender As
Object, ByVal e As
System.Windows.Forms.KeyEventArgs) Handles
Temp.KeyDown
        If e.KeyCode = Keys.Enter Then
            e.SuppressKeyPress = True
            Changed_Material(False)
        End If
    End Sub

    Private Sub X_comp_KeyDown(ByVal sender
As Object, ByVal e As
System.Windows.Forms.KeyEventArgs) Handles
X_comp.KeyDown
        If e.KeyCode = Keys.Enter Then
            e.SuppressKeyPress = True
            Changed_Material(True)
        End If
    End Sub

    Private Sub Changed_Material(ByVal test
As Boolean)
        Dim Row As Integer
        Dim Temperature, X As Double
        Temperature = Temp.Text
        X = X_comp.Text

        Row = Mat_Sys.SelectedIndex + 2
        xBook.Worksheets("Bandgap").cells(1,
1).value() = Temperature

xBook.Worksheets("Bandgap").cells(Row,
3).value() = X

xBook.Worksheets("Rel_Dielectric_Const").cel
ls(Row, 3).value() = X

xBook.Worksheets("Tunneling_mr").cells(Row,
3).value() = X

xBook.Worksheets("DOS_mr_e").cells(Row,
3).value() = X
```

```
xBook.Worksheets("DOS_mr_h").cells(Row,
3).value() = X

        DGrid1.Item(1, 0).Value =
xBook.Worksheets("Bandgap").cells(Row,
1).value
        DGrid1.Item(1, 1).Value =
Temperature
        DGrid1.Item(1, 2).Value =
xBook.Worksheets("Bandgap").cells(Row,
2).value
        DGrid1.Item(1, 3).Value =
xBook.Worksheets("Rel_Dielectric_Const").cel
ls(Row, 2).value
        DGrid1.Item(1, 4).Value =
xBook.Worksheets("Tunneling_mr").cells(Row,
2).value

        DGrid2.Item(1, 0).Value =
xBook.Worksheets("DOS_mr_e").cells(Row,
2).value
        DGrid2.Item(2, 0).Value =
xBook.Worksheets("DOS_mr_h").cells(Row,
2).value

    End Sub

    Private Sub DGrid4_KeyUp(ByVal sender As
Object, ByVal e As
System.Windows.Forms.KeyEventArgs) Handles
DGrid4.KeyUp
        If Control.ModifierKeys =
Keys.Control Then
            Select Case e.KeyCode
                Case Keys.V
                    Paste(DGrid4)
            End Select
        End If
    End Sub

    Private Sub DGrid5_KeyUp(ByVal sender As
Object, ByVal e As
System.Windows.Forms.KeyEventArgs) Handles
DGrid5.KeyUp
        If Control.ModifierKeys =
Keys.Control Then
            Select Case e.KeyCode
                Case Keys.V
                    Paste(DGrid5)
            End Select
        End If
    End Sub

    Private Sub Paste(ByVal dgrid As
DataGridView)
        Dim clipboard As String
        Dim temp1(), temp2() As String
        Dim size, i, j, RowCount, row, col
As Integer

        col = dgrid.CurrentCell.ColumnIndex
'base-0
        row = dgrid.CurrentCell.RowIndex
'base-0
        RowCount = dgrid.RowCount 'base-1

        clipboard =
System.Windows.Forms.Clipboard.GetText
        temp1 = clipboard.Split(vbNewLine)
        size = temp1.Length 'base-1

        If RowCount < size + row Then
            dgrid.Rows.Add(size + row -
RowCount)
        End If

        For i = 0 To size - 1 Step 1
            temp2 = temp1(i).Split(vbTab)
            For j = 0 To temp2.Length - 1
Step 1
                dgrid.Item(col + j, row +
i).Value = temp2(j)
            Next
        Next

    End Sub

    Private Sub N_Sweep(ByVal dgrid As
DataGridView)
        Dim i As Integer

        For i = 1 To 6 Step 1
            dgrid.Rows.Add()
        Next

        dgrid.Item(0, 0).Value = 5.0E+18
        dgrid.Item(0, 1).Value = 7.5E+18
        dgrid.Item(0, 2).Value = 1.0E+19
        dgrid.Item(0, 3).Value = 2.5E+19
        dgrid.Item(0, 4).Value = 5.0E+19
        dgrid.Item(0, 5).Value = 7.5E+19
        dgrid.Item(0, 6).Value = 1.0E+20

        dgrid.Item(1, 0).Value = 5.0E+18
        dgrid.Item(1, 1).Value = 7.5E+18
        dgrid.Item(1, 2).Value = 1.0E+19
        dgrid.Item(1, 3).Value = 2.5E+19
        dgrid.Item(1, 4).Value = 5.0E+19
        dgrid.Item(1, 5).Value = 7.5E+19
        dgrid.Item(1, 6).Value = 1.0E+20
    End Sub

    Private Sub N_Sweep_Jp()
        Dim i, rows As Integer
        Dim Nad(,), Nstar As Double

        rows = DGrid4.RowCount - 1 '0-base

        If IsNumeric(DGrid4.Item(0,
rows).Value) Then
        Else
            rows = rows - 1
        End If
        ReDim Nad(1, rows)

        For i = 0 To rows Step 1
            Nad(0, i) = DGrid4.Item(0,
i).Value 'Nd
            Nad(1, i) = DGrid4.Item(1,
i).Value 'Na
            Nstar = Nad(0, i) * Nad(1, i) /
(Nad(0, i) + Nad(1, i))
            DGrid4.Item(2, i).Value =
Nstar.ToString("0.#####e0")
            DGrid4.Item(3, i).Value = Sqrt(1
/ Nstar).ToString("0.#####e0")
        Next

        Dim xSheet As
Microsoft.Office.Interop.Excel.Worksheet
```

```
        Dim path As String
        Dim j, L, steps As Integer
        Dim pi, q, m0, h_bar, c, e0, T, k,
kT As Double
        Dim er, Eg, mr(2), m_eff(2), Nc, Nv,
es As Double
        Dim Na, Nd, Efn, Efp, Vbi As Double
        Dim Va, X, E_bar, eV, Edel, Estep,
D, terms(2), Vp, Jp(1) As Double

        path =
System.IO.Directory.GetCurrentDirectory() &
"\ETD_Calculations.xlsx"
        xSheet =
xBook.Worksheets("Fermi_Integral")

        pi = 3.1415926536
        q = 1.602176E-19 'C
        m0 = 510998.91 'eV
        h_bar = 0.000000000000000658211899
'eV*Sec
        c = 299792000.0 'm/Sec
        e0 = 0.0000000000000008854188 'F/cm
        k = 0.00008617343 'eV/K
        T = DGrid1.Item(1, 1).Value 'K
        kT = k * T 'eV

        er = DGrid1.Item(1, 3).Value
        Eg = DGrid1.Item(1, 2).Value 'eV
        mr(0) = DGrid2.Item(1, 0).Value 'N-
type
        mr(1) = DGrid2.Item(2, 0).Value 'P-
type
        mr(2) = DGrid1.Item(1, 4).Value
'Tunneling

        es = e0 * er 'F/cm
        m_eff(0) = mr(0) * m0 / c ^ 2 'eV
(N-type)
        m_eff(1) = mr(1) * m0 / c ^ 2 'eV
(P-type)
        m_eff(2) = mr(2) * m0 / (c ^ 2) 'eV
(Tunneling)
        Nc = 0.000001 * Sqrt(1 / 2) * (kT *
m_eff(0) / (pi * h_bar ^ 2)) ^ 1.5 'cm^-3
        Nv = 0.000001 * Sqrt(1 / 2) * (kT *
m_eff(1) / (pi * h_bar ^ 2)) ^ 1.5 'cm^-3

        DGrid2.Item(1, 1).Value =
Nc.ToString("0.###e0") 'N-type
        DGrid2.Item(2, 1).Value =
Nv.ToString("0.###e0") 'P-type


        For i = 0 To rows Step 1
            Nd = DGrid4.Item(0, i).Value 'N-
type
            Na = DGrid4.Item(1, i).Value 'P-
type
            Nstar = Nd * Na / (Nd + Na)
            DGrid4.Item(2, i).Value =
Nstar.ToString("0.###e0")
            DGrid4.Item(3, i).Value = (Nstar
^ -0.5).ToString("0.###e0")

            Eg = DGrid1.Item(1, 2).Value 'eV
            Eg = BNG(Nd, Na, Eg)
            DGrid4.Item(11, i).Value =
Eg.ToString("0.#####")

            'Firmi_Levels1()
            'N-type region
            'Firmi_Levels1()
            'N-type region
            If CheckBox1.Checked = True Then
                Efn = Firmi_Levels2(xSheet,
Nd, Nc) 'Only accurate for InGaAs (53/47)
            Else
                Efn = Firmi_Levels(xSheet,
Nd, Nc) ', Nc(0))
            End If

            Efn = Eg - Efn * kT
            DGrid4.Item(9, i).Value =
Efn.ToString("0.####")

            'P-type region
            Efp = Firmi_Levels(xSheet, Na,
Nv)
            Efp = Efp * kT
            DGrid4.Item(10, i).Value =
Efp.ToString("0.####")

            DGrid1.Refresh()
            DGrid2.Refresh()
            DGrid3.Refresh()
            DGrid4.Refresh()

            Vp = 0
            Jp(0) = -1
            Vbi = Efn - Efp 'eV
            Dim temp(1) As Double
            steps = 1000 * (Efn - Efp - Eg)
'DGrid3.RowCount - 2
            For j = 0 To steps Step 1
                Va = j / 1000
'DGrid3.Item(0, j).Value '(Efn + Efp - Eg) /
2 'eV
                X = 100 * Sqrt(q * (Vbi -
Va) * Na * Nd / (2 * es * (Na + Nd))) 'V/m
                E_bar = h_bar * X * Sqrt(2)
/ (pi * Sqrt(m_eff(2) * Eg)) 'eV

                Estep = (Vbi - Va - Eg) /
500
                D = 0
                For L = 0 To 500 Step 1
                    eV = Estep * L
                    If eV < Vbi - Eg - Va -
eV Then
                        Edel = eV
                    Else
                        Edel = Vbi - Eg - Va
- eV
                    End If
                    temp(0) = eV + Eg
                    temp(1) = -Vbi + Va + Eg
+ eV
                    D = D + (Fcv(temp(0),
Efn, kT) - Fcv(temp(1), Efp, kT)) * (1 -
Exp(-2 * Edel / E_bar)) * Estep
                Next
                terms(0) = (q * X / (36 * pi
* h_bar ^ 2)) * Sqrt(2 * m_eff(2) / Eg) /
10000
                terms(1) = Exp(-pi *
Sqrt(m_eff(2)) * (Eg ^ 1.5) / (2 * Sqrt(2) *
h_bar * X))
                terms(2) = (4 * Sqrt(2 *
m_eff(2)) * (Eg ^ 1.5) / (3 * h_bar))
```

```
                Jp(1) = (D * terms(0) *
terms(1))

                If Jp(1) > Jp(0) Then
                    Jp(0) = Jp(1)
                    Vp = Va
                Else
                    j = steps + 100
                End If
            Next

            DGrid4.Item(4, i).Value = Vp
            DGrid4.Item(5, i).Value =
Jp(1).ToString("0.#####e0")
            DGrid4.Item(6, i).Value =
terms(0).ToString("0.#####e0")
            DGrid4.Item(7, i).Value =
D.ToString("0.#####e0")
            DGrid4.Item(8, i).Value =
Log(terms(1)).ToString("0.#####e0")
            DGrid4.Item(12, i).Value =
X.ToString("0.#####e0")
        Next

    End Sub

    Private Sub N_Sweep_Va()
        Dim i, rows As Integer
        Dim Nad(,), Nstar As Double

        rows = DGrid5.RowCount - 1 '0-base

        If IsNumeric(DGrid5.Item(0,
rows).Value) Then
        Else
            rows = rows - 1
        End If

        ReDim Nad(1, rows)

        For i = 0 To rows Step 1
            Nad(0, i) = DGrid5.Item(0,
i).Value 'Nd
            Nad(1, i) = DGrid5.Item(1,
i).Value 'Na
            Nstar = Nad(0, i) * Nad(1, i) /
(Nad(0, i) + Nad(1, i))
            DGrid5.Item(2, i).Value =
Nstar.ToString("0.#####e0")
            DGrid5.Item(3, i).Value = Sqrt(1
/ Nstar).ToString("0.#####e0")
        Next

        Dim xSheet As
Microsoft.Office.Interop.Excel.Worksheet
        Dim path As String
        Dim j, L, steps As Integer
        Dim pi, q, m0, h_bar, c, e0, T, k,
kT As Double
        Dim er, Eg, mr(2), m_eff(2), Nc, Nv,
es As Double
        Dim Na, Nd, Efn, Efp, Vbi As Double
        Dim Va, X, E_bar, eV, Edel, Estep,
D, terms(2), Vp, Jp(1) As Double

        path =
System.IO.Directory.GetCurrentDirectory() &
"\ETD_Calculations.xlsx"
        xSheet =
xBook.Worksheets("Fermi_Integral")

        pi = 3.1415926536
        q = 1.602176E-19 'C
        m0 = 510998.91 'eV
        h_bar = 0.000000000000000658211899
'eV*Sec
        c = 299792000.0 'm/Sec
        e0 = 0.00000000000008854188 'F/cm
        k = 0.00008617343 'eV/K
        T = DGrid1.Item(1, 1).Value 'K
        kT = k * T 'eV

        er = DGrid1.Item(1, 3).Value
        Eg = DGrid1.Item(1, 2).Value 'eV
        mr(0) = DGrid2.Item(1, 0).Value 'N-
type
        mr(1) = DGrid2.Item(2, 0).Value 'P-
type
        mr(2) = DGrid1.Item(1, 4).Value
'Tunneling

        es = e0 * er 'F/cm
        m_eff(0) = mr(0) * m0 / c ^ 2 'eV
(N-type)
        m_eff(1) = mr(1) * m0 / c ^ 2 'eV
(P-type)
        m_eff(2) = mr(2) * m0 / (c ^ 2) 'eV
(Tunneling)
        Nc = 0.000001 * Sqrt(1 / 2) * (kT *
m_eff(0) / (pi * h_bar ^ 2)) ^ 1.5 'cm^-3
        Nv = 0.000001 * Sqrt(1 / 2) * (kT *
m_eff(1) / (pi * h_bar ^ 2)) ^ 1.5 'cm^-3
        DGrid2.Item(1, 1).Value =
Nc.ToString("0.###e0") 'N-type
        DGrid2.Item(2, 1).Value =
Nv.ToString("0.###e0") 'P-type

        Va = TextBox1.Text 'j / 1000
'DGrid3.Item(0, j).Value '(Efn + Efp - Eg) /
2 'eV

        For i = 0 To rows Step 1
            Nd = DGrid5.Item(0, i).Value 'N-
type
            Na = DGrid5.Item(1, i).Value 'P-
type
            Nstar = Nd * Na / (Nd + Na)
            DGrid5.Item(2, i).Value =
Nstar.ToString("0.###e0")
            DGrid5.Item(3, i).Value = (Nstar
^ -0.5).ToString("0.###e0")

            Eg = DGrid1.Item(1, 2).Value 'eV
            DGrid5.Item(11, i).Value =
Eg.ToString("0.#####")

            'N-type region
            Efn = Firmi_Levels(xSheet, Nd,
Nc)
            Efn = Eg - Efn * kT
            DGrid5.Item(9, i).Value =
Efn.ToString("0.####")

            'P-type region
            Efp = Firmi_Levels(xSheet, Na,
Nv)
            Efp = Efp * kT
            DGrid5.Item(10, i).Value =
Efp.ToString("0.####")

            DGrid1.Refresh()
```

```
            DGrid2.Refresh()
            DGrid3.Refresh()
            DGrid4.Refresh()
            DGrid5.Refresh()

            Vbi = Efn - Efp 'eV
            Dim temp(1) As Double
            steps = 1000 * (Efn - Efp - Eg)
'DGrid3.RowCount - 2
            If Va < Efn - Efp - Eg Then
                X = 100 * Sqrt(q * (Vbi -
Va) * Na * Nd / (2 * es * (Na + Nd))) 'V/m
                E_bar = h_bar * X * Sqrt(2)
/ (pi * Sqrt(m_eff(2) * Eg)) 'eV

                Estep = (Vbi - Va - Eg) /
500
                D = 0
                For L = 0 To 500 Step 1
                    eV = Estep * L
                    If eV < Vbi - Eg - Va -
eV Then
                        Edel = eV
                    Else
                        Edel = Vbi - Eg - Va
- eV
                    End If
                    temp(0) = eV + Eg
                    temp(1) = -Vbi + Va + Eg
+ eV
                    D = D + (Fcv(temp(0),
Efn, kT) - Fcv(temp(1), Efp, kT)) * (1 -
Exp(-2 * Edel / E_bar)) * Estep
                    terms(0) = (q * X / (36
* pi * h_bar ^ 2)) * Sqrt(2 * m_eff(2) / Eg)
/ 10000
                    terms(1) = Exp(-pi *
Sqrt(m_eff(2)) * (Eg ^ 1.5) / (2 * Sqrt(2) *
h_bar * X))
                    terms(2) = (4 * Sqrt(2 *
m_eff(2)) * (Eg ^ 1.5) / (3 * h_bar))

                    Jp(1) = (D * terms(0) *
terms(1))
                Next
                    DGrid5.Item(4, i).Value = Va
                    DGrid5.Item(5, i).Value =
Jp(1).ToString("0.#####e0")
                    DGrid5.Item(6, i).Value =
terms(0).ToString("0.#####e0")
                    DGrid5.Item(7, i).Value =
D.ToString("0.#####e0")
                    DGrid5.Item(8, i).Value =
Log(terms(1)).ToString("0.#####e0")
                    DGrid5.Item(12, i).Value =
(X / 100).ToString("0.#####e0")
                End If
            Next

        End Sub

        Private Sub Button3_Click(ByVal sender
As System.Object, ByVal e As
System.EventArgs) Handles Button3.Click

            Select Case Bands.SelectedTab.Name
                Case "tab1"
                Case "tab2"
                    N_Sweep(DGrid4)
                Case "tab3"
                    N_Sweep(DGrid5)
            End Select
DoNothing:
        End Sub

        Private Sub Graph1_Click(ByVal sender As
System.Object, ByVal e As System.EventArgs)
Handles Graph1.Click
            Dim IVD(,), Parameters(10), temp2 As
Double
            Dim i, count, temp1 As Integer

            temp1 = DGrid3.RowCount
            count = temp1
            For i = 1 To temp1 Step 1
                If DGrid3.Item(2, temp1 -
i).Value > 0 Then
                    i = temp1 + 1
                Else
                    count = count - 1
                End If
            Next

            ReDim IVD(2, count)
            For i = 0 To count Step 1
                IVD(0, i) = DGrid3.Item(0,
i).Value
                temp2 = DGrid3.Item(1, i).Value
                IVD(1, i) = Abs(temp2)
                temp2 = DGrid3.Item(2, i).Value
                IVD(2, i) = Abs(temp2)
            Next

            Parameters(0) = DGrid3.Item(3,
2).Value '"Vbi-0 (V)"
            Parameters(1) = DGrid3.Item(3,
4).Value '"Wd (nm)"
            Parameters(2) = DGrid3.Item(3,
6).Value '"Wn (nm)"
            Parameters(3) = DGrid3.Item(3,
8).Value '"Wp (nm)"
            Parameters(4) = DGrid3.Item(3,
10).Value '"E-field (V/cm)"
            Parameters(5) = DGrid3.Item(3,
12).Value '"Pre-factor (1/ohm-cm/eV)"
            Parameters(6) = DGrid3.Item(4,
12).Value '"Arg. (cm/V)"
            Parameters(7) = DGrid3.Item(3,
14).Value '"Efn (eV)"
            Parameters(8) = DGrid3.Item(4,
14).Value '"Efp (eV)"
            Parameters(9) = DGrid3.Item(3,
18).Value '"Vp (V)"
            Parameters(10) = DGrid3.Item(4,
18).Value '"Jp (A/cm^2)"


            Dim Graph1 As New Form2(IVD,
Parameters)
            Graph1.ShowDialog()
        End Sub
End Class
```

The following code controls the J-V plotting routine (Appendix A.2). Description of the programs operation and function can be found in Chapter 3.5.

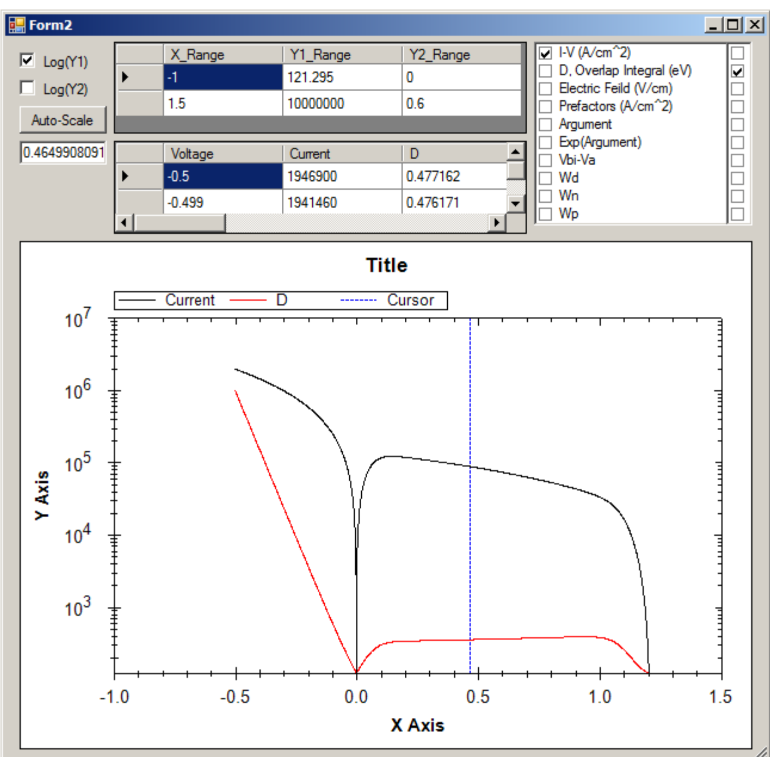

Appendix A.2: Secondary window plotting J-V results.

```
Imports ZedGraph
Imports System.Math
Public Class Form2

    Private Sub Form2_Load(ByVal sender As
System.Object, ByVal e As System.EventArgs)
Handles MyBase.Load

    End Sub

    Public Sub New(ByVal IVD(,) As Double,
ByVal parameters() As Double)
        InitializeComponent()

        Dim Graph1 As GraphPane =
zg1.GraphPane
        Dim LeftCurve, RightCurve, Cursor As
LineItem
        Dim DataLeft, DataRight, line As New
PointPairList
        Dim i, count As Integer

        count = IVD.GetLength(1) - 1
        For i = 0 To count Step 1
            DataLeft.Add(IVD(0, i), IVD(1,
i))
            DataRight.Add(IVD(0, i), IVD(2,
i))
        Next

        LeftCurve =
Graph1.AddCurve("Current", DataLeft,
Color.Black, SymbolType.None)
        RightCurve = Graph1.AddCurve("D",
DataRight, Color.Red, SymbolType.None)
        Graph1.CurveList("D").IsY2Axis =
True

        zg1.AxisChange()
        Graph1.YAxis.Scale.Min =
parameters(10) / 1000
        Graph1.YAxis.Type = AxisType.Log

        line.Add((Graph1.XAxis.Scale.Min +
Graph1.XAxis.Scale.Max) / 2,
Graph1.Y2Axis.Scale.Min)
        line.Add((Graph1.XAxis.Scale.Min +
Graph1.XAxis.Scale.Max) / 2,
Graph1.Y2Axis.Scale.Max)
        Cursor = Graph1.AddCurve("Cursor",
line, Color.Blue, SymbolType.None)
        Cursor.Line.Style =
Drawing2D.DashStyle.Dash

        AxisRange.Rows.Add()
        AxisRange.Rows.Add()
```

```
        AxisRange.Item(0, 0).Value =
Graph1.XAxis.Scale.Min
        AxisRange.Item(0, 1).Value =
Graph1.XAxis.Scale.Max
        AxisRange.Item(1, 0).Value =
Graph1.YAxis.Scale.Min
        AxisRange.Item(1, 1).Value =
Graph1.YAxis.Scale.Max
        AxisRange.Item(2, 0).Value =
Graph1.Y2Axis.Scale.Min
        AxisRange.Item(2, 1).Value =
Graph1.Y2Axis.Scale.Max

        zg1.Refresh()

        Dim Curves(9) As String
        Curves(0) = "I-V (A/cm^2)"
        Curves(1) = "D, Overlap Integral
(eV)"
        Curves(2) = "Electric Feild (V/cm)"
        Curves(3) = "Prefactors (A/cm^2)"
        Curves(4) = "Argument"
        Curves(5) = "Exp(Argument)"
        Curves(6) = "Vbi-Va"
        Curves(7) = "Wd"
        Curves(8) = "Wn"
        Curves(9) = "Wp"

        For i = 0 To Curves.Length - 1 Step
1
            Y1Axis.Items.Add(Curves(i),
False)
            Y2Axis.Items.Add(" ", False)
        Next
        count = Y1Axis.Items.Count

Y2Axis.SetBounds(Y2Axis.Bounds.Location.X,
Y2Axis.Bounds.Location.Y,
Y2Axis.Bounds.Width, 4 + count * 15)

Y1Axis.SetBounds(Y1Axis.Bounds.Location.X,
Y1Axis.Bounds.Location.Y,
Y1Axis.Bounds.Width, 4 + count * 15)
        Y1Axis.SetItemCheckState(0,
CheckState.Checked)
        Y2Axis.SetItemCheckState(1,
CheckState.Checked)

        Lists.Columns.Add("Voltage",
"Voltage")
        Lists.Columns.Add("Current",
"Current")
        Lists.Columns.Add("D", "D")
        Lists.Columns.Add("E-Feild", "E-
Feild")
        Lists.Columns.Add("Pre-F", "Pre-F")
        Lists.Columns.Add("Arg", "Arg")
        Lists.Columns.Add("Exp(Arg)",
"Exp(Arg)")
        Lists.Columns.Add("Vbi-Va", "Vbi-
Va")
        Lists.Columns.Add("Wd", "Wd")
        Lists.Columns.Add("Wn", "Wn")
        Lists.Columns.Add("Wp", "Wp")

        count = IVD.GetLength(1) - 1
        For i = 0 To count Step 1
            Lists.Rows.Add()
            Lists.Item(0, i).Value = IVD(0,
i)
            Lists.Item(1, i).Value = IVD(1,
i)
            Lists.Item(2, i).Value = IVD(2,
i)
            Lists.Item(3, i).Value =
parameters(4) * Sqrt(1 - IVD(0, i) /
parameters(0))
            Lists.Item(4, i).Value =
parameters(5) * Lists.Item(3, i).Value *
IVD(2, i)
            Lists.Item(5, i).Value =
Abs(parameters(6) / Lists.Item(3, i).Value)
            Lists.Item(6, i).Value = Exp(-
Lists.Item(5, i).Value)
            Lists.Item(7, i).Value =
parameters(0) - IVD(0, i)
            Lists.Item(8, i).Value =
parameters(1) * Sqrt(1 - IVD(0, i) /
parameters(0))
            Lists.Item(9, i).Value =
parameters(2) * Sqrt(1 - IVD(0, i) /
parameters(0))
            Lists.Item(10, i).Value =
parameters(3) * Sqrt(1 - IVD(0, i) /
parameters(0))
        Next
    End Sub

    Private Sub LogY1_CheckedChanged(ByVal
sender As System.Object, ByVal e As
System.EventArgs) Handles
LogY1.CheckedChanged
        Dim Graph1 As GraphPane =
zg1.GraphPane

        If LogY1.Checked = True Then
            Graph1.YAxis.Type = AxisType.Log
        Else
            Graph1.YAxis.Type =
AxisType.Linear
        End If
        zg1.Refresh()

    End Sub

    Private Sub LogY2_CheckedChanged(ByVal
sender As System.Object, ByVal e As
System.EventArgs) Handles
LogY2.CheckedChanged
        Dim Graph1 As GraphPane =
zg1.GraphPane

        If LogY2.Checked = True Then
            Graph1.Y2Axis.Type =
AxisType.Log
        Else
            Graph1.Y2Axis.Type =
AxisType.Linear
        End If
        zg1.Refresh()

    End Sub

    Private Sub AxisRange_KeyUp(ByVal sender
As Object, ByVal e As
System.Windows.Forms.KeyEventArgs) Handles
AxisRange.KeyUp
        If e.KeyCode = Keys.Enter Then
            e.SuppressKeyPress = True
```

```
            Dim Graph1 As GraphPane =
zg1.GraphPane

            Graph1.XAxis.Scale.Min =
AxisRange.Item(0, 0).Value
            Graph1.XAxis.Scale.Max =
AxisRange.Item(0, 1).Value
            Graph1.YAxis.Scale.Min =
AxisRange.Item(1, 0).Value
            Graph1.YAxis.Scale.Max =
AxisRange.Item(1, 1).Value
            Graph1.Y2Axis.Scale.Min =
AxisRange.Item(2, 0).Value
            Graph1.Y2Axis.Scale.Max =
AxisRange.Item(2, 1).Value

        End If

        zg1.Refresh()
    End Sub

    Private Sub
Y1Axis_SelectedIndexChanged(ByVal sender As
System.Object, ByVal e As System.EventArgs)
Handles Y1Axis.SelectedIndexChanged
        Dim i, index, count As Integer
        Dim Graph2 As GraphPane =
zg1.GraphPane
        Dim Curve As LineItem
        Dim NewData As New PointPairList

        index = Y1Axis.SelectedIndex + 1
        If Y1Axis.GetItemChecked(index - 1)
= True Then
            If Y2Axis.GetItemChecked(index -
1) = True Then

Graph2.CurveList.Remove(Graph2.CurveList(Lis
ts.Columns(index).Name))

Y2Axis.SetItemCheckState(index - 1,
CheckState.Unchecked)
            End If
            count = Lists.RowCount - 1
            For i = 0 To count Step 1
                NewData.Add(Lists.Item(0,
i).Value, Lists.Item(index, i).Value)
            Next

            Curve =
Graph2.AddCurve(Lists.Columns(index).Name,
NewData, Color.Black, SymbolType.None)
        Else

Graph2.CurveList.Remove(Graph2.CurveList(Lis
ts.Columns(index).Name))
        End If

        zg1.Refresh()
    End Sub

    Private Sub
Y2Axis_SelectedIndexChanged(ByVal sender As
Object, ByVal e As System.EventArgs) Handles
Y2Axis.SelectedIndexChanged
        Dim i, index, count As Integer
        Dim Graph1 As GraphPane =
zg1.GraphPane
        Dim Curve As LineItem
        Dim Data As New PointPairList

        index = Y2Axis.SelectedIndex + 1
        If Y2Axis.GetItemChecked(index - 1)
= True Then
            If Y1Axis.GetItemChecked(index -
1) = True Then

Graph1.CurveList.Remove(Graph1.CurveList(Lis
ts.Columns(index).Name))

Y1Axis.SetItemCheckState(index - 1,
CheckState.Unchecked)
            End If
            count = Lists.RowCount - 1
            For i = 0 To count Step 1
                Data.Add(Lists.Item(0,
i).Value, Lists.Item(index, i).Value)
            Next
            Curve =
Graph1.AddCurve(Lists.Columns(index).Name,
Data, Color.Red, SymbolType.None)

Graph1.CurveList(Lists.Columns(index).Name).
IsY2Axis = True
        Else

Graph1.CurveList.Remove(Graph1.CurveList(Lis
ts.Columns(index).Name))
        End If

        zg1.Refresh()

    End Sub

    Private Sub AutoScale_Click(ByVal sender
As System.Object, ByVal e As
System.EventArgs) Handles AutoScale.Click
        Dim graph1 As GraphPane =
zg1.GraphPane

        zg1.AxisChange()
        AxisRange.Item(0, 0).Value =
Graph1.XAxis.Scale.Min
        AxisRange.Item(0, 1).Value =
Graph1.XAxis.Scale.Max
        AxisRange.Item(1, 0).Value =
Graph1.YAxis.Scale.Min
        AxisRange.Item(1, 1).Value =
Graph1.YAxis.Scale.Max
        AxisRange.Item(2, 0).Value =
Graph1.Y2Axis.Scale.Min
        AxisRange.Item(2, 1).Value =
graph1.Y2Axis.Scale.Max

        zg1.Refresh()
    End Sub

    Private Sub zg1_MouseMove(ByVal sender
As Object, ByVal e1 As
System.Windows.Forms.MouseEventArgs) Handles
zg1.MouseMove
        ' Save the mouse location
        Dim mousePt As New PointF(e1.X,
e1.Y) '(e.X, e.Y)

        ' Find the Chart rect that contains
the current mouse location
```

```
        Dim pane As GraphPane =
sender.MasterPane.FindChartRect(mousePt)

        ' If pane is non-null, we have a
valid location.  Otherwise, the mouse is not
        ' within any chart rect.
        If Not pane Is Nothing Then

            Dim x, y As Double
            ' Convert the mouse location to
X, Y scale values
            pane.ReverseTransform(mousePt,
x, y)

            Dim curve1 As CurveItem
            Dim list As IPointListEdit
            Dim mypane As GraphPane =
zg1.GraphPane
            Dim LastIndex, IndexWidth,
TempIndex As Integer
            Dim dataM = New PointPairList
zg1.GraphPane.CurveList.Remove(zg1.GraphPane
.CurveList("Cursor"))

            IndexWidth = Int(LastIndex / 20)
            dataM.Add(x,
mypane.YAxis.Scale.Min)
            dataM.Add(x,
mypane.YAxis.Scale.Max)
            Dim myCurve As LineItem =
mypane.AddCurve("Cursor", dataM, Color.Blue,
SymbolType.None)
            myCurve.Line.Style =
Drawing2D.DashStyle.Dash
            TextBox1.Text = x

            zg1.Refresh()
            TextBox1.Refresh()
        End If

    End Sub

    Private Sub TextBox1_KeyUp(ByVal sender
As Object, ByVal e As
System.Windows.Forms.KeyEventArgs) Handles
TextBox1.KeyUp
        If e.KeyCode = Keys.Enter Then
            e.SuppressKeyPress = True
            Dim Graph1 As GraphPane =
zg1.GraphPane
            Dim Cursor As LineItem
            Dim line As New PointPairList


zg1.GraphPane.CurveList.Remove(zg1.GraphPane
.CurveList("Cursor"))

            line.Add(TextBox1.Text,
Graph1.YAxis.Scale.Min)
            line.Add(TextBox1.Text,
Graph1.YAxis.Scale.Max)
            Cursor =
Graph1.AddCurve("Cursor", line, Color.Blue,
SymbolType.None)
            Cursor.Line.Style =
Drawing2D.DashStyle.Dash
            zg1.Refresh()
        End If
    End Sub

End Class
```

APPENDIX B

ImageJ Area Analysis Macro

The macro prompts the user to select a directory containing all of the image files to be ran. ImageJ runs one file at a time, beginning by automatically determining the region of interest and maximizing the zoom to fit that region. The macro is paused and the image is then made available for the user to define the device edge. Additionally, various image processing tools become available to speed up the analysis. Finally, the user continues the macro, whereupon the device dimensions are automatically fitted with an ellipse and the results are recorded as well as the final image. Magnification, device location, and mask defined size values are automatically extracted from the image files.

```
macro "Measure Ellipse Batch (Manual mode)" {
	requires("1.33s");
	run("Set Measurements...", " display area fit ");
	run("Clear Results");
	dir = getDirectory("Choose a Directory ");
	list = getFileList(dir);
	setBatchMode(false);

	for (i=0; i<list.length; i++) {
		path = dir+list[i];
		open(path);

	fname=toLowerCase(getInfo("image.filename")); //toLowerCase(File.name);
//***************************************************************************
//Find bounds of partial field (Origin is top-left corner of image;
//   1) Left Edge
//   2) Right Edge
//   3) Top
//   4) Bottom

		run("RGB Color");
		y=384;
		x=512;
		do {
			x=x-1;
```

```
			v = getPixel(x,y);
			red = (v>>16)&0xff;  // extract red byte (bits 23-17)
			green = (v>>8)&0xff; // extract green byte (bits 15-8)
			blue = v&0xff;       // extract blue byte (bits 7-0)
		} while (red!=0 || green!=255 || blue!=0);
		Xmin=x+1;

		x=512;
		do {
			x=x+1;
			v = getPixel(x,y);
			red = (v>>16)&0xff;  // extract red byte (bits 23-17)
			green = (v>>8)&0xff; // extract green byte (bits 15-8)
				blue = v&0xff;       // extract blue byte (bits 7-0)
		} while (red!=0 || green!=255 || blue!=0)
		Xmax=x-1;

		x=512;
		y=384;
		do {
			y=y-1;
			v = getPixel(x,y);
			red = (v>>16)&0xff;  // extract red byte (bits 23-17)
			green = (v>>8)&0xff; // extract green byte (bits 15-8)
			blue = v&0xff;       // extract blue byte (bits 7-0)
		} while (red!=0 || green!=255 || blue!=0);
		Ymin=y+1;

		y=384;
		do {
			y=y+1;
			v = getPixel(x,y);
			red = (v>>16)&0xff;  // extract red byte (bits 23-17)
			green = (v>>8)&0xff; // extract green byte (bits 15-8)
			blue = v&0xff;       // extract blue byte (bits 7-0)
		} while (red!=0 || green!=255 || blue!=0);
		Ymax=y-1;

		//run("Revert");
	run("32-bit");
		RangeX=(Xmax-Xmin);
		RangeY=(Ymax-Ymin);

		makeRectangle(Xmin, Ymin, RangeX, RangeY);
		run("To Selection");
//***************************************************************************



//***************************************************************************
//Extracting magnification directly from TIFF file tag
```

```
//Gets the tag, and parses it to get the pixel size information
			tagnum=34118;
			tag = call("TIFF_Tags.getTag", path, tagnum);
			i0 = indexOf(tag, "Mag = ");
				if (i0==-1) exit ("Scale information not found");

			i1 = indexOf(tag, "=", i0);
			i2 = indexOf(tag, "X", i1);
				if (i1==-1 || i2==-1 || i2 <= i1+4)
					exit ("Parsing error! Maybe the file structure changed?");

			text = substring(tag,i1+1,i2+1);

//Parse text string to find magnification number
			TextSize = lengthOf(text);
			Mag = "";
			j = 0;

			do {
				Char = substring(text, j, j+1);
				if (Char!=" " && Char!="K" && Char!="M" && Char!="X")

				Mag=Mag+Char;
				j = j+1;
			} while (Char!="K" && Char!="M" && Char!="X");

			if (Char=="K")
				Mag = parseFloat(Mag)*1000;
			else if (Char=="K")
				Mag = parseFloat(Mag)*1000000;
			else
				Mag = parseFloat(Mag)*1;

			Dist =  365856*Mag/60000;
			run("Set Scale...", "distance="+Dist+" known=680799.42 pixel=1 unit=nm");
//*************************************************************************


//*************************************************************************
//Perform thresholding

			run("Threshold...");
			setAutoThreshold("Minimum");
			waitForUser("(1) Adjust thresholding, \n(2) Do Wand to outline, \n(3) Selection
Brush for adjustments, \n(4) Click 'OK' when done \n   - 'r' to revert image \n   - 'shift + t' adjust
threshold levels");
//*************************************************************************

			run("Measure");
			row = nResults-1;
			fname=getResultLabel(row);
```

```
LocX = parseFloat(substring(fname,1,2));
LocY = parseFloat(substring(fname,3,4));
LocCol = substring(fname,5,6);
        LocCol = charCodeAt(LocCol,0)-64;
LocRow = parseFloat(substring(fname,6,7));
        if (LocRow==0)  LocRow = 10;

        if (LocCol<6) {
                if (LocRow==1) MDL = 0.1;
                else if (LocRow==2) MDL = 0.3;
                else if (LocRow==3) MDL = 0.5;
                else if (LocRow==4) MDL = 0.7;
                else if (LocRow==7) MDL = 0.9;
                else if (LocRow==8) MDL = 1.2;
                else if (LocRow==9) MDL = 1.6;
                else if (LocRow==10) MDL = 2.0;
                }
        else {
                if (LocRow==1) MDL = 0.2;
                else if (LocRow==2) MDL = 0.4;
                else if (LocRow==3) MDL = 0.6;
                else if (LocRow==4) MDL = 0.8;
                else if (LocRow==7) MDL = 1.0;
                else if (LocRow==8) MDL = 1.4;
                else if (LocRow==9) MDL = 1.8;
                else if (LocRow==10) MDL = 3.0;
                }

        if (LocRow==5 || LocRow==6){
                if (LocCol==1 || LocCol==2) MDL = 4.0;
                if (LocCol==3) MDL = 10;
                if (LocCol==8) MDL = 20;
                if (LocCol==9 || LocCol==10) MDL = 5.0;
                }

setResult("X",row,LocX);
setResult("Y",row,LocY);
setResult("Column",row,LocCol);
setResult("Row",row,LocRow);
setResult("Length (um)",row,MDL);
updateResults();

                setForegroundColor(255, 255, 0);
                run("Revert");

                run("Draw");
                saveAs("Tiff", dir + "Output_" + fname);
                close();
        }
}
```

APPENDIX C

Fabrication & Processing Traveler

The following is a table containing the fabrication process used for this work. The left hand column contains the fabrication procedure as well as required information and metrology results for continued processing. The right hand column is for additional comments and results.

1) Cleave Sample a) Width: b) Height: c) Markings?	
2) Surface Prep? a) InP cap etch b) Other?	
3) Lithography 1 a) IPA Clean b) Dehydration bake c) Spin LOR 5A i) Ramp up: 2 sec to 500 RPM ii) Stay: 2 sec @ 500 RPM iii) Ramp up: 2 sec to 4000 RPM iv) Stay: 45 sec @ 4000 RPM v) Ramp Down: ~3-5 sec d) Spin PMMA i) Ramp up: 2 sec to 500 RPM ii) Stay: 2 sec @ 500 RPM iii) Ramp up: 2 sec to 4000 RPM iv) Stay: 45 sec @ 4000 RPM v) Ramp Down: ~3-5 sec e) Bake @ 1800C for 10 min. f) Exposure i) Rows, Col ii) Die spacing (Rows, Col) iii) Alignment Cross iv) $I_{Filament}$ (A) v) $I_{Probe}/I_{Start}/I_{Finish}$ vi) Stage tilt vii) AutoFocus (z=Ax+By+C) (1) Y = Ax + By, +C (2) RMS g) Develop PMMA i) MIBK:IPA (1:3) – 75 sec	

Step	
ii) Blow dry (no DI rinse) h) Develop LOR5A i) CD26:DI (1:1) – 75 sec ii) CD26 – 10 sec iii) Di Rinse & blow dry i) Inspect with Optical microscope j) SEM inspection (optional)	
4) Metal #1 Deposition a) Prepare NANO 38 for evaporator i) Replace kapton tape ii) Replace NPRL Au boat with ours iii) Add Au to boat (~3.5) iv) Replace Zn pellet (if needed) v) Check thickness monitor crystal vi) Remove sample platen vii) Close door b) DI:HCl (10:1) – 10 sec. i) DI rinse & blow dry c) Load samples d) Pump down chamber (< 5e-6 Torr) e) Setup Recipe i) Layer 1: Au, 20nm ii) Layer 2: Zn, 20nm iii) Layer 3: Au, 160m f) Run recipe i) Layer 1 (use “auto/manual”) ii) Layer 2: fully automated iii) Layer 3 (use “auto/manual”) g) Finish i) Vent chamber & remove samples ii) Remove our Au boat and replace with NPRL’s iii) Pump down chamber	
5) Lift-Off a) Heat PG Remover i) 80^0C – 90^0C (set temp to ~115^0C) ii) 1st beaker: lift-off iii) 2nd beaker: clean-up b) Rinse & blow dry c) Optical inspect d) O2 Ash (Lam 490) e) HCl:DI (1:1) f) IPA Rinse g) Optical inspect h) Profilometry (metal thickness)	
6) Mesa Isolation Etch a) Citric Acid: H_2O_2 (20:1) i) ~1 nm/min b) Profilometry (metal + mesa)	

i) Etch depth (mesa thick.) c) Etch rate? d) SEM inspect i) Metal thickness ii) Mesa thickness	
7) Level 1 electrical testing a) Observe NDR? i) Sizes measured? ii) J_P, J_V, PVCR? b) Observations:	
8) BCB Coat a) Set "Blue M" oven to 140^0C w/N_2 b) Set hot plate to 140^0C c) IPA Clean d) Dehydration bake e) Spin AP3000 i) Ramp up: 2 sec to 500 RPM ii) Stay: 2 sec @ 500 RPM iii) Ramp up: 2 sec to 3000 RPM iv) Stay: 60 sec @ 3000 RPM v) Ramp Down: ~3-5 sec f) Spin BCB i) Ramp up: 2 sec to 500 RPM ii) Stay: 2 sec @ 500 RPM iii) Ramp up: 2 sec to 3000 RPM iv) Stay: 60 sec @ 3000 RPM v) Ramp Down: ~3-5 sec g) Bake @ 1400C >5min. h) Cure in "Blue M" oven i) Place sample in oven (flat) ii) Ramp oven to 250^0C (w/N_2) iii) Start timer when temp > 245^0C iv) Cure for 60 min. v) Remove samples & turn oven off	
9) BCB Etch back a) Fast Etch (400-600 nm/min) i) SF_6:O_2 (sccm) ii) Pressure & electrode spacing iii) Power b) Slow Etch (200-300 nm/min) i) SF_6:O_2 (sccm) ii) Pressure & electrode spacing iii) Power c) Measure BCB thick: Nanospec (nm) i) Refractive index = 1.54 ii) 5 locations away from edge (1) On top and below big bar d) BCB to Etch (t_{BCB} –t_{final_BCB}) i) t_{final_BCB} = (t_{mesa}+t_{metal}) ii) ****BCB measures thick. when it is thin (<~500 nm)*******	

e) Fast Etch BCB: i) Etch time (total) ii) Measure: t_{BCB} (STDev) (nm) iii) Calculate: $t_{BCB} - t_{final_BCB}$ (nm) iv) Rate: R_{fast} (nm/min) f) Slow Etch BCB: i) Etch for some time ii) Measure: t_{BCB} (STDev) (nm) iii) Calculate: $t_{BCB} - t_{final_BCB}$ (nm) iv) Rate: R_{fast} (nm/min) g) SEM Inspect: h) Post BCB electrical testing i) Observe NDR? i) Sizes measured? ii) J_P, J_V, PVCR? j) Observations:	
10) Lithography 2 a) IPA Clean b) Dehydration bake c) Spin LOR 5A: 1st Coat i) Ramp up: 2 sec to 500 RPM ii) Stay: 2 sec @ 500 RPM iii) Ramp up: 2 sec to 4000 RPM iv) Stay: 45 sec @ 4000 RPM v) Ramp Down: ~3-5 sec d) Bake @ 1800C for 1 min. e) Spin LOR 5A: 2nd coat i) Ramp up: 2 sec to 500 RPM ii) Stay: 2 sec @ 500 RPM iii) Ramp up: 2 sec to 4000 RPM iv) Stay: 45 sec @ 4000 RPM v) Ramp Down: ~3-5 sec f) Spin PMMA i) Ramp up: 2 sec to 500 RPM ii) Stay: 2 sec @ 500 RPM iii) Ramp up: 2 sec to 4000 RPM iv) Stay: 45 sec @ 4000 RPM v) Ramp Down: ~3-5 sec g) Bake @ 1800C for 10 min. h) Exposure i) Rows, Col ii) Die spacing (Rows, Col) iii) $I_{Filament}$ (A) iv) $I_{Probe}/I_{Start}/I_{Finish}$ v) Stage tilt i) Develop PMMA i) MIBK:IPA (1:3) – 75 sec ii) Blow dry (no DI rinse) j) Develop LOR5A i) CD26:DI (1:1) – 135 sec ii) CD26 – 10 sec	

iii) Di Rinse & blow dry k) Inspect with Optical microscope l) SEM inspection (optional)	
11) Metal #1 Deposition a) Prepare NANO 38 for evaporator i) Replace kapton tape ii) Replace NPRL Au boat with ours iii) Add Au to boat (~6) iv) Check thickness monitor crystal v) Remove sample platen vi) Close door b) Load samples c) Pump down chamber (< 5e-6 Torr) d) Setup Recipe i) Layer 3: Au, 400m e) Run recipe i) Layer 3 (use "auto/manual") f) Finish i) Vent chamber & remove samples ii) Remove our Au boat and replace with NPRL's iii) Pump down chamber	
12) Lift-Off a) Heat PG Remover i) $80^0C - 90^0C$ (set temp to $\sim 115^0C$) ii) 1st beaker: lift-off iii) 2nd beaker: clean-up b) Rinse & blow dry c) Optical inspect	
13) Processing Completed: proceed to Electrical Testing	

APPENDIX D

Peak Including Valley Extraction Tool

The following is the main body code for the "Peak Including Valley Extract Tool" (PIVET). The program is written with VB.net, using the Microsoft Visual Studio development environment. The main code is activated when the "Find Me" button is clicked in the main window (Appendix D.1).

Appendix D.1: Main window for PIVET.

```
Imports System.Math

Public Class PIVET

    Private Sub PIVET_Load(ByVal sender As
System.Object, ByVal e As System.EventArgs)
Handles MyBase.Load

        Dim Alg_List() As String
        Dim Alg As New Get_Algorithm
'PIVET_algorithms.Form1
        Dim count1, i As Integer
        Alg_List = Alg.List_Algorithms
        count1 = Alg_List.GetLength(0) - 1
        Algorythm.Text = Alg_List(0)
        For i = 0 To count1
            Algorythm.Items.Add(Alg_List(i))
        Next

        Dim Format_List() As String
        Dim Format As New Get_FileFormat
        Dim count2 As Integer
        Format_List = Format.Format_List
        count2 = Format_List.GetLength(0) -
1
        F_List.Text = Format_List(0)
        For i = 0 To count2
            F_List.Items.Add(Format_List(i))
        Next

    End Sub

    Private Sub Execute_Click(ByVal sender
As System.Object, ByVal e As
System.EventArgs) Handles Execute.Click
        Dim FileName(), identifiers(3),
SendFileNames(2) As String
        Dim FileNumber(1) As Integer

'********************************************
***
        'Get Filename information:
        '   (1)   path\file_name
        '   (0)   path\
        '   (2)   \file_name.
        FileName = GetFileName()
        If FileName(0) = "False" Then
            Messages1.Text = "No File"
            Messages2.Text = "No File"
            Messages1.Refresh()
            Messages2.Refresh()
            GoTo end_of_program
        Else
            Messages1.Text = "Let's Get
Started"
            Messages2.Text = "Let's Get
Started"
            Messages1.Refresh()
            Messages2.Refresh()
        End If
        '

'********************************************
***

        If ConstAlg.Checked = True Then
            identifiers =
analize_name(FileName(0)) ', AlgTypes,
FFormats, FR)

            Dim GetAlg2 As New
Get_Algorithm2
'PIVET_algorithms.Get_Algorithm2
            GetAlg2.ShowDialog()
            identifiers(3) =
GetAlg2.Selected_Alg2
        End If
```

```
        FileNumber(0) = (FileName.Length -
1) / 2
        SendFileNames(1) = FileName(0)
        For i = 1 To FileNumber(0) Step 1
            FileNumber(1) = i

            Messages1.Text = "File " &
FileNumber(1) & " of " & FileNumber(0) & "
<" & FileName(2 * i) & ">:  "
            Messages1.Refresh()

            SendFileNames(0) = FileName(2 *
i - 1)
            SendFileNames(2) = FileName(2 *
i)
            Analyze_File(SendFileNames,
identifiers, FileNumber)
        Next

end_of_program:

        Messages1.Text = "I am finished.
Please let me rest."
        Messages2.Text = "I am finished.
Please let me rest."
        Messages1.Refresh()
        Messages2.Refresh()

    End Sub

    Private Sub Analyze_File(ByVal
filename() As String, ByVal identifiers() As
String, ByVal FileNumber As Array)  '(ByVal
filename0 As String, ByVal filename1 As
String, ByVal filename2 As String, ByVal
identifiers() As String, ByVal FileNumber As
Array)
        Dim i, counter, sheetcount,
output(1), row As Integer
        Dim settings(5), Data0(,), Data1(,),
Area(), Temperatures(), scalar As Double
        Dim x1App, x2App As New
Microsoft.Office.Interop.Excel.Application
'Excel.Application
        Dim x1book, x2book As
Microsoft.Office.Interop.Excel.Workbook
        Dim x1sheet As
Microsoft.Office.Interop.Excel.Worksheet
        'Dim filename(2) As String
        Dim Algorithms As New Get_Algorithm
'PIVET_algorithms.Form1
        Dim Formats As New Get_FileFormat


''*******************************************
****
        'filename(0) = filename0
        'filename(1) = filename1
        'filename(2) = filename2



'*******************************************
***
        'Look at File name for identifiers:
        '    (0) Algorithm
        '    (1) file format
        '    (2) forward/reverse peaks
        '    (3) Second Algorythm for
comparison
        '
        'If one isn't found, user must
supply one.
        If ConstAlg.Checked = False Then
            ReDim identifiers(3) 'As String
            identifiers =
analize_name(filename(0)) ', AlgTypes,
FFormats, FR)

            'ReDim Preserve identifiers(3)
            Dim GetAlg2 As New
Get_Algorithm2
'PIVET_algorithms.Get_Algorithm2
            GetAlg2.ShowDialog()
            identifiers(3) =
GetAlg2.Selected_Alg2
        End If
        '
'*******************************************
***



'*******************************************
***
        'Create output excel file
        x1App.Visible = False
        x1App.DisplayAlerts = False
        x2book = x1App.Workbooks.Add
'(filename(1) & "\output\" & filename(2))
        If
System.IO.Directory.Exists(filename(1) +
"output") = False Then

System.IO.Directory.CreateDirectory(filename
(1) + "output\")
        End If
        x2book.SaveAs(filename(1) &
"output\" & filename(2))
        '
        '
        'Create Worksheets
        '    (1) Combined IV data
        '    (2) Extracted Data
        '        --> And Populate it
        sheetcount = x2book.Sheets.Count

x2book.Worksheets.Add(After:=x2book.Workshee
ts(sheetcount), Count:=2)
        x2book.Worksheets(sheetcount +
1).Name = "Combined IV"
        x2book.Worksheets(sheetcount +
2).Name = "Extracted Data"
        '
        x2book.Worksheets("Extracted
Data").cells(1, 1).value = "File Name"
        x2book.Worksheets("Extracted
Data").cells(1, 2).value = "Append"
        x2book.Worksheets("Extracted
Data").cells(1, 3).value = "X"
        x2book.Worksheets("Extracted
Data").cells(1, 4).value = "Y"
```

```
        x2book.Worksheets("Extracted
Data").cells(1, 5).value = "Grid"
        x2book.Worksheets("Extracted
Data").cells(1, 6).value = "Temperature"
        x2book.Worksheets("Extracted
Data").cells(1, 7).value = Geometry.Text & "
(" & Units.Text & ")"
        x2book.Worksheets("Extracted
Data").cells(1, 8).value = "Undercut"
        x2book.Worksheets("Extracted
Data").cells(1, 9).value = "Width (X)"
        x2book.Worksheets("Extracted
Data").cells(1, 10).value = "Height (Y)"
        x2book.Worksheets("Extracted
Data").cells(1, 11).value = "Diameter (um)"
        x2book.Worksheets("Extracted
Data").cells(1, 12).value = "Area (cm2)"
        x2book.Worksheets("Extracted
Data").cells(1, 13).value = "Vp (Rev.)"
        x2book.Worksheets("Extracted
Data").cells(1, 14).value = "Vv (Rev.)"
        x2book.Worksheets("Extracted
Data").cells(1, 15).value = "Ip (Rev.)"
        x2book.Worksheets("Extracted
Data").cells(1, 16).value = "Iv (Rev.)"
        x2book.Worksheets("Extracted
Data").cells(1, 17).value = "Jp (A/cm2)"
        x2book.Worksheets("Extracted
Data").cells(1, 18).value = "Jv (A/cm2)"
        x2book.Worksheets("Extracted
Data").cells(1, 19).value = "PVCR (Rev.)"
        x2book.Worksheets("Extracted
Data").cells(1, 20).value = "Vp (For.)"
        x2book.Worksheets("Extracted
Data").cells(1, 21).value = "Vv (For.)"
        x2book.Worksheets("Extracted
Data").cells(1, 22).value = "Ip (For.)"
        x2book.Worksheets("Extracted
Data").cells(1, 23).value = "Iv (For.)"
        x2book.Worksheets("Extracted
Data").cells(1, 24).value = "Jp (A/cm2)"
        x2book.Worksheets("Extracted
Data").cells(1, 25).value = "Jv (A/cm2)"
        x2book.Worksheets("Extracted
Data").cells(1, 26).value = "PVCR (For.)"

        x2book.Worksheets("Sheet1").delete()
        x2book.Worksheets("Sheet2").delete()
        x2book.Worksheets("Sheet3").delete()

        x2book.Save()

        Messages2.Text = "Output File
Created and Formatted."
        Messages2.Refresh()
        '

'*********************************************
***



'*********************************************
***
        'Open File
        'Get initial settings
        Select Case identifiers(1)

            Case Is = "K4200"

                Messages2.Text = "Working
with a Keithley 4200 Formatted input File"
                Messages2.Refresh()

                x1book =
x2App.Workbooks.Open(filename(0))
                settings =
Formats.K4200_settings(x1book)
                settings(0) = settings(0) -
2

                'settings;
                '    (0) # of worksheets = #
of IV curves
                '    (1) compliance
                '    (2) Starting voltage
                '    (3) voltage step
                '    (4) voltage = 0 V
                '    (5) number of data
points

            Case Is = "PSU"

                Messages2.Text = "Working
with a PSU Formatted input File"
                Messages2.Refresh()

                settings(0) = 1

            Case Is = "NPRL"

            Case Else
                GoTo skip_analysis
        End Select
        '

'*********************************************
***


'*********************************************
***
        'loop for each dataset
        counter = 1
        row = 1
        For i = 0 To (settings(0) - 1) Step
1
            Messages2.Text = "Data Set " &
(i + 1) & " of " & settings(0)
            Messages2.Refresh()


'************************************
            'Collect data set
            Select Case identifiers(1)

                Case Is = "K4200"

                    If i >= 1 Then
                        x1sheet =
x1book.Worksheets(i + 3)

x2book.Worksheets("Extracted
Data").cells(row + 1, 1).value = x1book.Name
'x1book.Worksheets(i + 3).name

x2book.Worksheets("Extracted
Data").cells(row + 1, 2).value =
x1book.Worksheets(i + 3).name
```

```
                    Else
                        x1sheet =
x1book.Worksheets(i + 1)

x2book.Worksheets("Extracted
Data").cells(row + 1, 1).value = x1book.Name
'x1book.Worksheets(i + 3).name

x2book.Worksheets("Extracted
Data").cells(row + 1, 2).value =
x1book.Worksheets(i + 3).name
                    End If
                    Data0 =
Formats.K4200_All(x1sheet)

x2book.Worksheets("Combined IV").cells(1,
counter + 1).value = x1sheet.Name

                Case Is = "PSU"
                    Data0 =
Formats.PSU_All(filename(0))

x2book.Worksheets("Combined IV").cells(1,
counter + 1).value = filename(2)

                Case Is = "NPRL"

                Case Else
                    GoTo skip_analysis
            End Select

            x2book.Worksheets("Extracted
Data").cells(row + 1, 11).value = "=sqrt((I"
& (row + 1) & "-2*H" & (row + 1) & ")*(J" &
(row + 1) & "-2*H" & (row + 1) & "))"

            x2book.Worksheets("Combined
IV").cells(2,
counter).resize(Data0.GetLength(0), 2).value
= Data0
            x2book.Worksheets("Combined
IV").cells(1, counter).value = "Voltage"
            counter = counter + 2
            row = row + 1

'***********************************

'***********************************
            'If there is a peak and valley
in quadrant 3 (reverse)
            If identifiers(2) = "FandR" Or
identifiers(2) = "Reverse" Then


'***********************************
                'Get reverse bias data
                'and convert to quadrant 1
                Data1 =
Algorithms.Reverse_Data(Data0)

'***********************************



'***********************************
                'use desired algorithm
                Select Case identifiers(0)
                    Case Is = "Sean1"
                        output =
Algorithms.PVF_Sean_v1(Data1, settings(1))
                    Case Is = "Sean2"
                        output =
Algorithms.PVF_Sean_v2(Data1, settings(1))
                    Case Is = "David1"
                        output =
Algorithms.PVF_David_v1(Data1, settings(1))
                    Case Is = "David2"
                        output =
Algorithms.PVF_David_v2(Data1)
                    Case Is = "None"

                    Case Else
                        GoTo skip_analysis
                End Select

'***********************************

                If identifiers(0) <> "None"
Then


x2book.Worksheets("Extracted
Data").cells(row, 13).Value = Data1(0,
output(0)) 'Vpeak

x2book.Worksheets("Extracted
Data").cells(row, 14).Value = Data1(0,
output(1)) 'Vvalley

x2book.Worksheets("Extracted
Data").cells(row, 15).Value = Data1(1,
output(0))   'Ipeak

x2book.Worksheets("Extracted
Data").cells(row, 16).Value = Data1(1,
output(1))   'Ivalley

x2book.Worksheets("Extracted
Data").cells(row, 17).value = "=O" & row &
"/L" & row   'Jpeak

x2book.Worksheets("Extracted
Data").cells(row, 18).value = "=P" & row &
"/L" & row  'Jvalley

x2book.Worksheets("Extracted
Data").cells(row, 19).Value = "=O" & row &
"/P" & row  'PVCR
                End If


'***********************************
                'use desired algorithm
                Select Case identifiers(3)
                    Case Is = "Sean1"
                        output =
Algorithms.PVF_Sean_v1(Data1, settings(1))
                    Case Is = "Sean2"
                        output =
Algorithms.PVF_Sean_v2(Data1, settings(1))
                    Case Is = "David1"
                        output =
Algorithms.PVF_David_v1(Data1, settings(1))
                    Case Is = "David2"
                        output =
Algorithms.PVF_David_v2(Data1)
                    Case Is = "None"

                    Case Else
```

```
                    GoTo skip_analysis
                End Select

'************************************

                If identifiers(3) <> "None"
Then


x2book.Worksheets("Extracted
Data").cells(settings(0) + row + 3,
13).Value = Data1(0, output(0)) 'Vpeak

x2book.Worksheets("Extracted
Data").cells(settings(0) + row + 3,
14).Value = Data1(0, output(1)) 'Vvalley

x2book.Worksheets("Extracted
Data").cells(settings(0) + row + 3,
15).Value = Data1(1, output(0))   'Ipeak

x2book.Worksheets("Extracted
Data").cells(settings(0) + row + 3,
16).Value = Data1(1, output(1))   'Ivalley

x2book.Worksheets("Extracted
Data").cells(settings(0) + row + 3,
17).value = "=O" & settings(0) + row + 3 &
"/L" & settings(0) + row + 3   'Jpeak

x2book.Worksheets("Extracted
Data").cells(settings(0) + row + 3,
18).value = "=P" & settings(0) + row + 3 &
"/L" & settings(0) + row + 3  'Jvalley

x2book.Worksheets("Extracted
Data").cells(settings(0) + row + 3,
19).Value = "=O" & settings(0) + row + 3 &
"/P" & settings(0) + row + 3  'PVCR
                End If
            End If

'************************************
            'If there is a peak and valley
in quadrant 1 (Forward)
            If identifiers(2) = "FandR" Or
identifiers(2) = "Forward" Then


'************************************
                'Get reverse bias data
                'convert to quadrant 1
                Data1 =
Algorithms.Forward_Data(Data0)

'************************************



'************************************
                'use desired algorithm
                Select Case identifiers(0)
                    Case Is = "Sean1"
                        output =
Algorithms.PVF_Sean_v1(Data1, settings(1))
                    Case Is = "Sean2"
                        output =
Algorithms.PVF_Sean_v2(Data1, settings(1))
                    Case Is = "David1"
                        output =
Algorithms.PVF_David_v1(Data1, settings(1))
                    Case Is = "David2"
                        output =
Algorithms.PVF_David_v2(Data1)
                    Case Is = "None"

                    Case Else
                        GoTo skip_analysis
                End Select

'************************************

                If identifiers(0) <> "None"
Then


x2book.Worksheets("Extracted
Data").cells(row, 20).Value = Data1(0,
output(0)) 'Vpeak

x2book.Worksheets("Extracted
Data").cells(row, 21).Value = Data1(0,
output(1)) 'Vvalley

x2book.Worksheets("Extracted
Data").cells(row, 22).Value = Data1(1,
output(0))   'Ipeak

x2book.Worksheets("Extracted
Data").cells(row, 23).Value = Data1(1,
output(1))   'Ivalley

x2book.Worksheets("Extracted
Data").cells(row, 24).value = "=V" & row &
"/L" & row   'Jpeak

x2book.Worksheets("Extracted
Data").cells(row, 25).value = "=W" & row &
"/L" & row   'Jvalley

x2book.Worksheets("Extracted
Data").cells(row, 26).Value = "=V" & row &
"/W" & row   'PVCR
                End If


'************************************
                'use desired algorithm
                Select Case identifiers(3)
                    Case Is = "Sean1"
                        output =
Algorithms.PVF_Sean_v1(Data1, settings(1))
                    Case Is = "Sean2"
                        output =
Algorithms.PVF_Sean_v2(Data1, settings(1))
                    Case Is = "David1"
                        output =
Algorithms.PVF_David_v1(Data1, settings(1))
                    Case Is = "David2"
                        output =
Algorithms.PVF_David_v2(Data1)
                    Case Is = "None"

                    Case Else
```

```
                GoTo skip_analysis
            End Select

'***********************************

            If identifiers(3) <> "None"
Then


x2book.Worksheets("Extracted
Data").cells(settings(0) + row + 3,
20).Value = Data1(0, output(0)) 'Vpeak

x2book.Worksheets("Extracted
Data").cells(settings(0) + row + 3,
21).Value = Data1(0, output(1)) 'Vvalley

x2book.Worksheets("Extracted
Data").cells(settings(0) + row + 3,
22).Value = Data1(1, output(0))   'Ipeak

x2book.Worksheets("Extracted
Data").cells(settings(0) + row + 3,
23).Value = Data1(1, output(1))   'Ivalley

x2book.Worksheets("Extracted
Data").cells(settings(0) + row + 3,
24).value = "=V" & (settings(0) + row + 3) &
"/L" & (settings(0) + row + 3)  'Jpeak

x2book.Worksheets("Extracted
Data").cells(settings(0) + row + 3,
25).value = "=W" & (settings(0) + row + 3) &
"/L" & (settings(0) + row + 3)  'Jvalley

x2book.Worksheets("Extracted
Data").cells(settings(0) + row + 3,
26).Value = "=V" & (settings(0) + row + 3) &
"/W" & (settings(0) + row + 3)  'PVCR
            End If

        End If

'***********************************


        Select Case Units.Text
                Case Is = "cm"
                    scalar = 1
                Case Is = "um"
                    scalar = 0.0001
                Case Is = "nm"
                    scalar = 0.0000001
            End Select


            Select Case Geometry.Text
                Case Is = "Length (sq)"

x2book.Worksheets("Extracted
Data").cells(row, 9).value = "=G" & (row)

x2book.Worksheets("Extracted
Data").cells(row, 10).value = "=G" & (row)

x2book.Worksheets("Extracted
Data").cells(row, 12).value = "=(" & scalar
& "*K" & row & ")^2"  'Area(row - 1)  'area
                Case Is = "Radius"

x2book.Worksheets("Extracted
Data").cells(row, 9).value = "=2*G" & (row)

x2book.Worksheets("Extracted
Data").cells(row, 10).value = "=2*G" & (row)

x2book.Worksheets("Extracted
Data").cells(row, 12).value = "=PI()*(" &
scalar & "*K" & row & "/2)^2"  'Area(row -
1)  'area
                Case Is = "Diameter"

x2book.Worksheets("Extracted
Data").cells(row, 9).value = "=G" & (row)

x2book.Worksheets("Extracted
Data").cells(row, 10).value = "=G" & (row)

x2book.Worksheets("Extracted
Data").cells(row, 12).value = "=PI()*(" &
scalar & "*K" & row & "/2)^2"  'Area(row -
1)  'area
                Case Is = "Area"
x2book.Worksheets("Extracted
Data").cells(row, 9).value = "=2*sqrt(G" &
(row) & "/pi())"

x2book.Worksheets("Extracted
Data").cells(row, 10).value = "=2*sqrt(G" &
(row) & "/pi())"

x2book.Worksheets("Extracted
Data").cells(row, 12).value = "=PI()*(" &
scalar & "*K" & row & "/2)^2"   'Area(row -
1)  'area
            End Select

        Next
        '

'********************************************
***


'********************************************
***
        'Send x1Book to find_outliers
function
        'calculating averages and standard
deviations
        'flagging 1-2 sigma (yello), 2-3
sigma (orange), > 3 sigma (red)
        Messages2.Text = "Finding Outliers"
        Messages2.Refresh()

        x1sheet =
x2book.Worksheets("Extracted Data")
        If identifiers(0) <> "None" Then
            find_outliers(x1sheet,
identifiers(2))
        End If
        '

'********************************************
***
```

```
skip_analysis:
        x2book.Save()
        x2book.Close()
end_of_program:
        x1App.Quit()
        x2App.Quit()
    End Sub

    Public Function GetFileName() As Array
        Dim path(3), FileName(2),
FileText(), FullName(), Name() As String
        Dim SReader As
System.IO.StreamReader
        Dim SWriter As
System.IO.StreamWriter
        Dim OpenDir As New
FolderBrowserDialog
        Dim OpenFile As New OpenFileDialog
        Dim counter, count, i, j As Integer

        'Get path of default directory text
file
        path(0) =
System.IO.Directory.GetCurrentDirectory() &
"\default_directory.txt"

        If System.IO.File.Exists(path(0)) =
True Then 'does the text file exist?

            SReader =
System.IO.File.OpenText(path(0)) 'Open text
file
            path(1) = SReader.ReadLine
'Read text (first line is last opened
directory)
            SReader.Close()
'Close stream reader

            If
System.IO.Directory.Exists(path(1)) = False
Then  'Does directory exist?
                SWriter =
System.IO.File.CreateText(path(0))
                OpenDir.SelectedPath =
System.IO.Directory.GetCurrentDirectory()
                If OpenDir.ShowDialog =
DialogResult.OK Then
                    path(1) =
OpenDir.SelectedPath
                Else
                    path(1) =
System.IO.Directory.GetCurrentDirectory()
                End If
                SWriter.WriteLine(path(1))
                SWriter.Close()
            End If
        Else
            SWriter =
System.IO.File.CreateText(path(0))
            OpenDir.SelectedPath =
System.IO.Directory.GetCurrentDirectory()
            If OpenDir.ShowDialog =
DialogResult.OK Then
                path(1) =
OpenDir.SelectedPath
            Else
                path(1) =
System.IO.Directory.GetCurrentDirectory()
            End If
            SWriter.WriteLine(path(1))
            SWriter.Close()
        End If

        OpenFile.Multiselect = True
        OpenFile.InitialDirectory = path(1)
        If OpenFile.ShowDialog =
DialogResult.OK Then
            FullName = OpenFile.FileNames
            Name = OpenFile.SafeFileNames
            count = FullName.Length - 1
            ReDim FileName(2 * (count + 1))

            For j = 0 To count Step 1
                FileName(2 * j + 1) =
FullName(j)
                FileName(2 * j + 2) =
Name(j)
                For i = 1 To FileName(2 * j
+ 2).Length Step 1
                    If Mid(FileName(2 * j +
2), FileName(2 * j + 2).Length - i + 1, 1) =
"." Then
                        FileName(2 * j + 2)
= Mid(FileName(2 * j + 2), 1, FileName(2 * j
+ 2).Length - i) & ".xlsx"
                    End If
                Next
            Next

            SReader =
System.IO.File.OpenText(path(0)) 'Open text
file
            i = 0
            Do
                ReDim Preserve FileText(i)
                FileText(i) =
SReader.ReadLine
                i = i + 1
            Loop While SReader.Peek <> -1
            SReader.Close()

            counter =
OpenFile.SafeFileName.Length
            path(2) = Mid(FileName(1), 1,
(FileName(1).Length - counter))
            FileText(0) = path(2)

            SWriter =
System.IO.File.CreateText(path(0))
            For i = 0 To FileText.Length - 1
Step 1

SWriter.WriteLine(FileText(i))
            Next

            SWriter.Close()
            FileName(0) = path(2)
        Else
            FileName(1) = "False"
        End If


        Return FileName
    End Function

    Public Function analize_name(ByVal FName
As String) As Array ',
        Dim count(2), size As Integer ',
start, i, j As Integer
```

```
        Dim str, AFP(3) As String

        If AFP(0) = "" Then
            Dim GetAlg As New Get_Algorithm
            GetAlg.ShowDialog()
            AFP(0) = GetAlg.Selected_Alg
        End If

        If AFP(1) = "" Then
            Dim GetFormat As New
Get_FileFormat
            GetFormat.ShowDialog()
            AFP(1) =
GetFormat.Selected_Format
        End If

        If AFP(2) = "" Then
            Dim GetFR As New FandR_Peaks
'PIVET.FandR_Peaks
            GetFR.ShowDialog()
            AFP(2) = GetFR.selected_FR
        End If

        AFP(3) = ""

        Return AFP
    End Function

    Public Sub find_outliers(ByVal xlsheet
As Microsoft.Office.Interop.Excel.Worksheet,
ByVal Fand_orR As String)
        Dim i, j, k, l, row_count, color,
col_mod As Integer
        Dim Data0(,), averages(), STDev() As
Double
        Dim col(4) As Char

        row_count =
xlsheet.Application.WorksheetFunction().Coun
tA(xlsheet.Range("A:A")) - 2
        xlsheet.Cells(row_count + 3, 1) =
"Average"
        xlsheet.Cells(row_count + 4, 1) =
"STDev"

        For l = 0 To 1 Step 1
            ReDim Data0(4, row_count),
averages(4), STDev(4)

            If l = 0 Then
                If Fand_orR = "FandR" Or
Fand_orR = "Forward" Then
                    col_mod = 12
                    col(0) = "L"
                    col(1) = "M"
                    col(2) = "P"
                    col(3) = "Q"
                    col(4) = "R"
                End If
            Else
                If Fand_orR = "FandR" Or
Fand_orR = "Reverse" Then
                    col_mod = 5
                    col(0) = "E"
                    col(1) = "F"
                    col(2) = "I"
                    col(3) = "J"
                    col(4) = "K"
                End If
            End If

            For i = 0 To row_count Step 1
                Data0(0, i) =
xlsheet.Cells(i + 2, col_mod).value()
                Data0(1, i) =
xlsheet.Cells(i + 2, col_mod + 1).value()
                Data0(2, i) =
xlsheet.Cells(i + 2, col_mod + 4).value()
                Data0(3, i) =
xlsheet.Cells(i + 2, col_mod + 5).value()
                Data0(4, i) =
xlsheet.Cells(i + 2, col_mod + 6).value()
                For j = 0 To 4 Step 1
                    averages(j) = Data0(j,
i) / (row_count + 1) + averages(j)
                Next
            Next

            xlsheet.Cells(row_count + 3,
col_mod).value() = "=AVERAGE(" & col(0) &
"2:" & col(0) & (row_count + 2) & ")"
'averages(0)"
            xlsheet.Cells(row_count + 3,
col_mod + 1).value() = "=AVERAGE(" & col(1)
& "2:" & col(1) & (row_count + 2) & ")"
'averages(1)
            xlsheet.Cells(row_count + 3,
col_mod + 4).value() = "=AVERAGE(" & col(2)
& "2:" & col(2) & (row_count + 2) & ")"
'averages(2)
            xlsheet.Cells(row_count + 3,
col_mod + 5).value() = "=AVERAGE(" & col(3)
& "2:" & col(3) & (row_count + 2) & ")"
'averages(3)
            xlsheet.Cells(row_count + 3,
col_mod + 6).value() = "=AVERAGE(" & col(4)
& "2:" & col(4) & (row_count + 2) & ")"
'averages(4)


            If row_count <> 0 Then
                For j = 0 To 4 Step 1
                    For i = 0 To row_count
Step 1
                        STDev(j) = STDev(j)
+ (averages(j) - Data0(j, i)) ^ 2
                    Next
                    STDev(j) = (STDev(j) /
row_count) ^ 0.5
                Next

                xlsheet.Cells(row_count + 4,
col_mod).value() = "=STDEV(" & col(0) & "2:"
& col(0) & (row_count + 2) & ")"
'averages(0)"
                xlsheet.Cells(row_count + 4,
col_mod + 1).value() = "=STDEV(" & col(1) &
"2:" & col(1) & (row_count + 2) & ")"
'averages(1)
                xlsheet.Cells(row_count + 4,
col_mod + 4).value() = "=STDEV(" & col(2) &
"2:" & col(2) & (row_count + 2) & ")"
'averages(2)
                xlsheet.Cells(row_count + 4,
col_mod + 5).value() = "=STDEV(" & col(3) &
"2:" & col(3) & (row_count + 2) & ")"
'averages(3)
                xlsheet.Cells(row_count + 4,
col_mod + 6).value() = "=STDEV(" & col(4) &
```

```
"2:" & col(4) & (row_count + 2) & ")"
'averages(4)

                For j = 1 To 3 Step 1
                    Select Case j
                        Case Is = 1
                            color = 65535
                        Case Is = 2
                            color = 49407
                        Case Is = 3
                            color = 255
                    End Select

                    For i = 0 To row_count
Step 1

                        For k = 0 To 1 Step
1
                            If j * STDev(k)
< Abs(averages(k) - Data0(k, i)) Then

x1sheet.Cells(i + 2, k + col_mod).select()
                                With
x1sheet.Application.Selection.interior
                                    .color =
color

.tintandshade = 0

.patterntintandshade = 0
                                End With
                            End If
                        Next

                        For k = 4 To 6 Step
1
                            If j * STDev(k -
2) < Abs(averages(k - 2) - Data0(k - 2, i))
Then

x1sheet.Cells(i + 2, col_mod + k).select()
                                With
x1sheet.Application.Selection.interior
                                    .color =
color

.tintandshade = 0

.patterntintandshade = 0
                                End With
                            End If
                        Next

                    Next
                Next
            End If
        Next
    End Sub

    Public Function DieLocation(ByVal
FileName As String) As Double

    End Function

    Private Sub Button1_Click(ByVal sender
As System.Object, ByVal e As
System.EventArgs) Handles Button1.Click
        Dim FileName(), identifiers(3),
SendFileNames(2) As String
        Dim FileNumber(1), FileCount, i,
RowCount, row As Integer
        Dim x1app As New
Microsoft.Office.Interop.Excel.Application
        Dim X1Book, X2Book As
Microsoft.Office.Interop.Excel.Workbook
        Dim X1Sheet, X2Sheet As
Microsoft.Office.Interop.Excel.Worksheet


'*********************************************
***
        'Get Filename information:
        '    (1)  path\file_name
        '    (0)  path\
        '    (2)  \file_name.
        FileName = GetFileName()
        If FileName(0) = "False" Then
            Messages1.Text = "No File"
            Messages2.Text = "No File"
            Messages1.Refresh()
            Messages2.Refresh()
            GoTo TheEnd
        Else
            Messages1.Text = "Let's Get
Started"
            Messages2.Text = "Let's Get
Started"
            Messages1.Refresh()
            Messages2.Refresh()
        End If
        FileCount = (FileName.Count - 1) / 2
        '

'*********************************************
***


'*********************************************
***
        'Create output excel file
        x1app.Visible = False
        x1app.DisplayAlerts = False
        If System.IO.File.Exists(FileName(0)
+ "Compiled.xlsx") = True Then
            X2Book =
x1app.Workbooks.Open(FileName(0) +
"Compiled.xlsx")
        Else
            X2Book = x1app.Workbooks.Add
            X2Book.SaveAs(FileName(0) +
"Compiled.xlsx")
            X2Book.Worksheets(1).name =
"Extracted Data"
            X2Book.Worksheets("Extracted
Data").cells(1, 1).value = "File Name"
            X2Book.Worksheets("Extracted
Data").cells(1, 2).value = "Append"
            X2Book.Worksheets("Extracted
Data").cells(1, 3).value = "X"
            X2Book.Worksheets("Extracted
Data").cells(1, 4).value = "Y"
            X2Book.Worksheets("Extracted
Data").cells(1, 5).value = "Grid"
            X2Book.Worksheets("Extracted
Data").cells(1, 6).value = "Temperature"
            X2Book.Worksheets("Extracted
Data").cells(1, 7).value = Geometry.Text & "
(" & Units.Text & ")"
```

```
            X2Book.Worksheets("Extracted
Data").cells(1, 8).value = "Undercut"
            X2Book.Worksheets("Extracted
Data").cells(1, 9).value = "Width (X)"
            X2Book.Worksheets("Extracted
Data").cells(1, 10).value = "Height (Y)"
            X2Book.Worksheets("Extracted
Data").cells(1, 11).value = "Diameter (um)"
            X2Book.Worksheets("Extracted
Data").cells(1, 12).value = "Area (cm2)"
            X2Book.Worksheets("Extracted
Data").cells(1, 13).value = "Vp (Rev.)"
            X2Book.Worksheets("Extracted
Data").cells(1, 14).value = "Vv (Rev.)"
            X2Book.Worksheets("Extracted
Data").cells(1, 15).value = "Ip (Rev.)"
            X2Book.Worksheets("Extracted
Data").cells(1, 16).value = "Iv (Rev.)"
            X2Book.Worksheets("Extracted
Data").cells(1, 17).value = "Jp (A/cm2)"
            X2Book.Worksheets("Extracted
Data").cells(1, 18).value = "Jv (A/cm2)"
            X2Book.Worksheets("Extracted
Data").cells(1, 19).value = "PVCR (Rev.)"
            X2Book.Worksheets("Extracted
Data").cells(1, 20).value = "Vp (For.)"
            X2Book.Worksheets("Extracted
Data").cells(1, 21).value = "Vv (For.)"
            X2Book.Worksheets("Extracted
Data").cells(1, 22).value = "Ip (For.)"
            X2Book.Worksheets("Extracted
Data").cells(1, 23).value = "Iv (For.)"
            X2Book.Worksheets("Extracted
Data").cells(1, 24).value = "Jp (A/cm2)"
            X2Book.Worksheets("Extracted
Data").cells(1, 25).value = "Jv (A/cm2)"
            X2Book.Worksheets("Extracted
Data").cells(1, 26).value = "PVCR (For.)"
            X2Book.Save()
        End If
        X2Sheet =
X2Book.Worksheets("Extracted Data")

        For i = 1 To FileCount Step 1
            Messages1.Text = "File #" & i &
" of " & FileCount
            Messages1.Refresh()
            Messages2.Text = FileName(i * 2)
            Messages2.Refresh()
            X1Book =
xlapp.Workbooks.Open(FileName(i * 2 - 1))
            X1Sheet =
X1Book.Worksheets("Extracted Data")
            RowCount =
X1Sheet.Application.WorksheetFunction.CountA
(X1Sheet.Range("B:B")) - 1
            If RowCount > 0 Then
                row =
X2Sheet.Application.WorksheetFunction.CountA
(X2Sheet.Range("B:B")) + 1
                X2Sheet.Cells(row,
1).resize(RowCount, 26).value =
X1Sheet.Cells(2, 1).resize(RowCount,
26).value
                X2Book.Save()
            End If
        Next

        X2Book.Save()
        X2Book.Close()
        X1Book.Close()

TheEnd:
        xlapp.Quit()

        Messages1.Text = "Done"
        Messages1.Refresh()
        Messages2.Text = "Done"
        Messages2.Refresh()

    End Sub
End Class
```

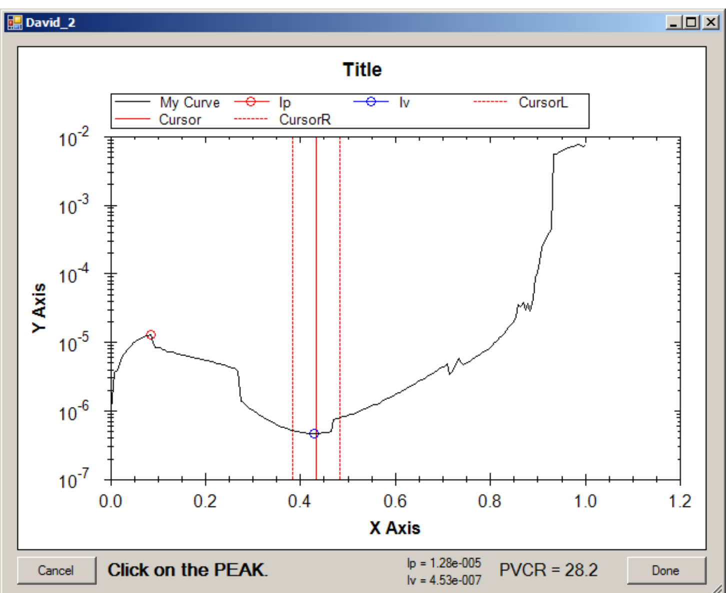

Appendix D.2: Window for manually picking peak and valley locations (algorithm David-2).

After execution a series of windows will open asking for desired input information. If selected, the David-2 algorithm will open a new window displaying the current I-V characteristic, and requires the user to point out the peak and valley (Appendix D.2). The following code is associated with the “David-2” algorithm.

```
Public Class David_2

    Public values(1), index(1) As Integer

    Private Sub David_2_Load(ByVal sender As
System.Object, ByVal e As System.EventArgs)
Handles MyBase.Load
        Label1.Text = "Click on the PEAK."

        Dim LastIndex, IndexWidth, IndexMain
As Integer
        Dim mypane As GraphPane =
zg1.GraphPane
        Dim list As IPointListEdit
        Dim dataL = New PointPairList
        Dim dataM = New PointPairList
        Dim dataR = New PointPairList
        Dim Peak = New PointPairList
        Dim Valley = New PointPairList
        list = mypane.CurveList("My
Curve").Points
        LastIndex = list.Count - 1
        IndexMain = Int(LastIndex / 2)
        IndexWidth = Int(LastIndex / 20)


        dataL.Add(list(IndexMain -
IndexWidth).X, mypane.YAxis.Scale.Min)
        dataL.Add(list(IndexMain -
IndexWidth).X, mypane.YAxis.Scale.Max)

        dataM.Add(list(IndexMain).X,
mypane.YAxis.Scale.Min)
        dataM.Add(list(IndexMain).X,
mypane.YAxis.Scale.Max)

        dataR.Add(list(IndexMain +
IndexWidth).X, mypane.YAxis.Scale.Min)
        dataR.Add(list(IndexMain +
IndexWidth).X, mypane.YAxis.Scale.Max)

        Dim myCurveL As LineItem =
mypane.AddCurve("CursorL", dataL, Color.Red,
SymbolType.None)
        myCurveL.Line.Style =
Drawing2D.DashStyle.Dash
        Dim myCurve As LineItem =
mypane.AddCurve("Cursor", dataM, Color.Red,
SymbolType.None)
        Dim myCurveR As LineItem =
mypane.AddCurve("CursorR", dataR, Color.Red,
SymbolType.None)
        myCurveR.Line.Style =
Drawing2D.DashStyle.Dash

        Peak.Add(list(IndexMain).X,
list(IndexMain).Y)
        Dim PeakPoint As LineItem =
mypane.AddCurve("Ip", Peak, Color.Red,
SymbolType.Circle)
        Valley.Add(list(IndexMain).X,
list(IndexMain).Y)
        Dim ValleyPoint As LineItem =
mypane.AddCurve("Iv", Peak, Color.Blue,
SymbolType.Circle)
    End Sub

    Public Sub New(ByVal data2(,) As Double,
ByVal length As Integer)

        InitializeComponent()

        Dim i As Integer
        Dim mypane As GraphPane =
zg1.GraphPane
        Dim data = New PointPairList

        For i = 0 To length Step 1
            data.Add(data2(0, i), data2(1,
i))
        Next

        Dim myCurve As LineItem =
mypane.AddCurve("My Curve", data,
Color.Black, SymbolType.None)
        mypane.YAxis.Type = AxisType.Log
        zg1.AxisChange()
        zg1.Refresh()

    End Sub

    Private Sub zg1_MouseMove(ByVal sender
As ZedGraph.ZedGraphControl, ByVal e1 As
System.Windows.Forms.MouseEventArgs) Handles
zg1.MouseMove
        ' Save the mouse location
        Dim mousePt As New PointF(e1.X,
e1.Y) '(e.X, e.Y)

        ' Find the Chart rect that contains
the current mouse location
        Dim pane As GraphPane =
sender.MasterPane.FindChartRect(mousePt)

        ' If pane is non-null, we have a
valid location.  Otherwise, the mouse is not
        ' within any chart rect.
        If Not pane Is Nothing Then

            Dim x, y As Double
            ' Convert the mouse location to
X, Y scale values
```

```
            pane.ReverseTransform(mousePt,
x, y)

            Dim curve1 As CurveItem
            Dim list As IPointListEdit
            Dim i As Integer
            Dim mypane As GraphPane =
zg1.GraphPane
            Dim LastIndex, IndexWidth,
TempIndex As Integer
            Dim dataL = New PointPairList
            Dim dataM = New PointPairList
            Dim dataR = New PointPairList

            curve1 =
zg1.GraphPane.CurveList("My Curve")
            list = curve1.Points
            LastIndex = list.Count - 1

            For i = 0 To (LastIndex - 1)
Step 1
                If list(i).X > x Then

                    If (list(i).X - x) < (x
- list(i - 1).X) Then
                        TempIndex = i
                    Else
                        TempIndex = i - 1
                    End If


zg1.GraphPane.CurveList.Remove(zg1.GraphPane
.CurveList("CursorL"))

zg1.GraphPane.CurveList.Remove(zg1.GraphPane
.CurveList("Cursor"))

zg1.GraphPane.CurveList.Remove(zg1.GraphPane
.CurveList("CursorR"))

                    IndexWidth =
Int(LastIndex / 20)

                    If (TempIndex -
IndexWidth) < 0 Then
                        dataL.Add(list(0).X,
mypane.YAxis.Scale.Min)
                        dataL.Add(list(0).X,
mypane.YAxis.Scale.Max)
                    Else

dataL.Add(list(TempIndex - IndexWidth).X,
mypane.YAxis.Scale.Min)

dataL.Add(list(TempIndex - IndexWidth).X,
mypane.YAxis.Scale.Max)
                    End If


dataM.Add(list(TempIndex).X,
mypane.YAxis.Scale.Min)

dataM.Add(list(TempIndex).X,
mypane.YAxis.Scale.Max)

                    If (TempIndex +
IndexWidth) > LastIndex Then

dataR.Add(list(LastIndex).X,
mypane.YAxis.Scale.Min)

dataR.Add(list(LastIndex).X,
mypane.YAxis.Scale.Max)
                    Else

dataR.Add(list(TempIndex + IndexWidth).X,
mypane.YAxis.Scale.Min)

dataR.Add(list(TempIndex + IndexWidth).X,
mypane.YAxis.Scale.Max)
                    End If

                    If Label1.Text = "Click
on the PEAK." Then
                        Dim myCurveL As
LineItem = mypane.AddCurve("CursorL", dataL,
Color.Red, SymbolType.None)
                        myCurveL.Line.Style
= Drawing2D.DashStyle.Dash
                        Dim myCurve As
LineItem = mypane.AddCurve("Cursor", dataM,
Color.Red, SymbolType.None)
                        Dim myCurveR As
LineItem = mypane.AddCurve("CursorR", dataR,
Color.Red, SymbolType.None)
                        myCurveR.Line.Style
= Drawing2D.DashStyle.Dash
                    Else
                        Dim myCurveL As
LineItem = mypane.AddCurve("CursorL", dataL,
Color.Blue, SymbolType.None)
                        myCurveL.Line.Style
= Drawing2D.DashStyle.Dash
                        Dim myCurve As
LineItem = mypane.AddCurve("Cursor", dataM,
Color.Blue, SymbolType.None)
                        Dim myCurveR As
LineItem = mypane.AddCurve("CursorR", dataR,
Color.Blue, SymbolType.None)
                        myCurveR.Line.Style
= Drawing2D.DashStyle.Dash
                    End If


                    If (TempIndex -
IndexWidth) < 0 Then
                        index(0) = 0
                    Else
                        index(0) = TempIndex
- IndexWidth
                    End If

                    If (TempIndex +
IndexWidth) > LastIndex Then
                        index(1) = LastIndex
                    Else
                        index(1) = TempIndex
+ IndexWidth
                    End If

                    i = LastIndex + 1
                End If
            Next

            zg1.Refresh()

        End If
        Return
    End Sub
```

```
    Private Sub zg1_click(ByVal sender As
System.Object, ByVal e1 As
System.Windows.Forms.MouseEventArgs) Handles
zg1.Click
        ' Save the mouse location
        Dim mousePt As New PointF(e1.X,
e1.Y)

        ' Find the Chart rect that contains
the current mouse location
        Dim pane As GraphPane =
sender.MasterPane.FindChartRect(mousePt)

        ' If pane is non-null, we have a
valid location.  Otherwise, the mouse is not
        ' within any chart rect.
        If Not pane Is Nothing Then

            Select Case Label1.Text
                Case Is = "Click on the
PEAK."
                    Max(index(0), index(1))
                    Label1.Text = "Click on
the VALLEY."
                    Label2.Text = "Ip = " &
zg1.GraphPane.CurveList("My
Curve").Points(values(0)).Y.ToString("e2")
                Case Is = "Click on the
VALLEY."
                    Min(index(0), index(1))
                    Label1.Text = "Click on
the PEAK."
                    Label3.Text = "Iv = " &
zg1.GraphPane.CurveList("My
Curve").Points(values(1)).Y.ToString("e2")
            End Select

            If zg1.GraphPane.CurveList("My
Curve").Points(values(1)).Y <> 0 Then
                Label4.Text = "PVCR = " &
(zg1.GraphPane.CurveList("My
Curve").Points(values(0)).Y /
zg1.GraphPane.CurveList("My
Curve").Points(values(1)).Y).ToString("F1")
            End If
        End If
            Label1.Refresh()

            Return
        End Sub

    Private Sub Done_Click(ByVal sender As
System.Object, ByVal e As System.EventArgs)
Handles Done.Click
        Me.Close()
    End Sub

    Private Sub Cancel_Click(ByVal sender As
System.Object, ByVal e As System.EventArgs)
Handles Cancel.Click
        Dim i As Integer
        For i = 0 To 1 Step 1
            values(i) = 0
        Next

        Me.Close()
    End Sub

    Private Sub Max(ByVal IndexL As Integer,
ByVal IndexR As Integer)
        Dim i As Integer
        Dim Ip As Double
        Dim mypane As GraphPane =
zg1.GraphPane
        Dim list As IPointListEdit
        Dim Peak = New PointPairList

        list = mypane.CurveList("My
Curve").Points
        Ip = 0
        For i = IndexL To IndexR Step 1
            If list(i).Y > Ip Then
                Ip = list(i).Y
                values(0) = i
            End If
        Next


zg1.GraphPane.CurveList.Remove(zg1.GraphPane
.CurveList("Ip"))
        Peak.Add(list(values(0)).X,
list(values(0)).Y)
        Dim PeakPoint As LineItem =
mypane.AddCurve("Ip", Peak, Color.Red,
SymbolType.Circle)

    End Sub

    Private Sub Min(ByVal IndexL As Integer,
ByVal IndexR As Integer)
        Dim i As Integer
        Dim Iv As Double
        Dim mypane As GraphPane =
zg1.GraphPane
        Dim list As IPointListEdit
        Dim Peak = New PointPairList
        Dim Valley = New PointPairList

        Peak = mypane.CurveList("Ip").Points
        list = mypane.CurveList("My
Curve").Points
        Iv = Peak(0).Y
        For i = IndexL To IndexR Step 1
            If list(i).Y < Iv Then
                Iv = list(i).Y
                values(1) = i
            End If
        Next


zg1.GraphPane.CurveList.Remove(zg1.GraphPane
.CurveList("Iv"))
        Valley.Add(list(values(1)).X,
list(values(1)).Y)
        Dim ValleyPoint As LineItem =
mypane.AddCurve("Iv", Valley, Color.Blue,
SymbolType.Circle)

    End Sub

End Class
```